The Use of Pulsed Electron Beams to Extend TEM Capabilities

A Dissertation
SUBMITTED TO THE FACULTY OF
UNIVERSITY OF MINNESOTA
BY

Elisah J. VandenBussche

IN PARTIAL FULFILLMENT OF THE REQUIREMENTS
FOR THE DEGREE OF
DOCTOR OF PHILOSOPHY

Prof. David J. Flannigan, Advisor

July 2021

© Elisah J. VandenBussche, 2021

Acknowledgments

First and foremost, I would like to thank my advisor, Dave Flannigan. The constant reminders to stay curious and careful guidance on how to satisfy that curiosity carefully and ethically have made me a better scientist and person. The group culture he has taken great pains to establish is collaborative and supportive, and is the only reason I'm here today, finishing up my PhD with my sanity intact. Most of all, throughout my time at the University of Minnesota, Dave has seen and supported me as a whole person and not just a researcher, fostering and encouraging me to pursue my passions even when they took time away from my research. He has been a mentor in the truest sense of the word and I cannot thank him enough.

Speaking of that great group culture, I would also certainly not be here (not least because we'd never have a working microscope) if not for the rest of the Flannigan group, both current and alumni. Thank you all for your time, your willingness be a second set of eyes on my code or the laser table when I got stuck, and your fun conversation in that closet of an office. I truly wish I hadn't missed out on the last year of time with you all in that space, because I learned so much from you and always enjoyed the camaraderie we shared. I'm so glad to have known and worked with each of you. An extra thank you and shout out to the UEM maintenance team, both past (Spencer and Ryan) and present (Dan, Wyatt, and Jialiang). Your commitment to keeping the lab running is the lifeblood of the group, and I hope you all know how grateful I am for your time.

I'd also like to thank the many mentors outside of my research that helped me grow and figure out my next steps. Samira Azarin, for modeling caring and effective teaching and eventually giving me the opportunity to take on a Unit Ops section; I learned so much

from her and from the students I was lucky enough to work with. Megan Voorhees at the Institute on the Environment for fostering an empowering environment and deep, thoughtful conversations through which I've discovered invaluable aspects of leadership and service to community. Elise Harrington for including me thoroughly into her Science, Technology and Environmental Policy course and for her enthusiastic willingness to help me make a career transition that is pretty intimidating. Dorothy Cheng for taking a chance on me in my first formal leadership role at UMN, where I got a glimpse into the inner workings of higher education and a better understanding of the equity issues that students face. And of course all the peer mentors, especially the women in CEMS and in CSE, who shared their struggles and their triumphs and showed me what it means to extend a hand as we scale the STEM education ladder together, rather than pulling it up behind us as we climb.

I also want to thank those that made CEMS feel like a home, instead of a job, throughout my time here. Julie and Teresa, without whom I'm confident the department would regularly implode, for always being there to help us navigate all aspects of graduate school. My first-year cohort, who got me through certainly the most imposter-syndrome-inducing year of my life. My roundtable committee and all the other committees who have done the job since I arrived, who built an environment of camaraderie and created a space to continuously connect with my fellow members of CEMS. The older students, especially Mark, Boo, Tom, Ron, Dayne, Frankie, and Mia, for passing on their traditions and including me so thoroughly into the CEMS culture from the moment I arrived. The lifelong friends I made in this department, for all the nights and weekends of blowing off steam, talking about science and decidedly *not* talking about science. And of course, Matt Palys:

we met when he was driving the welcome wagon my first week in CEMS, and now we're leaving, married. Being in CEMS has changed my life permanently and for the better, so thank you to everyone who was a part of that.

And last but certainly not least, I would like to thank my parents and my brother, for all their support, for all the good times visiting and traveling together during my PhD, for their forgiveness when I didn't call regularly, and for a great relationship that continues to be formative.

Dedication

This thesis is dedicated to my parents, who raised me never to doubt that I could do whatever I set my mind to. You taught me that life is about what you do with what you're given, and that continues to guide me. Thank you for everything. I love you.

Abstract

Due to the high resolutions and high scattering cross-sections accessible using fast electrons, characterization of electronic materials using transmission electron microscopy (TEM) is indispensable in applied materials science and engineering. Modern TEMs are highly versatile, allowing high resolution characterization of structure and morphology, chemical analysis, beam-induced current mapping or even ultrafast structural dynamics at high spatial resolution. This dissertation discusses three ways in which pulsed electron beams can be used to extend these capabilities even further.

First, the push to shrink dimensionality, and the subsequent impact of thermal effects, has led to the development of methods capable of being used to quantify nanoscale thermal transport. In order to use pulsed electron beams to determine transient temperatures at atomic length scales, it is possible to rely upon the Debye-Waller (DW) effect, in which the attenuation of Bragg scattering is related to atomic thermal energies. However, other factors, in addition to mean atomic displacements, can affect (and even dominate) the intensity of Bragg reflections, distorting the measurement. In this work, the degree to which structural specimen effects impact thermal measurements are quantitatively studied in order to better facilitate the use of pulsed electron beams to determine transient specimen temperatures.

Second, the process by which photoexcited semiconductors return to the ground state consists of a series of strongly-correlated, many-body interactions which overlap in space and time. Such behaviors have both fundamental and practical implications, which include insights into the quantum nature of matter and control of device and materials behaviors in electronic and optoelectronic applications. Because the behavior of collective

lattice oscillations depends on the structural and electronic properties of the material through which they propagate, coherent acoustic phonons (CAPs) resulting from such properties can be used as an intrinsic, multi-faceted characterization tool. Indeed, optical CAP spectroscopy has been used to access depth-dependent structural properties of materials and buried interfaces, but is limited in its in-plane spatial resolution. In this work, we demonstrate an analogous CAP spectroscopy using UEM, in which CAP phase velocity measured in real space is shown to be sensitive to changes in atomic structure. This facilitates future work in using UEM to access spatially-resolved information about buried structures and optoelectronic properties *via* high-resolution, real-space measurements.

Third, the energy with which electrons propagate in the TEM column leads inevitably to damage, which particularly limits the study of radiation-soft materials such as organic materials, biological specimens, and any other samples containing low-Z atoms. In this work, we show that pulsed electron beams can be used to mitigate the damage caused to organic specimens compared to a stochastically-emitted electron beam. We demonstrate this effect both in the organic crystal hexatriacontane and in the hybrid metal halide perovskite, methylammonium lead iodide. Further, the temporal manipulation of pulsed beams can be leveraged to gain kinetic insights into the processes of beam damage. We show preliminary results in which the disparate damage rates in perovskites potentially elucidate a novel step in the damage mechanism.

Table of Contents

Acknowledgments i

Dedication iv

Abstract v

Table of Contents vii

List of Tables x

List of Figures xi

Chapter 1 | Introduction 1
1.1 | Pulsed Beams in TEM: A History of Increasing Time Resolution 3
1.1.1 State-of-the-art TEM capabilities 3
1.1.2 Overcoming Detector-Limited time Resolution: Pump-Probe Microscopy... 8
1.1.3 Early Approaches to Fast TEM 15
1.1.4 Advent of Femtosecond TEM 16
1.2 | Thermal Measurements in Ultrafast Experiments 18
1.2.1 TEM In Situ Thermometry Techniques 19
1.2.2 Debye Waller Effect 21
1.3 | Coherent Acoustic Phonon Spectroscopy 23
1.3.1 Post-Photoexcitation Energy Dissipation in Semiconductors 23
1.3.2 Phonons as a Characterization Tool 25
1.4 | Electron Beam Damage 27
1.4.1 Radiation Damage in Organic Materials 27
1.4.2 Beam Damage and Degradation in Halide Perovskites 30
1.4.3 Pulsed Beams as Damage Mitigation 32
1.4.4 Pulsed Beams as a Kinetic Tool 34

Chapter 2 | Equipment & Methods 37
2.1 | Specimen Preparation 37
2.1.1 Aluminum 37
2.1.2 Gallium Arsenide 39
2.1.3 Hexatriacontane 42
2.1.4 Methylammonium Lead Iodide 47
2.2 | Pulsed-Beam/Ultrafast Electron Microscope 49
2.2.1 Femtosecond Laser System 51
2.2.2 Transmission Electron Microscope and Integration 53
2.2.3 Pulsed Beam Dose Rate Characterization 59
2.2.4 Pulsed Beam Stability 68
2.2.5 UEM Parameters and Characterization 71

Chapter 3 | Error Mitigation in Debye-Waller-Based In Situ Thermometry 75
3.1 | Experimental Methods 76

3.1.1 Aluminum as a Model Material ... *76*
3.1.2 PBED Pattern Analysis ... *77*
3.1.3 Circular Hough Transform ... *78*
3.1.4 In Situ Temperature Measurements ... *79*
3.2 | Results and Discussion ... 79
3.2.1 Sensitivity of I_{hkl} to Specimen Orientation ... *79*
3.2.2 In Situ Temperature Measurements from Diffraction-Ring Radii and I_{hkl} ... *83*
3.2.3 Sources of Error: Specimen Tilting ... *85*
3.2.4 Normalization of Tilting Data ... *93*
3.2.5 Sources of Error: Specimen In-Plane Translation ... *96*
3.2.6 Sources of Error: Specimen Out-of-Plane Translation ... *99*
3.3 | Summary and Conclusions ... 101

Chapter 4 | Coherent Acoustic Phonon Spectroscopy in Gallium Arsenide ... 103
4.1 | Experimental Methods ... 104
4.1.1 Specimen Morphological Characterization ... *104*
4.1.2 Capturing Coherent Acoustic Phonons in UEM ... *107*
4.1.3 UEM Parameters ... *110*
4.1.4 UEM Control Experiments and Repeatability ... *111*
4.1.5 Experimental Confirmation of Pulsed Laser Annealing ... *115*
4.1.5 Space-Time Contour Plot Analysis ... *117*
4.1.6 Determination of Phase-Velocity Behavior ... *120*
4.1.7 Comparison of Dispersion Behaviors ... *123*
4.1.8 Calculation of Expected Bulk Speeds of Sound ... *124*
4.1.9 Effect of Tilting on Velocity ... *127*
4.2 | Results and Discussion ... 128
4.2.1 CAP Propagation Dynamics ... *128*
4.2.2 Effect of Crystallinity on CAP Propagation ... *129*
4.3 | Summary and Conclusion ... 133

Chapter 5 | Pulsed Beam Damage Mitigation in Organic Crystals ... 134
5.1 | Experimental Methods ... 135
5.1.1 Hexatriacontane as a Model Material ... *135*
5.1.2 Experimental Parameters ... *136*
5.1.3 Bragg-Spot Fading Curve Method ... *138*
5.2 | Results and Discussion ... 143
5.2.1 Ultra-low Dose Comparison: Pulsed vs. Thermionic Beam ... *143*
5.2.2 Effect of Shortening Time Between Pulses ... *149*
5.2.3 Increasing the Number of Electrons Per Packet ... *152*
5.3 | Summary and Conclusion ... 154

Chapter 6 | Pulsed Beam Damage Mitigation & Elucidation in Metal Halide Perovskites ... 156
6.1 Experimental Methods ... 158
6.1.1 Data Collection & Experimental Parameters ... *158*
6.1.2 Diffraction Pattern Analysis ... *160*

6.1.3 Bragg Peak Analysis ... *162*
6.1.4 Planar Density of Iodide ... *164*
6.2 Results and Discussion ... 166
6.2.1 Direct Comparison: Pulsed vs. Thermionic Electron Beam ... *166*
6.2.2 Effect of Varying Time Between Pulses and Electrons per Packet ... *167*
6.2.3 Preferential Damage of Iodide-Containing Planes ... *173*
6.2.4 Relationship Between Fading Curve and Beam Temporal Profile ... *177*
6.3 Summary and Conclusions ... 182

Chapter 7 | Conclusion & Outlook ... 184

Bibliography ... 186

Appendix A | List of Common Abbreviations & Acronyms ... 226

Appendix B | List of Publications, Presentations, and Posters ... 228
B.1 | Publications ... 228
B.2 | Oral Presentations ... 229
B.3 | Poster Presentations ... 230

Appendix C | Derivation of Equation 3.3 ... 230

List of Tables

Table 3.1 | **ANOVA results for the data shown in Figure 3.7.** F represents the ratio of mean squared variance of tilt angle divided by the mean squared error. P represents the probability of a falsely disproven hypothesis, such that a value of over 0.05 means that the effect of tilting is not statistically significant……………………………….…………96

Table 3.2 | **Statistical analysis of data in Figure 3.8.** Individual t-tests completed between position 1 and positions 2-8, respectively. All statistical significance was measured to 95% confidence……………………………………………………………………………..99

Table 4.1 | **Parameters of the Equation 4.1 fits to the data in Figure 4.4.** The errors are one standard error of the fit……………………………………………….…………115

Table 5.1 | **Experimental parameters and associated errors for all experiments presented in Chapter 5.** Also shown is one repetition that is not shown but is reported here to demonstrate repeatability (Exps. 3.3 and 3.4). Exp. = Experiment number, where the first number is the figure number in Ch 5 (*i.e.*, if the first number is a 6, the experiment appears in Figure 5.6), and the second number is the specific experiment referred to. Beam Type = pulsed beam (Pulsed) or random thermionic beam (Therm). TBP = time between electron-packet arrival at the specimen. E/P = electrons per packet. Beam Area = size of the electron beam. Acq. Time = camera exposure used to acquire each diffraction pattern. Total Time = the total time required to conduct the fading-curve experiment up to a predetermined total dose. Final ΔI_{110} = the final average intensity value of the *110* Bragg spots up to the total accumulated dose specific to the experiment………,,,…………137

Table 6.1 | **Experimental parameters and associated errors for all experiments presented in Chapter 6.** Exp. = Experiment number, where the letter identifies whether the experiment was pulsed (P) or thermionic (T) and the number identifies the order in which the experiments were conducted. Beam Type = pulsed beam (Pulsed) or random thermionic beam (Therm). TBP = time between electron-packet arrival at the specimen. E/P = electrons per packet. Beam Area = size of the electron beam. Acq. Time = camera exposure used to acquire each diffraction pattern. Total Time = the total time required to conduct the fading-curve experiment up to a predetermined total dose. Final ΔI_{110} = the final average intensity value of the *110* Bragg spots up to the total accumulated dose specific to the experiment…………………………………..……..…………………159

List of Figures

Figure 1.1 | **An overview of the capabilities of TEM.** High-resolution imaging can be used to view atomic columns, as demonstrated here in LaFeAsO, where the atomic columns of the [001] zone axis are clearly visible. Scale bar is 1 nm. Diffraction, shown here in the form of a convergent beam electron diffraction (CBED) pattern, can be used to gather 3D structural information. Scale bar is 2 nm^{-1}. High energy-resolution EELS spectra such as the one shown here for L-alanine zwitterion are now possible, and in situ microscopy is used to extend TEM into the millisecond time domain as shown here for the crystallization of $Y_2Fe_5O_{12}$ from an amorphous YFeO film. Scale bar is 2 μm…………………………...5

Figure 1.2 | **Illustration of spatiotemporal scales in physical processes.** Several representative physical processes are shown, including transition states, protein folding, dendrite growth, and phonon propagation. Spatiotemporal resolution reachable by fast-camera-based in situ microscopy is shown in purple………………………………………9

Figure 1.3 | **The concept of an electron shutter to image atomic motion.** The black lines represent the shape of the electron packet in time, where wider packets interact with the specimen for a longer time. This is represented by blurring of the atoms as they move, since the electron shutter is "open" for a longer time. When the electron pulse is short enough in time, blurring is minimal, allowing clear imaging of the specimen at a particular time point…………………………………………………………………………..……….11

Figure 1.4 | **Stroboscopic signal acquisition in ultrafast electron microscopy.** An ultrafast laser pulse arrives at the specimen and excites a response, which decays over a period of nanoseconds to microseconds. An electron pulse arrives at the specimen some time, Δt, later, capturing the specimen response at that time point. This process repeats at time intervals of 1/f while the CCD shutter remains open, where the same time delay Δt is probed each time, until sufficient CCD signal is collected to form an image or diffraction pattern with satisfactory signal to noise. Once the signal collection is complete, the time delay Δt is updated and the process is repeated for a different time point. This is completed for each time point necessary to build up a video of dynamics………………………………………………………………………………14

Figure 1.5 | **Schematic of cascade of damage events.** An incoming electron can collide with either specimen electrons or nuclei and initiate a cascade of events that begins in the first few femtoseconds and continues for microseconds before the energy from the collision is fully decayed……………………………………………………….…………………..35

Figure 2.1 | **Characterization of a representative *pc*-Al TEM specimen.** (a) Parallel-beam diffraction pattern (DP) acquired with a camera length of 200 mm and with an accelerating voltage of 200 kV. The diameter of the selected-area aperture was 800 μm. (b) Corresponding bright-field image of a portion of the *pc*-Al specimen shown in (a), shown at high magnification to render particles distinguishable. The diameter of the objective aperture was 100 μm. (c) Grain-size distribution determined from the image in

(b). Sizes are plotted in terms of area due to variation in characteristic particle lengths depending on direction of measurement. The histogram bin size is 146.7 nm^2 (set by choosing to have 15 total bins), and the distribution is fit with a lognormal function (solid blue curve) having a mean of 600 ± 350 nm^2. The error is one standard deviation of the fit……………………………………………………………..………………………..39

Figure 2.2 | **Gallium arsenide specimen preparation.** Gallium arsenide specimen preparation. (a) SEM micrograph of GaAs crystal after trenches are milled. For scale, the trenches are 30 μm wide. (b) Ion beam image of specimen just before liftout procedure, in which the liftout tool (shown in the upper right corner) will be welded to the nearest corner of the thin section, after which the last piece holding the section in place (upper left corner) will be cleaved. For scale, the trenches are 30 μm wide. (c) SEM micrograph of GaAs lamella welded to copper grid (right). Thinning has been completed on the right half of the lamella. (d) Ion beam image of specimen shown in (c), in profile. For scale, the thin part of the specimen is about 100 nm thick. (e) Bright field TEM image of specimen after insertion into specimen holder. Dark lines are bend contours, used to measure CAPs as they travel through the specimen during UEM experiments. More details on this in Chapter 4…………………………………………………………….…………..……………...41

Figure 2.3 | **Representative hexatriacontane specimen.** (a) Bright field image showing two overlapping C36 microcrystals near a grid bar. (b) Indexed diffraction pattern of the [001] crystallographic zone axis, typical of the hexatriacontane specimens used in the experiments in Chapter 5………………………...………..…………………….……..…43

Figure 2.4 | **Measured and calculated Bragg-spot intensity ratios for select reflections from crystalline C36.** Individual data points represent the values of I_{220}/I_{120} (black squares) and I_{310}/I_{120} (red circles) as a function of C36 crystal thickness (in number of unit cells) calculated from data reported by Dorset. The error bars represent the estimated standard error based on the accuracy of the analysis technique and the estimated accuracy of digitizing the data from the source graph. The horizontal lines correspond to the intensity-ratio values measured here from the diffraction patterns shown in Figure 5.3, as generated with a thermionic (dotted) and a pulsed (dashed) beam. Note that red horizontal lines corresponding to the I_{310}/I_{120} ratio overlap with one another………………………..46

Figure 2.5 | **Polycrystalline methylammonium lead iodide specimen.** Polycrystalline methylammonium lead iodide specimen. (a) Structure of $MAPbI_3$. Crystallographic axes are shown in the lower left of the panel. (b) Low-magnification bright-field image of the TEM specimens (scale bar = 5 μm). The diffraction pattern (inset; scale bar = 5 nm^{-1}) was obtained from the red-circled region. (c) Intensity plot from azimuthally averaging the pattern in (b) inset. Red peaks are those used for monitoring beam-induced intensity changes (see Chapter 6 for more details). The space group used for indexing was *I4*/*mcm*, though the structure is not yet universally agreed upon………………………….………….…...48

Figure 2.6 | **Schematic of integration of laser into TEM.** (a) Photo of TEM in Flannigan UEM lab with entry points of pump laser (green) and probe laser (purple) marked with arrows. A closer view of the periscopes on the outside of the TEM is shown in Figure 2.8. (b) Schematic showing pump-probe scheme in action, where laser pulses, shown in green, are directed onto the specimen to excite a material response. After a certain time Δt, an electron packet arrives at the specimen to probe the response, eventually registering on the detector. The probe pulse is generated by the fourth harmonic laser extracting a packet of photoelectrons from the cathode, as shown below in Figure 2.9. The temporal spacing between electron pulses and pump pulses is the same, and is the inverse of the laser repetition rate *f*……………………………………………..……….……………50

Figure 2.7 | **Schematic diagram of the lower laser table.** Schematic diagram of the lower laser table. The PHAROS outputs a first harmonic of 1030 nm which is frequency doubled using the HIRO. The first harmonic is split from the second harmonic and directed along the delay stage. The second harmonic is split such that half of the beam travels a collinear path with the fundamental frequency. The second beam is frequency doubled to a fourth harmonic. Both beams are directed to a top table which only has plane mirrors used to direct the beams to the height of the entry ports on the TEM (shown in Figure 2.6). The fourth harmonic is sent to the gun for photoelectron extraction and the first harmonic is used for specimen excitation………………………………………………..…………52

Figure 2.8 | **Thermionic 200 kV TEM modified for laser-driven pulsed or pump-probe operation.** (a) Photograph of the modified TEM highlighting (red rectangle) the optical periscope with which the fs UV laser pulses are directed onto the LaB_6 electron source. The fs laser system is behind the laser safety curtain to the left outside the frame of the image. (b) Close-up view of the optical periscope highlighted in (a). Denoted in the image are: (1) The optical periscope assembly. (2) An external focusing lens mounted on a 3-axis positioner. (3) Micrometers for manipulating one of the internal mirrors. Direction of the incident UV pulses is indicated by the light-blue arrow.…………………….….……...55

Figure 2.9 | **Generation and characteristics of the pulsed electron beam.** Generation and characteristics of the pulsed electron beam. (a) Schematic of the source region of the modified TEM. The fs laser pulses enter through an optical port and are directed onto the source to generate timed electron packets. These are then accelerated and directed to the specimen using conventional methods. (b) Schematic illustration of the shape of electron pulse emission probability. Distribution follows a Gaussian shape to match the character of the laser pulses during laser-cathode contact (here, 300 fs FWHM). Probability of emission is functionally zero outside of laser-cathode contact because of lack of cathode heating. (c) Concept of controlled, precisely-timed electron emission compared to conventional random (thermionic) emission for the same beam current. The laser repetition rate (*f*; pulses per second) dictates the time between electron emission (f^{-1}) for the pulsed approach. Laser-pulse energy is tuned to select the desired number of electrons, and the

temporal emission probability [$P(t)$] is confined to the pulse duration as described above……………………………………………………………………………………..56

Figure 2.10 | **Photoelectrons per laser pulse generated from the TEM LaB_6 source as a function of pulse energy.** (a) Representative behavior of the photoelectrons per pulse for high pulse energies relative to those used to conduct the ultralow-dose-rate experiments. This plot is provided only as a general example of the overall behavior below the onset of saturation. (b) Photoelectrons per pulse at the low pulse energies used for the ultralow-dose-rate experiments reported here. It is important to note that while the data shown in each panel are self-consistent, variation across the data sets is present. For example, in (a), the number of electrons generated per pulse for a laser pulse energy of 10 nJ was 89 ± 14, while in (b), the number was 20 ± 1 for a pulse energy of 12.3 nJ. The reason for this is that the data sets were acquired in separate trials. Though the qualitative behaviors will be consistent (*e.g.*, linear response in the relatively low pulse-energy regime), variations in LaB_6 photocathode condition, precise laser alignment onto the photocathode, and the precise laser focusing condition onto the photocathode all are expected to cause variation in the absolute photoelectron values. For all experiments, the incident photon energy was 4.8 eV (fourth harmonic of the 1.03-μm fundamental wavelength of the Yb:KGW fs laser), and the pulse duration was 300 fs FWHM for the fundamental beam (*i.e.*, lower bound for the UV pulses). The error bars represent one standard error over ten separate measurements………..……………………………………………………………...60

Figure 2.11 | **Comparison of beam current measurement methods.** Number of electrons per unit time measured at the detector ($N_{det.}$, Method 2) relative to the number of electrons measured at the specimen with a Faraday cup for the same amount of time ($N_{Faraday}$, Method 1) for a range of laser pulse energies incident on the TEM photocathode. Error bars represent the standard error over 10 separate measurements. ……..……………….……...62

Figure 2.12 | **Methods for determining the electron beam size.** (a) Directly measured beam size for a range of intensity values in “LM” magnification mode (black squares). A polynomial fit to the data is shown in red. (b) Directly measured beam size for a range of intensity values in “M” magnification mode (black triangles). A polynomial fit to the data is shown in red. (c) Calculated beam size as a function of intensity value for three different methods over the intensity range of interest: (1) Fit to directly-measured “LM”-mode data (black). (2) Fit to directly-measured “M”-mode data (blue). (3) Geometrical approach based on the ratio of total to measured counts (red)……….……………….………..…...66

Figure 2.13 | **Representative example of the long-term stability of the pulsed photoelectron beam over a 24-hour period.** The data were obtained by summing the counts of an image of the electron source acquired at 15-minute intervals and then converting to the number of electrons incident on the detector. The mean value is 1.565 ± 0.005 x 10^6 counts (electrons), where ± 0.005 x 10^6 (*i.e.*, ±0.3%) is two standard deviations from the mean. The slope of the least-squares fit line (red) is -25.7, signifying a drop of

25.7 counts per hour, or approximately 0.0016% of the mean over 24 hours. To further emphasize the high long-term stability, the grey box denotes a ±0.64% deviation from the mean. ……………………………………….…………………………...………...69

Figure 2.14 | **Demonstration of specimen spatial stability over a three-hour span.** (a) Bright-field image of a single C36 crystal obtained with a 0.8 nA beam current (recall that beam currents of femtoamps were used in the damage studies). (b) False-colored difference image formed by subtracting (A) from a bright-field image of the same crystal acquired three hours later. The blue areas represent a loss of counts (*i.e.*, area became darker), and the red areas represent a gain in counts (*i.e.*, area became brighter)………...71

Figure 3.1 | **Illustration of the sensitivity of I_{hkl} to specimen tilt angle.** (a) Reciprocal-space shape function $D(\mathbf{q})$ for a 50- (black) and 120-nm (red) thick crystal having relatively large in-plane dimensions, such that $D(0,0,q_z)$ is plotted versus q_z, the magnitude of the reciprocal-space vector component normal to the plane of the foil. Here, $q_z = 0$ is defined as the center of the specimen. (b) Square of the shape functions shown in (a). The blue horizontal line at $D(\mathbf{q})$ and $D(\mathbf{q})^2 = 0$ is to highlight where I_{hkl} goes to zero. (c) Deviation parameter $s_\mathbf{g}$ versus specimen tilt angle for the *200* family of reflections. (d) Overlay of (c) (blue line) onto $D(\mathbf{q})^2$ illustrating the angles at which I_{hkl} goes to zero. Here, the intensity drops to zero at ±0.09° and ±0.23° for a 120- (red) and a 50-nm (black) thick crystal, respectively, as indicated by the red and black horizontal and vertical lines, respectively…………………………………………………………………………82

Figure 3.2 | **Comparison of *in situ* thermal measurements of 120-nm thick *pc*-Al specimens.** Three methods are shown and compared: direct readout of the specimen-holder thermocouple (black squares), calculation from thermal expansion *via* diffraction-ring contraction (red circles), and calculation using the DW effect *via* changes in $\frac{I_{220}}{I_{o,220}}$ (blue triangles). The data was generated from the *220* Debye-Scherrer ring and represents the average of five separate DPs acquired in random order. Error bars represent one standard deviation from the average………………………………………………………….……85

Figure 3.3 | **Percent change in I_{220} generated from *pc*-Al thin-film specimens as a function of tilt angle.** (a) Change in I_{220} over a range of specimen tilt angles spanning 30° (±15°). (b) Change in I_{220} over a range of tilt angles spanning 2° (±1°). For all experiments, error bars are one standard deviation generated from the average intensity of five separate DPs obtained in random order of tilt angle. A one-way analysis of variance carried out on all of the data confirms that the effect of changing tilt angle is statistically significant at the 0.05 level (see Table 3.1). The effect of tilting holds for all Debye-Scherrer rings and does not fall below the 0.05 level when it is normalized to the subtracted background, total number of counts, or intensity of any other peak (see Figures 3.6 and 3.7). All patterns were acquired with a camera length of 250 mm at 200 kV and with an 800-μm selected-area aperture……………………………………………………………………...88

Figure 3.4 | **Anomalous changes in Debye-Scherrer-ring intensities with specimen tilt angle for *pc*-Al films.** (a) Azimuthally-averaged radial profile for 120-nm thick *pc*-Al tilted to ±45° (black, red). A profile obtained at normal incidence (0º) is shown for comparison (blue). Peaks are labeled with the corresponding *hkl* indices. (b) Magnified view of the *111*, *200*, and *220* reflections. The behavior of peak intensity upon tilting away from normal incidence is denoted with arrows……………………..…………………91

Figure 3.5 | **Illustration of the magnitude of an erroneous temperature assignment using the DW effect.** (a) Change in I_{220} as a function of specimen tilt angle shown in Figure 3.3a. The data is fit with a cubic polynomial, which was used to calculate a relationship for the error in specimen temperature if one assumed the observed change in I_{220} were due entirely to the DW effect. (b) Relationship of error in temperature as a function of specimen tilt angle, as determined from the polynomial fit to experimental data shown in (a). As discussed in the text, the relationships here are not universal but rather are specific to the particular specimen region of interest probed…………………………93

Figure 3.6 | **Representative rotationally-averaged radial profiles for *pc*-Al.** Each peak is fit out to six times its FWHM. The red area denotes the subtracted intensity from the *220* peak. The blue area denotes the intensity of the *111* peak…………………………..94

Figure 3.7 | **Demonstration of effect of normalization on Figure 3.2 data.** (a) Percent change in intensity of the *220* ring versus alpha-tilt angle. Error bars are standard deviations over five data points. (b)-(d) Percent change in intensity normalized to subtracted background, 111 peak intensity, and total counts, respectively………..……..95

Figure 3.8 | **Effects of in-plane specimen translation on I_{220}.** (a) Schematic map showing the extent and direction of in-plane specimen translation for positions 2 through 8 relative to the reference position 1. The translations were performed with the microscope goniometer. Each grid square is 10 nm x 10 nm. (b) Change in I_{220} at each position on the specimen. The average change in I_{220} at positions 2 through 8 are relative to the average value of I_{220} at position 1, which is set to zero. All DPs were acquired in random order of position with a camera length of 250 mm at 200 kV and with an 800-µm selected-area aperture. Error bars are one standard deviation of the average of the five individual measurements per position………………………………………..……………......98

Figure 3.9 | **Effect of changes in specimen height on I_{220}.** (a) Percent change in I_{220} versus position in *z* direction relative to eucentric height, as measured with the microscope goniometer. All DPs were acquired in random order of *z* position with a camera length of 250 mm at 200 kV and with an 800-µm selected-area aperture. (b) Data shown in (a) normalized to total counts in each respective image. Error bars are one standard deviation over five measurements for all data points……………………………………………101

Figure 4.1 | ***In situ* photothermal anneal of a GaAs lamella.** (a) Selected-area electron diffraction (SAED) pattern of a pre-annealed GaAs specimen viewed along the $[11\bar{2}]$

crystallographic zone axis. Three Bragg spots are indexed for reference. The light cyan disk marks the approximate region of the pattern that was azimuthally averaged to obtain the profiles shown in subsequent panels. (b) SAED pattern of the post-annealed specimen viewed along the [$11\bar{2}$] zone axis. The *000* beam is indexed for reference, and the light magenta disk marks the approximate azimuthally-averaged region. (c) Total-intensity profile (Bragg and diffuse) of the pre-annealed specimen. (d) Bragg-only intensity profile (solid blue line and light cyan fill) of the pre-annealed specimen. The total-intensity profile shown in panel (c) (blue dotted line) is included for comparison. (e) Illustrative comparison of the pre- and the post-annealed diffuse-only intensity at the same observed scattering vector as the <*111*> planes (calculated position shown for reference). Peak shifts from the calculated position may arise from residual tensile strain or a slight systematic error in the calibration of the microscope……………………………………….…………………..105

Figure 4.2 | **Demonstration of UEM imaging of CAPs in a free-standing, pre-annealed GaAs lamella.** (a) Representative UEM bright-field image at t = 85 ps (*i.e.*, 85 ps after *in situ* photoexcitation). The red rectangle indicates the region within which phonon dynamics were tracked and quantified. (b) Magnified view of the select region shown in (a). Three select positions (colored lines) at which average image counts were monitored are shown. Relative positions of the lines are labeled, with the position of the red line set as the origin. The white arrow indicates the observed direction of the propagating phonon wavetrain. (c) Average region-of-interest (ROI) image counts at the select positions shown in (b) as a function of time. Propagation of a single representative phonon wavefront is highlighted with the dotted line to exemplify how velocity can be determined from such profiles. The wavefront arrives at the 106-nm and 212-nm markers approximately 16 ps and 31 ps, respectively, after passing the origin, thus indicating a phase-velocity magnitude, $|v_p|$, of 6.8 nm/ps for this particular phonon. The fits straddling the dotted line are simple undamped sine functions and are meant to highlight the localized oscillatory response arising from the individual phonon wavefront………………………………..109

Figure 4.3 | **UEM control experiments.** (a) Representative bright-field UEM image of a GaAs lamella. The red line marks a region of interest (ROI) used to generate line profiles for the control experiments. (b) Contrast profiles from the ROI shown in (a) for the same time point (60 ps) but generated over 45 minutes of total control-experiment time. That is, the pump laser was not shuttered, but the retroreflector was fixed in position over the entire experiment time. (c) STCP generated from a control experiment, where the pump laser was shuttered while UEM images were acquired over a 45-minute duration…………..113

Figure 4.4 | **Control experiment to test for the presence of temporal aliasing.** Phase-velocity dispersion behaviors are shown for a 1-ps step and 5-ps step experiment, as well as for the phonon behavior shown in V2. Error bars are one standard deviation of 10 separate fitting routines to the associated STCP data…………………………………….…...115

Figure 4.5 | **Control experiment testing for pulsed laser annealing.** Contrast profiles from the ROI used in this experiment (see Figure 4.3a) during *in situ* photothermal annealing at 35 mJ/cm^2 and a 50-kHz repetition rate. As for the control experiments discussed above, images were acquired over a 45-minute span. Because the retroreflector was again fixed in position, the changing profiles are indicative of a specimen which is not returning fully to the ground state between experimental repetitions, leading to accumulation of energy and therefore a change in specimen position, orientation, and morphology with photothermal annealing time……………………………………………117

Figure 4.6 | **Dynamics and dispersion of CAPs from UEM imaging.** (a,b) Representative UEM bright-field images of a GaAs lamella at t = 375 ps (left) and t = 390 ps (right) showing the presence of contrast bands arising from propagating CAPs. The red rectangles mark the position of an ROI from which contrast profiles were acquired, as shown in (c). The colored arrows highlight two individual CAP wave fronts, and the white arrow indicates the propagation direction. (c) ROI profiles from the UEM images shown in (a) (upper plot) and (b) (lower plot). Wavefronts produce a drop in average counts owing to increased scattering strength and are fit with a peak function to quantify position with time (colored inverted peak fits to the data). The dashed vertical lines spanning both plots mark the position of a select wavefront and illustrate the propagating nature of the contrast feature. (d) Concept of the generation of a space-time contour plot (STCP) from the ROI profiles. For each UEM image in a temporal series (*e.g.*, t_1, t_2, *etc.*, where each time point is an individual snapshot), counts are averaged along one spatial dimension of a 2D ROI to produce a temporal intensity profile with one spatial dimension. These profiles are then combined into an STCP, where single wavefronts appear as sloped lines revealing speed and direction (*i.e.*, velocity, v). (e) Select UEM image with ROI indicated (red rectangle), from which the STCP shown in (f) was generated. (f) STCP spanning from t = -5 ps to 485 ps. Each dark band is a phonon wavefront (the position of a select wavefront is indicated with the white dashed line). The $|v_p|$ of the marked wavefront is 16.8 nm/ps. (g) Time-domain v_p dispersion behavior determined *via* STCP analysis from a UEM image series. Only dark bands which could be accurately fit are included; more details can be found in Section 4.1.6. Error bars on the data points are one standard deviation of the average of 10 repetitions of the analysis procedure for the same data……………….….119

Figure 4.7 | **As-generated and normalized STCPs.** (a) An as-generated STCP. (b) The same STCP as shown in (a) but with rows and columns normalized by the average of each respective row and column. An additional smoothing algorithm has been applied to each data set using Origin for appearance only……………………..……………………..121

Figure 4.8 | **Extraction of CAP v_p from STCPs.** Orange disks mark the lowest-count positions along the phonon wavefront feature, and the red line is a least-squares fit to these points. The slope of the fit line gives v_p…………………………………………………...123

Figure 4.9 | **Determination of crystallographic direction associated with CAP wavefront propagation direction.** Shown is a representative UEM bright-field image superimposed onto the associated SAED (Bragg spots indexed). The diffraction pattern is rotated clockwise by 88.8° relative to the real-space image to correct for the rotation that occurs upon changing from imaging to diffraction mode in the TEM. The select ROI for generating the STCP is shown as a solid red line and extended to guide the eye using the dashed portion. By placing the direct beam spot (not indexed) on this line, the crystallographic direction which is represented by the angle of the ROI can be determined. Here, the angle of the ROI line matches the angle between the direct beam and the ($\bar{1}31$) reflection, indicating that the approximate crystallographic direction of the CAPs is the [$\bar{1}31$] direction……………………………………………………………………..125

Figure 4.10 | **Time-dependent phase velocity (v_p) for pre- and post-annealed GaAs.** The data are fit (solid curves) with the single exponential decay function shown in the upper-right corner of the plot. The asymptotes for each curve ($v_{p,0}$) are indicated with horizontal, colored dashed lines, and the values determined from the fit are shown. The error bars on the data points are one standard deviation of the average of 10 separate fits of the wavefront peaks in the associated STCPs (not shown), and errors on the asymptotic values for $v_{p,0}$ are one standard error of fits to the v_p data………………………………..131

Figure 5.1 | **High-dose example of the Bragg-spot fading-curve method for monitoring beam-induced damage as a function of accumulated dose.** (a) Representative diffraction patterns (DPs) from a C36 microcrystal as a function of dose (e·Å^{-2}). (b) Difference in intensity of the *110* Bragg spots as a function of dose relative to the intensities at nominally zero dose. Here, $\Delta I_{110} = (I_{110} - I_{o,110})/I_{o,110}$, where I_{110} is the average *110* Bragg-spot intensity at a non-zero dose, and $I_{o,110}$ is the average intensity at nominally zero dose. The DPs and fading curve shown here are also displayed in Figure 1 in the main text. It is emphasized that the example fading curve shown is for a large total dose relative to the ultra-low dose experiments that were the focus of study..…………………………..140

Figure 5.2 | **Method for determining the value of ΔI_{110} at a predetermined total dose.** The vertical blue line marks the position of a dose of 0.063 e·Å^{-2}, the black line is the linear least-squares fit to the data (black circles), and the horizontal red line marks the position of the value of ΔI_{110} at the predetermined dose, as per solution to the equation for the linear least-squares fit…………………………………………………………………………141

Figure 5.3 | **Comparison of pulsed and random (thermionic) electron-beam damage for the same dose rate.** Dose rate is 7.8 x 10^{-7} e·Å^{-2}·s^{-1}. Representative (a) pulsed- and (b) random-beam diffraction patterns of a C36 microcrystal with the *110* Bragg spots used to generate the fading curves in panel (c) highlighted. (c) Fading curves and least-squares fits for the pulsed and random beams. The slope of the line fit to the random-beam data is steeper than that of the pulsed beam by a factor of 1.8. Pertinent specifications are as follows: Pulsed-beam current and illuminated area were 1.6 ± 0.24 fA and 132.4 μm^2,

respectively (0.01 zeptoamps per nm^2). Random-beam current and illuminated area were 1.6 ± 0.22 fA and 131.5 μm^2, respectively. The pulsed beam was generated with a 300-fs FWHM pulsed laser operated at f = 10 kHz (f^{-1} = 100 μs). The laser pulse energy incident on the TEM photocathode was set such that the number of electrons per packet was measured to be 1.03 ± 0.15...145

Figure 5.4 | **Comparison of damage induced by pulsed and random (thermionic) electron-beam irradiation for the same dose rate.** Dose rate is 9 x 10^{-6} e·Å^{-2}·s^{-1}. Fading curves and least-squares fits for the pulsed and random beams are shown. The slope of the line fit to the random-beam data is steeper than that of the pulsed beam by a factor of 1.9. Pertinent specifications are as follows: Pulsed-beam current and illuminated area were 31.7 ± 3.54 fA and 219.4 μm^2, respectively. Random-beam current and illuminated area were 32.0 ± 3.45 fA and 220.7 μm^2, respectively. The pulsed beam was generated with a 300-fs FWHM pulsed laser operated at f = 200 kHz (f^{-1} = 5 μs). The laser pulse energy was set such that the number of electrons per packet was measured to be 1.04 ± 0.11. 151

Figure 5.5 | **Effect of the number of electrons per packet and the duration between each packet on damage.** (a) Change in I_{110} after a total accumulated dose of 0.063 e·Å^{-2}. Error bars represent the standard error over four separate experiments. All data points were generated using a pulsed beam, and the same size specimen area was irradiated for each (within 0.5%). (b) Change in I_{110} after a total accumulated dose of 0.063 e·Å^{-2} for a pulsed beam with 20 electrons per packet and f^{-1} = 5 μs (f = 200 kHz) compared to a random (thermionic) beam of the same current (0.5 pA) and for the same size irradiated specimen area (within 1%; same dose rate = 1.8 x 10^{-4} e·Å^{-2}·s^{-1}). Error bars represent the standard error over five separate experiments..154

Figure 6.1 | **Quantification of damage to $MAPbI_3$.** (a) Low-magnification bright-field image of the TEM specimens (scale bar = 5 μm). The diffraction pattern (inset; scale bar = 5 nm^{-1}) was obtained from the red-circled region. (b) Intensity plot from azimuthally averaging the pattern in (a). Red peaks are those used for monitoring beam-induced intensity changes. The space group used for indexing was *I4/mcm*, though the structure is not yet universally agreed upon.[1,2] (c) Bragg-intensity fading curve for a pulsed electron beam (dose rate = 0.001 e·Å^{-2}·s^{-1}; beam size = 245 ± 3 μm^2; 50.4 ± 1.0 e/p; f^{-1} = 2 μs). Red curve is to determine ΔI at 10 e·Å^{-2}, which here is -19.2%...162

Figure 6.2 | **Comparison of pulsed and thermionic beam.** Shown are Bragg-peak intensity fading curves for $MAPbI_3$ for pulsed (blue) and thermionic (red) beams delivered at the same dose rate (0.001 e·Å^{-2}·s^{-1}). Fits to the data are for determining ΔI at 10 e·Å^{-2}, which here is -19.2% for the pulsed beam and -23.2% for the conventional thermionic beam (as indicated by the blue and red horizontal dot-dashed lines, respectively). The beam was spread over an area of 245 ± 3 μm^2 for both types. The pulsed beam consisted of 50.4 ± 1.0 e/p and f^{-1} = 2 μs (*i.e.*, a 500-kHz repetition rate)..167

Figure 6.3 | **Effect of e/p and f^{-1} on damage to $MAPbI_3$ for a total dose of 10 e·Å^{-2}.** (a) Bragg-intensity reduction (ΔI) for pulsed (blue) and thermionic (therm., red) beams administered at a dose rate of 0.001 e·Å^{-2}·s^{-1}. The time between electron pulses in microseconds (f^{-1}) is noted below the number of electrons per pulse (e/p). Error bars for 50 e/p, 100 e/p, and thermionic are one standard deviation over 2, 4, and 2 separate experiments, respectively. (b) Bragg-intensity reduction (ΔI) for pulsed (blue) and thermionic (therm., red) beams administered at a dose rate of 0.01 e·Å^{-2}·s^{-1}. Error bars for 200 e/p, 400 e/p, and thermionic are one standard deviation over 2, 2, and 3 separate experiments, respectively……………………………………..………………..170

Figure 6.4 | **Correlating iodide planar density with damage and beam profile.** (a) 0% iodine peak is the 022 family of planes. Iodine is shown in purple and lead in grey. (b) 66% iodine peak is the 020 family of planes. Iodine is shown in purple and lead in grey. (c) 79% iodine peak is the 110 family of planes. Iodine is shown in purple and lead in grey. In (a)-(c), nitrogen, carbon, and hydrogen are not shown in the figure. They are included in the calculation but affect the % iodine value by 2% or less. (d) Comparison of damage caused to planes corresponding to different amounts of iodide by beams with different temporal profiles. Damage is shown in terms of intensity loss compared with the overall specimen; see Section 6.1.3 for more details. Linear fits are added for illustrative purposes, to make slope differences obvious, and are not necessarily phenomenologically correlated to any physical process. Damage caused by thermionic beam shown in red, with a solid line and solid red triangles. Damage caused by 200 E/P pulsed beam shown in blue, with a dashed line and hollow blue squares. Damage caused by 400 E/P pulsed beam shown in blue, with a dotted line and solid blue circles. Error bars are standard deviation over 2, 2, and 3 independent experiments (for pulsed 200, pulsed 400, and thermionic, respectively)…………………………………………………………….…………174

Figure 6.5 | **Demonstration of the two-step mechanism in perovskite damage processes.** (a) Total damage (dark blue, filled circles) is plotted on the same graph as degree of disparate damage to iodide containing planes (light blue, hollow squares). Note that in this plot, in both cases, the highest degree of damage is at the top of the plot, which is reversed from earlier plots in this chapter. Error bars for total damage are standard deviations over 3, 2, and 2 experiments respectively. Error bars for disparate damage are standard errors of the linear fit. (b) Fading curve for the *020* plane, damaged using a pulsed 200 E/P beam (blue squares) and a thermionic beam (red circles) both at a dose rate of 0.01 e·Å^{-2}·s^{-1}. These plots correspond to experiment numbers T10 and P5. Fits are plotted alongside the data; equation 6.1 was used as the equation of best fit in both cases……………………178

Figure 6.6 | **Effect of beam temporal profile on damage time constants.** Plotted is the ratio between the first and second time constants (variables described further in Section 6.1.3) for each electron beam temporal profile. Each plane from Figure 6.4 is plotted

separately. Error bars are standard deviations over 3, 2, and 2 experiments respectively…………………………………………………………………………..181

Chapter 1 | Introduction

Since its invention in the 1930s by Ruska and Knoll, transmission electron microscopy (TEM) technology has undergone significant R&D efforts, to the point where it has become an indispensable tool for materials characterization, in addition to being useful for studying problems rooted in solid state physics.[3] The capability of TEM to produce both real-space (imaging) and reciprocal-space (diffraction) information on the same specimen has produced myriad discoveries over the decades, allowing the study through both modes of everything from crystal defects to polymer crystal structure to cell organelles.[4–17] Work in the 1940s on energy loss in electrons also led to the simultaneous development of electron energy-loss spectroscopy (EELS) for microanalysis of specimen chemistry, bonding, and morphology.[18–21]

The usefulness of TEM stems from the fast electrons it uses as a probe. Electrons accelerated to hundreds of electron-Volts (eV) reach velocities of 55-94% the speed of light, which renders their wavelength on the order of a few picometers according to the de Broglie relation. Since according to the Rayleigh criterion, the wavelength of the probing medium determines its resolution, this translates to a theoretical resolution for TEM that is 1-2 orders of magnitude smaller than atomic radii. However, these fast electrons also contribute to a primary limitation for TEM: electron beam damage. As fast electrons collide with specimen electrons and nuclei, they wreak havoc whose nature depends on the specimen type, acceleration voltage, temperature, and other environmental factors. Damage limits TEM resolution by causing specimen movement, breaking down specimen crystallinity and structure over time, and also makes it difficult to draw conclusions about

the material *ex-situ* as all observations in the TEM are potentially affected. As will be detailed in Section 1.2, there are myriad mitigation methods employed to reduce damage, but as of yet it is impossible to eliminate entirely. Ongoing efforts therefore focus on new and better ways to reduce damage, sometimes by combining methods.

Additionally, TEM in its typical iteration is largely a static technique, with insights centered on material structure and morphology rather than material behavior. High-readout-rate cameras have made in situ TEM possible, in which behavior can be studied at high spatial resolution, but the cameras are limited to microsecond frame rates. Efforts to extend the temporal resolution of TEM into the nanosecond range and beyond are detailed further in Section 1.1, and have successfully reached time resolutions in the hundreds of femtoseconds.

The central theme of the work described in this dissertation is the use of pulsed electron beams to extend the capabilities of TEM. First, I present work in which pulsed electron beams are used as the basis of a pump-probe experiment called ultrafast electron microscopy, or UEM. I will expand upon the existing uses of UEM through investigations of thermal measurements at ultrafast timescales as well as the demonstration of a real-space analog to coherent acoustic phonon (CAP) spectroscopy to measure hidden morphology. Then, I establish the use of pulsed beams to reduce electron beam damage as well as to elucidate its mechanisms. I finish by providing some conclusions and a view of the next steps for this work.

In this chapter, I will place this work in the context of TEM instrument development and lay out the background and motivation for conducting thermal measurements in

ultrafast experiments, and for CAP spectroscopy in real space. I will then describe the background for beam damage in the TEM in two main material types studied here, aliphatic organic crystals and metal halide perovskites, and motivate the use of pulsed beams to mitigate and explore damage mechanisms.

1.1 | Pulsed Beams in TEM: A History of Increasing Time Resolution

1.1.1 State-of-the-art TEM capabilities

Advances in TEM instrumentation can be categorized as having to do with three distinct dimensions: space, energy, and time. In this section, I will focus on improvements related to the time domain, but will first contextualize this work by briefly providing background on the state-of-the-art in space and energy, beginning with advances in spatial resolution. A major advance making high spatial resolution possible is spherical aberration correction, which corrects for the inherent difference in the focal distance for electrons entering the lens at different angles, which cannot be eliminated by clever engineering.[22–24] The point-spread disk which results after the objective lens in place of a point has been a major obstacle to accessing atomic resolution.[22,25,26] It was suggested and theoretically demonstrated decades ago that a multipole corrector could be used to reduce the point-spread function, but only in the late 1990s was the concept actually demonstrated in a TEM, using two hexapoles and four additional lenses to improve the spatial resolution of the TEM from 0.24 to 0.14 nm.[27–32] Quadrupole-octopole versions have also been demonstrated, and correctors can be installed before the specimen to decrease the point-spread disc in scanning TEM (STEM) mode (probe-corrected) or after to correct image aberration

(image-corrected).[26,33] Several other solutions, aside from this hardware-based approach, have been suggested over the decades as well, many of them also relying on technology that has only recently been sufficiently developed for the solutions to be practical.[34–36] Due to these technology developments, aberration-corrected microscopy is now commercially available and accessible in user facilities, allowing regular achievement of 60 pm resolution, on the order of the Bohr radius (53 pm) in studies on a wide range of materials in in multiple TEM modalities.[25,35–45]

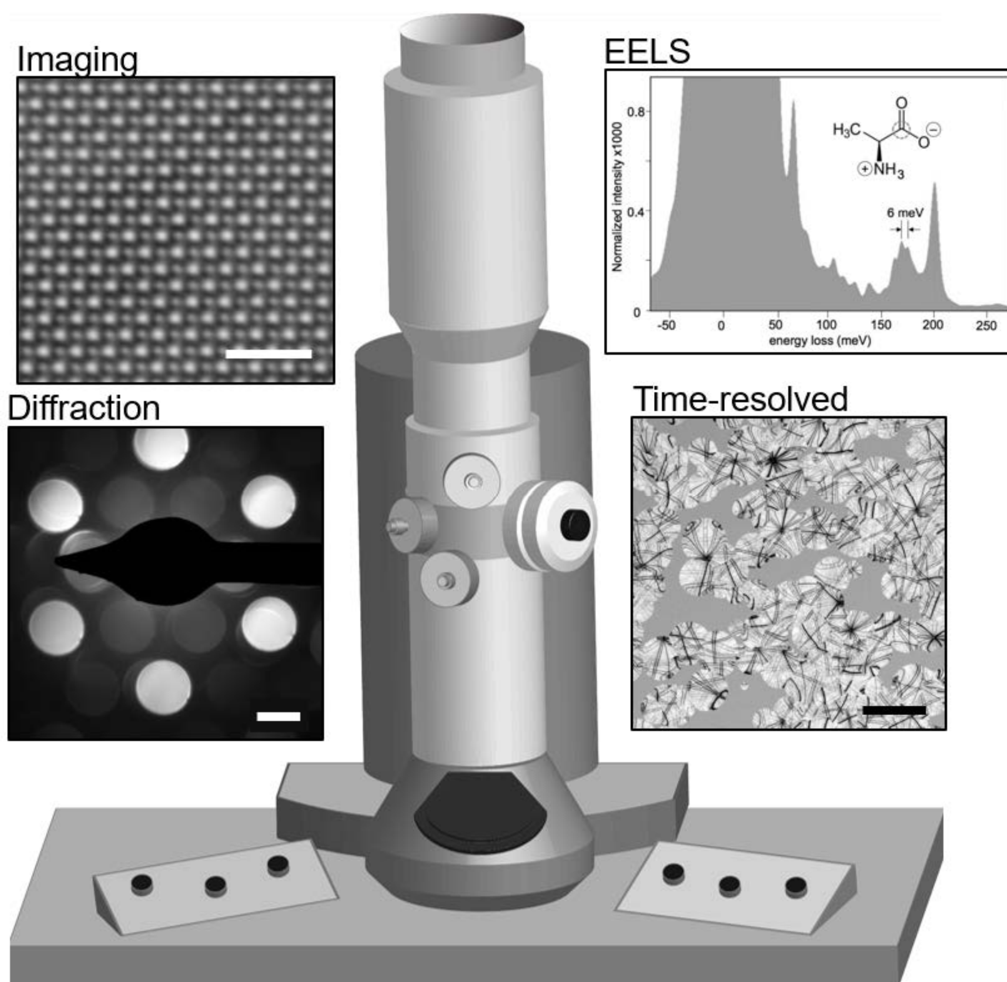

Figure 1.1 | An overview of the capabilities of TEM. High-resolution imaging can be used to view atomic columns, as demonstrated here in LaFeAsO, where the atomic columns of the [001] zone axis are clearly visible.[46] Scale bar is 1 nm. Diffraction, shown here in the form of a convergent beam electron diffraction (CBED) pattern, can be used to gather 3D structural information. Scale bar is 2 nm^{-1}. High energy-resolution EELS spectra such as the one shown here for L-alanine zwitterion are now possible, and in situ microscopy is used to extend TEM into the millisecond time domain as shown here for the crystallization of $Y_2Fe_5O_{12}$ from an amorphous YFeO film.[47,48] Scale bar is 2 μm.

Another type of aberration outlined by Scherzer is chromatic aberration, in which the inherent energy spread in a beam causes variation in focal length due to the non-uniform wavelength distribution at the lens.[22–24] While needle-shaped tips such as field emission guns (FEGs) emitting without any heating have a small energy spread of hundreds of meV, chromatic aberrations can still appear as spherical aberration pushes the limit of resolution, especially in heat-assisted and thermionic tips.[22,26,49,50] In addition, as will be discussed below, not all microscopy applications can use FEG tips as some require a broader emitting surface. Aside from use of a FEG tip, another way to reduce chromatic aberration is to reduce the energy spread of the beam through a method known as monochromation, which reduces the energy spread of the electron beam to tens of meV or less.[51–54] Several different designs have been employed to accomplish this, some based on mechanically selecting electrons of a particular energy, and some based on deflectors which project an achromatic source image.[55–62] Using this technology, probe sizes, which are closely related to spatial resolution in high-resolution STEM, have been reduced from about 1-2 Å down to less than 78 pm at 300 keV.[63,64] Monochromation of the electron beam not only reduces the impact of chromatic aberration on resolution but also is very beneficial for increasing the energy resolution in EELS, enabling analysis of fine spectral features with an energy resolution up to 4.2 meV.[48] This has allowed the development of vibrational spectroscopy in the TEM, taking advantage of the various spatial scales of vibrational signals to access new information in a variety of materials.[49,54,62,65–68]

Finally, although electron microscopy is typically focused on the properties of a material rather than its behavior, the extension of TEM into the time domain via *in situ*

microscopy – beginning with the recording of dislocation motion in the 1950s and becoming increasingly popular in the 1980s thanks to the many demonstrations of results by Sinclair and coworkers – shifted this paradigm and allowed new questions to be asked and answered.[69–71] The addition of specialized holders and column modifications enabled a wide array of external stimuli to be applied to the specimen while observing the result with the electron beam, from mechanical loading to electrical and magnetic fields to temperature control to optical excitation to various gaseous and liquid environments.[72–92] *In situ* microscopy benefits from the same aberration corrector technology as conventional TEM, with high-resolution recordings of material behavior and even atomic-scale movement becoming possible.[93–98]

While the ability to study ever faster processes *in situ* has long been of interest, high resolution capabilities have driven this interest further, because the ability to work at high resolutions increases the necessary frame rate for a given process. That is, features of interest move very quickly across the small fields of view that necessarily exist at high resolution, and thus high detector rates are necessary to capture such movement. The desire to reach higher temporal resolution introduces additional requirements due to the need for millisecond or faster frame rates. High-brightness sources are needed, where brightness is defined as number of electrons per unit area of the source or beam, which emit enough electrons within the acquisition time of a single frame to capture behavior with sufficient signal in each frame. Related to this is the need for higher quantum efficiency in detectors, such that all electrons that reach the detector contribute to usable signal.[99,100] Detectors based on complementary metal-oxide semiconductor (CMOS) technology have

significantly improved quantum efficiency (0.7 compared with <0.1 for the more common charge-coupled device (CCD) detectors) and have technically been shown to reach 1600 frames per second, but is limited in practical applications because of the computer processing speeds and storage limitations associated with this much data generation and thus 100s of frames per second is more typical.[101,102] The push for faster camera readouts is also continuous, and each of these former requirements become more stringent as the accessible frame rate increases.[103–105]

1.1.2 Overcoming Detector-Limited time Resolution: Pump-Probe Microscopy

While *in situ* TEM has indeed allowed insight into many time-dependent processes, many other material behaviors occur on time scales faster than even the best camera technology can reach. These include phase transformations and interface motion, magnetic switching, phonons, reactions, electron-phonon coupling, nanomechanical vibrations, and dislocation motion.[106–121] In order to capture these processes in *in situ* TEM, the movement of the feature in question – a dislocation, an interface, etc. – within the acquisition time of one frame must be less than the intended spatial resolution of the experiment.[122] In other words, in order to resolve a feature to 10 nm resolution, it cannot move more than 10 nm during the acquisition time without significantly blurring the image and negating the resolution. This limits feature motion to velocities of 3×10^{-6} meters per second for a 300 fps video rate and 10 nm resolution, slow compared to relevant velocities in many of the processes listed above. Accordingly, in order to overcome detector-limited time resolution,

other approaches must be considered. Figure 1.2 shows a schematic plot of the combined spatial and temporal extents to which key ultrafast phenomena operate, as well as the range which can be accessed by fast cameras.

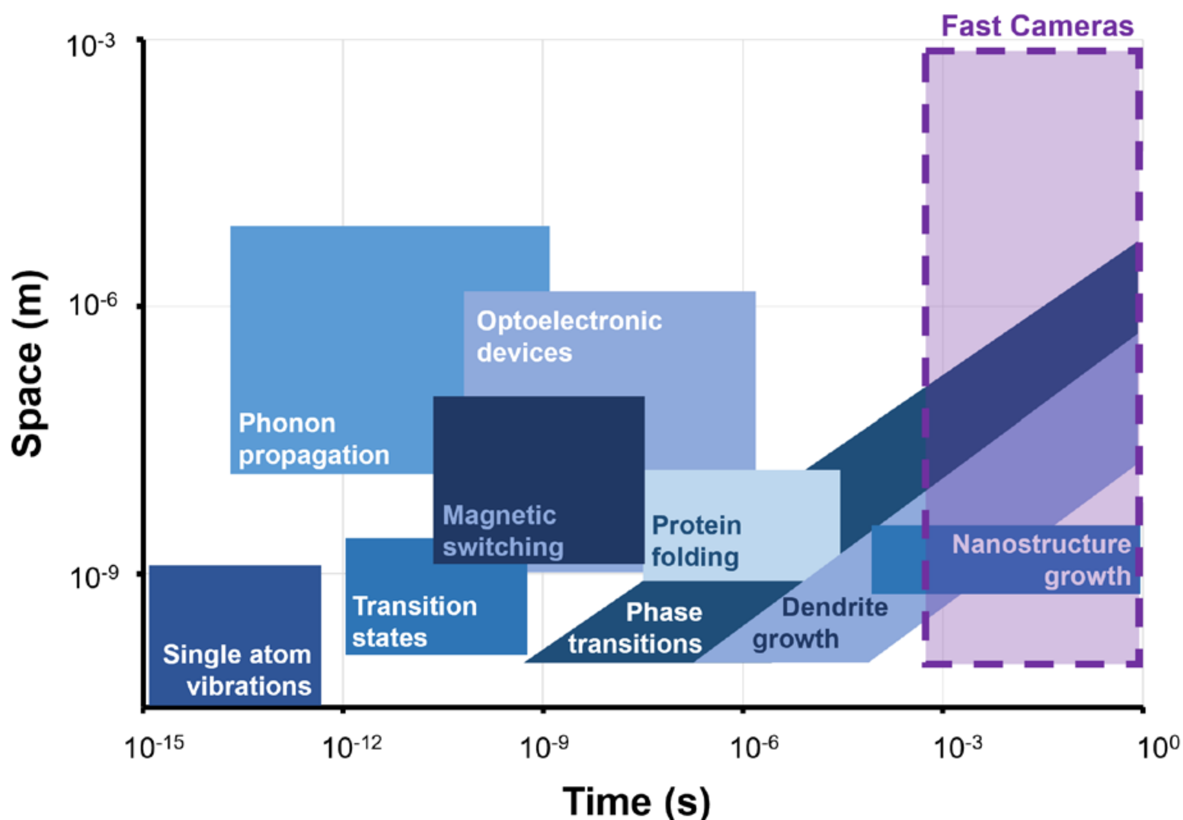

Figure 1.2 | Illustration showing approximate spatiotemporal scales for several representative physical processes. Spatiotemporal resolution reachable by fast-camera-based in situ microscopy is shown in purple.

The fast cameras discussed above represent one way of achieving high time resolution – using a continuous signal, the electron beam in this case, with a fast shutter that captures signal over short time intervals. However, high time resolution can also be

achieved by exploiting the opposite idea – a continuously open shutter with a pulsed incident signal. This latter approach is used to push TEM resolution beyond detector limits, and adopts already-developed techniques for high-speed optical imaging. To understand this, it is perhaps useful to lay out the analogy to light strobe photography as invented by Harold E. Edgerton in the 1930s, where instead of using a very fast shutter to capture processes like bullets traveling, liquids mixing, and athletes moving, a very short and bright burst of light is used to illuminate the process for only about 30 microseconds (μs), such that the open-shuttered camera can only "see" the process for that 30 μs.[123–127] In this way, the flash of light acts as the shutter, creating still images, frozen in time, of previously unresolvable processes. In summary, a short, high-fluence pulse is necessary; the number of photons in each pulse must be enough to create a usable image, and the duration of each pulse must be such that the motion to be resolved is slow by comparison. In the context of fast TEM, the use of electron packets follows the same principle – when a packet of length τ passes through a specimen, it captures the specimen at the moment of interaction, a moment which is also of length τ. That is, if a one-nanosecond-long electron packet passes through a specimen, it carries information about what the specimen looked like in that one nanosecond, which is then read by the detector as though the detector shutter was only open for one nanosecond. The shutter speed necessary to capture the motion depends on the speed of the motion itself – as with the fast camera discussion above, the motion of the feature of interest within the duration of the probing pulse must be less than the resolution of the technique at that magnification. This concept is illustrated in Figure 1.3. Note that

while the analogy with light strobe photography holds for some discussion, there are some additional challenges posed by using charged particles as the pulsed probe.

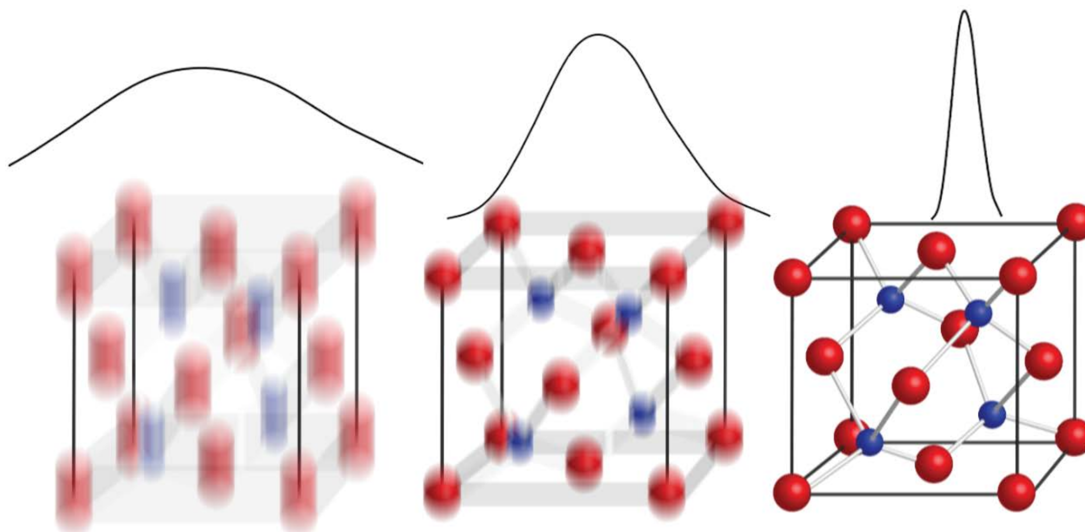

Figure 1.3 | The concept of the use of an electron shutter to image atomic motion is illustrated. The black lines represent the shape of the electron packet in time, where wider packets interact with the specimen for a longer time. This is represented by blurring of the atoms as they move, since the electron shutter is "open" for a longer time. When the electron pulse is short enough in time, blurring is minimal, allowing clear imaging of the specimen at a particular time point.

The analogy of electron probe packets to light strobe photography illuminates some challenges associated with this method. One such challenge is that in order to best understand material behaviors in time, it is instructive to image more than one timepoint in the process under study. For example, in the electron packet discussion above, if an

additional one-nanosecond-long packet passes through 500 ns later, it captures the specimen at that new timepoint, giving the experimenter information about how the specimen changed over 500 ns, with a "shutter speed" of 1 ns. However, in order to acquire this second image separately from the first, a detector readout speed of faster than 500 ns would be necessary, which, as discussed above, has not been achieved.

An additional challenge highlighted by the analogy to light strobe photography is that the amount of light – or number of electrons – emitted in a single pulse must be sufficient to resolve necessary features with adequate signal-to-noise ratio (SNR). In the realm of electron microscopy, this is a twofold challenge. First, high numbers of electrons must be emitted from the gun within the short time governed by the desired time resolution. Second, these electron packets must travel down the column without significant broadening caused by Coulombic or space-charge effects due to electron-electron repulsion. Space-charge effects spread the electron packet both transversely and longitudinally, reducing the accessible spatial and temporal resolution, respectively. In short, overcoming detector limitations using the electron packet shutter approach requires gathering sufficient SNR using electron packets and overcoming limited detector readout speeds.

There are two general approaches to resolving these two challenges in fast TEM, and both make use of the pump-probe approach. In this scheme, a specimen response is launched by an external stimulus, called the "pump," and a packet of electrons, called the "probe," is used to observe the specimen at some time point, Δt, after the arrival of the pump. The triggering of such a response at a known point in time allows the temporal scale of material responses to be measured and the evolution of responses in time to be

quantitatively observed. The pump-probe cycle can optionally be repeated many times in an experiment at a frequency known as the repetition rate, which raises the concept of reversibility. In the context of this work, a phenomenon referred to as reversible is one where the dynamical process can be exactly repeated at the repetition rate of the experiment, and fully relaxes between perturbations. The degree of precision of reversibility required to be considered reversible is determined by the spatial resolution; for a spatial resolution of 100 nm, the system must return to within 100 nm of its original state to be considered reversible. Reversibility precision requirements become more stringent as experiments are conducted at higher resolution. Irreversible processes refer to those processes that cannot be reverted to their original state within the timeframe dictated by repetition rate, without introducing additional stimuli into the system. As I will describe below, this concept forms the distinction between the two main approaches to fast TEM.

There are two methods to achieve high (sub-μs) temporal resolution. One approach is the stroboscopic configuration, where the electron packets are small ($1 – 10^4$ electrons per packet), reducing the need for high bunch-charge generation at the cathode and reducing space-charge effects, but the signal in a single packet is not nearly sufficient for images or even diffraction patterns, so the pump-probe process is repeated thousands or even millions of times per time point Δt. This leads to long camera acquisition times, eliminating the readout rate problem. However, this configuration requires that the process is perfectly reversible within the time scale of the electron-packet repetition. The process of stroboscopic signal collection is illustrated in Figure 1.4.

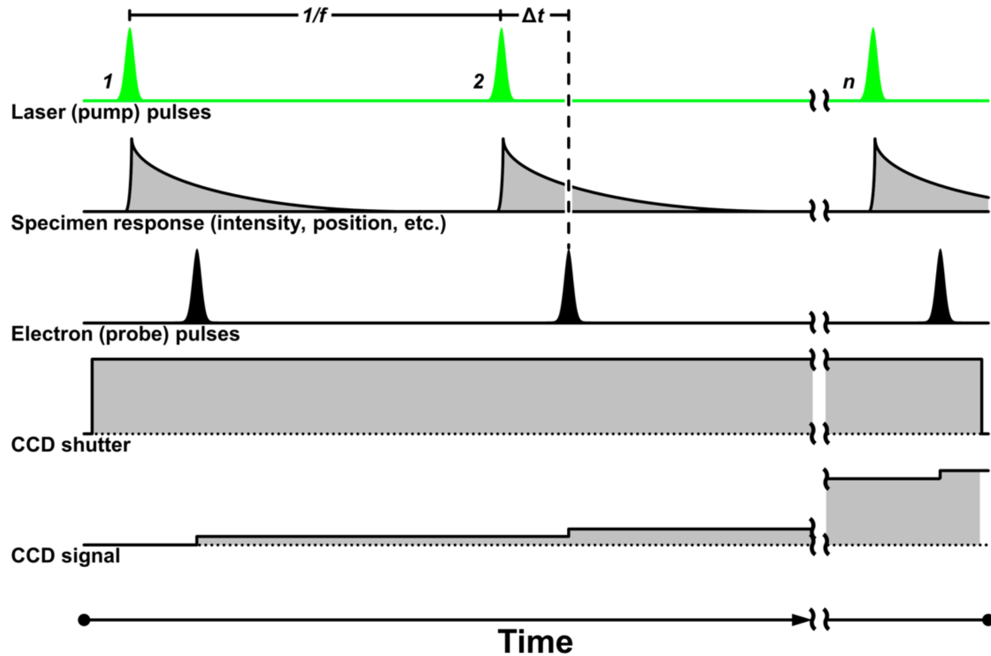

Figure 1.4 | Stroboscopic signal acquisition in ultrafast electron microscopy. An ultrafast laser pulse arrives at the specimen and excites a response, which decays over a period of nanoseconds to microseconds. An electron pulse arrives at the specimen some time, Δt, later, capturing the specimen response at that time point. This process repeats at time intervals of $1/f$ while the CCD shutter remains open, where the same time delay Δt is probed each time, until sufficient CCD signal is collected to form an image or diffraction pattern with satisfactory signal to noise. Once the signal collection is complete, the time delay Δt is updated and the process is repeated for a different time point. This is completed for each time point necessary to build up a video of dynamics.

In the second approach, the aptly-named single-shot configuration, a modified electron gun and electron-optical configuration allows the user to generate very large packets of electrons (10^7-10^9 electrons per packet). This provides sufficient signal in one

electron packet for an image or diffraction pattern, eliminating the need for repeating the process and allowing for study of irreversible processes. However, both challenges mentioned above – the need to generate and propagate high bunch-charge electron packets and the need for much faster readout times than are available -- are relevant for this configuration. All fast TEM described in this work will focus on stroboscopic TEM, but single-shot techniques are included in the brief historical review in Section 1.1.3 for completeness.

1.1.3 Early Approaches to Fast TEM

In early demonstrations of fast TEM at Moscow State University in the late 1960s, a pulsed voltage was applied to the modulator of the electron gun, enabling a pulsed beam with 100 ns time resolution.[115] Later updates using deflecting plates to spatially vary the path of the beam allowed for 10 ns pulsed beams by using a small aperture to allow only those passing through the center of the column to be propagated.[128] This technique also allowed for a pulsed beam repetition rate – or number of electron pulses per second – of 4.1 kHz, allowing for stroboscopic microscopy.[128] Beam deflection was also used by Bostanjoglo at TU Berlin in the 1970s, where 10-ns temporal resolution was achieved with spatial resolution of a few hundred nanometers.[113] In 1987, an electron-optical flash technique was reported, increasing the brightness of the pulsed electron beam and allowing for direct single-shot imaging of nanoscale phenomena. Image deflection technology was employed to overcome the readout speed limitation – successive images were deflected onto different areas of the detector to allow only 100 ns between images – and was

improved further to allow 5 ns exposure times with only about 25 ns between images.[129–136] The spatial resolution for these techniques is a few hundred nanometers.[137]

In the late 1990s, Bostanjoglo and coworkers incorporated a pulsed laser into their TEM, where photon pulses were directed onto the electron gun and extracted packets of electrons via the photoelectric effect, forming a pulsed beam without a need for beam blanking.[137–139] By combining this with a second pulsed laser directed onto the specimen to excite dynamics in situ, the time interval between the arrival of the two laser pulses could be modulated in order to image different moments in the evolution of post-excitation dynamics.[140–142] This laser pump-probe configuration forms the basis of many modern nanosecond and ultrafast TEM installations.

The work of Bostanjoglo and coworkers on single-shot nanosecond TEM, or dynamic TEM (DTEM) was revived and improved at Lawrence Livermore National Laboratory in the U.S. in the early 2000s. Work on stroboscopic study of materials via a sub-nanometer-pulsed electron beam continued after Bostanjoglo and coworkers began to focus on DTEM, including incorporation into scanning electron microscopy (SEM) systems for noncontact circuit testing – eventually leading to scanning ultrafast electron microscopy, which will be addressed below – but it was not until the mid-2000s that it was again applied in a TEM.[143–148]

1.1.4 Advent of Femtosecond TEM

Although early demonstrations of DTEM extended *in situ* TEM significantly in the time domain, many of the processes that drove interest in DTEM, such as electron-phonon

coupling, nanomechanical dynamics, and structural transformations at the atomic scale still cannot be resolved on the scale of nanoseconds. In fact, the atomic resolution capabilities of the TEM described in Section 1.1.1 have driven interest in the ability to extend this to the timescales on which atoms move, *i.e*. femtoseconds and below. This grand vision of watching chemical and material transformations occur on their fundamental temporal and spatial scales is limited in DTEM by the large minimum electron packet size, although significant instrumentation development efforts are working to overcome this.[110,117,149–152]

In response to the goal of imaging atomic processes on the femtosecond scale, ultrafast electron microscopy was developed at California Institute of Technology (Caltech) in the late 2000s. Zewail and coworkers had been using stroboscopic pump-probe ultrafast electron diffraction (UED) to study reversible femtosecond-scale processes, and as a logical extension of this technique, the ultrafast stroboscopic pulsed laser pump-probe approach was incorporated into a conventional TEM using updated femtosecond laser technology.[153–155] This technique, called UEM, pushed the temporal resolution of all TEM modalities into the sub-picosecond regime, and the use of the stroboscopic approach enables many time points to be imaged in the same specimen location, meaning that videos of dynamics can be built up from many images at different time points.[156–159] Additionally, by pushing the number of electrons per pulse into the single-electron regime, completely eliminating space-charge effects, the full spatial resolution capabilities of the TEM can be utilized.[160,161] The approach can be extended to diffraction and spectroscopy capabilities already inherent to the TEM, enabling correlated real, reciprocal, and momentum space study at time and length scales that were previously impossible.

To date, work in the Flannigan group has focused largely on stroboscopic UEM. Thus, it will be the focus of Chapters 3 and 4, the chapters that deal with time-resolved microscopy. Further details of the Flannigan group UEM at the University of Minnesota will be given in Chapter 2. While UEM and DTEM are complementary techniques, they are optimized for different types of materials processes and therefore extending the temporal and spatial resolutions of both is a worthwhile pursuit. Additionally, extending both techniques to a more complete parameter space in terms of repetition rates, frame rates, maximum video lengths, and specimen materials further increases the applicability of fast TEM to the many open questions in materials science today.

1.2 | Thermal Measurements in Ultrafast Experiments

As devices relying on computer chips continue to shrink even while becoming more powerful, the increase in power density means that effective heat dissipation is imperative to avoid severe reductions in efficiency and reliability. Many energy storage and generation technologies also suffer from heat-related degradation. To complicate matters, devices increasingly incorporate combinations of materials with disparate thermal properties, through which thermal transport must be carefully managed. The complexity and heterogeneity of commercially-relevant systems emphasizes the need for elucidation of thermal spatial behavior in a variety of materials, including the impact of interfaces and other morphology. Ultrafast structural techniques such as UEM, UED, and ultrafast X-ray imaging and diffraction are well-suited to this task due to their high spatial and temporal sensitivity, and because the pump excitation mechanism often includes some form of

heating (for example laser heating in laser-driven UEM and UED). These techniques have thus been successful in furthering visualization of the atomic to microscale structural responses of materials to ultrafast excitation.[110,153–155,162–173] However, quantifying thermal energy at the scales needed to better understand its transport across interfaces and through nanostructured materials requires what is essentially an extremely high-resolution thermometer, which has not yet been developed.

1.2.1 TEM In Situ Thermometry Techniques

There are several techniques which have been used to measure thermal energy *in situ* in TEMs. The addition of microelectromechanical systems (MEMS) to TEM specimen holders has made rapid changes in temperature possible with high stability both in terms of temperature and specimen drift, facilitating a renewed interest in developing methods to measure temperature in situ at the nanoscale.[174] Temperature in these MEMS devices is monitored using a thermocouple, but this relies on external calibration and reflects only a single temperature for the entire specimen. Additionally, the ability to measure thermal energy during other *in situ* experiments that do not directly incorporate heating, such as laser excitation and mechanical testing experiments, would enable quantitative measurement of temperature-dependent materials properties and thermal stresses. Finally, this technique is not compatible with stroboscopic ultrafast experiments due to low readout rates.

Some solutions incorporate temperature measurement into the specimen preparation, such as depositing thin film thermocouples onto TEM specimens, including

materials for which melting or evaporation can identify characteristic temperatures, or incorporating nanotube thermometers where the thermal expansion of a filling material shifts the location of a meniscus.[175–181] These approaches are effective but indirect, and therefore require extremely accurate knowledge of nanoscale material properties. Also, the specimen preparation involved is often prohibitively complex and may unintentionally alter specimen properties due to the presence of an additional material. This technique is often limited to certain temperature ranges and materials due to material compatibility and use of characteristic temperatures. Lastly, it is again not compatible with ultrafast experiments because the timescale of temperature measurement is long compared with that of the thermal phenomena being studied.

As of yet, the most effective way to glean transient thermal information from UED and UEM experiments is through the analysis of time-dependent changes in the specimen diffraction pattern (CP). A common approach is to use the coherent, elastically-scattered electrons in parallel- or convergent-beam diffraction.[160,182–188] (Use of incoherent diffuse scattering is also possible and has been explored, including by Flannigan group members.[189–193]) Specific to the oft-used parallel-beam geometries, changes in Bragg-spot or Debye-Scherrer-ring positions are sometimes used, but peaks are often broadened in ultrafast experiments due to limited coherence, sample quality, and pattern ellipticity, making precise determination of small position changes challenging. As a more accessible alternative, intensities are frequently analyzed, as they are typically the most easily quantifiable parameter for commonly-employed digital detectors.

1.2.2 Debye Waller Effect

One particularly well-known process that can give rise to changes in coherent beam intensity is the Debye-Waller (DW) effect. For electron scattering experiments, the DW effect can be used to describe the intensity modulation of diffracted beams due to temperature-dependent atomic displacements from an average crystal lattice position. In essence, a DW exponential factor incorporated into the atomic scattering factor accounts for the uncertainty in the atomic lattice position due to isotropic, temperature- and time-dependent oscillations (note that the DW factor is necessarily a higher-order tensor for anisotropic oscillations).

An expression for the relative intensities of coherent diffracted beams with respect to the DW effect is shown in Equation 1.1.

$$\frac{I_{hkl}}{I_{o,hkl}} = \exp\left(-\frac{4\pi^2}{3}\cdot\frac{\langle u^2\rangle - \langle u^2\rangle_o}{d_{hkl}^2}\right) \qquad (1.1)$$

Here, I_{hkl} is the integrated intensity of an *hkl* diffracted beam, $\langle u^2\rangle$ is the mean-square atomic displacement (to which the DW factor is proportional), $I_{o,hkl}$ and $\langle u^2\rangle_o$ are the intensity and displacement reference values (respectively), and d_{hkl} is the interplanar spacing of the atomic planes giving rise to the *hkl* beam under consideration. Though a seemingly simple expression, an appreciation for the complexity of the effect can be gained by noting the following: $\langle u^2\rangle$ is dependent on both temperature and atomic mass (thus illustrating that the DW factor is also temperature dependent), $\frac{I_{hkl}}{I_{o,hkl}}$ is dependent on the square of the electron scattering vector – which in turn is sensitive to changes in interplanar spacing and bond lengths (illustrated by Bragg's law, for example), and lattice

imperfections (in addition to atomic vibrations) also contribute to the incoherent scattering signal. To illustrate one facet of the overall complexity, Equation 1.2 shows the dependence of $\langle u^2 \rangle$ on temperature and atomic mass for a monatomic solid such as aluminum.[194]

$$\langle u^2 \rangle = \frac{2\hbar}{m}\left[\frac{\coth\left(\hbar\sqrt{D}/2kT\right)}{\sqrt{D}}\right] \qquad (1.2)$$

Here, $\hbar$ is the reduced Planck's constant, m is the atomic mass, D is the dynamical matrix of the crystal (which pertains to the allowed phonon frequencies for a given wave vector), k is the Boltzmann constant, and T is the temperature.

In ultrafast scattering experiments, the DW effect is frequently invoked to explain transient reductions in coherent-beam intensities arising from photoexcitation of phonon modes and commensurate increases in $\langle u^2 \rangle$. Therefore, measurement of the transient response of $\frac{I_{hkl}}{I_{o,hkl}}$ can provide insight into fundamental time-dependent materials properties, such as electron-phonon and phonon-phonon coupling behaviors, photothermal effects, and phase-change dynamics.[195–203] Care must be exercised, however, because factors other than changes in $\langle u^2 \rangle$ can also significantly affect coherent-beam intensities.[183,204–206] One such effect is elastic deformation caused by photothermal expansion, which can result in significant changes in specimen orientation *via* a variety of motions that may not occur uniformly across the probed region of interest.[26,116,160,202,207–212] This can lead to a change in I_{hkl} through, for example, modulation of the deviation parameter (*i.e.*, the degree to which the intersection of the Ewald sphere deviates from the center of the reciprocal-lattice position) and also by changing the specimen region being probed.[213] Such effects can

overwhelm intensity changes arising from a change in $\langle u^2 \rangle$, as will be illustrated in Chapter 3.[88,205,214] Importantly, such photothermal deformations can be induced on the order of hundreds of femtoseconds to picoseconds, and speed-of-sound elastic strain waves can propagate several nanometers in hundreds of femtoseconds.[116,210,215–218] Thus, the myriad effects that can contribute to changes in I_{hkl} – in addition to the DW effect – must be identified, quantified, and deconvolved in order to conduct precise ultrafast measurements meant to provide new insights into intrinsic materials properties and to accurately inform and guide theoretical development.

1.3 | Coherent Acoustic Phonon Spectroscopy

1.3.1 Post-Photoexcitation Energy Dissipation in Semiconductors

This section seeks to provide basic theoretical context for the work described in Chapter 4. As it is not an exhaustive review of post-excitation dynamics or thermal carrier behavior, interested readers are encouraged to see references 209 and 219 for more detail. There are two main thermal carriers in solids: electrons and phonons. Electrons are the primary energy carrier in metals, and phonons in all other solids, but as will be described below, the thermal behavior of both types of carriers is linked. Electron and vibrational state energy levels are well-described by quantum mechanics in single atoms or molecules, but in energetically stable solids such as the crystals studied here, these discrete energy levels form semi-continuous bands. The dispersion relation which describes these bands can also be used to understand the properties of materials; for example, the filling of electronic bands at zero temperature defines metallic or insulator behavior. At nonzero

temperatures, the filling of bands by electrons and phonons is described by Fermi-Dirac and Bose-Einstein statistics, whose exact distribution is strongly related to the energy in the system.[219,220]

Super-bandgap ultrafast photoexcitation of semiconducting materials strongly shifts this distribution, inducing a cascade of strongly-correlated, many-body interactions as the system returns to the ground state.[221,222] The process is initiated via absorption of photon packet energy into the electron density of the specimen, which occurs within tens of fs. The result is a dense, high-energy bath of charge carriers whose properties depend on electron screening in the material and the density of states.[223] This excited population of electrons transitions – typically within a few picoseconds – to atomic-scale structural responses *via* carrier-lattice coupling and excitation of optical phonons. The exact timing of this process depends again on the density of states and the degree to which electrons are excited within or between bands (intra vs. interband transition).[224–226]

The generation of structural motion (*i.e.*, phonons) through coupling with the electron distribution occurs via either deformation potential or thermoelasticity mechanisms. Note that electrostriction and the inverse piezoelectric effect are also mechanisms for phonon generation but are not relevant to the material systems studied here. During excitation of phonon branches via deformation potential, the electron population is redistributed causing changes to electron orbital overlap, which then affects covalent bond strength. Thermoelasticity is related to thermal expansion, in which bond kinetic energy is increased causing deformation of the crystal.[227] As the latter mechanism occurs upon temperature change, and the former occurs simply through electron

distributions, which may or may not be related to temperature, realistic generation mechanisms are a mixture of thermoelasticity and deformation potential.[209,228] Once an excited phonon population is generated, phonon-phonon coupling ensues over tens of picoseconds, wherein initial population of discrete phonon states decays through excitation of lower-energy optical and acoustic modes. Resulting from this is a non-equilibrium population of propagating CAPs, the precise transient behaviors of which are influenced by the intrinsic electronic and structural properties of the material, as well as the specimen boundary conditions and the manner of excitation.[26,209,211,229,230]

These interactions all overlap significantly in both space and time and influence one another as they do, making them difficult to fully explicate. However, as mentioned above, transient decay behavior is closely related to specimen morphology (which determines boundary conditions) and specimen structural and electronic properties. This suggests that elucidation of individual events, such as generation of certain phonons, can provide considerable insight into the material under investigation, especially as specific phonons may travel through the bulk of the specimen or across its surface and thus be influenced by spatially-inhomogeneous properties such as interfaces and buried structures. This is the principle behind CAP spectroscopy, which will be explored in the next section.

1.3.2 Phonons as a Characterization Tool

Owing to the associated nanoscale structural perturbations, all-optical time-domain spectroscopic methods conducted in a pump-probe reflection geometry can be used to elucidate transient CAP responses.[231] With these techniques, depth-dependent information

can be gathered and used to generate insight into underlying electronic and structural behaviors *via* the acousto-optic and optoelectronic properties of the material.[232] Indeed, this approach has been used to study a range of varied structures, including ion-implanted crystals and nanoporous thin films, radiation-damaged materials and polycrystalline texturing, and non-periodic structures and morphologies of plant and animal cells.[233–242]

Due to the often discrete and heterogeneously-distributed nature of surface, interfacial, and compositional structure and morphology, combining real-space imaging with ultrafast probes would better enable determination of local transient responses and, thus, the resulting impacts on bulk intrinsic properties. All-optical techniques, such as time-domain Brillouin scattering, enable depth-dependent and in-plane imaging with nanometer and micrometer spatial resolutions, respectively.[232–235,238,243,244] While sufficient for probing structures with commensurate native length scales, imaging nanoscale in-plane dynamics and the associated impact of variable morphology and composition with these techniques is challenging. Importantly, UEM is well-suited for imaging in-plane nanoscale dynamics on picosecond timescales.[155,167,245] Indeed, UEM has been used to directly image both in-plane and *z*-direction CAP dynamics (*e.g.*, nucleation and launch, propagation, and time-domain phase-velocity dispersion) with combined nanometer-picosecond spatiotemporal resolutions.[26,116,120,211,212,229,230] Further, ultrafast parallel- and convergent-beam diffraction can also be conducted with UEM, thus enabling correlative studies of unit-cell and nanoscale structural dynamics in reciprocal and real space, respectively, on the same specimen region.[160,185,188,212,230] All of these

factors would make an analogous CAP spectroscopy technique in UEM particularly useful to advancing materials characterization.

1.4 | Electron Beam Damage

1.4.1 Radiation Damage in Organic Materials

In TEM, structural damage caused during electron-specimen interactions results in significant degradation of spatial resolution, which ultimately limits the quality and the accuracy of the information obtained. Indeed, the progression of damage during exposure leads to uncertainties in agreement between the acquired data and the intrinsic (*i.e.*, artifact-free) properties of the material. The specific nature of the damage and the overall degree to which it occurs depends on a number of variables; including the electron-beam characteristics, the specimen properties, and the experimental requirements.[246] In so-called "soft" specimens such as organic and biological materials, damage is often extensive (relative to metals or archetypal semiconductors, for example) and occurs through radiolysis, sometimes called ionization damage.

During radiolysis, an incident electron scatters inelastically when colliding with specimen electrons, leaving behind extraneous energy in the specimen. In the case of paraffins, which are the material used in this work, the specimen imparts 37 eV on average to the specimen, with a spread of anywhere from a few eV or less to around 100 eV.[247] The approximate threshold for a specimen electron to be impacted by this collision to the extent that causes damage is 4.8 eV, although lower amounts of energy may cause some excitation.[247]

Upon collision, the specimen electrons may be excited into higher-energy states or may be ejected from the specimen atom electron cloud entirely, leaving behind ions or free radicals in the specimen. Free radicals may combine with other nearby free radicals, which can travel along long-chain paraffins to form cross-linking bonds, and this crosslinking causes additional bending of the chain resulting in overall crystal thinning.[248] Broken bonds left behind by ejected electrons may lead to severing of chains, after which resulting light hydrocarbons or hydrogen molecules may no longer be stable in the solid state and may therefore diffuse to the surface of the specimen and evaporate into the microscope column, causing mass loss in the specimen. Both of these processes also cause loss of crystallinity and therefore Bragg peak intensity fading as the order in the organic crystal is degraded.[248,249] The ejected electrons themselves become what are known as secondary electrons, which may continue to travel out of the specimen, leaving behind a positive charge in the specimen, or continue to collide further with other specimen electrons.

Excited specimen electrons will of course decay back to their ground state, accompanied by phonons or Auger electrons due to the conservation of energy. Auger electrons behave similarly to secondary electrons, in that they can either be ejected from the specimen entirely or continue to collide further with specimen electrons. Secondary and Auger electrons are estimated to cause over 80% of the damage to organic specimens during radiolysis.[247] The primary reason for this outsized impact is the high scattering cross section associated with these electrons; while incident electrons impact the specimen with 200 keV worth of energy, and therefore have a relatively low likelihood of scattering, and an even lower likelihood of scattering inelastically, the Auger and secondary electrons

carry on the order of tens of eV in energy, corresponding to very large scattering cross sections and therefore a likelihood of not only scattering inelastically but doing so multiple times.[28,250,251] Phonons that accompany specimen electron return to the ground state are essentially local heating, which while overall specimen temperature increases are not likely to occur in any measurable fashion, lead to significant elevation of local energy. Valuable to note here is that the local thermal energy in the specimen significantly impacts the likelihood and extent of beam damage in general. For example, increasing temperature by only 1 K can cause damage to increase by 3%, and an increase of 9 K can increase damage by 28%.[252,253] This implies a non-linear and cumulative relationship between local damage events that overlap spatially and temporally. This concept will be explored in more detail in Chapter 5.

Though the factors and the mechanisms associated with beam damage are numerous and multi-faceted, a number of practical approaches have been shown to significantly reduce negative effects of radiolysis.[254] For example, cryogenic methods operate by holding the specimen at reduced temperatures during exposure in order to lower diffusion and kinetic reaction rates, to reduce mass loss, and to minimize the impact of beam-induced thermal effects, especially for poorly-conducting materials.[255,256] This has led to significant advances in the ability to study highly-sensitive specimens, such as soft matter and biological structures, at sub-nanometer spatial scales.[257–260] Radiolysis in particular can also be reduced by going to higher accelerating voltages owing to associated lower inelastic scattering cross sections, though a commensurate decrease in overall scattering signal also occurs.[254] Minimizing exposure of the specimen to electron

irradiation *via* low-dose and low-dose-rate methods and the use of conductive coatings and substrates have also proven beneficial.[261–265] Further related to controlling damage through dose, the method of dose fractionation, which is based on the acquisition of fast, multi-frame scans or brief, stroboscopic multi-image series, has been shown to be a viable approach for minimizing beam-induced artifacts.[266–268]

1.4.2 Beam Damage and Degradation in Halide Perovskites

Comprehensive understanding of high power-conversion efficiencies of metal-halide perovskite (MHP) photovoltaic cells requires elucidation of atomic and nanoscale properties and behaviors of these materials.[269,270] Structural, chemical, electronic, and dynamic properties at this scale are accessible with TEM, but the stability of MHPs is such that electron-beam damage can be significant, while connections to photon-induced damage can be drawn.[271–273] Indeed, sensitivity of MHPs to even low dose rates (~1 $e \cdot Å^{-2} \cdot s^{-1}$) may limit what can be learned about fundamental structure/function relationships and illustrates the importance of developing new methods for probing degradation and uncovering new behaviors.[274–276]

Additionally, MHPs continue to experience structural instabilities when exposed to stimuli such as thermal heating, electrical bias, light irradiation, or exposure to moisture.[271,276–282] While significant efforts are under way to limit these instabilities, they are not yet well understood and pose a significant limitation to commercialization.[278,283–307] Parallels have been drawn between the degradation mechanisms under several of these stimuli, especially heat and UV radiation, and those observed during TEM experiments,

indicating that a more thorough understanding of electron beam damage may aid in gaining insight to stability issues in other, more industrially relevant contexts.[273,276,290,308,309] Additionally, morphological features, especially those visible in the TEM such as local defects, grain boundaries, phase disorder, and localized strain, have been shown to negatively impact stability.[274,310–317] On the other hand, the use of directed electron beam damage to fabricate novel nanostructures has been suggested.[308,318] For all of these reasons, elucidating electron beam damage and the conditions under which it is mitigated can be useful to the intelligent design of perovskite-based electronic devices in addition to being valuable for fundamental science.

Electron beam damage in perovskites proceeds according to a combination of mechanisms. The organic components in the material experience radiolysis, explained in more detail in Section 1.4.1. Displacement or knock-on damage is also relevant, in which incoming electron collisions with specimen atomic nuclei transfer sufficient energy to introduce point defects into the specimen. Buildup of positive charge through emission of secondary electrons or Auger electrons, as described above, is also especially destructive to specimens that rely on ionic bonding.[273] Investigation of beam damage mechanisms is still in progress, including through work described in this thesis, but some understanding of the process has begun to come to light in recent years. Generally, it is thought to occur through a combination of charging, ionic excitation, and heating leading to ion migration and separation of the organic and inorganic constituents.[276,319] In $MAPbI_3$, the most commonly studied MHP and the one on which this work will focus, iodide ion migration is generally considered to be the main component of defect migration due to its low barrier

to diffusion.[320–325] Iodide migration is coupled with migration and evaporation of the methylammonium cation, which experiences radiolysis and is weakly bonded to the lead-iodide cage.[273,276] The existence of specimen charging or an applied electric field accelerates the rate of ionic migration, posing an additional issue in both TEM and photovoltaic device settings.[295,301–306] Finally, the MHP entirely decomposes into a PbI_2 structure, which can be detected in the diffraction pattern. Heating-induced structural transformations may also play a role in degradation of the specimen under the electron beam.[326]

A number of methods, such as cryo-electron microscopy and low-dose imaging and diffraction, which have been shown to reduce deleterious beam effects.[327,328] Cryo-electron microscopy is especially helpful for damage that stems from phase transformation and also reduces ion diffusion rates.[273] Low-dose imaging simply reduces the total number of incident electrons and therefore reduces the number of damaging collisions. Reducing accelerating voltage and therefore reducing incident electron energy can prevent knock-on damage, but also reduces spatial resolution and increases radiolysis.[268]

1.4.3 Pulsed Beams as Damage Mitigation

Transfer of energy from an incident electron to a material initiates a cascade of structural and electronic excitations, each of which is active within a characteristic temporal window.[253] Accordingly, interesting questions can be posed pertaining to the feasibility of taking advantage of the temporal aspects of dose delivery in order to mitigate damage. Indeed, self-healing has been implicated in the recovery and the dose-rate-

dependent damage thresholds observed for inorganic materials, hybrid metal halide perovskites, biomolecules, and tissues.[271,329–334] In light of this, delivering dose in a segmented fashion with a well-defined duration between each packet of electrons is a potentially intriguing approach to reducing or even circumventing the negative effects of certain damage mechanisms. Interestingly, the effects of pulsed-electron irradiation on damage to tissues, cells, and biomolecules is studied in the field of radiobiology, often by utilizing femtosecond (fs) pulsed-laser plasma accelerators.[332,335] In electron microscopy, the potential benefits of using a pulsed electron beam to mitigate damage have been speculated upon for decades.[110,154,336] Further, though not attempting to leverage relaxation or self-healing, proposals for extending the concept of diffract-before-destroy to TEM have also been discussed.[337–340] In this approach, sufficient information would be acquired before any damage has occurred by using a single, brief, large number-density electron packet. Unlike X-ray photons, however, electrons in such a dense packet will experience significant Coulomb repulsion, which will degrade coherence and limit image resolution.[150,341] This unwanted effect necessitates the use of high energies and/or post-emission recompression schemes.[162,342–344]

In order to systematically test the effects on damage of using a pulsed source in the TEM, and especially for direct comparisons to conventional methods, one ideally would have an extremely high level of control over key aspects of the discrete electron packets. Such aspects include the number of electrons in each packet, the duration of each packet, the time between each packet, and the number of packets per unit time. As will be described in more detail in Chapters 2 and 5, implementation of fs laser-driven

photocathodes and picosecond chopped beams in TEMs provides such control, and a few intriguing observations noting potential damage reduction when using a pulsed source have indeed been reported.[110,154,163,345–348] For example, diffraction-spot intensities from crystals of copper 7,7,8,8-tetracyanoquinodimethane and polyethylene oxide under pulsed-beam illumination from a laser-driven photocathode were observed to be stable over inordinately long continuous exposure times.[349,350] More recently, apparent mitigation of damage was observed in $MgCl_2$ when using a segmented beam consisting of picosecond electron bunches, each regularly spaced in time by ~160 ps (*i.e.*, a repetition rate of 6 GHz).[351] However, as in pulsed-beam radiobiology studies, the precise effects on damage of pulsing the beam, and the relationship with dose rate, are largely unknown.[352] Indeed, no study has yet determined the fundamental effects of precisely delivering each individual electron to the specimen with an extremely well-defined and highly-tunable time between each. Further, under such finely-controlled conditions, no direct comparisons have been made to conventional low-dose methods for precisely the same dose rate and the same total dose.

1.4.4 Pulsed Beams as a Kinetic Tool

In addition to the mitigation strategies discussed above, femtosecond (fs) laser-driven and picosecond chopped-beam sources in modified TEMs offer additional means for mitigating and studying damage.[349–351,353,354] These methods employ temporally-modulated beams, where electrons are delivered to the specimen in discrete pulses with well-defined durations between each, rather than in the random fashion of conventional sources (*e.g.*, thermionic). Indeed, time-dependent aspects of charging and thermal energy,

as well as the dynamic self-healing properties of MHPs, suggest there may be insights into these temporal mechanisms that can be achieved by using well-timed pulses.[271,333,334,355]

To clarify the potential usefulness of a carefully-timed pulsed beam in elucidating damage mechanisms, it is instructive to consider the full cascade of damage events in time. Figure 1.5 illustrates this schematically, giving approximate timelines for many different damage events which may affect various specimens. As described briefly in Section 1.4.2, the incoming electron may excite or eject specimen electrons, or it may collide with a specimen nucleus and move it to an interstitial or even remove it from the specimen entirely at specimen edges. The dissipation of related heat and charge, along with diffusion of defects, is the longest-lived result of an incoming electron collision.

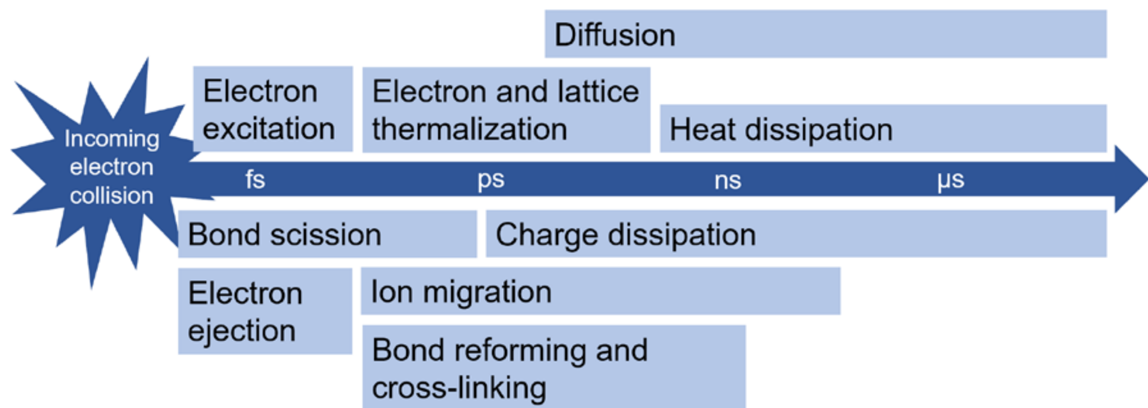

Figure 1.5 | Schematic of cascade of damage events. An incoming electron can collide with either specimen electrons or nuclei and initiate a cascade of events that begins in the first few femtoseconds and continues for microseconds before the energy from the collision is fully decayed.

These events are not independent; they overlap in space and time and impact one another significantly. As one example, the presence of local heating may significantly change diffusion rates, and as another, the distribution of electrons and phonons determines time constants for the many-body interactions occurring throughout. If each incoming electron (or, more accurately, each one that causes damage within a given radius of influence) initiates some version of this cascade, it can be imagined that where in time the subsequent electron arrives would significantly impact the details of its cascade. Therefore, exploiting properties of pulsed electron beams - in which carefully timed electrons can be sent to interact with the specimen at somewhat pre-determined points in this timeline - could lead to new insights into damage mechanisms, especially at the fast timescales which are difficult to study by other means.

In using pulsed electron beams to study beam damage, the pulsed beam serves the role both of the initiator and the probe for the damage events. The use of pulsed electron beams as an initiator of reactions for study is well established; such experiments have been done for decades on polymers, gases, inorganic materials, and more.[67,356–366] There are also cases in which pulsed e-beams have been used both as the initiator and the probe, for example in annealing of ion-implantation damage in semiconductors or in synthesis of silicon dioxide nanoparticles, although these studies do not focus on kinetics and the probe is generally confined to post-mortem analysis.[367–370] To my knowledge, varying the temporal profile of pulsed electron beams to study the kinetics of radiation damage has not yet been attempted.

Chapter 2 | Equipment & Methods

This chapter details the experimental methods and equipment operation necessary to achieve the experimental results described in this dissertation. I will begin by discussing the specimen preparation needed for each set of experiments; the order follows that of the chapters. I will then describe the equipment used in the University of Minnesota UEM lab, which consists of a TEM and a femtosecond laser, as well as the basics of operation that are specific to the lab (general TEM operation and use of laser optics is not described here). Finally, I will describe the characterization of TEM and UEM experimental parameters. Further details of individual experimental parameters are given in the Experimental Methods sections of each chapter.

2.1 | Specimen Preparation

2.1.1 Aluminum

All aluminum specimens were deposited onto 200-nm-thick holey silicon nitride membranes (Ted Pella, 21535), which were plasma cleaned with a 4-to-1 mixture of argon and oxygen for two minutes prior to deposition. The membranes were 0.5 x 0.5 mm square with 2.5-μm diameter holes distributed at a 10-μm pitch. Aluminum was sputter deposited from a target (AEM, ≥4N purity) onto the cleaned substrates to a thickness of 120 nm under argon at a rate of 8 nm/min using DC magnetron sputtering in an AJA ATC 2000 Sputter System. This resulted in continuous film coverage of the entire membrane. Five individual specimens were prepared in separate sputtering depositions so that experimental repeatability and statistical significance could be determined; this also enabled the

incorporation of the effects of random error in the analyses (*e.g.*, associated with fluctuations in holder temperature and microscope conditions). Figure 2.1 displays the structural characterization, as well as a corresponding grain-size distribution, representative of the specimens. Grain-size and grain-number analyses were performed on several regions of all specimens using an automatic particle-measuring function, as well as the multi-point and area-measurement tools in Fiji.[371] In this way, the average grain size in area was found to be 600 ± 350 nm^2, and the average number of grains within the membrane areas was $4.2 \pm 0.1 \times 10^8$ (the error is one standard deviation of the average). An 800-µm diameter selected-area aperture was used, giving an illuminated area of 398 μm^2 and illuminating $6.3 \pm 2.4 \times 10^5$ grains.

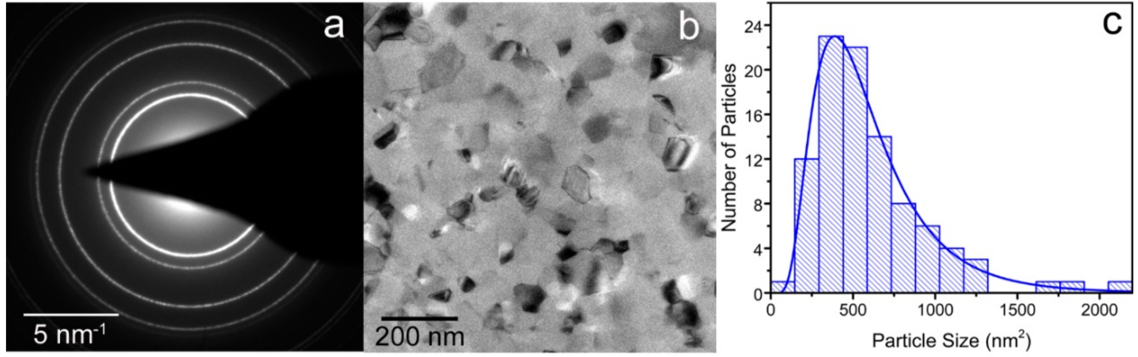

Figure 2.1 | Characterization of a representative *pc*-Al TEM specimen. (a) Parallel-beam diffraction pattern (DP) acquired with a camera length of 200 mm and with an accelerating voltage of 200 kV. The diameter of the selected-area aperture was 800 µm. (b) Corresponding bright-field image of a portion of the *pc*-Al specimen shown in (a), shown at high magnification to render particles distinguishable. The diameter of the objective aperture was 100 µm. (c) Grain-size distribution determined from the image in (b). Sizes are plotted in terms of area due to variation in characteristic particle lengths depending on direction of measurement. The histogram bin size is 146.7 nm^2 (set by choosing to have 15 total bins), and the distribution is fit with a lognormal function (solid blue curve) having a mean of 600 ± 350 nm^2. The error is one standard deviation of the fit.

2.1.2 Gallium Arsenide

The GaAs lamella was prepared from a bulk, undoped *100*-oriented GaAs crystal (MTI Corporation) using FIB milling and a lift-out procedure (FEI Helios NanoLab G4 dual-beam FIB). First, a diamond-cleaved section of bulk GaAs crystal was adhered onto an aluminum SEM stub (Ted Pella 12.7mm, 16111N) and placed into the specimen loading stage of the FIB. After appropriate FIB system alignments, a rectangle (30 x 5 x 2 µm, 750

pA) of platinum was deposited onto the crystal surface. Then, two 30 x 8 x 8 μm trenches were cut into the material using ion bombardment, with the trench depths 2 μm apart. Smaller trenches were cut closer to one another to thin the middle section. Finally, the lift-out tool was welded to the upper right corner of the thin middle section, and trenches were cut to release part of this section from the rest of the crystal. The cut section was then welded to a copper half-moon grid (Ted Pella PELCO, 10FIBC05) and thinned further. Due to minor issues with SEM alignment, the typical dog-bone or dumbbell shape could not be achieved and the resulting GaAs lamella (100 nm thick) was instead a relatively flat cantilever. While ion bombardment is typically the final step to finish a FIB specimen, this step was not completed to maximize the amorphous layer resulting on both the top and bottom of the GaAs lamella. Upon inspection in the TEM, the specimen was oriented along the $[11\bar{2}]$ zone axis (*i.e.*, the incident electron wave vector in the electron microscope was parallel to the $[11\bar{2}]$ crystallographic direction).

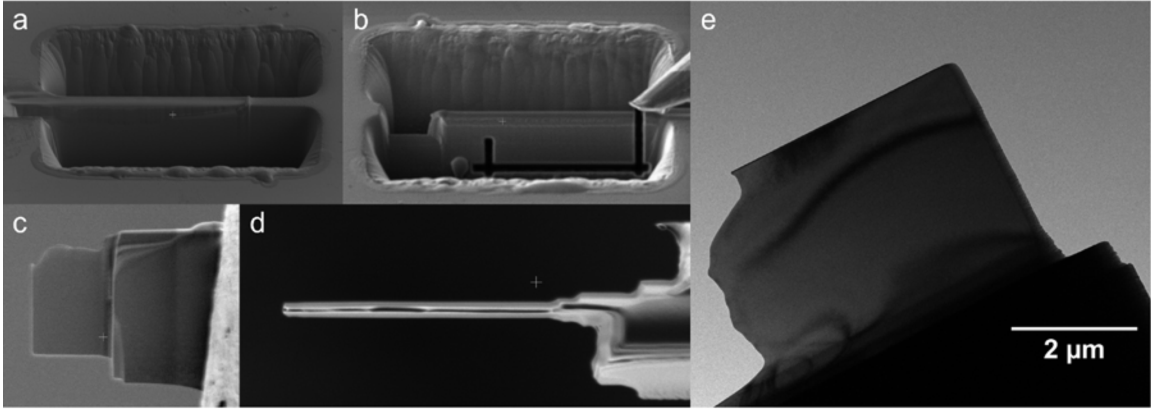

Figure 2.2 | Gallium arsenide specimen preparation. (a) SEM micrograph of GaAs crystal after trenches are milled. For scale, the trenches are 30 μm wide. (b) Ion beam image of specimen just before liftout procedure, in which the liftout tool (shown in the upper right corner) will be welded to the nearest corner of the thin section, after which the last piece holding the section in place (upper left corner) will be cleaved. For scale, the trenches are 30 μm wide. (c) SEM micrograph of GaAs lamella welded to copper grid (right). Thinning has been completed on the right half of the lamella. (d) Ion beam image of specimen shown in (c), in profile. For scale, the thin part of the specimen is about 100 nm thick. (e) Bright field TEM image of specimen after insertion into specimen holder. Dark lines are bend contours, used to measure CAPs as they travel through the specimen during UEM experiments. More details on this in Chapter 4.

The FIB-prepared GaAs lamella was photothermally annealed *in situ* using a diode-pumped, solid-state Yb:KGW pulsed laser (Light Conversion PHAROS, 300-fs pulse duration full-width at half-maximum, fwhm). Pulse duration was measured with a scanning autocorrelator (Light Conversion GECO). The train of laser pulses was directed

onto the specimen *via* alignment through an optical periscope integrated into the side of the UEM (more on the UEM instrument below). The repetition rate (50 kHz; 20 μs between pulses) and pulse fluence (35 mJ/cm^2; estimated spot size of 120 μm, fwhm) used to anneal the specimen were such that complete thermal dissipation between pulses did not occur, thus resulting in an elevated steady-state temperature (see the Supporting Information for an experiment that confirmed this). The laser wavelength was 515 nm (hv = 2.4 eV) generated with a harmonics module (Light Conversion HIRO).

2.1.3 Hexatriacontane

Hexatriacontane specimens used in the beam damage experiments (detailed in Chapter 3) were prepared by drop casting a solution of C36 (Fluka Analytical, 98% purity) in decane (Acros, 99+% purity) onto a copper grid with a 12-nm-thick amorphous carbon substrate (Electron Microscopy Sciences, Q225-CR4), upon which the solvent was allowed to evaporate in air. A conductive support grid was used in order to reduce the effects of beam-induced specimen charging.[261,372]

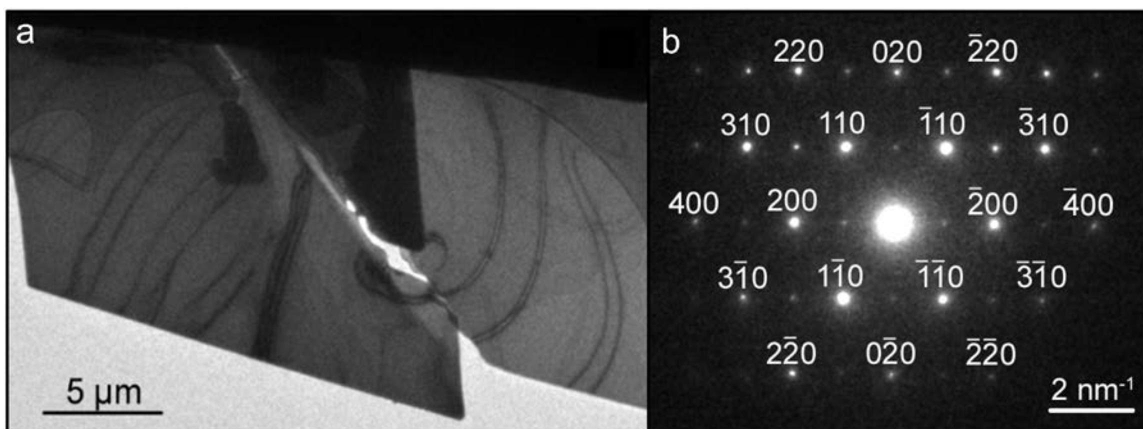

Figure 2.3 | Representative hexatriacontane specimen. (a) Bright field image showing two overlapping C36 microcrystals near a grid bar. (b) Indexed diffraction pattern of the [001] crystallographic zone axis, typical of the hexatriacontane specimens used in the experiments in Chapter 5.

Specimen thickness may affect the damage rates in some organic crystals.[263,373,374] Thus, determining the thicknesses of the C36 microcrystals studied here was deemed critical for making direct comparisons between pulsed- and thermionic-beam experiments. However, owing to the extreme beam sensitivity and softness of the microcrystals, it is generally challenging to directly measure thickness either during or immediately before the beam-damage experiment without modifying the structure in a way that could affect the outcome. Measuring crystal thickness after the beam-damage experiment also poses a challenge due to potential mass loss, though this is likely to be minor owing to the low doses and low dose rates studied here. A useful and important feature of C36 microcrystals is that thickness varies by integer multiples of the *c*-axis unit-cell length.[371,375,376] Thus, intact crystals will vary in thickness by $n \cdot (c$-axis length), where $n = 1, 2, 3,$ *etc.*

In order to rule out any influence of thickness on observed differences in damage between the pulsed and thermionic beams, a variety of methods were used to determine the distribution of thicknesses of C36 microcrystals. Thus, the overall likelihood of conducting experiments on crystals of significantly different thickness was established. One method involved measuring the thicknesses of a large number of C36 microcrystals using atomic force microscopy (AFM). The crystals were prepared in the same manner as those used in the beam-damage studies. The center thicknesses of 107 individual, isolated (*i.e.*, non-overlapping) microcrystals were recorded. Of this set, 106 were found to be 19.1-nm thick, while one was found to be 23.8-nm thick, thus indicating the specimen preparation methods produce a nearly monodisperse thickness distribution.

Other methods employed here made use of the behavior of Bragg-spot intensities with thickness, mainly following work by Dorset.[376] One such approach relies on the systematic change in Bragg-spot intensity ratios of the *110* and *200* families of planes with C36 crystal thickness (*i.e.*, number of stacked unit cells along the *c*-axis direction). Though mainly a qualitative measurement, it does allow one to determine if two specific crystals of interest are of approximately the same thickness. For example, for the pulsed and thermionic diffraction patterns shown in Figure 5.3, the I_{200}/I_{110} ratios were 1.12 and 1.18, respectively, indicating the thicknesses were nearly the same. Dorset has also shown that an *n*-beam dynamical description is most appropriate for modeling Bragg-spot intensities from C36 crystals.[376,377] Indeed, the results of this work demonstrated that forbidden peaks readily appear in C36 crystals that are at least 24-nm thick. As no forbidden peaks were observed in the diffraction patterns analyzed in the beam-damage studies reported here, it

is likely that all specimens were less than 24-nm thick, as indicated by the independent AFM measurements.

Dynamical scattering can contribute to allowed Bragg spots as well. Further, because the structure factors of particular reflections for C36 are more affected by *n*-beam scattering than others (*e.g.*, the *220* and *310* compared to the *120*, respectively), and because such scattering is a function of thickness, analyzing intensity ratios of such Bragg spots is another way to determine crystal thickness.[376] The results of applying this method here are summarized in Figure 2.4. By comparing calculations of Bragg-spot intensity ratios from data reported in Ref. 376 to the experimental data reported in Figure 5.3 (for example), it was found that the thicknesses for both C36 crystals match, within error, the expected values arising from crystals that are 19-nm thick. Taken altogether, the results of the methods used here make it reasonable to conclude that the vast majority of C36 microcrystals formed using the described preparation methods were of uniform thickness (*i.e.*, 19 nm), and that the likelihood that beam-damage experiments were conducted on microcrystals of differing thicknesses is low.

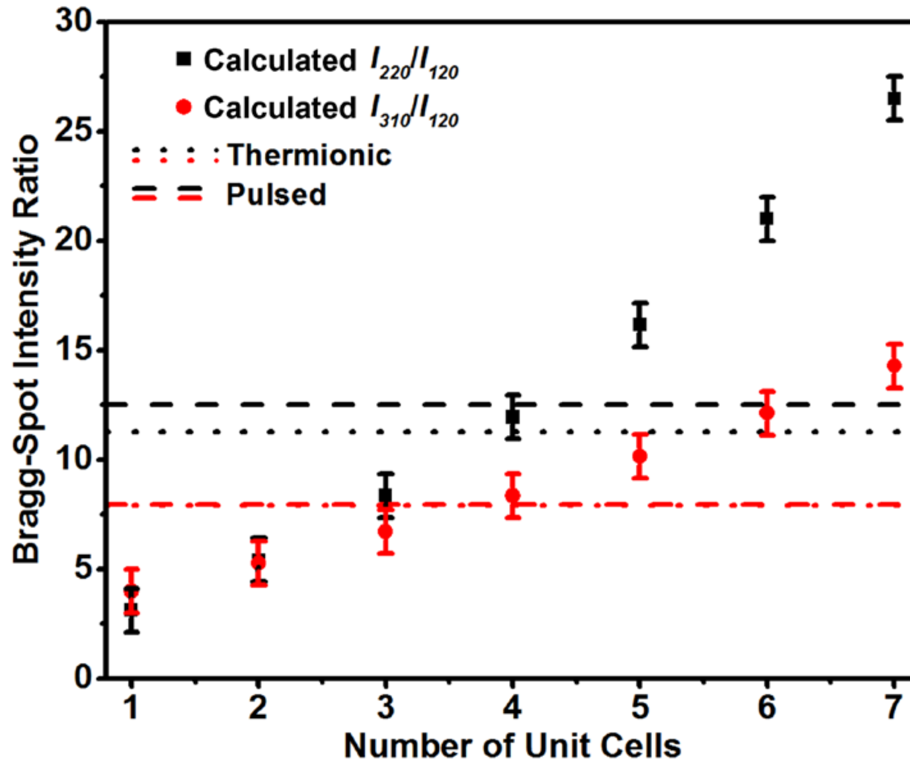

Figure 2.4 | Measured and calculated Bragg-spot intensity ratios for select reflections from crystalline C36. Individual data points represent the values of I_{220}/I_{120} (black squares) and I_{310}/I_{120} (red circles) as a function of C36 crystal thickness (in number of unit cells) calculated from data reported by Dorset.[376] The error bars represent the estimated standard error based on the accuracy of the analysis technique and the estimated accuracy of digitizing the data from the source graph. The horizontal lines correspond to the intensity-ratio values measured here from the diffraction patterns shown in Figure 5.3, as generated with a thermionic (dotted) and a pulsed (dashed) beam. Note that red horizontal lines corresponding to the I_{310}/I_{120} ratio overlap with one another.

2.1.4 Methylammonium Lead Iodide

Polycrystalline methylammonium lead iodide specimens were synthesized by spin coating a 0.3-M solution of $MAPbI_3$ with 10% molar excess MAI in a 4:1 volume ratio of DMF:DMSO onto holey amorphous-carbon grids (Quantifoil, Electron Microscopy Sciences) (Figure 2.5b). First, the grid was reversibly adhered to a silicon support using a drop of toluene followed by heating at 100 °C for 1 min. Next, 0.2 mL of $MAPbI_3$ solution was dropped onto the supported grid while spinning at 3000 rpm for 2 min. Finally, the grid was annealed at 100 °C for 1 hr. This produced freestanding, polycrystalline $MAPbI_3$ islands spanning the 2.5-μm holes of the grids (Figure 2.5b). Accordingly, each island was determined from the bright-field TEM images to be 4.8 ± 0.2 μm^2 in area (error is one standard deviation from the mean). It is clear from the diffraction pattern (Figure 2.5b inset) that while the specimens are not single-crystalline, they also certainly are not polycrystalline as such a designation is typically imagined. The diffraction patterns are consistent with a small number of crystallites (on the order of tens) of various orientations appearing within the selected area aperture.

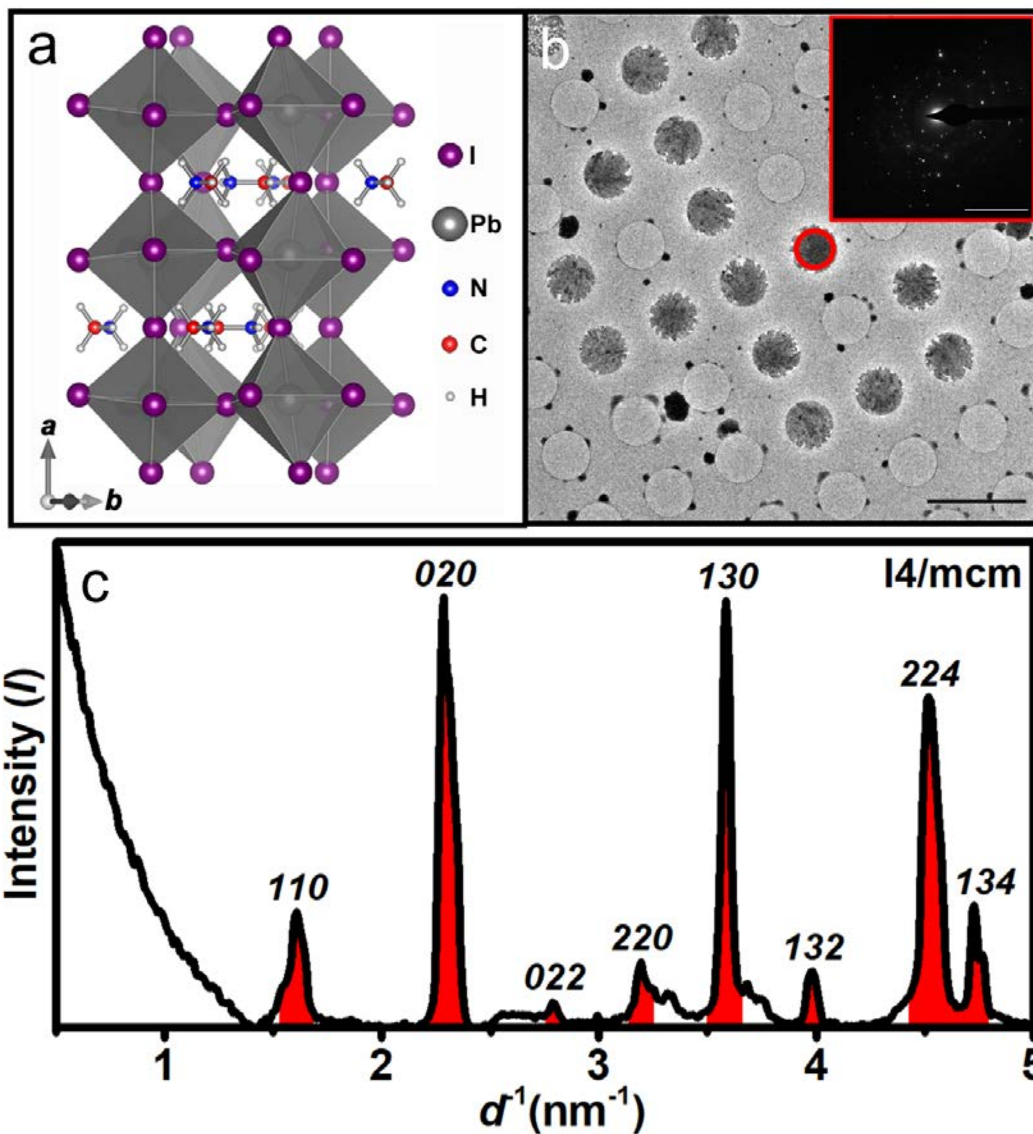

Figure 2.5 | Polycrystalline methylammonium lead iodide specimen. (a) Structure of $MAPbI_3$.[378] Crystallographic axes are shown in the lower left of the panel. (b) Low-magnification bright-field image of the TEM specimens (scale bar = 5 μm). The diffraction pattern (inset; scale bar = 5 nm^{-1}) was obtained from the red-circled region. (c) Intensity plot from azimuthally averaging the pattern in (b) inset. Red peaks are those used for monitoring beam-induced intensity changes (see Chapter 6 for more details). The space

group used for indexing was *I4/mcm*, though the structure is not yet universally agreed upon.[1,2,277]

2.2 | Pulsed-Beam/Ultrafast Electron Microscope

The Flannigan Group UEM is a recently-developed, unique instrument built at the University of Minnesota in the basement of Amundson Hall. It consists of a PHAROS femtosecond pulsed laser system (Light Conversion) and an FEI Tecnai Femto TEM (Thermo Fisher Scientific), which will be described individually below. This equipment can be operated as a standard TEM, as shown in Chapter 3, as a pump-probe stroboscopic UEM, as shown in Chapter 4, or as a standard TEM with a pulsed electron beam, as shown in Chapters 5 and 6. Setup and characterization of the microscope in both of the latter configurations will be described in detail below. Figure 2.6 schematically shows the integration of the laser into the TEM.

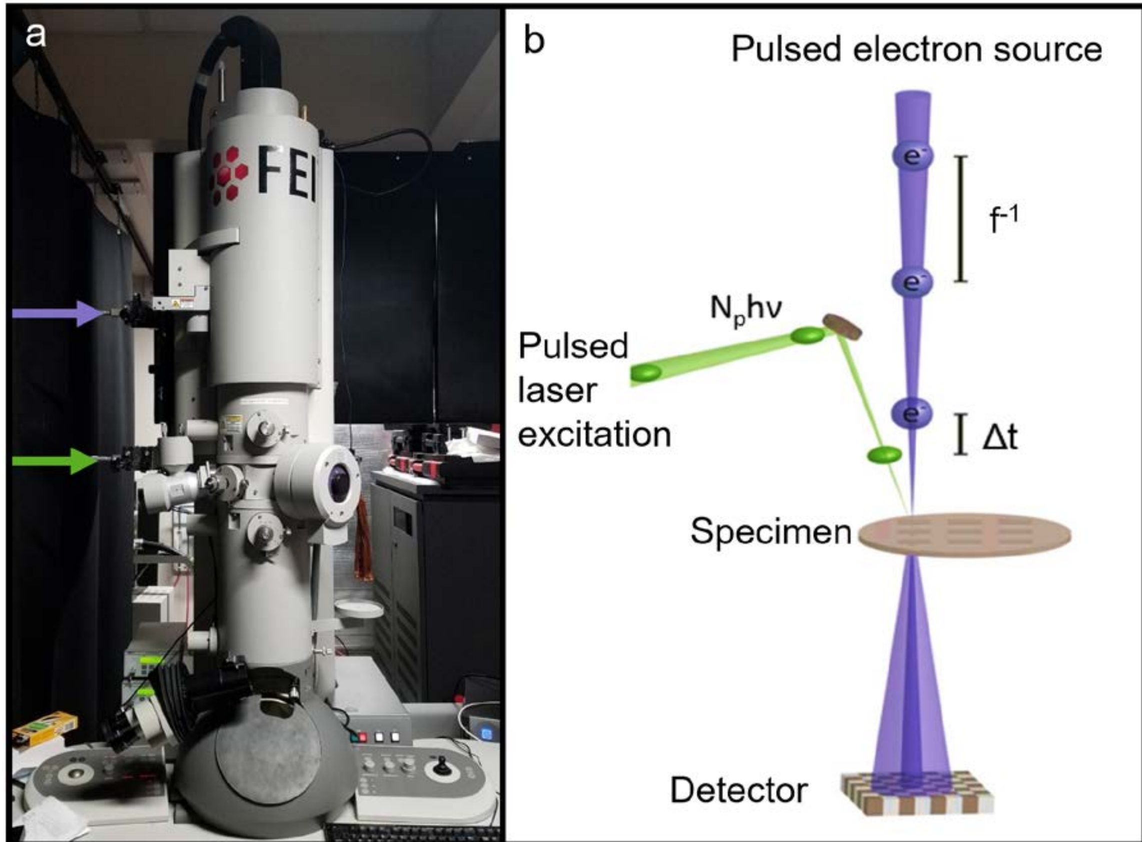

Figure 2.6 | Schematic of integration of laser into TEM. (a) Photo of TEM in Flannigan UEM lab with entry points of pump laser (green) and probe laser (purple) marked with arrows. A closer view of the periscopes on the outside of the TEM is shown in Figure 2.8. (b) Schematic showing pump-probe scheme in action, where laser pulses, shown in green, are directed onto the specimen to excite a material response. After a certain time Δt, an electron packet arrives at the specimen to probe the response, eventually registering on the detector. The probe pulse is generated by the fourth harmonic laser extracting a packet of photoelectrons from the cathode, as shown below in Figure 2.9. The temporal spacing between electron pulses and pump pulses is the same, and is the inverse of the laser repetition rate f.

2.2.1 Femtosecond Laser System

As described in Section 1.1.4, one method of pulsed-electron-beam generation is the use of an ultrafast pulsed laser to extract packets of photoelectrons from the cathode of a TEM. The laser used in this work was a femtosecond-pulsed Light Conversion PHAROS with 6 W maximum power, repetition rates (inverse of time between laser pulses) up to 1.1 MHz, and maximum pulse energies of 200 μJ. It is diode-pumped and based on a Yb:KGW solid state lasing medium which produces a fundamental wavelength is 1030 nm, corresponding to a 1.2 eV photon energy. Upon exiting the PHAROS, the beam is directed to a harmonics module where it is frequency doubled and tripled to produce 515 nm and 343 nm beams. The laser then traverses a home-built optics path to reach the TEM, in which dichroic mirrors are used to separate the beam paths of the different wavelengths. The 515 nm beam is split such that part of it is used as the pump for the specimen (the 343 nm and 1030 nm beams can also be used for this purpose, but are not done so in this work), and part of it is frequency doubled once again to produce a 258 nm line using a beta barium borate (BBO) crystal (Eksma Optics). This resulting fourth harmonic is sufficient to overcome the work function of the TEM cathode, which is made of lanthanum hexaboride (LaB_6), so is directed to the upper periscope of the TEM to act as the probe line.

In order to achieve a variable-delay pump-probe scheme, the time between arrival of the pump pulse and probe pulse must be controlled. This is done using a mechanical delay stage (PRO165LM-1000, Aerotech) which is one meter long and equipped with a retroreflector, leading to a 6.7-ns range of time points that can be accessed in fs experiments. The overall path of the laser on the lower laser table is shown in Figure 2.7.

Upon direction to the top table, the laser is directed toward periscopes mounted on the outside of the TEM, inside which are two mirrors which direct the probe and pump lines into the gun and specimen regions of the TEM, respectively. The integration of the laser into the TEM will be described further in the following section.

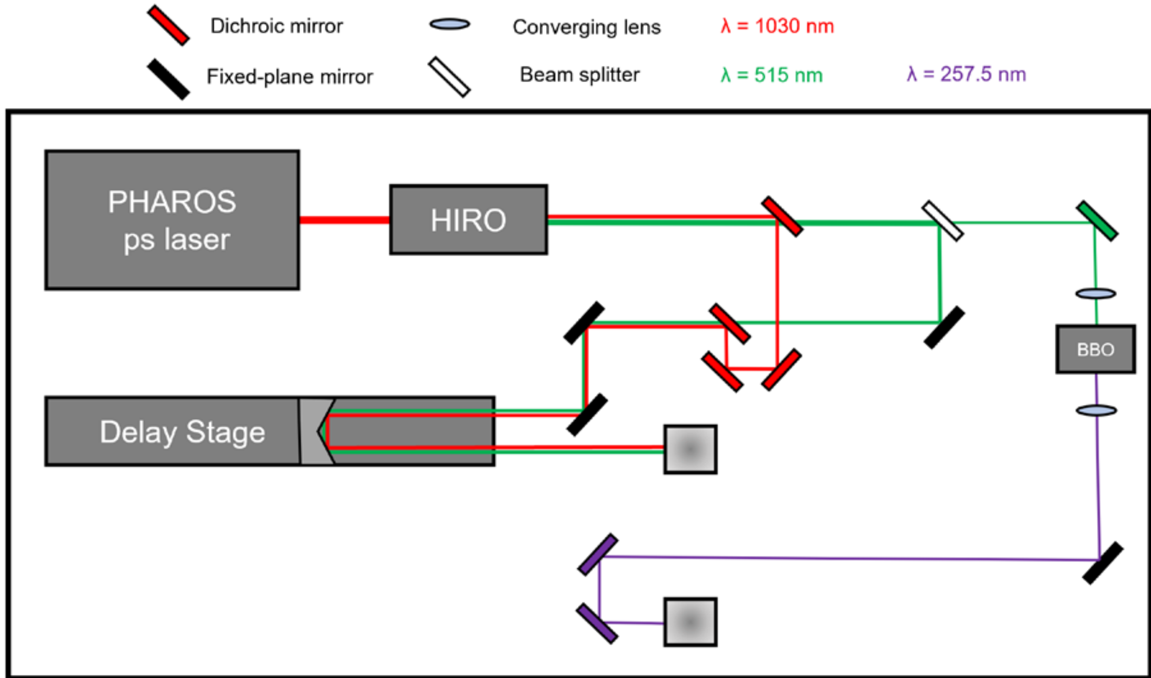

Figure 2.7 | Schematic diagram of the lower laser table. The PHAROS outputs a first harmonic of 1030 nm which is frequency doubled using the HIRO. The first harmonic is split from the second harmonic and directed along the delay stage. The second harmonic is split such that half of the beam travels a collinear path with the fundamental frequency. The second beam is frequency doubled to a fourth harmonic. Both beams are directed to a top table which only has plane mirrors used to direct the beams to the height of the entry ports on the TEM (shown in Figure 2.6). The fourth harmonic is sent to the gun for photoelectron extraction and the first harmonic is used for specimen excitation.

2.2.2 Transmission Electron Microscope and Integration

All experiments described in this work were conducted with a 200 kV FEI Tecnai FEMTO transmission electron microscope (Thermo Fisher Scientific) equipped with a Gatan OneView 16 megapixel CMOS camera (Chapters 4-6) or a Gatan Orius SC200B 4 megapixel fiber-coupled CCD camera (Chapter 3). The Tecnai FEMTO is equipped with a conventional thermionic electron gun and Wehnelt triode, and in almost all ways operates as a standard TEM. However, some modifications are made to accommodate laser-driven pulsed beam and ultrafast electron microscopy. A custom graphite-encircled LaB_6 cathode (Applied Physics Technologies) is used for all experiments. The LaB_6 is truncated such that the emissive surface is flat and 50 μm in diameter, increasing the contact area of the probe laser with the cathode. The graphite ensures that emission occurs mainly from the flat LaB_6 region and not from the shank, and it seems to also improve photoemission stability compared to bare LaB_6 cathodes, though experiments still need to be conducted to explicitly test this. A larger Wehnelt aperture (1.5 mm compared to a standard 0.7 mm aperture) is also used. A custom 1250- μm condenser aperture is also available in place of the standard smallest condenser aperture. These two modifications increase collection efficiency of electrons in low-beam-current experiments, although they do cause a reduction in spatial coherence.

The Tecnai FEMTO is equipped with two optical periscopes integrated into the side of the column. The upper periscope, highlighted in Figure 2.8, provides optical access to the LaB_6 cathode such that femtosecond (fs) laser pulses can be used to generate discrete packets of photoelectrons from a room-temperature (*i.e.*, not heated) source. The lower

periscope similarly provides optical access to the specimen region where 515-nm pulses are used to excite specimen dynamics. Both periscopes contain two adjustable mirrors for laser alignment upon entry into the microscope, as well as lenses positioned just before the periscope to control beam characteristics. The final mirror in both cases is internal to the TEM, which due to space constraints in these regions necessitates a precise alignment procedure to achieve spatially-consistent illumination of the cathode or specimen.

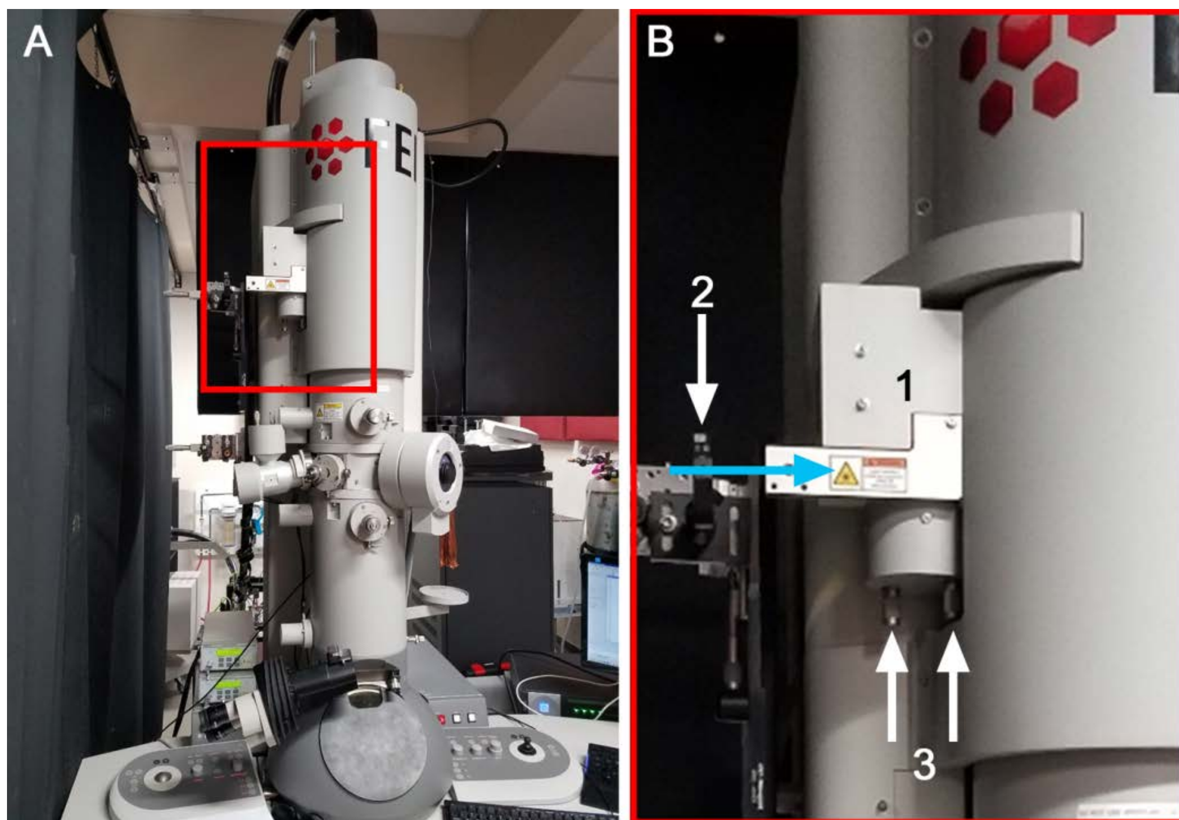

Figure 2.8 | Thermionic 200 kV TEM modified for laser-driven pulsed or pump-probe operation. (A) Photograph of the modified TEM highlighting (red rectangle) the optical periscope with which the fs UV laser pulses are directed onto the LaB_6 electron source. The fs laser system is behind the laser safety curtain to the left outside the frame of the image. (B) Close-up view of the optical periscope highlighted in (A). Denoted in the image are: (1) The optical periscope assembly. (2) An external focusing lens mounted on a 3-axis positioner. (3) Micrometers for manipulating one of the internal mirrors. Direction of the incident UV pulses is indicated by the light-blue arrow.

The pulsed electron beam generated using this technique mainly differs from a standard thermionic electron beam in the probability profile of electron emission. This is

demonstrated in Figure 2.9. This holds true for the pump-probe experimental scheme and is particularly important for the pulsed beam experiments, for reasons which will be explained further below.

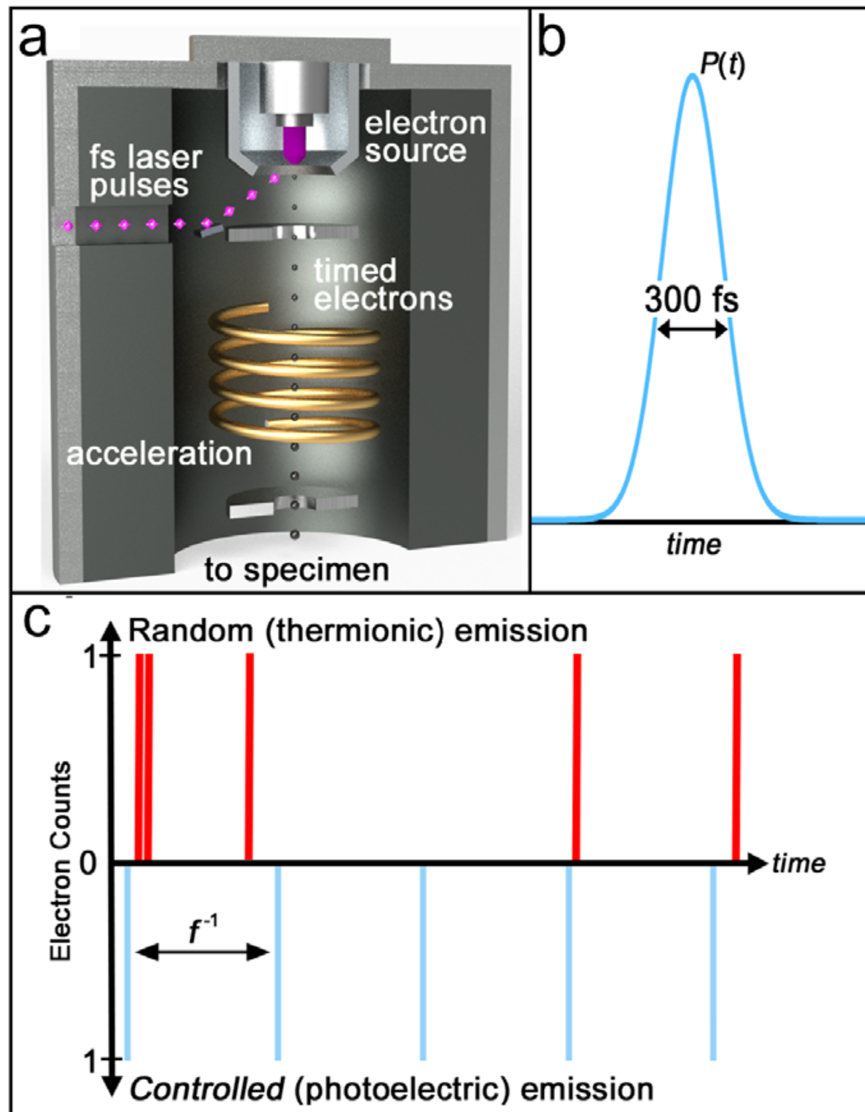

Figure 2.9 | Generation and characteristics of the pulsed electron beam. (a) Schematic of the source region of the modified TEM. The fs laser pulses enter through an optical port and are directed onto the source to generate timed electron packets. These are then

accelerated and directed to the specimen using conventional methods. (b) Schematic illustration of the shape of electron pulse emission probability. Distribution follows a Gaussian shape to match the character of the laser pulses during laser-cathode contact (here, 300 fs FWHM). Probability of emission is functionally zero outside of laser-cathode contact because of lack of cathode heating. (c) Concept of controlled, precisely-timed electron emission compared to conventional random (thermionic) emission for the same beam current. The laser repetition rate (f; pulses per second) dictates the time between electron emission (f^{-1}) for the pulsed approach. Laser-pulse energy is tuned to select the desired number of electrons, and the temporal emission probability [$P(t)$] is confined to the pulse duration as described above.

Fine alignments of the probe laser are generally straightforward as long as the beam is aligned somewhat with the final mirror such that is directed onto the gun assembly. If not, this must be done by opening the column and aligning the laser while not under vacuum. If the laser beam contacts the Wehnelt assembly, it will extract photoelectrons which are visible on the camera when the cathode is cool. From there, periscope internal mirrors can be manipulated such that the beam travels through the Wehnelt aperture onto the cathode, using the illumination of the Wehnelt via extraction of electrons as a guide. Wehnelt electrons should generally not be used as probe electrons as the Wehnelt assembly is several hundred microns further down the column than the cathode, leading to a time delay between Wehnelt electrons and cathode electrons.

Pump alignments are somewhat more complex and in the context of this work are done by observing the burning of a Quantifoil (Electron Microscopy Sciences, Q225-CR4) carbon substrate on a copper TEM grid. When burning creates high contrast this technique is simple and effective – if burning not centered on the grid is observed, the periscope mirrors can be manipulated to center the pump laser on the specimen. However, in the absence of high contrast, or when a specimen (rather than a blank Quantifoil) is inserted in the specimen holder, this process is challenging to complete consistently. Work is under way in the Flannigan group to create a more robust and efficient procedure for such alignments.

Automation of the camera and delay stage allow users to conduct a UEM pump-probe experiment remotely, reducing total experiment time and reducing movement of the operator in the lab which can contribute to instability. The details of automation are described elsewhere[379] but briefly, one computer is used to control the laser and the optical delay stage, and another is used to control the TEM including the camera. The operator generates a list of time points according to the experimental needs, and sometimes randomizes them (further discussion of time order in Section 4.1.4). The spacing of time points is determined by the time resolution expected for the experiment (*e.g.*, 1-ps time resolution means the frames can be a minimum of 1 ps apart) and the total length of the experiment is determined by experimental stability and the length of the decay process being explored. For each time point, the delay stage is moved to a given time point, and the camera begins acquiring. The camera shutter remains open until sufficient SNR is

acquired (acquisition time determined in advance by the operator), upon which the laser computer begins to move the delay stage to the subsequent time point.

2.2.3 Pulsed Beam Dose Rate Characterization

The dependence of electron beam damage on dose rate and other imaging conditions can vary widely, and therefore in order to conduct beam damage experiments, it is vital to ensure imaging conditions are consistent across all experiments, and especially for directly-compared experiments. Thermionic beam current was controlled primarily using the cathode heat-to value. At times, spot size (*i.e.*, the C1 condenser-lens setting) was changed slightly to fine-tune the beam current, but this was kept as close to the largest spot size of one as possible in order to ensure consistency and to maintain similarity to the relatively large photoelectron beam spot size used here. Pulsed photoelectron beam current was controlled by varying the fs UV laser pulse energy, which was used to finely control the number of electrons generated per laser pulse (Figure 2.10), and *via* the laser repetition rate (f, pulses per second), which was used to control the number of discrete electron packets generated per unit time. While the overall linear behavior shown in Figure 2.10 is typical when operating well below the space-charge (*i.e.*, saturation) limit, the precise values of the slope and the intercept can be highly variable from one LaB_6 cathode to the next, and even from one experiment to the next.[150,161,341] Though the factors are likely numerous and highly synergistic, it is reasonable to assume the sources of variability include the changing condition of the cathode surface (*e.g.*, composition, morphology), variation in the laser focusing conditions on the cathode, variation in laser alignment onto

the cathode, *etc*. Additional details specific to Figure 2.10 are given in the caption. In light of this, care was taken to ensure each individual experiment, and each set of directly-compared experiments, were self-consistent and consistent, respectively. For example, the photoelectrons per laser pulse were measured and adjusted both before and after every experimental run, and the experiment was rejected and repeated if the difference was larger than the random error of the measurement. No reliance was placed on a predetermined quantitative relationship (*i.e.*, a universally applied calibration curve) between the UV laser pulse energy and the measured number of photoelectrons generated per pulse.

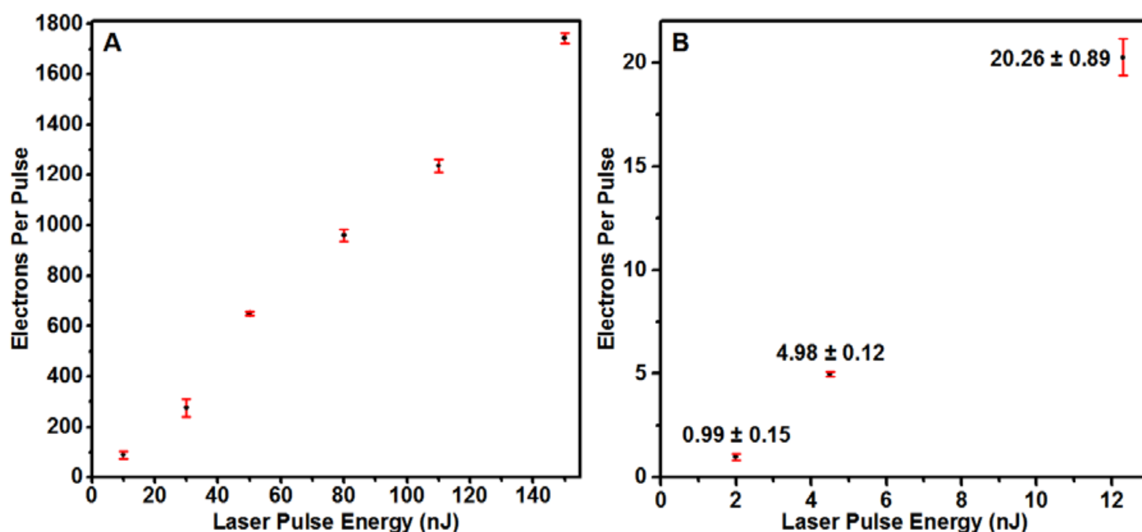

Figure 2.10 | Photoelectrons per laser pulse generated from the TEM LaB_6 source as a function of pulse energy. (a) Representative behavior of the photoelectrons per pulse for high pulse energies relative to those used to conduct the ultralow-dose-rate experiments. This plot is provided only as a general example of the overall behavior below the onset of saturation. (b) Photoelectrons per pulse at the low pulse energies used for the ultralow-dose-rate experiments reported here. It is important to note that while the data shown in

each panel are self-consistent, variation across the data sets is present. For example, in (a), the number of electrons generated per pulse for a laser pulse energy of 10 nJ was 89 ± 14, while in (b), the number was 20 ± 1 for a pulse energy of 12.3 nJ. The reason for this is that the data sets were acquired in separate trials. Though the qualitative behaviors will be consistent (*e.g.*, linear response in the relatively low pulse-energy regime), variations in LaB_6 photocathode condition, precise laser alignment onto the photocathode, and the precise laser focusing condition onto the photocathode all are expected to cause variation in the absolute photoelectron values. For all experiments, the incident photon energy was 4.8 eV (fourth harmonic of the 1.03-μm fundamental wavelength of the Yb:KGW fs laser), and the pulse duration was 300 fs FWHM for the fundamental beam (*i.e.*, lower bound for the UV pulses). The error bars represent one standard error over ten separate measurements.

Two methods were used to measure beam current. Method 1 consisted of using a Faraday cup integrated into the specimen holder (Gatan 636.MA double-tilt liquid-nitrogen holder) and connected to a 486 Keithley PicoAmmeter. Method 2 consisted of using the Gatan OneView CMOS camera to determine the counts per unit time and then conversion of this value to a number of electrons per unit time *via* a known scintillator calibration factor; note the calibration factor for the OneView camera is integrated into the software such that the number of electrons in the image is displayed. While it is reasonable to assume that the beam current measured with Method 1 can be directly related to the beam current used to irradiate the specimen, the geometry of Method 2 is such that the

relationship between the beam current at the specimen and the beam current at the detector must be determined. This was accomplished by determining the ratio of the number of electrons per unit time (N) measured with Method 2 (detector; $N_{det.}$) and Method 1 (Faraday cup; $N_{Faraday}$) at several laser-pulse energies (and therefore several beam currents). The results of such an experiment for $N_{det.}/N_{Faraday}$ are shown in Figure 2.11.

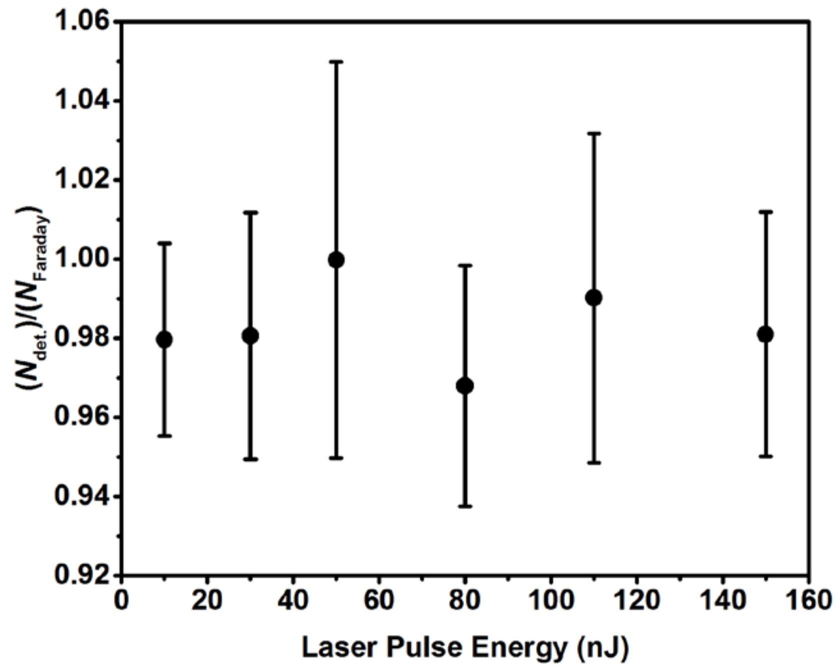

Figure 2.11 | Comparison of beam current measurement methods. Number of electrons per unit time measured at the detector ($N_{det.}$, Method 2) relative to the number of electrons measured at the specimen with a Faraday cup for the same amount of time ($N_{Faraday}$, Method 1) for a range of laser pulse energies incident on the TEM photocathode. Error bars represent the standard error over 10 separate measurements.

Figure 2.11 demonstrates that, for the same lens settings and projection-system conditions, approximately 98% of the electrons measured at the specimen plane with the Faraday cup are incident on the detector. A *t*-test at all laser pulse energies tested indicates there is no statistical difference between the two measurement methods to 95% confidence. Note that the *t*-statistic between the ratio data in Figure 2.11 and the value of 1 does not correspond to $p < 0.05$, indicating to 95% confidence that there is no statistical difference between the two forms of measurement. Also note that the overall variability was dominated by random error in the Faraday cup measurements (Method 1); measurements with the Faraday cup had up to 5% standard error, while those using the detector (Method 2) had a standard error of less than 1%. The result in Figure 2.11 and the statistical equivalency to 95% confidence indicates it is reasonable to approximate the beam current measured at the detector as the beam current incident on the specimen. Another critical benefit to using Method 2 is the significantly increased sensitivity relative to the Faraday cup and picoammeter; the low random error and high sensitivity relative to the Faraday cup method enabled accurate and precise measurement of the number of electrons per laser pulse – down to the lowest of one electron per packet studied here.

Accordingly, method 2 was used to monitor beam-current stability and to determine dose and dose rate for all experiments reported here. This was specifically accomplished by condensing the beam such that it fell entirely on the detector, which was then followed by acquisition of ten images with the same exposure time as the experiment of interest. The total counts for each image was obtained using Digital Micrograph 3. Ultra-Value Analysis was used to identify outliers in counts caused by (for example) X-ray detection.

This resulted in rejection of no more than one image in a particular set of 10 (typically all 10 could be used). For each of the usable images, the total electron counts were divided by the image acquisition time to get the electrons per unit time, from which the mean and standard error were determined. The number of electrons per each individual packet could then be determined by noting the laser repetition rate (f), which dictates the number of discrete packets generated per unit time.

Because the electron-beam size may influence the observed damage behaviors, and because it is a key parameter for calculating dose and dose rate, it must be determined accurately and applied uniformly for direct comparisons to be made.[380–382] For some experiments, the use of a small beam size (*via* a small condenser aperture) enabled the beam area to be directly measured. This was done by acquiring an image of the beam at the relevant intensity value and using a Hough transform to calculate the radius. When the beam shape was not circular, an edge-finding algorithm and numerical integration was used. When area could not be determined using a Hough transform or numerical integration (*e.g.*, because portions of the beam fell outside the detector), three additional methods were used (Figure 2.12). For one method, an image of the beam was acquired in "M" magnification mode (*i.e.*, standard TEM operation mode; nomenclature specific to FEI instruments) at all intensity values where the entire beam was visible on the detector, and the area was determined as described above. The relationship between intensity and beam size was then plotted and fit with a polynomial. Another method consisted of repeating this process but in "LM" magnification mode (*i.e.*, low magnification mode in which the objective lens is turned off; nomenclature again specific to FEI instruments),

enabling a wider range of intensity values to be directly measured. The difference in beam size between the “LM” and the “M” modes was determined, and the average value was used to scale the “LM” sizes to the “M” mode. A third method consisted of comparing total counts for a beam imaged entirely on the detector to the counts for a spread beam. By comparing the counts in these two measurements, the proportion of the spread beam falling on the screen can be determined. The area of the spread beam can then be calculated using geometrical arguments despite not being entirely captured on the detector.

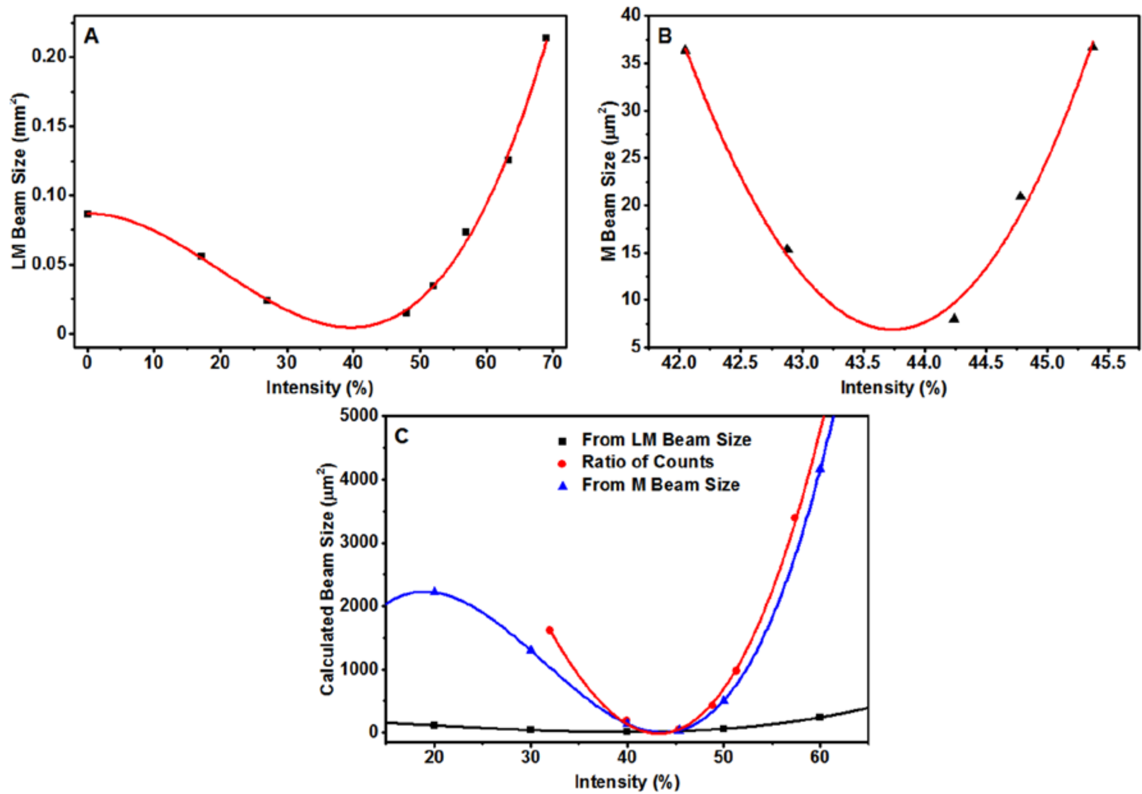

Figure 2.12 | Methods for determining the electron beam size. (a) Directly measured beam size for a range of intensity values in "LM" magnification mode (black squares). A polynomial fit to the data is shown in red. (b) Directly measured beam size for a range of intensity values in "M" magnification mode (black triangles). A polynomial fit to the data is shown in red. (c) Calculated beam size as a function of intensity value for three different methods over the intensity range of interest: (1) Fit to directly-measured "LM"-mode data (black). (2) Fit to directly-measured "M"-mode data (blue). (3) Geometrical approach based on the ratio of total to measured counts (red).

As can be seen from Figure 2.12c, there is good agreement between the "M" magnification method and the ratio of counts method. The "LM" magnification method

was therefore not used. By comparison with similar measurements done with smaller condenser apertures (and therefore under conditions wherein a larger range of intensity values could be directly measured), it was consistently found that both of the retained methods were accurate to within the error of the counts measurement and the Hough transform – about 2% and 1%, respectively – at the intensity values used in all experiments (*i.e.*, 50% to 60%). Thus, the intensity ratio method for beam-size determination was used for all experiments owing to the ease with which multiple measurements could be quickly performed. This method was typically repeated several times during a given experiment and at least once at the beginning of every experimental run. It is important to note that treating the beam shape as circular was found to be a reasonable approximation when a condenser aperture of 200 μm or smaller was used, which was the case for all experiments reported here.

Finally, in addition to controlling for beam size, effort was made to ensure the beam had the same convergence angle in both thermionic and pulsed modes. This was done by ensuring the laser was well-aligned with the center of the LaB_6 cathode and that the beam illuminated the entire cathode surface as uniformly as possible. In this way, use of the same lens settings and alignments in the illumination system for both modes of operation resulted in the same beam behavior. This was checked and verified by finding the optimal alignments through standard procedures in both modes and then comparing the resulting lens settings, which were then confirmed to be the same.

2.2.4 Pulsed Beam Stability

Instrument and lab-environment stability were especially critical to the successful execution of beam damage experiments discussed in Chapters 3-5, as the lowest-applied dose rates required over 22 continuous hours of data acquisition. Thus, long-term stability of the electron beam and the laboratory room temperature were regularly checked and continuously monitored. If the beam current (pulsed or thermionic) at the conclusion of a data-acquisition run was different from that at the start by more than the measured random error, or if the lab temperature changed by more than 1 ºC during the experiment, the data set was rejected and the experiment was repeated, regardless of the outcome. Lab temperature was continuously monitored at three locations: at the lab door, on the fs laser table, and at the TEM column. Changes of more than 1 ºC at any of these locations at any point during the run resulted in rejection of the entire experiment, again regardless of the outcome. To illustrate the high levels of long-term instrument and lab stability that were reached here, Figure 2.13 shows a representative plot of photoelectron counts (measured every 15 minutes by acquiring an image of the condensed beam) as a function of time over a 24-hour period. In this data, two standard deviations from the mean corresponds to a range of ±0.3% from the mean, and a drop in counts of 26 electrons per hour (or 0.0016% of the mean value) was detected, well below the range of standard deviation arising from random error.

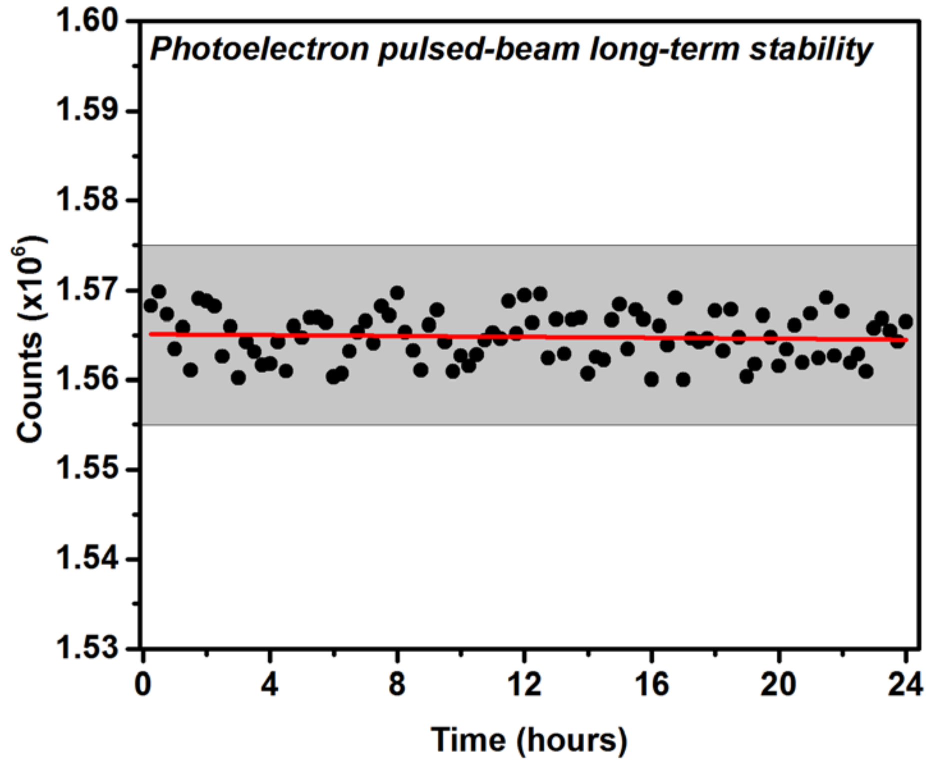

Figure 2.13 | Representative example of the long-term stability of the pulsed photoelectron beam over a 24-hour period. The data were obtained by summing the counts of an image of the electron source acquired at 15-minute intervals and then converting to the number of electrons incident on the detector. The mean value is 1.565 ± 0.005 x 10^6 counts (electrons), where ± 0.005 x 10^6 (*i.e.*, ±0.3%) is two standard deviations from the mean. The slope of the least-squares fit line (red) is -25.7, signifying a drop of 25.7 counts per hour, or approximately 0.0016% of the mean over 24 hours. To further emphasize the high long-term stability, the grey box denotes a ±0.64% deviation from the mean.

Determining specimen spatial stability with respect to drift under equilibrated conditions was necessary in order to ensure against potential systematic error arising from,

for example, gradual movement of portions of the microcrystal beyond the electron-beam illumination area. This is especially true in light of the extreme length of some experiments. Accordingly, the spatial position of the crystal under study was compared before and after the experiment, and minimal to no observable net drift outside of the electron-beam area was observed. Here, net drift refers to specimen drift that results in non-zero lateral motion in the *xy*-plane rather than motion about a single center-of-mass position, as would be expected for a stable and equilibrated system and environment. As suggested by Figure 2.13 and discussed in Section 2.2.4, this general observation is a result of the stable equilibrated experimental system and laboratory environment. To further illustrate the typical spatial stability of the specimens with respect to net drift, Figure 2.14 displays a bright-field image of a C36 crystal obtained with a 0.8 nA thermionic beam current (much higher than used in the ultralow-dose studies) and a difference image of another image of the same crystal obtained three hours later. As can be seen, only shifts in bend contour position are observed, indicative of slight beam-induced strain relaxation, while no lateral motion is observed at this magnification (the weaker false-colored contrast is noise). This particular experiment was replicated three separate times on three separate C36 crystals with the same results. This illustrates that to within the 12.5 nm/pixel of this particular experiment, the stability was such that no net specimen drift occurred over the three-hour period. This experiment demonstrates that when the system and laboratory was equilibrated and stable, any thermal drift occurs about a single center-of-mass position such that the specimen remained approximately centered within the electron beam, and no change in diffraction signal occurred due to drift.

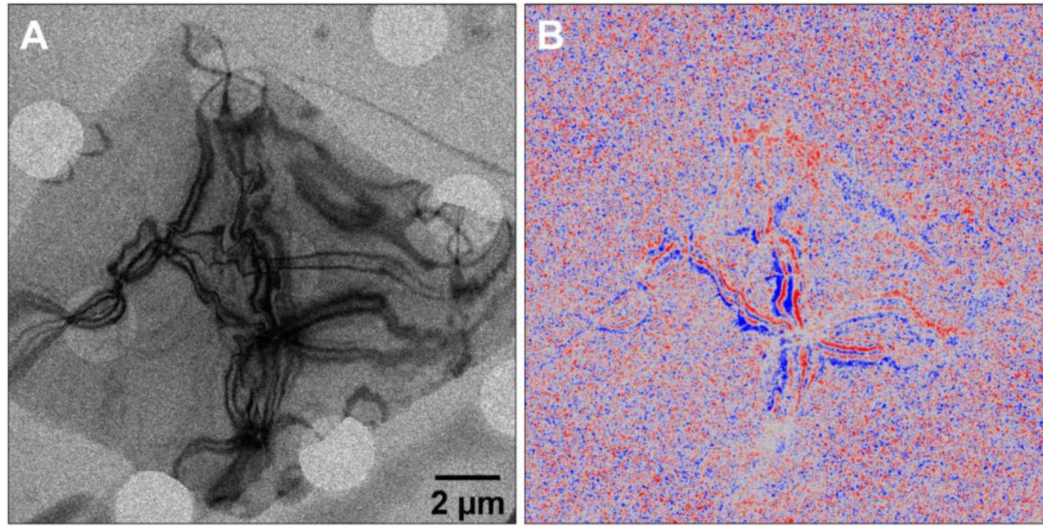

Figure 2.14 | Demonstration of specimen spatial stability over a three-hour span. (a) Bright-field image of a single C36 crystal obtained with a 0.8 nA beam current (recall that beam currents of femtoamps were used in the damage studies). (b) False-colored difference image formed by subtracting (a) from a bright-field image of the same crystal acquired three hours later. The blue areas represent a loss of counts (*i.e.*, area became darker), and the red areas represent a gain in counts (*i.e.*, area became brighter).

2.2.5 UEM Parameters and Characterization

Determination of laser parameters used for a specific experiment is based on myriad variables. Upper limits on power and pulse energy are determined by integrity of the optics, especially in the TEM periscope where the small mirrors are especially sensitive and difficult to replace. High powers and pulse energies can also ablate the cathode, limiting experimental stability in both the short- and long-term. Within these limits, probe

pulse energies must be determined by balancing experimental time and necessary time resolution. Specifically, a more powerful probe pulse will generate more electrons per pulse, as shown in Figure 2.9 above. Larger pulses of electrons will reduce the number of pump-probe cycles needed to build up sufficient SNR, reducing the acquisition time needed for each time point and therefore the experimental time. Long experimental times can introduce challenges with specimen and equipment stability, increasing the need for careful control experiments and the chance of irreversible effects that confound data analysis, such as specimen drift and reorientation. However, because space-charge effects arising from repulsive electron-electron forces spread the packet both vertically and horizontally as it travels through the column, larger electron packets also lead to lower spatial and temporal resolution. This tradeoff is assessed individually for the requirements of each experiment.

Aside from the number of electrons per packet, the electron packet duration (and therefore the time resolution of the experiment) is also affected by the laser pulse length. The pump pulse length is also relevant because a long specimen-pump interaction creates more complex dynamics, potentially rendering invalid assumptions that rely on a rapid, short-term heat and light stimulus. For most of the work in this thesis, pulse durations were measured using a home-built second harmonic generation frequency resolved optical grating (SHG-FROG). Further details on this procedure can be found in Ref. 383. Just before completion of the experiments described in Chapter 6, a Light Conversion GECO scanning autocorrelator was acquired to measure pulse duration more efficiently.

The repetition rate chosen must leave enough time for the specimen to fully recover between pump pulses. This is often determined and verified using a control experiment in

which the delay stage is set to a specific, constant location for the duration of a typical experiment. (An example is shown in Section 4.1.4.) The result of such a control experiment should be no visible motion of the specimen whatsoever, as the same time-point is being measured repeatedly. Any motion indicates that the specimen relaxation post-excitation is not occurring identically during each subsequent pump-probe cycle, indicating some irreversibility. This can be due to damage or other specimen changes, as in the case shown in Section 4.1.5, or it can be caused by an excessive repetition rate in which the energy introduced in each pump pulse cannot fully decay away before the ensuing pump pulse arrives.

For the UEM experiments described in Chapter 4, the time point determined to be the moment of excitation (also called time-zero) is what is referred to as experimental time-zero. This refers to the point at which dynamics are first observed in the specimen. True time-zero refers to the time point where the pump laser pulse and the electron packet arrive at the specimen at exactly the same time (or more accurately when the pump laser pulse arrives at the specimen while the electron packet is in the process of traveling through the specimen). True time-zero and experimental time-zero are equivalent if there is no delay between excitation and the first observable dynamics. However, previous work in the Flannigan group has shown that in some systems there can be a delay, even one on the order of 100 ps.[26] The delay is assumed to be related to the time in which energy deposited in the specimen decays through pathways that are not structurally visible within the time resolution of the UEM, such as electron scattering and even high-velocity and/or high-

frequency phonons. Owing to this reality, it is vital to differentiate between experimental and true time-zero when reporting UEM results.

Chapter 3 | Error Mitigation in Debye-Waller-Based In Situ Thermometry

When ultrafast experiments are conducted using a stroboscopic pump-probe approach, the large number of pump-probe cycles required to build up SNR introduces a high level of experimental complexity. Despite this, such approaches have been successfully used to study a wide range of structural dynamics across many chemical and materials systems.[26,119,121,196,207,384–395] The practice of conducting control experiments and identifying sources of error and artifacts is especially critical to this progress, as it enables rigorous evaluation of the accuracy, repeatability, and robustness of the results.[26,116,121,161,205,396] This is especially the case when attempting to assign universal behaviors to the intrinsic response of the system under study. As described in Section 1.2.2, the use of the DW effect to describe thermal behavior or other specimen properties is such a case.

The main goal of the work described in this chapter is to illustrate and quantify several practical experimental effects common to UED and UEM experiments – in addition to conventional *in situ* TEM experiments – that can act as sources of error and artifacts in ultrafast (and time-averaged) scattering measurements involving the DW effect. Using thin films of polycrystalline aluminum (*pc*-Al) as a test system, we analyze and discuss the effects of specimen displacement (*i.e.*, in-plane movement of the region being probed), effective changes in camera length, and specimen tilting/bending/bulging caused by thermal expansion, mainly from the perspective of how these would impact measurements of $\langle u^2 \rangle$ – and by extension time-domain phonon dynamics – *via* the DW effect. While the

impact of several practical experimental effects on shifts in Debye-Scherrer-ring positions during *in situ* thermal measurements have been studied, we focus exclusively here on the impact on the intensities of diffracted beams, analogous to previous work on temperature-dependent foil transmissivity conducted *via in situ* laser-heating experiments.[174,189,213,397] With systematic experiments, we show that such specimen motions can produce changes in I_{hkl} comparable to or significantly larger than those from the DW effect, absent any specimen temperature change. For example, we illustrate that tilting a particular small-grained *pc*-Al thin film by a small amount relative to the incident electron wave vector introduces the equivalent of significant temperature changes were they ascribed entirely to the DW effect. We also show that in-plane and *z*-direction specimen translations can lead to statistically-significant changes in I_{hkl}, again, in the absence of an actual temperature change. We discuss and quantify the underlying sources of these effects as related to thermally-induced specimen motion and orientation changes.

3.1 | Experimental Methods

3.1.1 Aluminum as a Model Material

Aluminum was chosen as the test material because it undergoes a large thermal expansion relative to other metals, values for $\langle u^2 \rangle$ have been reported, and deposition of thin, small-grained polycrystalline films for transmission studies *via* sputtering or thermal evaporation is straightforward.[398–401] Importantly for studies related to the DW effect, its low atomic mass relative to other elemental metals (*e.g.*, gold) means that the associated $\langle u^2 \rangle$ is more sensitive to temperature changes. Further, previous work explicitly illustrated

that thermally-induced specimen tilting significantly affects I_{hkl} for thin *single-crystal* specimens, obscuring changes due to the DW effect (though much less so for crystals of sub-nanometer thickness).[205,402–404] Accordingly, in an attempt to minimize this deleterious effect, *pc*-Al was studied; the hypothesis being that with a large number of crystal grains within the field of view, any effects due to changes in specimen position and orientation would be averaged out, assuming a uniform and random distribution of zone axes. The DW effect could therefore be isolated and accurately quantified. As will be demonstrated below, however, the experiments did not support this hypothesis, and non-thermal effects were still found to negatively impact I_{hkl} measurements from polycrystalline films, though to a much lesser degree than for single crystals.

3.1.2 PBED Pattern Analysis

All parallel-beam diffraction patterns (DPs) were analyzed in the same way. First, a circular Hough transform was used to find the most probable center position of the pattern using the *111*, *200*, and *220* diffraction rings owing to the use of a beam block for the *000* beam when obtaining the DPs. More details on the circular Hough transform are in Section 3.1.3. Second, an azimuthally-averaged radial profile of the pattern was obtained and plotted as counts versus d^{-1} (where d is in units of length for direct comparison to the spacings between reciprocal-lattice positions). Least-squares fitting with a pseudo-Voigt function was used to find the position and the full-width at half-maximum (FWHM) of each peak. Third, a straight-line baseline subtraction was used to isolate the peaks from the background (see Section 3.2.4). Using this method, accurate values for the area of each

peak were consistently obtained while minimizing the influence of peak-broadening effects. Note that while restricting fitting to a narrow portion of each peak is a more accurate way of determining the position owing to a reduction in the peak broadening due to asymmetries, this was not done because the focus of this work was instead on the areas. Accordingly, any ellipticity of the patterns was not corrected prior to fitting, as this was assumed to be constant across all measurements.

3.1.3 Circular Hough Transform

A Hough transform maps points in Cartesian space, such as the pixels in our diffraction patterns (DPs), into Hough space, with polar coordinates. A circular Hough specifically transform maps points in Cartesian space to cones in Hough space, where the apex of the cone is at the Cartesian x and y coordinates and each slice of the cone is a circle with radius z. Essentially, the algorithm draws a series of circles with various radii encompassing the expected radius of a particular ring on the DP. When the radius being tested matches that of the Bragg ring, the circles drawn by the algorithm produce an intense overlap, the location of which gives the coordinates of the center of the ring. This process is then repeated with all available Bragg rings to build up a statistically valid location for the center of the DP. Because each transform samples hundreds of points and the process is repeated multiple times, repeatable calculations of the center of the pattern are possible down to 0.1 pixel. Therefore, it is possible to detect sub-pixel shifts in ring diameter with proper peak fitting.[405]

3.1.4 In Situ Temperature Measurements

A liquid nitrogen (LN_2) double-tilt holder (Gatan, Model 636.MA) was used to control specimen temperature for the work detailed in Section 3.2.2. Experimental DPs were obtained at 50-K increments spanning 100 to 350 K. For each of the six temperatures, five separate parallel-beam DPs were acquired for a total of 30 separate patterns. The patterns were obtained in random temperature order (*e.g.*, first at 100 K, second at 250 K, third at 150 K, *etc.*) with acquisition times of 0.1 seconds per pattern. Following each temperature change, enough time was allowed to pass for the holder readout to stabilize (typically requiring ~30 minutes), with another 3 minutes allowed to pass once stabilized before the DP was acquired. Specimen drift following each temperature change was corrected by cross correlating real-space images acquired before and after the change. In this way, the same region of interest was studied, limited by random error and goniometer precision.

3.2 | Results and Discussion

3.2.1 Sensitivity of I_{hkl} to Specimen Orientation

As noted in Section 1.2.2, previous work has explicitly shown that *in situ* temperature measurements of thin, single-crystal specimens using the DW effect can be deleteriously affected by thermally-induced artifacts; such as bending, bulging, translating, and tilting (this has also been explicitly shown to be the case for temperature-dependent changes in scattering angle for polycrystalline foils).[174,205] This is primarily due to the high

sensitivity of I_{hkl} to changes in specimen orientation with respect to a fixed incident-electron wave vector ($\mathbf{k}_i$). Though models of this behavior are well developed, it will be helpful for the results and discussion that follow to provide a brief summary here.[88] The real-space specimen shape and dimensions directly affect the characteristics of the reciprocal-lattice points, as described by a shape function [denoted as $D(\mathbf{q})$ following De Graef,[88] where $\mathbf{q}$ is the reciprocal-space vector]. The $D(\mathbf{q})$ for a thin foil having relatively large in-plane dimensions is shown in Equation 3.1.

$$D(\mathbf{q}) = z_o \delta(q_x)\delta(q_y)\frac{\sin(\pi q_z z_o)}{\pi q_z z_o} \qquad (3.1)$$

Here, z_o is the real-space specimen thickness, and $q_{x,y,z}$ are the magnitudes of the reciprocal-space vector components (x,y are in the plane of the specimen, while z is normal to the plane). For this particular specimen geometry, the reciprocal-lattice points become rods (called relrods for short) owing to $q_{x,y}$ going to zero. Thus, the shape function normal to the specimen plane [$D(q_z)$] is a thickness-dependent sinc function (Figure 3.1a,b). Here, a 50- and 120-nm thick foil are compared in order to illustrate the effect of thickness on $D(q_z)$.

A consequence of $D(q_z)$ for thin foils is that the Bragg condition for such specimens is relaxed such that measurable I_{hkl} still occurs when the Ewald sphere does not exactly intersect the center of the reciprocal-lattice position. The extent of this deviation is defined as the deviation parameter, $s_\mathbf{g}$ (Equation 3.2).

$$s_\mathbf{g} = \frac{-\mathbf{g}\cdot(2\mathbf{k}_i+\mathbf{g})}{2|\mathbf{k}_i+\mathbf{g}|\cos\beta} \qquad (3.2)$$

Here, $\mathbf{g}$ is the reciprocal-lattice vector for a particular *hkl* reciprocal-lattice position, and β is the angle between $\mathbf{k}_i + \mathbf{g}$ and the foil normal. Importantly, this means that slight changes

in the tilt orientation of the thin foil with respect to $\mathbf{k}_i$ will produce corresponding changes in I_{hkl}, with the degree of intensity change depending directly upon specimen thickness [*i.e.*, how quickly $D(q_z)$ falls off from the center position]. This can be seen by noticing that $s_\mathbf{g}$ is equivalent to q_z in Figure 3.1 and therefore determines I_{hkl}, which is affected by specimen tilting for a fixed $\mathbf{k}_i$. The effect of tilting can be better appreciated from a more practical viewpoint by rewriting Equation 3.2 to include specimen tilt angle (α) and Bragg angle (Θ_{hkl}) (Equation 3.3).

$$s_\mathbf{g} = \frac{-2|\mathbf{g}||\mathbf{k}_i|\cos\phi - |\mathbf{g}|^2}{2\cos\beta\sqrt{|\mathbf{k}_i|^2 + 2|\mathbf{k}_i||\mathbf{g}|\cos\phi + |\mathbf{g}|^2}} \qquad (3.3)$$

Here, ϕ is equivalent to ($90° + \Theta_{hkl} + \alpha$), and β is ($2\Theta_{hkl} - \alpha$) (see Appendix C for the derivation of Equation 3.3). Figure 3.1c illustrates the effect of tilt angle on $s_\mathbf{g}$ for the *200* family of planes. This approach then allows for quantification of the fall-off in I_{hkl} with α. For example, the intensity of the *200* reflection goes to zero for α tilts of ±0.09° and ±0.23° for a 120- and a 50-nm thick foil, respectively (Figure 3.1d). Of course, this sensitivity is lessened for thinner specimens, with the limit being an atomic monolayer, as is the case for graphene.[404,406] This illustrates the sensitivity of I_{hkl} on changes in α for specimens that are tens of nanometers thick, thus posing a significant challenge to accurate and precise DW-effect measurements.

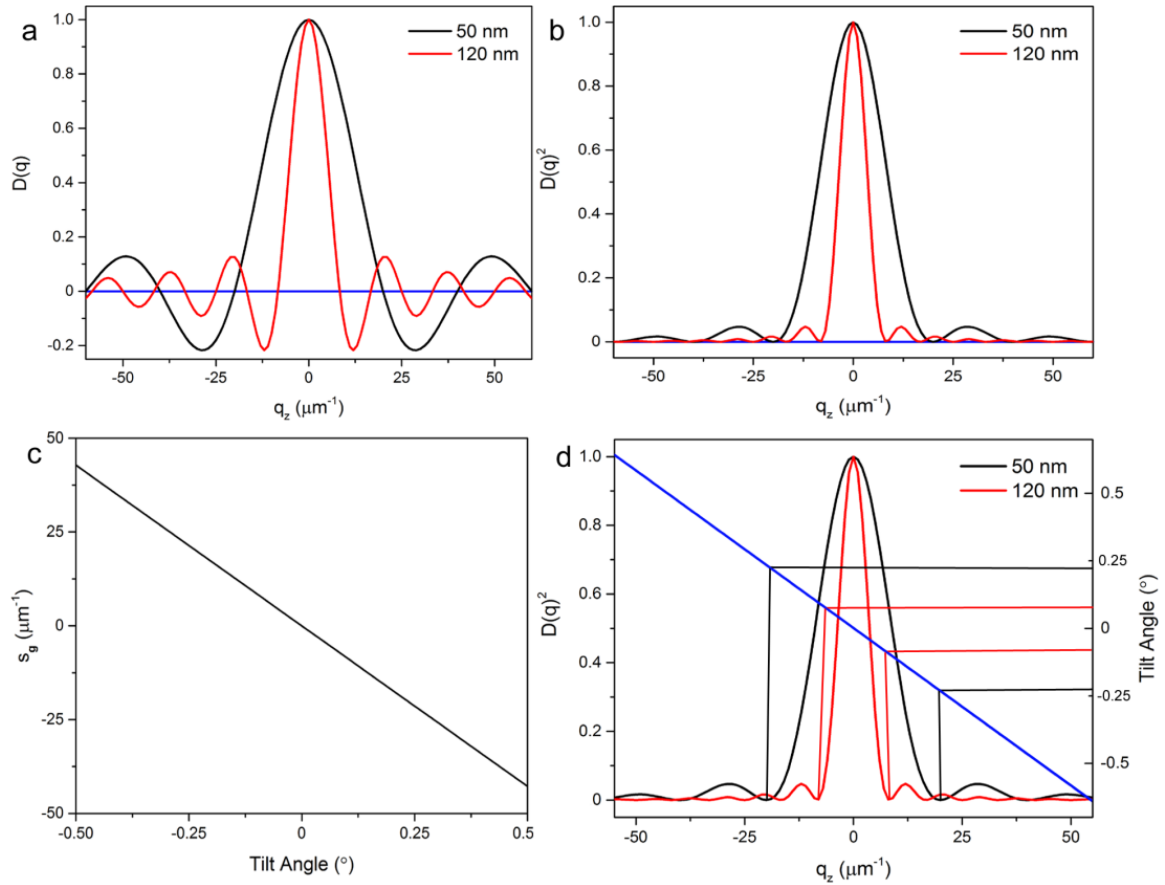

Figure 3.1 | Illustration of the sensitivity of I_{hkl} to specimen tilt angle. (a) Reciprocal-space shape function $D(\mathbf{q})$ for a 50- (black) and 120-nm (red) thick crystal having relatively large in-plane dimensions, such that $D(0,0,q_z)$ is plotted versus q_z, the magnitude of the reciprocal-space vector component normal to the plane of the foil. Here, $q_z = 0$ is defined as the center of the specimen. (b) Square of the shape functions shown in (a). The blue horizontal line at $D(\mathbf{q})$ and $D(\mathbf{q})^2 = 0$ is to highlight where I_{hkl} goes to zero. (c) Deviation parameter $s_\mathbf{g}$ versus specimen tilt angle for the *200* family of reflections. (d) Overlay of (c) (blue line) onto $D(\mathbf{q})^2$ illustrating the angles at which I_{hkl} goes to zero. Here, the intensity drops to zero at ±0.09° and ±0.23° for a 120- (red) and a 50-nm (black) thick crystal, respectively, as indicated by the red and black horizontal and vertical lines, respectively.

3.2.2 In Situ Temperature Measurements from Diffraction-Ring Radii and I_{hkl}

In light of the discussion thus far, it is at first glance reasonable to hypothesize that the effects of changes in specimen orientation on I_{hkl} could potentially be eliminated by using a small-grained, polycrystalline specimen rather than a single crystal. As mentioned in Section 3.1.1, this is because one might expect all zone-axis orientations to be uniformly represented for specimens having average grain sizes much smaller than the overall region of interest. To test this hypothesis, temperatures were calculated from DPs of *pc*-Al specimens using changes in diffraction-ring radii (thermal expansion) and I_{hkl} (DW effect). The former was calculated using a linear expression for thermal expansion with a coefficient of 23.5 x 10^{-6} K^{-1}, while the latter was done using the DW effect by means of Equation 1.1 and experimental data for $\langle u^2 \rangle$.[398,400,401] Calculated temperatures were also compared to the temperature set-points of the specimen holder, which previous work has shown to be an accurate indicator of actual specimen temperature for furnace-type heating holders, though systematic discrepancies for other *in situ* thermometry methods have been reported.[174,205,213,407,408] Details of DP collection are given in Section 3.1.4.

The results of the experiment are displayed in Figure 3.2. As can be seen, there is good agreement between the set-point temperature and the temperature determined from diffraction-ring contraction. It is worth noting that while the accuracy of the thermal-expansion method is high, the precision is rather low for this set of measurements, in some instances spanning ±40 K. This could potentially be improved by doing more measurements, which may reduce the random error, and by using smaller integration angles for more accurate determination of peak positions owing to a reduction in peak broadening

due to ellipticity.[174] The agreement between the temperatures measured using the DW effect and the other methods, however, is significantly worse, in some cases being off by more than 300 K. This indicates that measurements of I_{hkl} from small-grained polycrystalline specimens studied with large fields of view (*e.g.*, large probe sizes) are affected by factors other than changes in $\langle u^2 \rangle$. Additionally, the large standard deviation of several of the DW data points is indicative of poor repeatability, suggesting this particular approach is neither accurate nor precise for the type of specimens under study. Thus, this illustrates the importance of understanding and mitigating the other sources of intensity change in order to explicitly assign a specimen temperature *via* the DW effect.

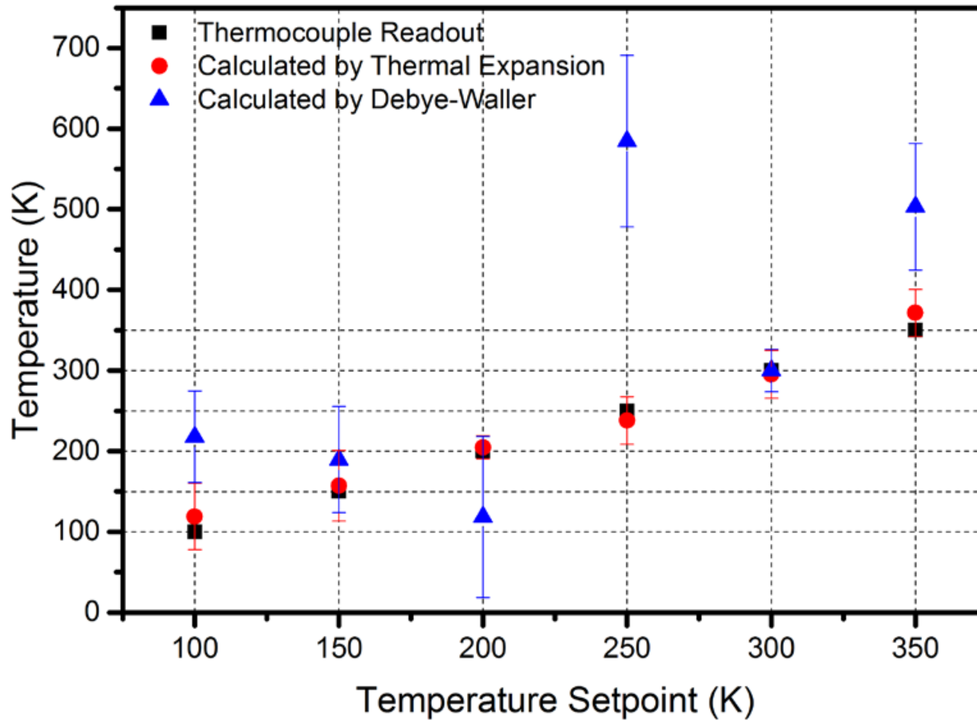

Figure 3.2 | Comparison of *in situ* thermal measurements of 120-nm thick *pc*-Al specimens. Three methods are shown and compared: direct readout of the specimen-holder thermocouple (black squares), calculation from thermal expansion *via* diffraction-ring contraction (red circles), and calculation using the DW effect *via* changes in $\frac{I_{220}}{I_{o,220}}$ (blue triangles). The data was generated from the *220* Debye-Scherrer ring and represents the average of five separate DPs acquired in random order. Error bars represent one standard deviation from the average.

3.2.3 Sources of Error: Specimen Tilting

Several systematic studies were conducted in order to identify and quantify the potential sources of error in the $\frac{I_{220}}{I_{o,220}}$ measurements in Figure 3.2. As will be shown, each

of the sources essentially involves a change in specimen position or orientation (tilting, bending, bulging, *x,y*-translation, *z*-translation), all of which are likely to occur to some degree during ultrafast pump-probe scattering measurements. Here, to mimic photoinduced specimen motion in a controllable manner, the spatial position and tilt was manipulated with the microscope goniometer, and multiple DPs were acquired and analyzed for the purposes of statistical analysis. That is, the effect of specimen tilting or translation on $\frac{I_{hkl}}{I_{o,hkl}}$ was quantified and analyzed in order to determine the statistical significance of any observed variations.

Specimen Tilting – As shown in Figure 3.3, it was found that specimen tilting had a statistically-significant effect on the change in I_{220} despite the small-grained polycrystalline nature of the Al thin film. For these experiments, five individual DPs were acquired at each tilt value, in random order, in order to mitigate beam or specimen drift effects. In this particular experiment, it was found that ΔI_{220} varied by nearly 4% over a tilt range of 30° (Figure 3.3a). Repeating the experiment over a total tilt-angle range of 2° (at finer tilt-angle steps) resulted in a ΔI_{220} of more than 1% (Figure 3.3b). The observed changes remain statistically significant and mostly unaltered after normalizing to various parameters (*e.g.*, background counts, *111* ring intensity, and total counts). See Figures 3.6 and 3.7 and Table 3.1 for the results of various normalizations and the statistical analysis. It is worth noting that, though the changes in I_{hkl} are statistically significant with tilt, they are substantially smaller than those expected for a single crystal of the same thickness (see Figure 3.1). This indicates that use of polycrystalline foils can significantly reduce – though not entirely eliminate – the influence of specimen tilting on DW-effect

measurements. The degree to which this reduction will impact such measurements will also depend on what material is under study, as atomic mass affects how $\frac{I_{hkl}}{I_{o,hkl}}$ behaves with temperature (see Equations 1.1 and 1.2). It is important to note that the *manner* in which ΔI_{220} varies with tilt angle in Figure 3.3 is specific to the particular specimen field of view from which the DPs were obtained; the approximate magnitude of the change is consistent across specimens, but the trend for ΔI versus tilt angle is not.

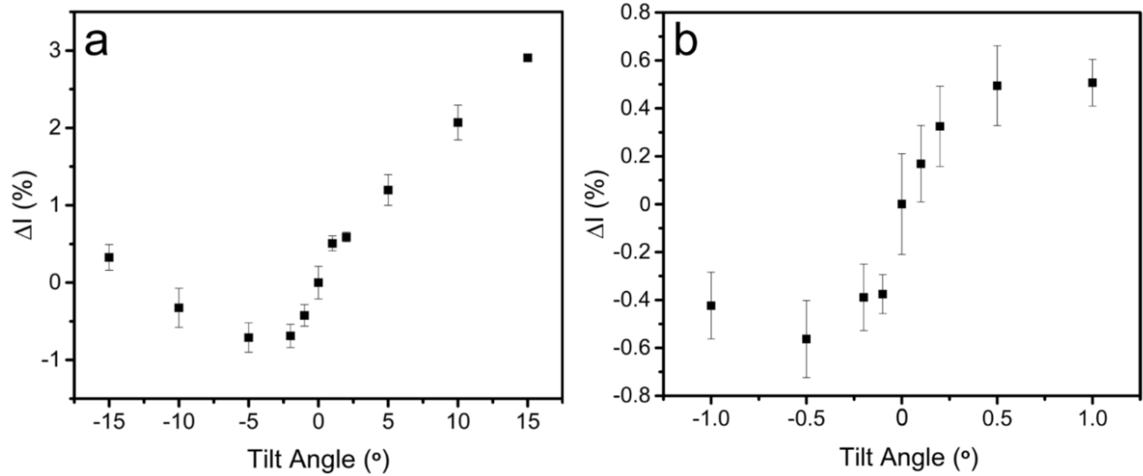

Figure 3.3 | Percent change in I_{220} generated from *pc*-Al thin-film specimens as a function of tilt angle. (a) Change in I_{220} over a range of specimen tilt angles spanning 30° (±15°). (b) Change in I_{220} over a range of tilt angles spanning 2° (±1°). For all experiments, error bars are one standard deviation generated from the average intensity of five separate DPs obtained in random order of tilt angle. A one-way analysis of variance carried out on all of the data confirms that the effect of changing tilt angle is statistically significant at the 0.05 level (see Table 3.1). The effect of tilting holds for all Debye-Scherrer rings and does not fall below the 0.05 level when it is normalized to the subtracted background, total number of counts, or intensity of any other peak (see Figures 3.6 and 3.7). All patterns were acquired with a camera length of 250 mm at 200 kV and with an 800-μm selected-area aperture.

Consideration of the effects of specimen tilting on both the electron-scattering condition and on the region probed suggests several possible sources for the observation shown in Figure 3.3. One possible source is a change in the specimen effective thickness

that occurs upon tilting of a thin film. Because this changes the amount of material with which the incident electrons interact, this essentially amounts to an increase in the occurrence of the various scattering mechanisms at work. Here, the change in effective thickness of the Al specimen at the maximum tilt-angle values shown in Figure 3.3 is calculated to be 4.3 nm, a 3.5% change. In addition, the change in effective thickness of the silicon nitride membrane for the same tilt angle is calculated to be 7 nm. While the effects of such changes in effective specimen thickness are certainly present, they do not solely account for the results observed from the tilting measurements. One reason for this is that one would expect changes in I_{hkl} arising solely from effective increases in specimen thickness to manifest as a parabolic curve having its vertex centered at 0° tilt, because the change in thickness is also parabolic when tilting about this position. Such behavior is not observed here. Note that repeating the tilting experiment on a thinner 50-nm *pc*-Al film also resulted in a statistically-significant change in I_{hkl} not explainable by effective increases in specimen thickness alone. Again, though this does not indicate such effects are negligible, it does indicate other more-influential effects are at work.

Unlike changes in effective thickness with tilting, which is judged to have only a minor impact, a potentially major contributing factor is texturing of the thin *pc*-Al film. It is known that grains comprising thin polycrystalline films of face-centered cubic (FCC) metals like Al, Au, Cu, and Ag commonly display some degree of in-plane preference for the [*111*] orientation.[409–414] In short, this arises from a thermodynamic drive to minimize surface energy through the preferential orientation of grains to expose the *111*-type planes, which have the highest planar density. This would result in a disproportionate number of

grains having a preferential orientation within a particular field of view and would manifest as tilt-angle-dependent intensity variations of particular Debye-Scherrer rings. For polycrystalline films of FCC metals having [*111*] texturing, one would expect I_{220} in the parallel-beam DPs to be higher when the plane of the specimen is normal to the incident electron beam compared to when it is not. The reason for this is that the *220*-type reflections are the first symmetry-allowed reflections for an FCC elemental metal when the crystal grain is oriented along the [*111*] zone-axis direction. Correspondingly, tilting the specimen away from normal incidence would lead to a decrease in the intensity of the *220*-type diffracted beams and to an increase in the intensity of the other beams.

Figure 3.4 summarizes the result of a tilt-angle study conducted on 120-nm thick *pc*-Al films meant to determine the presence of texturing and the potential effects on DW measurements. As expected from a textured film having grains displaying a preference for the [*111*] orientation, I_{220} was observed to decrease upon tilting away from normal incidence (here to ±45°). Further, the relative intensities of the *111* and *200* reflections were observed to increase with tilting. For such specimens, tilting during *in situ* photoexcitation or heating would result in deviations from expected DW-effect behaviors of $\frac{I_{hkl}}{I_{\text{o},hkl}}$. Note that the degree of texturing can be changed by annealing, but one must also be aware of possible effects of solid-state de-wetting when heating to temperatures below the melting point.[411,414]

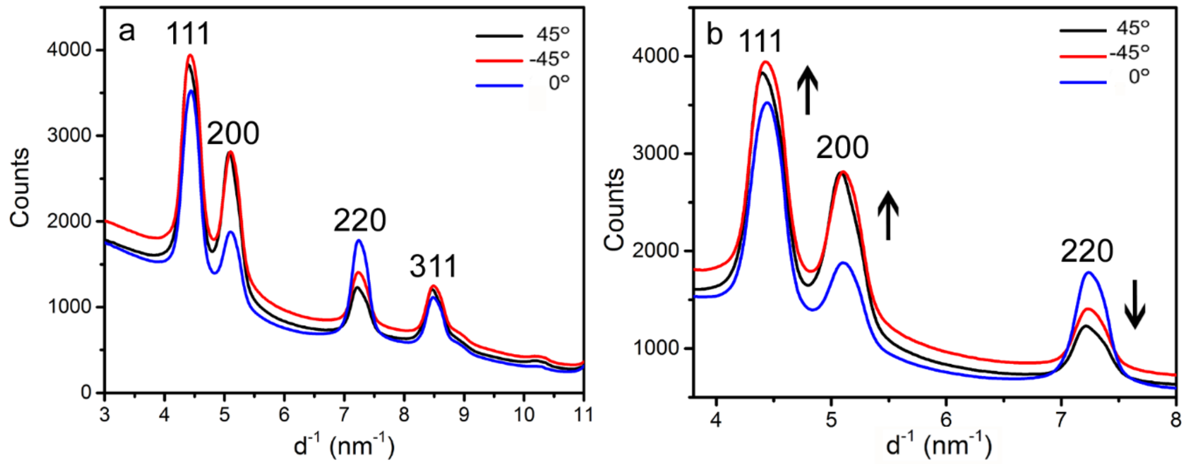

Figure 3.4 | Anomalous changes in Debye-Scherrer-ring intensities with specimen tilt angle for *pc*-Al films. (a) Azimuthally-averaged radial profile for 120-nm thick *pc*-Al tilted to ±45° (black, red). A profile obtained at normal incidence (0°) is shown for comparison (blue). Peaks are labeled with the corresponding *hkl* indices. (b) Magnified view of the *111*, *200*, and *220* reflections. The behavior of peak intensity upon tilting away from normal incidence is denoted with arrows.

Numerous theoretical and experimental studies, several of which are cited here, have indicated that varied mechanical motions – such as rippling, bulging, and local tilting – can arise within a few picoseconds following fs photoexcitation.[116,160,207,209,210,212,214,216,217,415–417] Accordingly, it is reasonable to conclude that such motions, which may be present during UED and UEM experiments, could produce errors and artifacts analogous to those detailed above. Thus, it is useful to get a sense of the degree to which such mechanical motions could affect transient lattice temperatures extracted *via* the DW effect beyond determining the potential impact on $\frac{I_{hkl}}{I_{o,hkl}}$.

A simple estimate can be determined by treating measured changes in I_{hkl} due entirely to specimen tilting as instead being due entirely to a photoinduced temperature change. To accomplish this, a cubic fit was performed on the data shown in Figure 3.3a, the result of which is shown in Figure 3.5. The fit was used to calculate a relationship between the tilt angle and the error in estimated temperature if the DW effect was invoked. Again, while the approximate magnitude is consistent across specimens, the exact relationship will differ – a further complicating effect when attempting to assign intrinsic materials behaviors to experimental measurements. Here the observed change in I_{220} arising from tilting up to 15° would correspond to a temperature change ranging nearly 100 K were it interpreted as arising only from the DW effect.

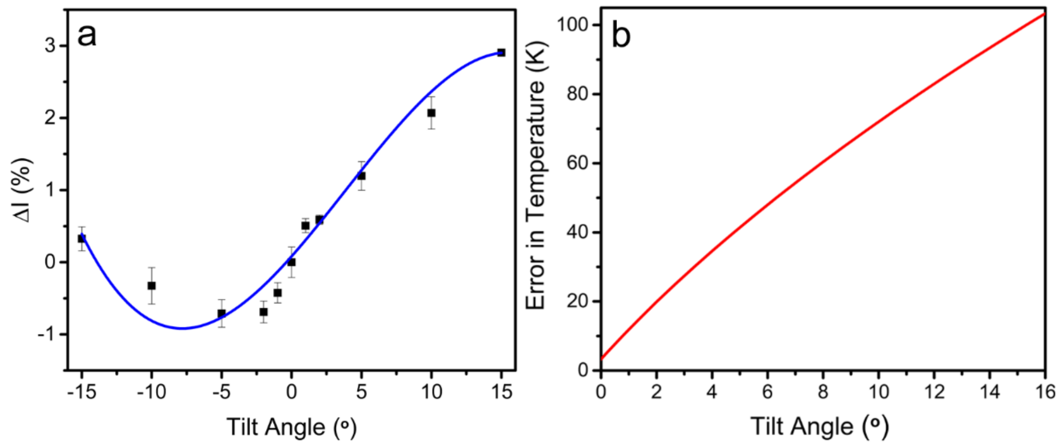

Figure 3.5 | Illustration of the magnitude of an erroneous temperature assignment using the DW effect. (a) Change in I_{220} as a function of specimen tilt angle shown in Figure 3.3a. The data is fit with a cubic polynomial, which was used to calculate a relationship for the error in specimen temperature if one assumed the observed change in I_{220} were due entirely to the DW effect. (b) Relationship of error in temperature as a function of specimen tilt angle, as determined from the polynomial fit to experimental data shown in (a). As discussed in the text, the relationships here are not universal but rather are specific to the particular specimen region of interest probed.

3.2.4 Normalization of Tilting Data

It is mentioned above that the tilting effects shown in Figure 3.2 remain statistically significant when normalizing to total counts, peak fit subtracted background, or intensity of other peaks. Figure 3.6 shows graphically the meaning of the latter two terms as they are used here, demonstrated on a representative radially averaged DP. Total counts refers to the summed intensity of the entire DP.

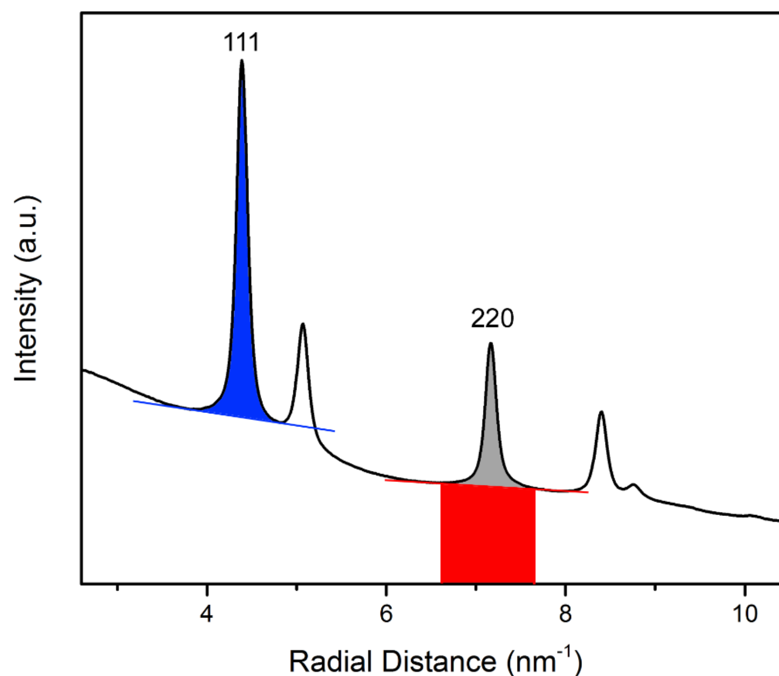

Figure 3.6 | Representative rotationally-averaged radial profiles for *pc*-Al. Each peak is fit out to six times its FWHM. The red area denotes the subtracted intensity from the *220* peak. The blue area denotes the intensity of the *111* peak.

Figure 3.7 shows the same data as is shown in Figure 3.2, as well as this data normalized to the three factors described above. It is clear from this figure that the relationship between intensity and tilt angle is not significantly changed by normalizing to any of these factors. However, to establish whether the trends are still statistically significant, an ANOVA is necessary. This is shown in Table 3.1. The F values represent the ratio of mean squared variance of tilt angle divided by the mean squared error. The P values represent the probability of a falsely disproven hypothesis, such that a value of over 0.05 means that the effect of tilting is not statistically significant. However, Table 3.1

shows that for all trends shown in Figure 3.7, the effect of tilting is still statistically significant.

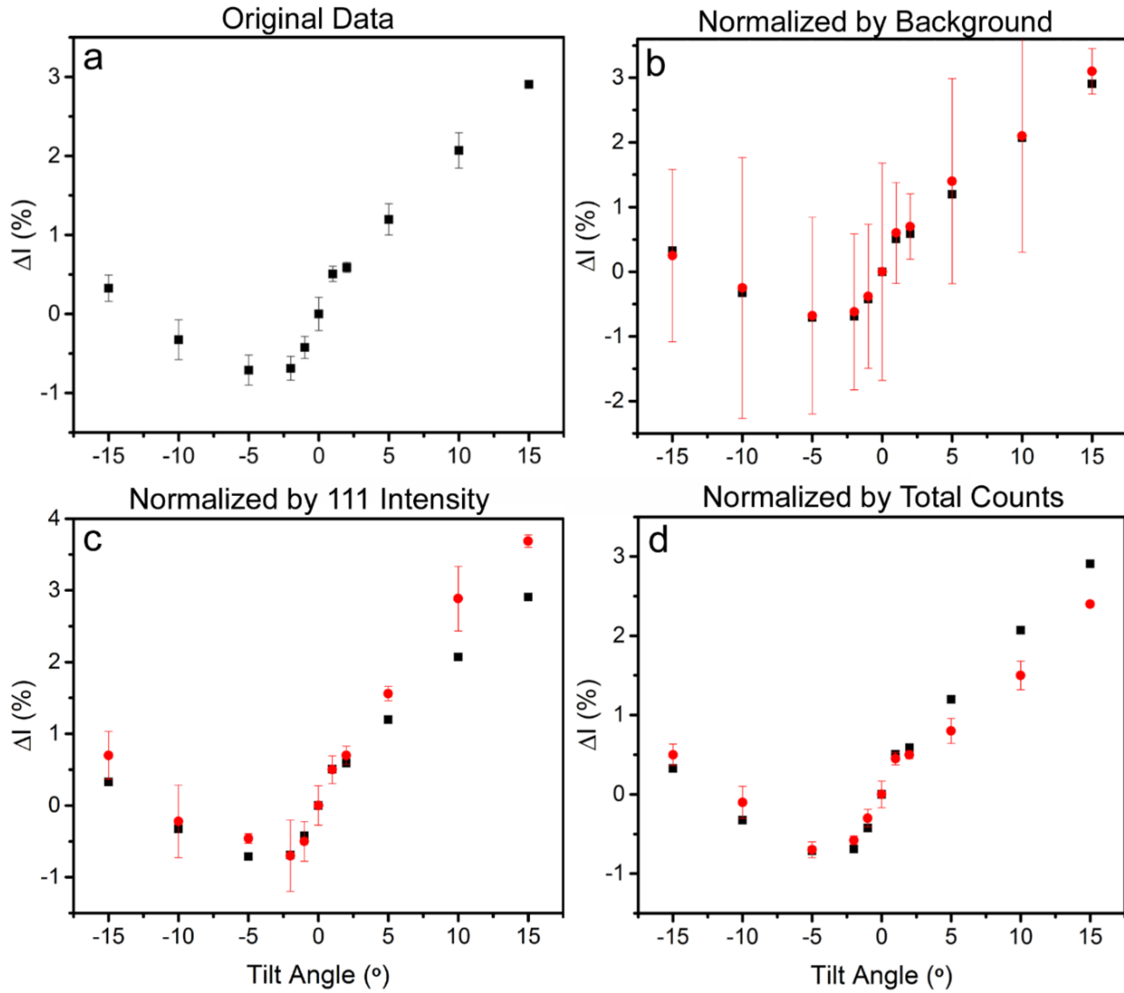

Figure 3.7 | Demonstration of effect of normalization on Figure 3.2 data. (a) Percent change in intensity of the *220* ring versus alpha-tilt angle. Error bars are standard deviations over five data points. (b)-(d) Percent change in intensity normalized to subtracted background, 111 peak intensity, and total counts, respectively.

Data	Value	
Intensity	F	109.9
	P	0.0
Intensity Normalized by Background	F	6.7
	P	1.0E-04
Intensity Normalized by Total Counts	F	37.2
	P	2.9E-10
Intensity Normalized by (111) Peak Intensity	F	12.5
	P	6.5E-07

Table 3.1 | ANOVA results for the data shown in Figure 3.7. *F* represents the ratio of mean squared variance of tilt angle divided by the mean squared error. *P* represents the probability of a falsely disproven hypothesis, such that a value of over 0.05 means that the effect of tilting is not statistically significant.

3.2.5 Sources of Error: Specimen In-Plane Translation

In addition to re-orientation in the form of local or whole-specimen tilting, it was explicitly shown that minor translations in the *x,y* plane of as little as 20 nm can produce statistically-significant changes in I_{hkl} (Figure 3.8). In essence, this arises from an effective change in the diffraction conditions owing to the polycrystalline nature of the specimen and because of likely deviation from exact parallelity of the incident electron beam.[174] The resulting effect is similar to that for the tilting experiments described and discussed above. That is, specimen tilting also causes a subtle shift in the illuminated area because incident beam paths are often slightly angled relative to the optic axis. Importantly, small in-plane shifts of the sort studied here would not be unexpected during UEM and UED experiments due to laser excitation and the resulting thermal expansion, with the degree of shifting expected to scale with fluence (laser-pulse energy per unit specimen area). Here, the effect

of relatively small specimen shifts in the *x,y* plane on changes in I_{hkl} was determined by acquiring DPs after translations of as little as 10 nm (Figure 3.8a). A t-test of five separate DPs acquired at eight unique positions (45 DPs in all) shows that I_{220} for the 120-nm thick *pc*-Al film changes by a statistically-significant amount due to the 10-nm in-plane shifts (see the Supplementary Materials for details of the statistical analysis). Indeed, the t-test indicates a very-low probability that I_{220} for any of the positions from which DPs were acquired (2 through 8) is statistically the same as the reference position (1) to the 95% confidence interval (Figure 3.8b). From this, it is reasonable to conclude that specimen translation could be an additional contributing factor to the results shown in Figures 3.2 and 3.3.

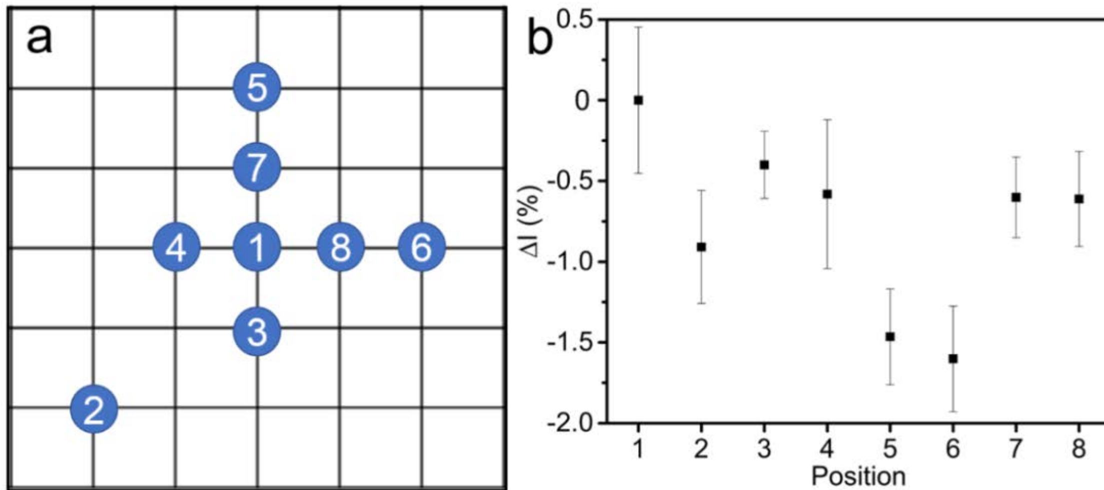

Figure 3.8 | Effects of in-plane specimen translation on I_{220}. (a) Schematic map showing the extent and direction of in-plane specimen translation for positions 2 through 8 relative to the reference position 1. The translations were performed with the microscope goniometer. Each grid square is 10 nm x 10 nm. (b) Change in I_{220} at each position on the specimen. The average change in I_{220} at positions 2 through 8 are relative to the average value of I_{220} at position 1, which is set to zero. All DPs were acquired in random order of position with a camera length of 250 mm at 200 kV and with an 800-µm selected-area aperture. Error bars are one standard deviation of the average of the five individual measurements per position.

From the data shown in Figure 3.8, it can be seen that relatively small specimen displacements, including those caused by shifts in illumination due to tilting, can affect significantly affect measured I_{hkl} values. The differences between DPs obtained at the slightly-different specimen positions are statistically significant to the 0.05 level, with five DPs per position, according to an ANOVA. The ANOVA F-value is 19.94, which

corresponds to a probability (P-value) of 5.3 x 10^{-10}. Table 3.2 uses t-tests to compare each position to position 1. The results demonstrate that, in addition to specimen position being a statistically significant factor in I_{220}, each individual position – except for position 3 – produces significantly different intensities compared to position 1.

Pos.	Distance from Pos. 1	t Statistic	Probability > t	95% Confidence Interval
2	28.3 nm	4.984	0.001	0.519 – 1.413
3	10 nm	2.17	0.062	-0.025 – 0.801
4	10 nm	3.063	0.015	0.167 – 1.185
5	20 nm	8.117	3.93 x 10^{-5}	1.05 – 1.89
6	20 nm	8.224	3.57 x 10^{-5}	1.113 – 1.98
7	10 nm	3.365	0.0098	0.186 – 0.995
8	10 nm	3.673	0.0063	0.254 – 1.111

Table 3.2 | Statistical analysis of data in Figure 3.8. Individual t-tests completed between position 1 and positions 2-8, respectively. All statistical significance was measured to 95% confidence.

3.2.6 Sources of Error: Specimen Out-of-Plane Translation

Finally, in addition to in-plane translations, it is the case that specimen bulging caused by photothermal expansion or *in situ* heating causes a significant change in out-of-plane (z) position, which effectively blurs high-resolution images and changes the diffraction camera length.[174,207,418] This causes a shift in diffracted-beam position on the detector, which can interfere with shifts caused solely by thermal expansion. Importantly, changes in camera length also affect the total number of counts in the DP. This is because the distance that electrons travel between the specimen and the detector is altered, while

the angle at which they scatter from the specimen for a change in z position is not, thus potentially affecting I_{hkl}.[203,207,216] To determine the extent to which such an effect impacts changes in I_{hkl} for the *pc*-Al specimens studied here, DPs were acquired over a range of specimen heights spanning a total of 0.18 μm (Figure 3.9). Here, all conditions were held fixed while the specimen z-position was changed with the microscope goniometer. As can be seen in Figure 8a, I_{220} was observed to change a statistically significant amount at the 0.05 level, with five individual DPs collected per Δz position. However, when the data is normalized to total image counts (Figure 3.9b), the observed variations are no longer significant. That is, normalization to total counts eliminates any statistical difference in I_{hkl} for changes in specimen z position. Note that the scatter in the intensity-change data (for five data points) ranges over 2% in some cases, indicating the measurement precision is still impacted by effective changes in z.

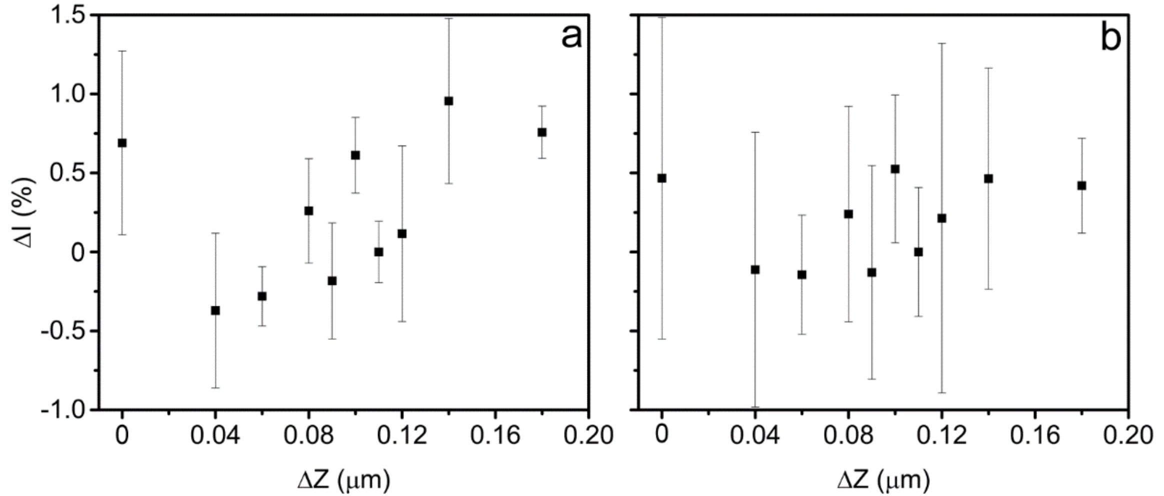

Figure 3.9 | Effect of changes in specimen height on I_{220}. (a) Percent change in I_{220} versus position in *z* direction relative to eucentric height, as measured with the microscope goniometer. All DPs were acquired in random order of *z* position with a camera length of 250 mm at 200 kV and with an 800-μm selected-area aperture. (b) Data shown in (a) normalized to total counts in each respective image. Error bars are one standard deviation over five measurements for all data points.

3.3 | Summary and Conclusions

In summary, we have explicitly shown that effects such as specimen tilting and in-plane translation can have non-negligible effects on temperatures calculated using the DW effect. These effects can, however, be mitigated – though not completely eliminated – by data analysis, statistical treatment, and specimen preparation. Indeed, normalizing peak intensity to the diffuse background or to other diffraction peaks does not render the effects due to tilting and translation statistically insignificant. However, normalizing intensity measurements in the DP to total image counts is effective for eliminating the otherwise

statistically-significant effects of changes in specimen position along the optic axis (*i.e.*, changes in z height). Thickness effects (*e.g.*, relrod size and drop-off in diffracted-beam intensity along the specimen normal) can be reduced by simply using the thinnest-possible specimen and the thinnest-possible substrate. Relatedly, the use of small-grained polycrystalline specimens will further aid in reducing tilting and translation effects, and analyzing multiple reflections can help elucidate, if not altogether eliminate, any anomalous behaviors arising from texturing. Overall, the results reported here explicitly illustrate the need to account for a number of practical experimental effects when attempting to attribute measured changes in static and transient diffracted-beam intensities to the DW effect.

Chapter 4 | Coherent Acoustic Phonon Spectroscopy in Gallium Arsenide

Femtosecond photoexcitation of semiconducting materials leads to generation of coherent acoustic phonons (CAPs), the behaviors of which are linked to intrinsic and engineered electronic, optical, and structural properties. While often studied with pump-probe spectroscopic techniques, the influence of nanoscale structure and morphology on CAP dynamics can be challenging to resolve with these all-optical methods, as mentioned in Section 1.3. Here, we show that the spatiotemporal capabilities of UEM can be used to differentiate the impact of amorphous and crystalline morphologies comprising semiconducting materials on time-domain CAP dispersion behaviors *via* imaging of nanoscale-picosecond in-plane propagating lattice perturbations. Using amorphized GaAs specimens prepared *via* focused ion-beam milling, subtle variations in CAP dispersion behaviors – as directly imaged with UEM – were observed following *in situ* pulsed-laser annealing and an associated increase in crystallinity. In addition to describing in detail the specific approaches taken to directly observe and quantify this behavior, we also discuss the manner in which subtle differences in dispersion responses manifest in space-time contour plots, while also illustrating the increased level of structural and dynamic information that can be obtained with UEM for studies such as these. We conclude by noting the implications of this work for connecting morphologically-dependent electronic and optical properties of semiconductors to lattice dynamics with techniques having high spatiotemporal resolutions.

4.1 | Experimental Methods

4.1.1 Specimen Morphological Characterization

The specimens studied here were thin lamella of undoped GaAs prepared from bulk crystals *via* focused ion-beam (FIB) milling (see Section 2.1.2 for preparation details). This archetypal semiconductor was chosen for study because it is known to support coherent optical and acoustic phonons that may have non-trivial connections to coherent charge-carrier phenomena.[419,420] In addition, the elastic properties are known to be dependent upon the degree of amorphization caused, for example, by ion bombardment and implantation, as occurs during FIB milling.[421] Indeed, surface amorphization is a well-known consequence of FIB milling, which leads to the formation of both amorphous and polycrystalline damage layers on the exposed faces of the lamella surrounding a region of higher crystallinity.[422,423] Electron diffraction patterns from such specimens display relatively sharp Bragg spots together with significant diffuse-scattering signal arising from the damage layers (Figure 4.1a). Following *in situ* photothermal annealing of such a specimen, during which the overall degree of crystallinity in the damage layers is increased, associated diffraction patterns show a commensurate decrease in the diffuse-scattering signal (Figure 4.1b-e) (see Section 2.1.2 for *in situ* photothermal annealing details). From here forward, Bragg scattering, Bragg peaks, and Bragg spots shall all refer to the relatively sharp Bragg spots observed in the patterns, while any reference to diffuse scattering or diffuse signal shall refer to the relatively diffuse ring arising from the FIB-damaged layers. Note that, while referred to as amorphous, it may be more accurate to classify the damaged layers as consisting of randomly-oriented nanocrystallites (ignoring any possible

texturing). Regardless, differentiation of these two types of signal and classification of the morphologies as relatively crystalline and relatively amorphous is adequate for the purposes of the work described here.

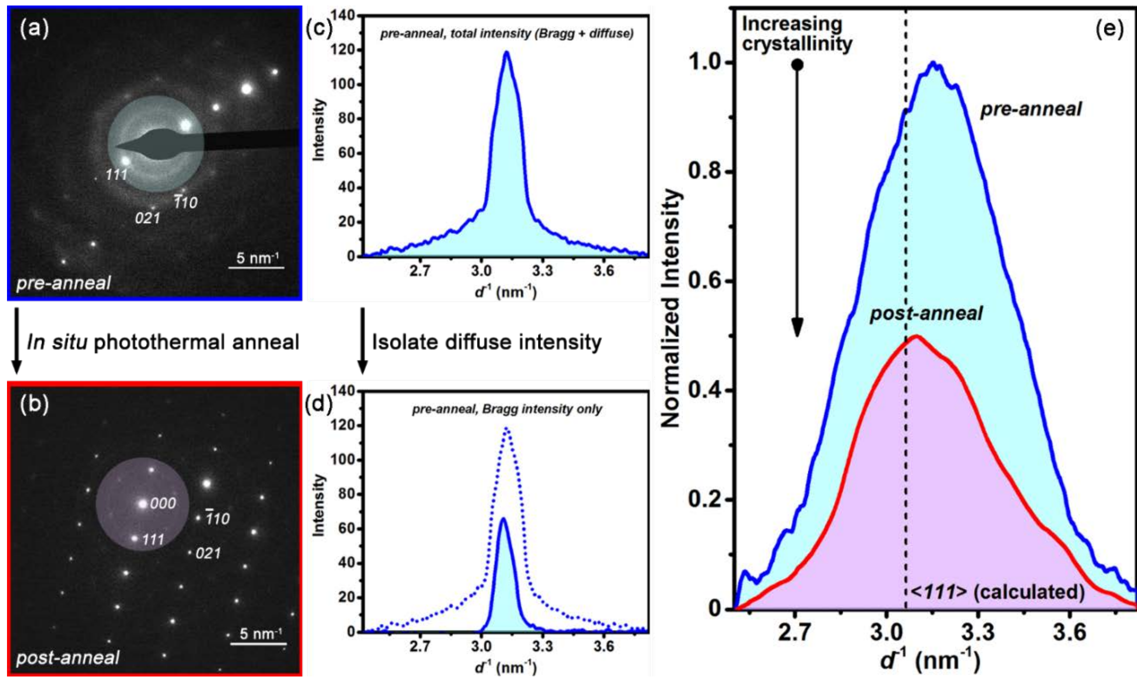

Figure 4.1 | *In situ* photothermal anneal of a GaAs lamella. (a) Selected-area electron diffraction (SAED) pattern of a pre-annealed GaAs specimen viewed along the $[11\bar{2}]$ crystallographic zone axis. Three Bragg spots are indexed for reference. The light cyan disk marks the approximate region of the pattern that was azimuthally averaged to obtain the profiles shown in subsequent panels. (b) SAED pattern of the post-annealed specimen viewed along the $[11\bar{2}]$ zone axis. The *000* beam is indexed for reference, and the light magenta disk marks the approximate azimuthally-averaged region. (c) Total-intensity profile (Bragg and diffuse) of the pre-annealed specimen. (d) Bragg-only intensity profile (solid blue line and light cyan fill) of the pre-annealed specimen. The total-intensity profile

shown in panel (c) (blue dotted line) is included for comparison. (e) Illustrative comparison of the pre- and the post-annealed diffuse-only intensity at the same observed scattering vector as the <*111*> planes (calculated position shown for reference). Peak shifts from the calculated position may arise from residual tensile strain or a slight systematic error in the calibration of the microscope.

The relative degree of crystallinity of the lamella before and after *in situ* photothermal annealing can be estimated from selected-area electron diffraction (SAED) patterns.[424] Here, this was essentially done by isolating the Bragg-scattered intensity from the total intensity *via* azimuthally averaging over select regions of the pattern containing the spots. This was followed by subtracting the Bragg intensity from the total signal once the underlying diffuse signal was quantified and removed. Bragg-spot intensity was isolated by least-squares fitting with a Gaussian peak-fitting algorithm.[353] This effectively extracts the diffuse-scattering signal so that direct comparison of the associated intensities of the pre- and post-annealed specimen can be made.

More specifically, pre- and post-annealed patterns were azimuthally averaged, and the lowest scattering-angle peak in each was integrated to obtain the total intensity, which included both the diffuse ring and the lowest-order Bragg spots. Next, the average intensity per unit area of the diffuse ring was calculated by averaging the integrated intensity of 10 separate, randomly-selected regions within the ring and then dividing by the area of each corresponding region. When a beam block was used (*e.g.*, see Figure 4.1a), the missing intensity of the diffuse ring was recovered by calculating the associated arc length and the

corresponding intensity based on the average value of the measured signal (here, no Bragg spots were covered by the beam-block image). The intensity of each of the Bragg peaks was determined using a 2D Gaussian fitting algorithm, and the underlying contribution by diffuse scattering was removed in order to isolate the Bragg-only scattering.[353] The total Bragg-peak intensity was then subtracted from the adjusted total integrated intensity, leaving the total diffuse-scattering intensity. The total diffuse-scattering intensity was also calculated using the diffuse intensity per unit area for comparison, and the values obtained using each approach differed by less than 1%. Finally, the Bragg-peak intensity (*i.e.*, that arising from the crystalline region of the specimen) as a percentage of the total intensity was compared for pre- and post-annealed patterns, thus returning an estimate of the increase in crystallinity following *in situ* photothermal annealing.

Here, following this method, percent crystallinity was calculated from the pre- and post-annealed specimen patterns (Figure 4.1) and was determined to be 23 ± 4% and 79 ± 2%, respectively, where uncertainties are standard deviations over five repetitions of the analysis.

4.1.2 Capturing Coherent Acoustic Phonons in UEM

Direct imaging of CAP dynamics with UEM is possible due to the combination of high spatiotemporal resolutions (routinely nanometer-picosecond) and the sensitivity of diffraction contrast to slight changes in overlap of the reciprocal lattice for thin foils and the Ewald sphere when at or near a Bragg-scattering condition.[215,425] Here, UEM bright-field imaging was used to quantify CAP dynamics in the pre- and post-annealed GaAs

lamella for direct comparison. For reference, the FIB-damaged outer layers of the lamella surrounded an inner relatively crystalline layer, and the incident electron wave vector was perpendicular to the lamella surfaces. Additional details of the UEM CAP experiments are given in the Materials and Methods section, and other pertinent but generally-applicable information is published elsewhere.[26,116,121,211,212,229] Following *in situ* femtosecond photoexcitation, coherent contrast waves arising from excitation of CAPs were observed in both the pre- and the post-annealed GaAs lamella. Figure 4.2 shows a summary of the CAP dynamics observed and quantified in the pre-annealed specimen (see Figure 4.2a for a representative UEM bright-field image). Similar results were obtained for the post-annealed specimen but with a different time-varying phase-velocity (v_p) dispersion behavior arising from differences in the elastic constants. As a shorthand, the pre-annealed experiment will be referred to throughout this chapter as V1, and the post-annealed experiment as V2. Though the individual phonon wavefronts produce an elastic unit-cell distortion that is likely on the order of a few picometers or less, orientation near or at a Bragg-scattering condition (*i.e.*, near or at an existing bend contour) ultimately gives rise to an associated coherent, oscillatory contrast response due to modulation of the excitation error.[26,215] In this way, CAP behaviors, such as emergence, propagation velocities (Figure 4.2b,c), and v_p dispersion, can be quantitatively tracked.

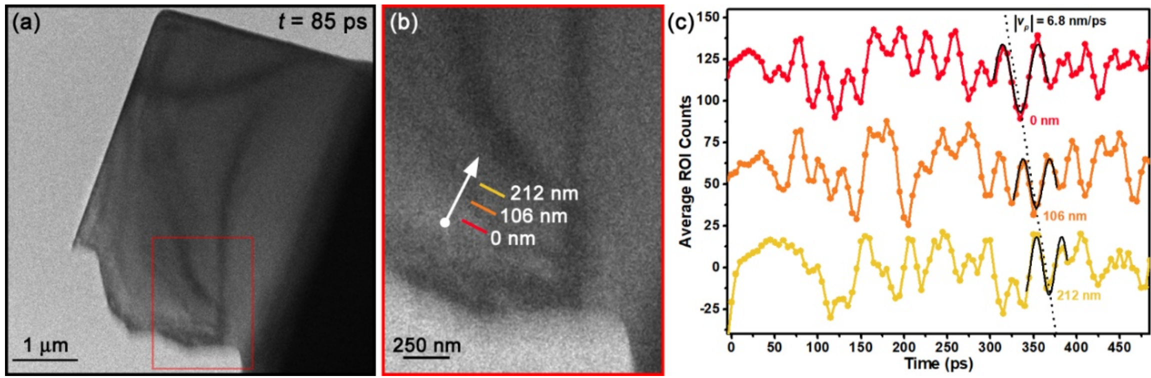

Figure 4.2 | Demonstration of UEM imaging of CAPs in a free-standing, pre-annealed GaAs lamella. (a) Representative UEM bright-field image at t = 85 ps (*i.e.*, 85 ps after *in situ* photoexcitation). The red rectangle indicates the region within which phonon dynamics were tracked and quantified. (b) Magnified view of the select region shown in (a). Three select positions (colored lines) at which average image counts were monitored are shown. Relative positions of the lines are labeled, with the position of the red line set as the origin. The white arrow indicates the observed direction of the propagating phonon wavetrain. (c) Average region-of-interest (ROI) image counts at the select positions shown in (b) as a function of time. Propagation of a single representative phonon wavefront is highlighted with the dotted line to exemplify how velocity can be determined from such profiles. The wavefront arrives at the 106-nm and 212-nm markers approximately 16 ps and 31 ps, respectively, after passing the origin, thus indicating a phase-velocity magnitude, $|v_p|$, of 6.8 nm/ps for this particular phonon. The fits straddling the dotted line are simple undamped sine functions and are meant to highlight the localized oscillatory response arising from the individual phonon wavefront.

4.1.3 UEM Parameters

The UEM was operated at 200 kV in pump-probe, bright-field imaging mode for the CAP experiments. The pump beam consisted of 515-nm wavelength pulses of 300-fs duration (fwhm), with an estimated spot size on the specimen of 120 μm fwhm and a resulting fluence of 0.75 mJ/cm^2. The probe consisted of discrete electron packets generated *via* the photoelectric effect by directing 258-nm wavelength laser pulses onto a graphite-encircled, 50 μm truncated LaB_6 cathode (Applied Physics Technologies). Here, the electron packets contained an average of 80 electrons each at the detector, and the CAP imaging experiments were conducted at a repetition rate of 20 kHz (50 μs between pulses/packets) with an acquisition time per image of 50 seconds. The arrival time between the pump laser pulse and the probe electron packet is controlled with a linear-bearing mechanical delay stage (Aerotech PRO165LM). All images and diffraction patterns were acquired with a 16-megapixel CMOS camera modified for continuous operation (Gatan OneView). Further information about the Ultrafast Electron Microscopy Lab at the University of Minnesota can be found in references [26,211,229,230] and in Section 2.2. The UEM videos reported here spanned from either -5 ps or -10 ps to 485 ps, with a step-size of 5 ps. Here, 0 ps is defined as experimental time zero, or the first moment when dynamics are detected, which may be different from true time zero (*i.e.*, the moment of femtosecond photoexcitation).[26]

4.1.4 UEM Control Experiments and Repeatability

Because the approach taken here to generate picosecond snapshots of CAP dynamics was to operate UEM in a stroboscopic pump-probe fashion, verification and demonstration of robustness and repeatability was accomplished by conducting various control experiments. Specimen drift and reorientation during a typical UEM scan is one possible source of false dynamics; diffraction contrast is especially sensitive to orientation changes with respect to a fixed incident electron wavevector.[215,425] To identify and account for such effects, UEM images within a scan can be acquired in a randomized fashion; that is, the images are acquired out of time order. This is accomplished using a script that identifies all the desired time points comprising a particular scan and then moves the retroreflector on the optical delay stage randomly from point to point to acquire all the desired images. By reordering the frames to time order in post-processing, non-reversible effects are readily identified as frame-to-frame abrupt changes in contrast lacking any apparent coherence. When this occurs, space-time contour plot (STCP) normalization (described below) can be carried out to minimize the interference of large-scale tilting.

Here, V1 was acquired in a temporally-sequential fashion (*i.e.*, not in the randomized time order described above) so that additional control experiments aimed at ensuring the observed CAP dynamics were repeatable and were not an artifact could be demonstrated. The results of two such experiments are shown in Figure 4.3 and consisted of repeating the UEM scan but at a single, fixed time point (*i.e.*, without moving the retroreflector on the optical delay stage). First, the same time point (60 ps in this case) was imaged repeatedly for 45 minutes, the same duration as the UEM scan to generate the

images comprising V1. The expected result of this experiment is that, while contrast features arising from CAPs are visible in the resulting images, they appear spatially fixed (*i.e.*, no motion is detected) because the images are all of the same time point. Such a result would indicate that dynamics are repeatable and robust. The result of this control experiment is shown in Figure 4.3b; the expected result is indeed observed, as contrast ascribed to CAPs are visible (shown as broad oscillations in line-profile intensity) but do not display any propagation behaviors (see, for comparison, Figure 4.2c, where propagation is explicitly illustrated). Second, an experiment was completed where the same range of time points as in the original experiment were imaged, but with the pump laser shuttered (*i.e.*, no specimen photoexcitation). Without *in situ* photoexcitation, no dynamics or apparent dynamics should be observed. If this is indeed the result, it indicates that the pump laser is triggering the dynamics. The result of this control experiment is shown in Figure 4.3c; the expected result is again observed, as the STCP shows no coherent dynamics, which would appear as dark lines with non-zero slope (see Figure 4.6 and Figure 4.7 below). Note that the observed contrast in Figure 4.3c results from motionless bend contours. These control experiments confirm that the images comprising V1, while acquired in time order, are nevertheless representative of photoinduced CAP dynamics.

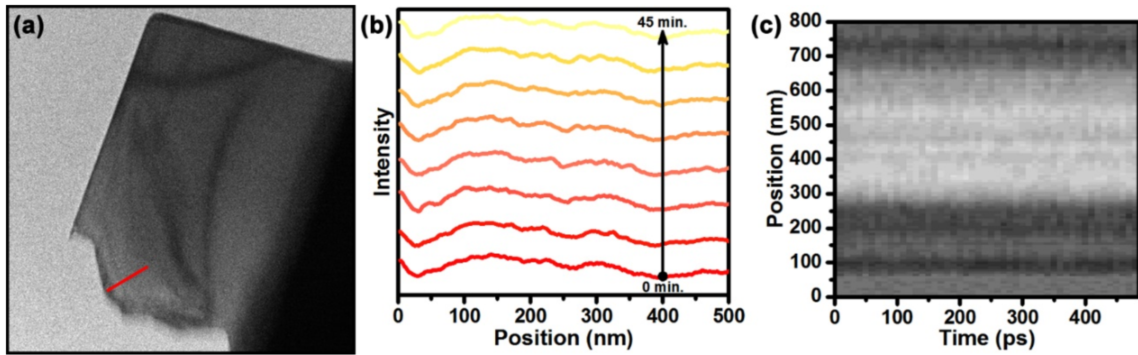

Figure 4.3 | UEM control experiments. (a) Representative bright-field UEM image of a GaAs lamella. The red line marks a region of interest (ROI) used to generate line profiles for the control experiments. (b) Contrast profiles from the ROI shown in (a) for the same time point (60 ps) but generated over 45 minutes of total control-experiment time. That is, the pump laser was not shuttered, but the retroreflector was fixed in position over the entire experiment time. (c) STCP generated from a control experiment, where the pump laser was shuttered while UEM images were acquired over a 45-minute duration.

In addition to long-term specimen drift and other sources of positional artifacts, temporal aliasing with respect to sampling rate is a concern for imaging dispersive phonons with UEM. Accordingly, bright-field UEM imaging of dispersive phonons in a GaAs lamella was conducted using both 1-ps step sizes and 5-ps step sizes. The resulting image series were analyzed, and the phase-velocity behaviors were extracted. The STCPs were then generated for each and compared to the results from V2 (5-ps step size; Figure 4.4). The resulting strong correlation between the separate data sets indicates, for these sampling rates and over these time windows, that no temporal aliasing was present. Experimental settings such as laser fluence, repetition rate, and microscope imaging conditions were the

same for all three experiments shown, but some fluctuations in intensity and image quality occurred due to room condition changes, leading to changes in the intensity of the pulsed electron beam. This led to some data points being necessarily eliminated due to low signal-to-noise ratio in the analysis. Nevertheless, fits to the dispersion behaviors for each data set (not shown in the plot for clarity) are the same within error, as summarized in Table 4.1. As stated in the main text, the dispersion data was least-squares fit with Equation 4.1.

$$v_p = v_{p,0} + Ae^{\left(-t/\tau\right)} \qquad (4.1)$$

Here, $v_{p,0}$ is the asymptotic phase-velocity value, A is a pre-exponential, t is time, and τ is a time constant.

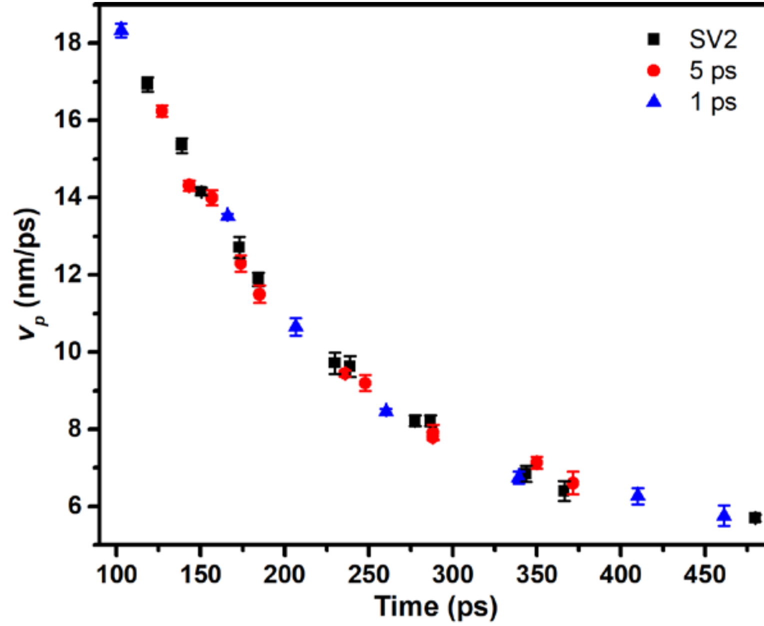

Figure 4.4 | Control experiment to test for the presence of temporal aliasing. Phase-velocity dispersion behaviors are shown for a 1-ps step and 5-ps step experiment, as well as for the phonon behavior shown in V2. Error bars are one standard deviation of 10 separate fitting routines to the associated STCP data.

Data set	$v_{p,0}$ (nm/ps)	*A*	τ (ps)
SV2 (5 ps)	5.10 ± 0.10	31.6 ± 0.9	120.8 ± 3.5
5 ps	5.16 ± 0.15	33.0 ± 1.4	114.7 ± 4.3
1 ps	5.21 ± 0.07	32.0 ± 0.4	119.4 ± 2.3

Table 4.1 | Parameters of the Equation 4.1 fits to the data in Figure 4.4. The errors are one standard error of the fit.

4.1.5 Experimental Confirmation of Pulsed Laser Annealing

Experimental confirmation of pulsed laser annealing was determined using the same control experiment as that shown in Figure 4.3b, where the same time point was

imaged repeatedly rather than varying the time points to build video frames. The resulting intensities are shown in Figure 4.5 – in contrast to Figure 4.3b, where the same contrast profile is present in each image (indicating the dynamics are unchanged from one frame to the next), the behavior is not consistent across all images, as evidenced by the varying profiles. This indicates that the specimen is not returning to the original, unperturbed state between pump-pulse excitation. This is likely due to the higher pump-pulse fluence and the higher repetition rate used for *in situ* photothermal annealing as compared to the phonon-dispersion experiments (50 kHz compared to 20 kHz). This results in an increase in specimen temperature with time, ultimately producing the change in crystalline and amorphous morphology shown in Figure 4.1.

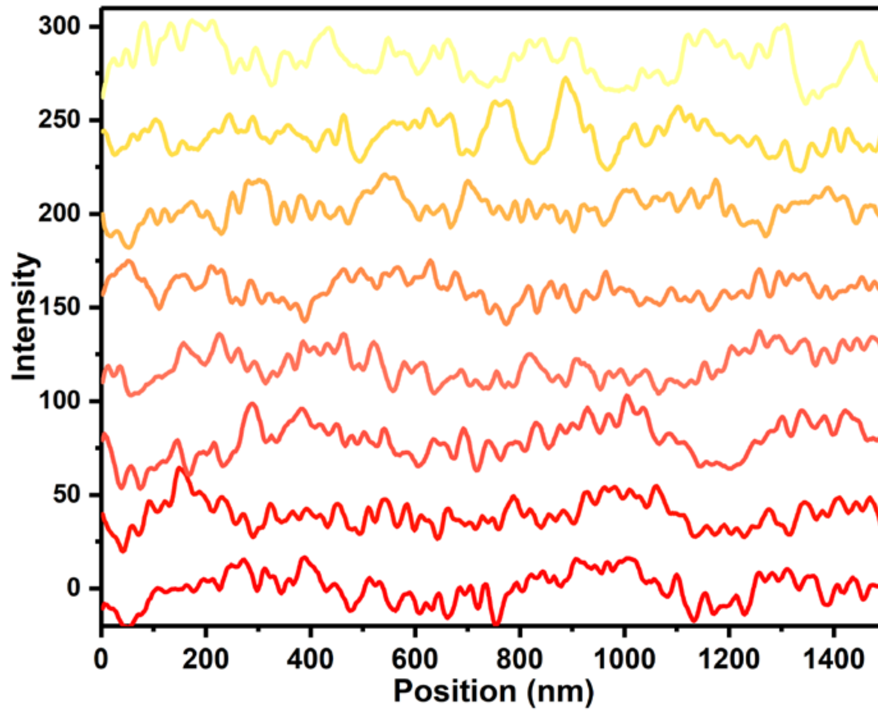

Figure 4.5 | Control experiment testing for pulsed laser annealing. Contrast profiles from the ROI used in this experiment (see Figure 4.3a) during *in situ* photothermal annealing at 35 mJ/cm^2 and a 50-kHz repetition rate. As for the control experiments discussed above, images were acquired over a 45-minute span. Because the retroreflector was again fixed in position, the changing profiles are indicative of a specimen which is not returning fully to the ground state between experimental repetitions, leading to accumulation of energy and therefore a change in specimen position, orientation, and morphology with photothermal annealing time.

4.1.5 Space-Time Contour Plot Analysis

Key to differentiating CAP behaviors for pre- and post-annealed GaAs specimens is quantification of the time-varying v_p dispersion behaviors for each. The method for

extracting this information from a UEM bright-field image series is summarized in Figure 4.6. Following establishment of a rectangular region of interest (ROI) oriented with the long axis parallel to the phonon propagation direction (see Section 4.1.2), average-intensity image profiles for each UEM temporal snapshot in the series are generated (Figure 4.6a-c). The width of the ROI is set such that a balance is struck between maximizing the signal-to-noise ratio and preserving the nature of the extent of the wavefront. Individual phonon wavefronts are identifiable as depressions in the profile counts arising from an increase in Bragg-scattered intensity for the reasons described above. Progress of each individual phonon across the ROI can then be tracked by combining the spatial intensity profiles together to form a space-time contour plot (STCP; Figure 4.6d). This procedure allows tracking of phonon movement with few-pixel (*i.e.*, 10 nm at the magnification used here) precision. Panels (e), (f) in Figure 4.6 show a representative UEM image of a pre-annealed GaAs specimen, a select ROI positioned within a section displaying active CAP dynamics and the resulting STCP. Individual phonon behaviors manifest as dark, linear features in the STCP, from which v_p can be extracted by determining the slope, the magnitude of which is then plotted as a function of time (Figure 4.6g), thus revealing the dispersion behavior.[26]

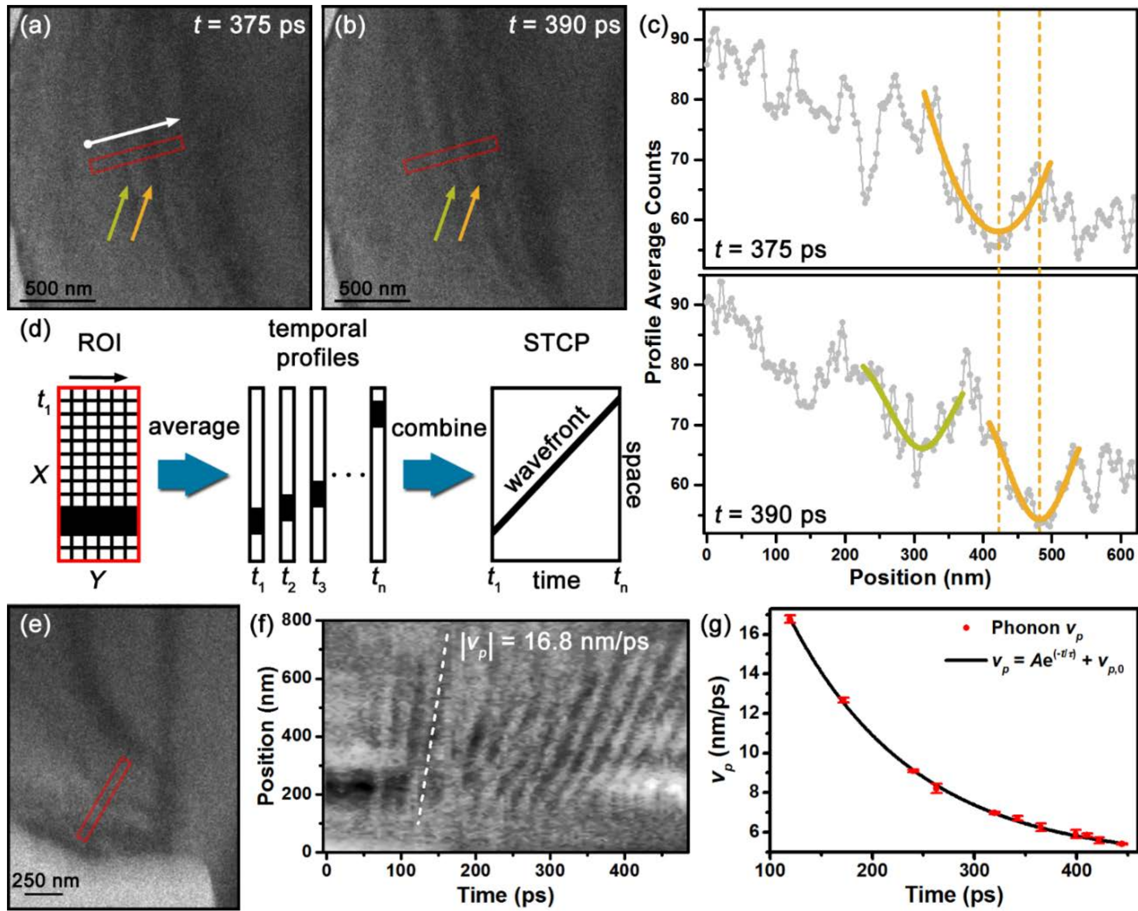

Figure 4.6 | Dynamics and dispersion of CAPs from UEM imaging. (a,b) Representative UEM bright-field images of a GaAs lamella at t = 375 ps (left) and t = 390 ps (right) showing the presence of contrast bands arising from propagating CAPs. The red rectangles mark the position of an ROI from which contrast profiles were acquired, as shown in (c). The colored arrows highlight two individual CAP wave fronts, and the white arrow indicates the propagation direction. (c) ROI profiles from the UEM images shown in (a) (upper plot) and (b) (lower plot). Wavefronts produce a drop in average counts owing to increased scattering strength and are fit with a peak function to quantify position with time (colored inverted peak fits to the data). The dashed vertical lines spanning both plots mark the position of a select wavefront and illustrate the propagating nature of the contrast

feature. (d) Concept of the generation of a space-time contour plot (STCP) from the ROI profiles. For each UEM image in a temporal series (*e.g.*, t_1, t_2, *etc.*, where each time point is an individual snapshot), counts are averaged along one spatial dimension of a 2D ROI to produce a temporal intensity profile with one spatial dimension. These profiles are then combined into an STCP, where single wavefronts appear as sloped lines revealing speed and direction (*i.e.*, velocity, v). (e) Select UEM image with ROI indicated (red rectangle), from which the STCP shown in (f) was generated. (f) STCP spanning from t = -5 ps to 485 ps. Each dark band is a phonon wavefront (the position of a select wavefront is indicated with the white dashed line). The $|v_p|$ of the marked wavefront is 16.8 nm/ps. (g) Time-domain v_p dispersion behavior determined *via* STCP analysis from a UEM image series. Only dark bands which could be accurately fit are included; more details can be found in Section 4.1.6. Error bars on the data points are one standard deviation of the average of 10 repetitions of the analysis procedure for the same data.

4.1.6 Determination of Phase-Velocity Behavior

Analysis of CAP characteristics from a UEM image series is done by first generating an STCP. This is done by extracting a line profile from the same location in each frame of the series and plotting temporally-consecutive profiles next one another such that the y-axis represents the spatial position along the profile and the x-axis represents the time elapsed following *in situ* femtosecond photoexcitation. A detailed description of the construction of STCPs is given above. Generally, background irreversible contrast movements are corrected for by normalizing each row and column of the STCP to the

average of each respective row and column. This approach ensures that if intensity changes occur due to tilting, fluctuations in beam counts, differences in background specimen contrast along the line profile, or specimen drift, the STCP fitting is not affected. Example as-generated and normalized STCPs are shown in Figure 4.7 for a side-by-side comparison.

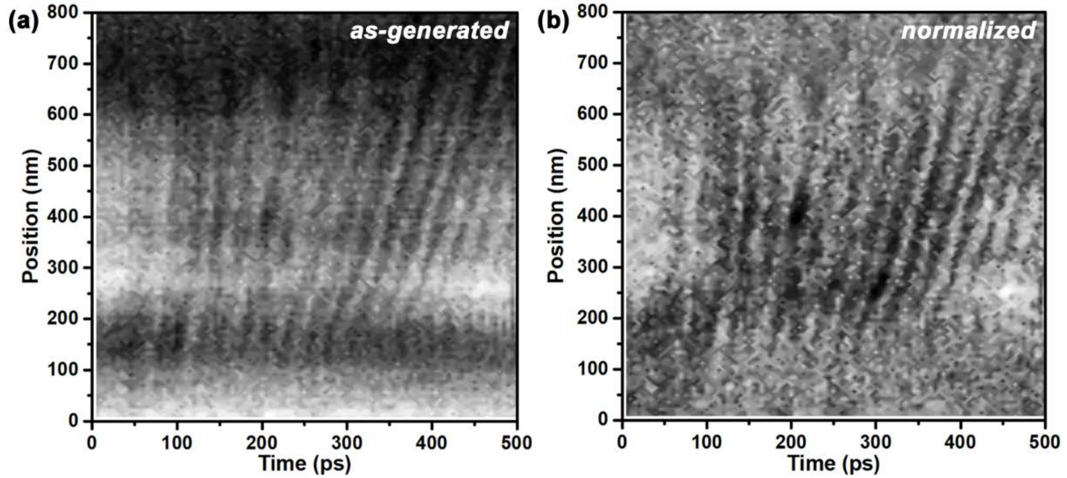

Figure 4.7 | As-generated and normalized STCPs. (a) An as-generated STCP. (b) The same STCP as shown in (a) but with rows and columns normalized by the average of each respective row and column. An additional smoothing algorithm has been applied to each data set using Origin for appearance only.

Values of v_p extracted from the STCPs are most accurate when the ROI is oriented perpendicular to the CAP propagation direction. Accordingly, an iterative process is used to determine the most-probable propagation direction. A set of ROIs are established, each originating from the same point but oriented at slightly different angles relative to one another and to the most-likely propagation direction. STCPs are then generated for each,

and v_p for the same wavefront is determined *via* fitting. The ROI returning the lowest v_p is set as the correct position for the full analysis owing to the associated geometric arguments. Here, template matching was used to ensure the ROI position was the same across the pre- and post-annealed data sets.[371] To extract v_p from STCPs, linear features arising from individual CAP wavefronts are identified, and the lowest-count pixels along the feature are found and linear least-squares fit (Figure 4.8). Phonon velocity is determined from the slope of the line. Here, the entire procedure, including selection, was completed 10 separate times for each line in order to estimate the error associated with the procedure. The standard deviation of these 10 repetitions of the fitting procedure form the error bars on the data points in the STCPs in Figures 4.4, 4.6g, and 4.10. Lines which did not produce repeatable velocities due to noise, such as the first two faintly visible dark lines in Figure 4.6f, were eliminated from the analysis shown in Figures 4.6 and 4.10.

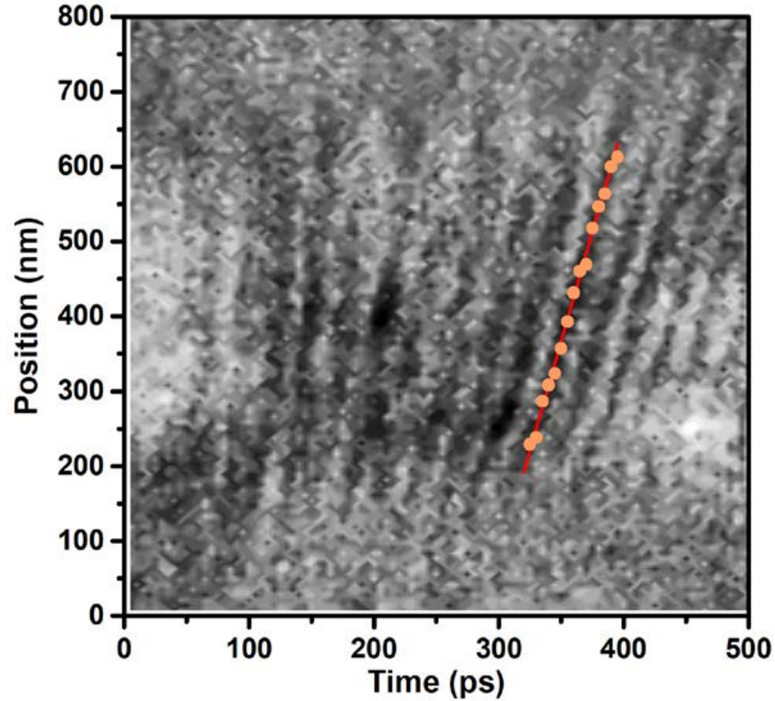

Figure 4.8 | Extraction of CAP v_p from STCPs. Orange disks mark the lowest-count positions along the phonon wavefront feature, and the red line is a least-squares fit to these points. The slope of the fit line gives v_p.

4.1.7 Comparison of Dispersion Behaviors

In order to ensure direct comparison between the pre- and post-annealed CAP dispersion behaviors, template matching between the two videos was completed with Fiji using a normalized cross-correlation algorithm which matches the images with sub-pixel accuracy.[371] Determination of the most-probable ROI orientation was completed on the pre- and post-annealed image series, and the same pixel values were selected algorithmically for both. This procedure returned the same relative orientation to within 0.5°, which is the angle associated with a 7-nm arc length and a radius of 800 nm (the

length of the ROI). This precision corresponds to a maximum velocity difference of only 2.5 pm/ps, as determined following the procedures described above. The same pixel values were used for the endpoints of each ROI, meaning that the only mismatch between the spatial analyses of the two image series is the template matching algorithm. Owing to the 7-nm arc length, v_p values were deemed to not be susceptible to such a small potential variation. That is, because v_p was determined by measuring the wavefront propagation along the ROI, and because the pixel sizes for the two series were the same, mismatch along the ROI between the two series would not result in a variation in v_p. Also, mismatch perpendicular to the ROI would not be expected to result in a measurable change in v_p because there is little change in wavefront behavior from one pixel to the next.

4.1.8 Calculation of Expected Bulk Speeds of Sound

To determine the expected speeds of sound in a fully crystalline GaAs specimen, it was necessary to know the crystallographic direction in which the CAP wavefronts were propagating. This was done by conducting correlative electron diffraction and bright-field imaging experiments on the specimen of interest. To accomplish this, the angle of rotation between imaging and diffraction modes in the microscope were determined by severely under-focusing the diffraction pattern such that the real-space image could be observed. Rotational template matching was incorporated to determine the illumination-condition-dependent angle between the two (88.8° clockwise in the case of the post-annealed specimen, for example). Upon correcting for this, the diffraction pattern could be accurately overlaid onto the real-space image (Figure 4.9). The ROI used to calculate the

STCP can then be superimposed onto the diffraction pattern at the correct angle and can be used to determine the crystallographic direction along which the wavefronts propagate. Here, this was approximately the [$\bar{1}31$] direction.

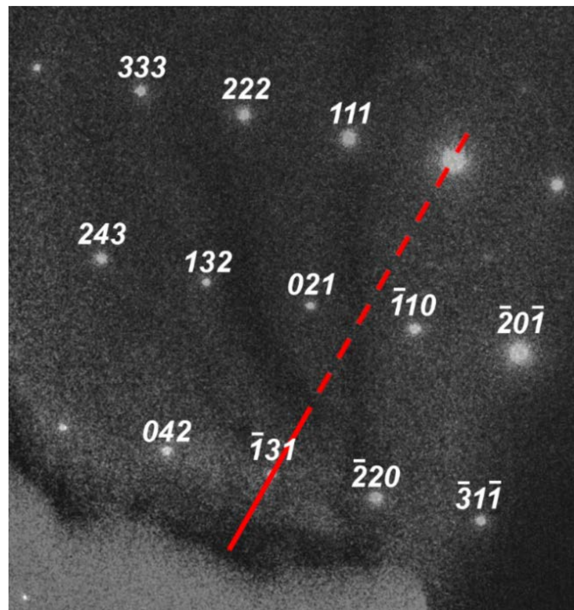

Figure 4.9 | Determination of crystallographic direction associated with CAP wavefront propagation direction. Shown is a representative UEM bright-field image superimposed onto the associated SAED (Bragg spots indexed). The diffraction pattern is rotated clockwise by 88.8° relative to the real-space image to correct for the rotation that occurs upon changing from imaging to diffraction mode in the TEM. The select ROI for generating the STCP is shown as a solid red line and extended to guide the eye using the dashed portion. By placing the direct beam spot (not indexed) on this line, the crystallographic direction which is represented by the angle of the ROI can be determined. Here, the angle of the ROI line matches the angle between the direct beam and the ($\bar{1}31$)

reflection, indicating that the approximate crystallographic direction of the CAPs is the [$\bar{1}31$] direction.

Here, the speed of sound in the [$\bar{1}31$] direction was approximated to be the same as that in the general <*111*> direction. Thus, the expected longitudinal speed of sound along this direction in crystalline GaAs can be calculated using Equation 4.2. Note that the longitudinal speed is used here because the experimentally-observed asymptotic value is a much better match to this than the transverse speeds, as has also been observed in crystalline Ge.[26]

$$v_l = \sqrt{\frac{C_{11}+2C_{12}+4C_{44}}{3\rho}} \qquad (4.2)$$

The elastic constants used in Equation 4.2 are C_{11} = 1.19 x 10^7 N/cm^2, C_{12} = 5.34 x 10^6 N/cm^2, and C_{44} = 5.96 x 10^6 N/cm^2, and ρ is the density of GaAs at 300 K. This results in a calculated longitudinal speed of sound of 5.4 nm/ps.[426] For the estimated speed of sound in a fully amorphous specimen, the following calculation was undertaken. First, it has been reported that amorphization of GaAs by ion bombardment causes a softening of the C_{11} and C_{44} elastic constants by 17% and 41%, respectively. Because the C_{12} softening was not reported, this value was approximated as that observed for Si, in which the transition from crystalline to amorphous causes a 10% softening of the C_{11}, a 13% softening of the C_{12}, and a 40% softening of the C_{44}.[427,428] Thus, the C_{12} softening is 10% of the range between C_{11} and C_{44}. By comparing this with the data for GaAs, an approximation is made

that C_{12} in GaAs softens by 19%. Using these elastic constants, the stiffness matrix was inverted, and the first term was inverted again in the standard procedure for acquiring Young's modulus from the stiffness tensor. The Young's modulus and the measured density of GaAs was then used to calculate an estimated speed of sound of 3.8 nm/ps.[429] This assumes a fully amorphous, isotropic GaAs specimen and is therefore a lower bound, as the disordered GaAs forming the upper and lower layers on the sandwich structure in the specimen studied here is not expected to be homogeneously disordered.

4.1.9 Effect of Tilting on Velocity

Inspection of the diffraction patterns in Figure 1 of the main text reveal that some specimen tilting occurred between experiments. Because Lamb-type guided-wave modes travel down the bisector of the GaAs plate, v_p could be affected by specimen tilting because the observed distance could differ from the actual distance traveled. Specifically, the relationship follows Equation 4.3.

$$d_{obs} = d_{true} \cos(\theta_{tilt}) \qquad (4.3)$$

Here, d_{obs} is the observed distance traveled, d_{true} is the actual distance traveled, and Θ_{tilt} is the degree of specimen tilting. This equation is only applicable to tilts where the axis of tilting is perpendicular to the direction of CAP travel or parallel to the wavefront, as these are the tilts which would change the observed distance measured in the velocity analysis. Following this geometrical argument, in order for the difference in velocities observed to be due to tilting, the ratio of the velocities must be equal to the cosine of the tilt angle. Using the final (asymptotic) velocities shown in Figure 4.10, this states that the angle of tilt necessary to achieve this change in velocities is 22°. Based on the diffraction patterns

shown in Figure 4.1, this is not possible, as such a large tilt would cause an entirely different orientation rather than a slight change in adherence to the zone axis. Continuing with this argument, a 1° tilt would cause a change in velocity from 4.720 nm/ps to 4.721 nm/ps, which is well within the error of the measurement. This indicates that while some degree of tilting likely occurred based on simple inspection of the diffraction patterns, it was not enough to cause the observed change in velocities between the pre- and the post-annealed states.

4.2 | Results and Discussion

4.2.1 CAP Propagation Dynamics

It is worth noting that while the STCP analyses performed here were conducted on a single, select ROI, inspection of the Supplementary Videos shows that CAPs were in fact initiated and launched from each vacuum-specimen interface, or lamella edge, following *in situ* photoexcitation. This indicates that the direction of CAP propagation is not dependent upon crystallographic orientation. Instead, acoustic-phonon launch from morphological features such as step-edges and interfaces, is hypothesized to arise from a rapid dephasing of directional phonon modes due to inherent differences in the interfacial boundary conditions at such features and the associated influence on the lattice response following photoexcitation.[212] Indeed, rapid dephasing of CAPs caused by crystal step-edges that are a single unit cell in height has been observed with UEM.[229] Further, the CAPs imaged here are hypothesized to be Lamb waves, as has been observed in single-

crystal, undoped Ge.[26,211] Such guided-wave modes generally display multiple orders in the frequency domain, most of which have hypersonic phase velocities with strong dispersion behaviors. However, it remains an open question as to why single-mode excitation appears to occur here and also in previous UEM studies.[26] Further, the observed single exponential decay of v_p in the time domain (Figure 4.6g) is subject to several explanations, such as enhanced carrier screening during charge-carrier equilibration and cooling.[26,419]

4.2.2 Effect of Crystallinity on CAP Propagation

Using the methods described above, CAP time-domain dispersion behaviors for the pre- and post-annealed GaAs specimen shown in Figure 4.1 were determined with UEM imaging (Figure 4.10). Methods for ensuring that CAP dynamics could be directly compared across the pre- and post-annealed specimen are described in the Supporting Information. For reference, the specific phonon wavetrains analyzed were each found to propagate approximately along the $[\bar{1}31]$ crystallographic direction, as determined with correlative imaging and diffraction (see the Supporting Information). As noted above, however, the particular crystallographic direction does not dictate CAP propagation direction. Here, determination of the wavetrain propagation direction with respect to crystallographic orientation was done in order to provide a common reference for the compared CAP behaviors. As can be seen in Figure 4.10, CAPs in both the pre- and post-annealed specimen display hypersonic phase velocities that exponentially decay to the range of longitudinal speeds of sound in GaAs. Importantly, however, the final asymptotic

velocity values ($v_{p,0}$) differ; in the pre-annealed state, $v_{p,0} = 4.76 \pm 0.14$ nm/ps, while $v_{p,0} = 5.13 \pm 0.08$ nm/ps in the post-annealed state, thus giving an increase in CAP velocity of 0.37 ± 0.15 nm/ps upon annealing and increased specimen crystallinity. The $v_{p,0}$ error values are standard errors of the fit of the exponential decay function to the data, while that of the difference is a propagated error. As is the case for the data in Figure 4.6g, error bars on the data points in Figure 4.10 are one standard deviation of 10 repetitions of the entire STCP fitting procedure.

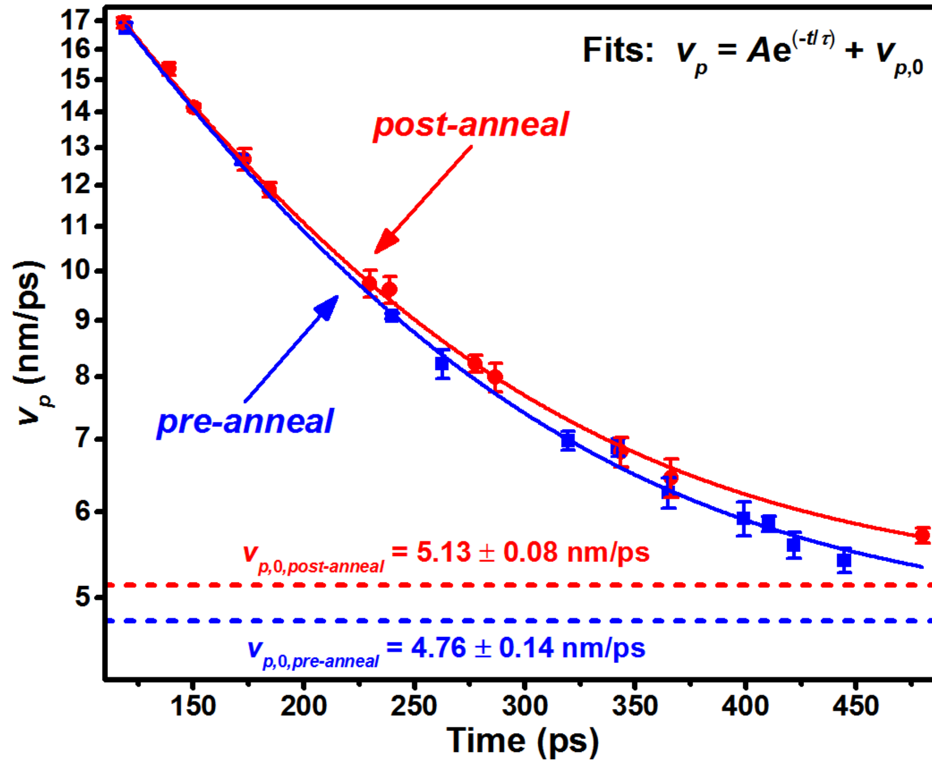

Figure 4.10 | Time-dependent phase velocity (v_p) for pre- and post-annealed GaAs (blue squares and red dots, respectively). The data are fit (solid curves) with the single exponential decay function shown in the upper-right corner of the plot. The asymptotes for each curve ($v_{p,0}$) are indicated with horizontal, colored dashed lines, and the values determined from the fit are shown. The error bars on the data points are one standard deviation of the average of 10 separate fits of the wavefront peaks in the associated STCPs (not shown), and errors on the asymptotic values for $v_{p,0}$ are one standard error of fits to the v_p data.

The observed difference in $v_{p,0}$ for the pre- and post-annealed specimen indicates that a change in morphology – namely an increase in relative crystallinity – is the source

of the difference and that UEM CAP imaging is sensitive to such variations. Comparison of the values of $v_{p,0}$ determined here to those for entirely crystalline and entirely amorphous GaAs is informative. The longitudinal speed of sound in the [$\bar{1}31$] direction for crystalline GaAs is estimated to be 5.4 nm/ps [33]. By comparison, it is expected that an amorphous specimen would support a significantly reduced speed of sound of 3.8 nm/ps, as estimated from the associated elastic constants (see Section 4.1.8 for details). Here, both the pre- and post-annealed state are some combination of crystalline and amorphous structure as a consequence of the FIB-preparation method used and the resulting damage layers. Though calculation of the precise dispersion behaviors in such a structure are non-trivial and beyond the scope of this work, the experimentally observed behavior in Figure 4.10 is in agreement with that expected for both a mixed morphology (*i.e.*, between the two $v_{p,0}$ extremes) and a post-anneal increase in crystallinity (*i.e.*, a commensurate increase in $v_{p,0}$).

Measurable differences between the asymptotic $v_{p,0}$ values for an as-prepared and an annealed specimen raises the question of whether it is generally possible to use UEM to access additional material information by measurement of phonon phase velocities. Indeed, acoustic-wave behavior has been used to study a broad range of optical phenomena and discrete structures, including the effect of heterostructure architectures and ion implantation on optical refraction, the structures of buried layers and interfaces, the constants associated with deformation potential, and the properties of bond stiffness and elasticity.[235,236,430–434] Accordingly, combining the relatively high spatiotemporal resolution of UEM imaging with modeling and controlled specimen geometries and compositions may lead to significant improvements in precision and accuracy, as well as

to new insights into structure-function relationships *via* correlative methods. In particular, significant impacts may be made on improving understanding of the influence of discrete nanoscale structures and morphologies – especially at both exposed and buried interfaces – on emergent optical and electronic properties of semiconducting materials.

4.3 | Summary and Conclusion

In summary, we have described a method based on UEM bright-field imaging for quantifying coherent acoustic-phonon dynamics, especially the time-domain dispersion behaviors that manifest in thin lamella of archetypal semiconducting materials like GaAs and Ge. We have shown that the combined nanometer-picosecond spatiotemporal resolutions of UEM imaging can be used to isolate and differentiate subtle differences in dynamics induced by changes in specimen structure and morphology. In particular, the high-resolution aspects of UEM relative to all-optical spectroscopic methods enable access to higher-order structural and temporal information, with correlative unit-cell and nanoscale studies potentially leading to a broader understanding of the underlying physical principles at work. We envision that extension of the methods described here to systems of increasing complexity and highly-varied composition will lead to new insights into semiconductor heterostructures and buried epitaxial interfaces, highly-beam-sensitive hybrid materials with sensitive compositional constraints, and engineered nanostructured materials for carrier-transport optimization.

Chapter 5 | Pulsed Beam Damage Mitigation in Organic Crystals

Despite development of myriad mitigation methods, radiation damage continues to be a major limiting factor in transmission electron microscopy. Intriguing results have been reported using pulsed-laser driven and chopped electron beams for modulated dose delivery, but the underlying relationships and effects remain unclear. Indeed, delivering precisely-timed single-electron packets to the specimen has yet to be systematically explored, and no direct comparisons to conventional methods within a common parameter space have been made. Here, using a model linear saturated hydrocarbon (*n*-hexatriacontane, $C_{36}H_{74}$), we show that precisely-timed delivery of each electron to the specimen, with a well-defined and uniform time between arrival, leads to a repeatable reduction in damage compared to conventional ultralow-dose methods for the same dose rate and the same accumulated dose. Using a femtosecond pulsed laser to confine the probability of electron emission to a 300-fs temporal window, we find damage to be sensitively dependent on the time between electron arrival (controlled with the laser repetition rate) and on the number of electrons per packet (controlled with the laser-pulse energy). Relative arrival times of 5, 20, and 100 μs were tested for electron packets comprised of, on average, 1, 5, and 20 electrons. In general, damage increased with decreasing time between electrons and, more substantially, with increasing electron number. Further, we find that improvements relative to conventional methods vanish once a threshold number of electrons per packet is reached. The results indicate that precise electron-by-electron dose delivery leads to a repeatable reduction in irreversible structural

damage, and the systematic studies indicate this arises from control of the time between sequential electrons arriving within the same damage radius, all else being equal.

5.1 | Experimental Methods

5.1.1 Hexatriacontane as a Model Material

Hexatriacontane ($C_{36}H_{74}$, C36) microcrystals were used as a model material for several reasons. First, damage due to electron-beam irradiation has been previously studied, and a range of critical doses (*i.e.*, dose producing a Bragg-spot intensity drop of e^{-1} or approximately 37%) have been reported.[376,377,435] This provides benchmarks and points of reference for results of both the thermionic- and the pulsed-beam experiments reported here. Second, microcrystals oriented along the [001] crystallographic zone axis and with easily-quantifiable dimensions suitable for study with TEM are readily formed *via* drop casting from an organic solvent (*e.g.*, decane) onto conductive amorphous carbon grids. In addition, the crystals so formed have a low intrinsic defect density and a nearly monodisperse thickness distribution (see Section 2.1.1). Thus, the influence of thickness on measured radiation damage is effectively normalized out for all experiments.[263] These properties are ideal for identifying multiple crystals suitable for beam-damage studies in order to generate statistics and for precisely determining geometric dimensions. It should be noted that care was exercised in accounting for elastic deformation, strain relaxation, and *n*-beam dynamical scattering in the crystals, as these effects will impact the measured Bragg-spot intensities.[376]

5.1.2 Experimental Parameters

Table 5.1 is a collection of pertinent parameters associated with all experiments presented and discussed in the main text (in addition to a repeat of the experiment shown in Figure 5.4; included to demonstrate repeatability). The experiment number corresponds to the figures in the main text; for example, experiment 3.1 is the first experiment associated with Figure 5.3, and experiment 5A.1 is the first experiment associated with Figure 5.5a. Experiments 4.3 and 4.4 are not shown in any figures but are included here to demonstrate repeatability.

Exp.	Beam Type	TBP (μs)	E/P	E/P Error	Beam Current (fA)	Beam Current Error (fA)	Beam Area (μm^2)	Dose Rate ($e \cdot Å^{-2} \cdot s^{-1}$)	Acq. Time (s)	Total Time (hrs)	Final ΔI_{110} (%)
3.1	Pulsed	100	1.03	0.15	1.6	0.24	132.4	7.76E-7	90	22.4	-0.81
3.2	Therm	n/a	n/a	n/a	1.6	0.22	131.5	7.77E-7	90	22.3	-1.55
4.1	Pulsed	5	1.04	0.11	33.3	3.45	218.9	9.52E-6	10	1.82	-0.93
4.2	Therm	n/a	n/a	n/a	32.2	3.71	218.6	9.20E-6	10	1.89	-1.66
4.3	Pulsed	5	0.99	0.12	31.7	3.72	219.4	9.04E-6	10	1.92	-0.92
4.4	Therm	n/a	n/a	n/a	32	3.45	220.7	9.06e-6	10	1.91	-1.73
5A.1	Pulsed	5	4.96	0.16	158.7	4.97	98.7	1.00E-4	5	0.173	-4.89
5A.2	Pulsed	5	5.02	0.05	160.8	1.64	98.8	1.02E-4	5	0.171	-5.60
5A.3	Pulsed	5	0.95	0.13	30.4	4.23	98.4	1.93E-5	5	0.898	-0.52
5A.4	Pulsed	5	0.89	0.14	28.5	4.56	98.7	1.81E-5	5	0.961	-1.31
5A.5	Pulsed	20	0.99	0.06	7.9	0.50	98.4	5.02E-6	5	3.46	-1.53
5A.6	Pulsed	20	1.08	0.10	8.6	0.78	98.9	5.47E-6	5	3.18	-3.75
5A.7	Pulsed	20	5.04	0.05	40.3	0.37	98.7	2.55E-5	5	0.680	-7.49
5A.8	Pulsed	20	4.96	0.06	39.7	0.52	98.6	2.52E-5	5	0.690	-7.70
5B.1	Pulsed	5	20.15	0.61	644.7	19.38	221.8	1.82E-4	2	0.096	-9.45
5B.2	Pulsed	5	19.71	0.56	630.6	18.07	221.1	1.78E-4	2	0.097	-9.72
5B.3	Pulsed	5	19.54	1.30	625.2	41.72	220.4	1.77E-4	2	0.098	-14.79
5B.4	Pulsed	5	20.32	1.13	650.2	36.17	220.1	1.85E-4	2	0.094	-11.25
5B.5	Pulsed	5	19.53	0.75	624.8	23.99	221.3	1.76E-4	2	0.098	-7.62
5B.6	Therm	n/a	n/a	n/a	627.5	16.92	220.8	1.78E-4	2	0.098	-9.86
5B.7	Therm	n/a	n/a	n/a	632.4	24.01	220.4	1.79E-4	2	0.097	-6.48
5B.8	Therm	n/a	n/a	n/a	636.9	15.99	220.9	1.80E-4	2	0.096	-7.82
5B.9	Therm	n/a	n/a	n/a	652.0	19.32	221.4	1.84E-4	2	0.094	-11.59
5B.10	Therm	n/a	n/a	n/a	649.1	18.60	220.0	1.84E-4	2	0.094	-10.85

Table 5.1 | Experimental parameters and associated errors for all experiments presented in Chapter 5, as well as one repetition that is not shown but is reported here to demonstrate repeatability (Exps. 4.3 and 4.4). Exp. = Experiment number, where the first number is the figure number in Ch 5 (*i.e.*, if the first number is a 3, the experiment appears in Figure 5.3), and the second number is the specific experiment referred to. Beam Type = pulsed beam (Pulsed) or random thermionic beam (Therm). TBP = time between electron-packet arrival at the specimen. E/P = electrons per packet. Beam Area = size of the electron beam. Acq.

Time = camera exposure used to acquire each diffraction pattern. Total Time = the total time required to conduct the fading-curve experiment up to a predetermined total dose. Final ΔI_{110} = the final average intensity value of the *110* Bragg spots up to the total accumulated dose specific to the experiment.

5.1.3 Bragg-Spot Fading Curve Method

A decrease of *110* Bragg-spot intensity as a function of dose and dose rate was used to track and quantify beam damage. An example at high total dose (relative to the experiments reported in the main text) of the type of data generated using this method is shown in Figure 5.1. In this case, a hexatriacontane ($C_{36}H_{74}$, C36) microcrystal was irradiated with a 0.57 nA thermionic (random) beam, and a series of diffraction patterns (DPs) were acquired at steadily increasing dose. Progression of the damage manifests as a loss of intensity in the Bragg spots, with the higher-order spots being more sensitive than those generated at lower scattering angles (*i.e.*, larger planar spacings). The average intensity of spots generated from a family of planes is then plotted as a function of dose in order to quantify a damage rate. The dose, D, is $D = (I \cdot t) \cdot A^{-1}$, where I is the beam current ($e \cdot s^{-1}$), t is the exposure time (s), and A is beam area ($Å^{-2}$). For each experiment described in this work, a single C36 crystal was centered in the field of view, and DPs were acquired at regular intervals up to a predetermined total dose (*e.g.*, 0.063 $e \cdot Å^{-2}$). The predetermined dose was selected by balancing the need for high stability with the need for a sufficient amount of reliable data for making comparisons and drawing conclusions. Note that while an exponentially-decaying fading curve is shown here and in Figure 5.1c, we also observed

linearly-decaying behaviors at high total doses. Variation in the functional form of Bragg-spot fading curves at high dose rates has been noted many times in the literature, especially in crystalline paraffins, and there are likely numerous possible sources.[252–254,351,372,436–442] However, the data displayed in Figures 5.2, 5.3, 5.4, and 5.5 below extend over comparatively small accumulated-dose ranges and, thus, remained within a regime where a linear appearance is expected. While further experiments regarding the origins of different fading-curve shapes are perhaps merited, such work is well outside the scope of the present study.

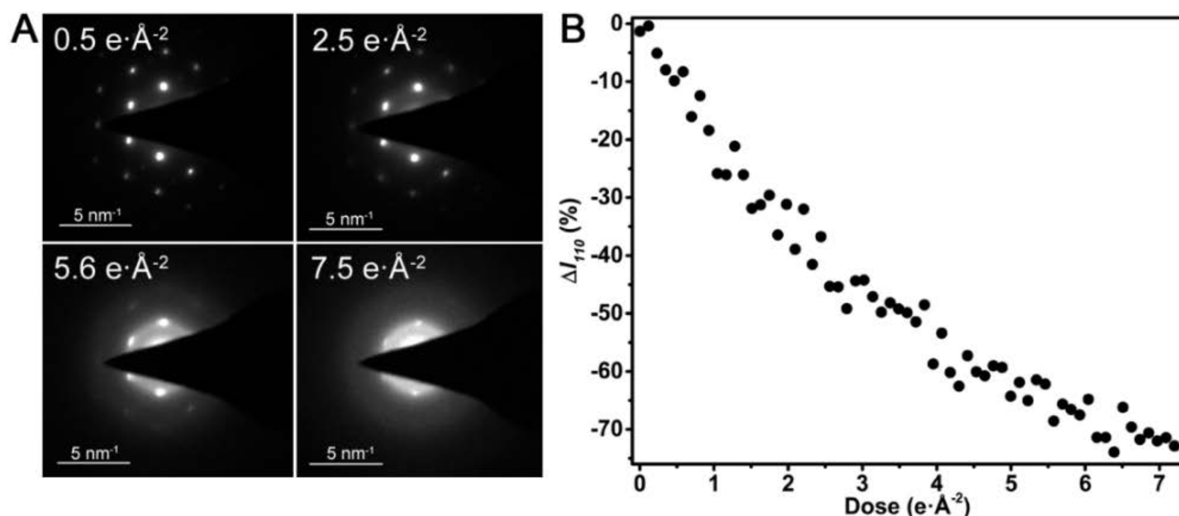

Figure 5.1 | High-dose example of the Bragg-spot fading-curve method for monitoring beam-induced damage as a function of accumulated dose. (a) Representative diffraction patterns (DPs) from a C36 microcrystal as a function of dose (e·Å^{-2}). (b) Difference in intensity of the *110* Bragg spots as a function of dose relative to the intensities at nominally zero dose. Here, $\Delta I_{110} = (I_{110} - I_{o,110})/I_{o,110}$, where I_{110} is the average *110* Bragg-spot intensity at a non-zero dose, and $I_{o,110}$ is the average intensity at nominally zero dose. The DPs and fading curve shown here are also displayed in Figure 1 in the main text. It is emphasized that the example fading curve shown is for a large total dose relative to the ultra-low dose experiments that were the focus of study.

For the low-dose experiments that were the subject of study here, fading curves were least-squares fit with a line, and the resulting fit equation was used to calculate the value of ΔI_{110} at a predetermined dose (*e.g.*, 0.063 e·Å^{-2}), as shown in Figure 5.2. Expectation of linearity at these low accumulated doses is further supported by noting that the value of ΔI_{110} at the predetermined dose was not affected by the overall functional form

of the fading curve. This was tested by completing a paired *t*-test on experimental data, with one set displaying a linearly-decaying behavior for a high total dose and the other displaying an exponentially-decaying behavior for a high total dose. The *p*-value on this paired *t*-test was 0.5, indicating no significant difference between the data generated from a linear *vs.* an exponential fading-curve behavior at 95% confidence.

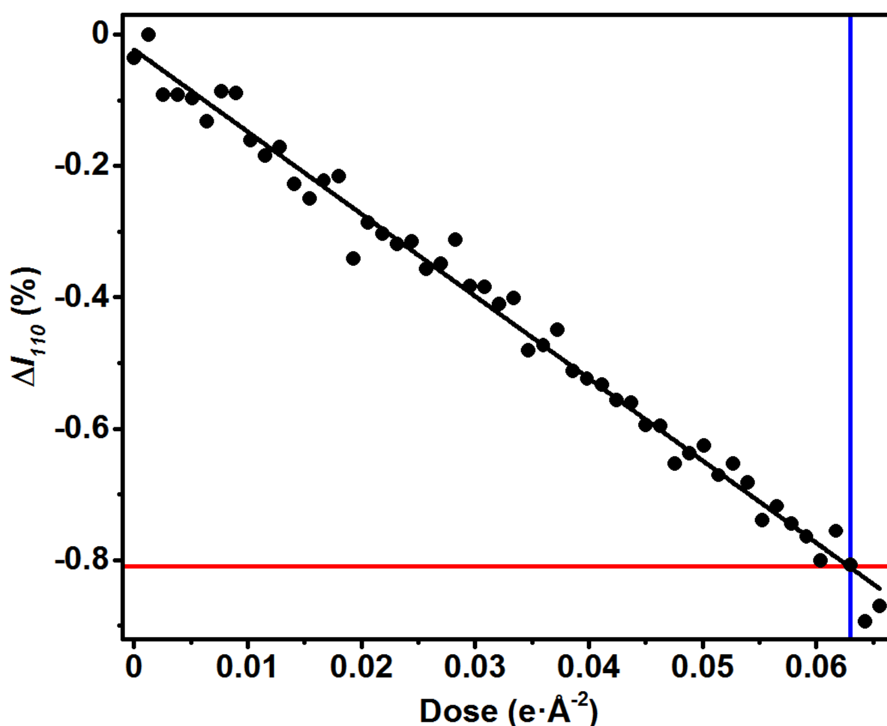

Figure 5.2 | Method for determining the value of ΔI_{110} at a predetermined total dose (here, 0.063 e·Å^{-2}). The vertical blue line marks the position of a dose of 0.063 e·Å^{-2}, the black line is the linear least-squares fit to the data (black circles), and the horizontal red line marks the position of the value of ΔI_{110} at the predetermined dose, as per solution to the equation for the linear least-squares fit.

After acquisition of all data and recording of all experimental parameters, the data analysis proceeded as follows. First, any shifts in position of the diffraction patterns was corrected using a template-matching plugin in Fiji to calculate the shifts (in pixels in the x and y directions) and a MATLAB code to carry out the correction.[371] This typically resulted in the loss of a few columns and rows of pixels around the frame edges, though no critical Bragg-spot information was lost. Next, the *110* Bragg peaks (the peaks of interest here) for all diffraction patterns in the stack were fit with a 2D Gaussian function, which included background determination. The intensities of the peaks were determined *via* background removal followed by numerical integration. Because the patterns were analyzed as a stack, the robustness of the automated fitting algorithm was routinely checked. This involved comparison of background values (which did not vary by more than 1% across all patterns) and comparison of peak fits for the first and last patterns, as well as those at all three quartiles, thus ensuring consistency of background correction and peak fitting across the entire stack. Finally, the intensities were plotted as a function of dose ($e \cdot Å^{-2}$), and the resulting plots were fit with a linear trend line for the low-dose data. The total change in intensity for each peak was then calculated for a predetermined accumulated dose (*e.g.*, 0.063 $e \cdot Å^{-2}$). Note that when peak fitting with a 2D Gaussian was not ideal, which occasionally occurred for patterns generated with pulsed beams due to, for example, a non-circular laser profile on the cathode, an edge-finding algorithm was used to calculate the peak area.

5.2 | Results and Discussion

5.2.1 Ultra-low Dose Comparison: Pulsed vs. Thermionic Beam

Effects of pulsed- and random thermionic-beam irradiation on *110* Bragg-spot intensities from individual C36 microcrystals for an identical ultralow dose rate of 7.8 x 10^{-7} $e \cdot Å^{-2} \cdot s^{-1}$ are summarized in Figure 5.3. For the pulsed mode, the number of electrons generated per laser pulse was 1.03 ± 0.15, and the time between arrival of each at the C36 microcrystal was f^{-1} = 100 μs (see the Supporting Information for details on the measurement of the number of electrons per packet). Intensities were monitored up to an accumulated dose of 0.066 $e \cdot Å^{-2}$ (see also Figure 5.2). Linear intensity decreases were observed for each over this relatively low range of accumulated dose. When elastic-bending and dynamical-scattering effects are negligible, Bragg-spot intensity attenuation as a function of dose is indicative of a loss of crystallinity due to increasing disorder and irreversible structural damage.[377] Here, the slopes of the responses differ by a factor of 1.8, with the rate of damage sustained for the pulsed beam being lower than that of the thermionic beam despite being applied at the same dose rate. See Figures 2.10 and 2.11 and Section 2.2 for descriptions of the methods used to measure beam current and beam size. Note that care was taken to ensure the C36 microcrystals studied were the same thickness (see Figure 2.4 and Section 2.1.3). Note also that, despite the necessary long experiment times, stability of the lab environment and the instruments was such that negligible net specimen drift occurred (*i.e.*, drift occurred about a single center-of-mass position after system and lab equilibration). This resulted in individual C36 microcrystals remaining positioned under the beam for the entire duration of each experiment for both

thermionic and pulsed-beam measurements (*i.e.*, net specimen drift was negligible for both conditions, as expected owing to the same dose rates and accumulated doses). This controls for systematic errors arising from potentially different net specimen drifts for the pulsed *vs.* thermionic experiments. Further, owing to the results, net specimen drift would need to consistently be greater for the thermionic condition despite being administered at the same dose rates (beam current and beam size) and under the same lab- and instrument-stability requirements as the pulsed condition. See Figure 2.13 for an illustrative example of the typical specimen spatial stability achieved and for a discussion of how lab-environment and instrument stabilities were monitored and assessed.

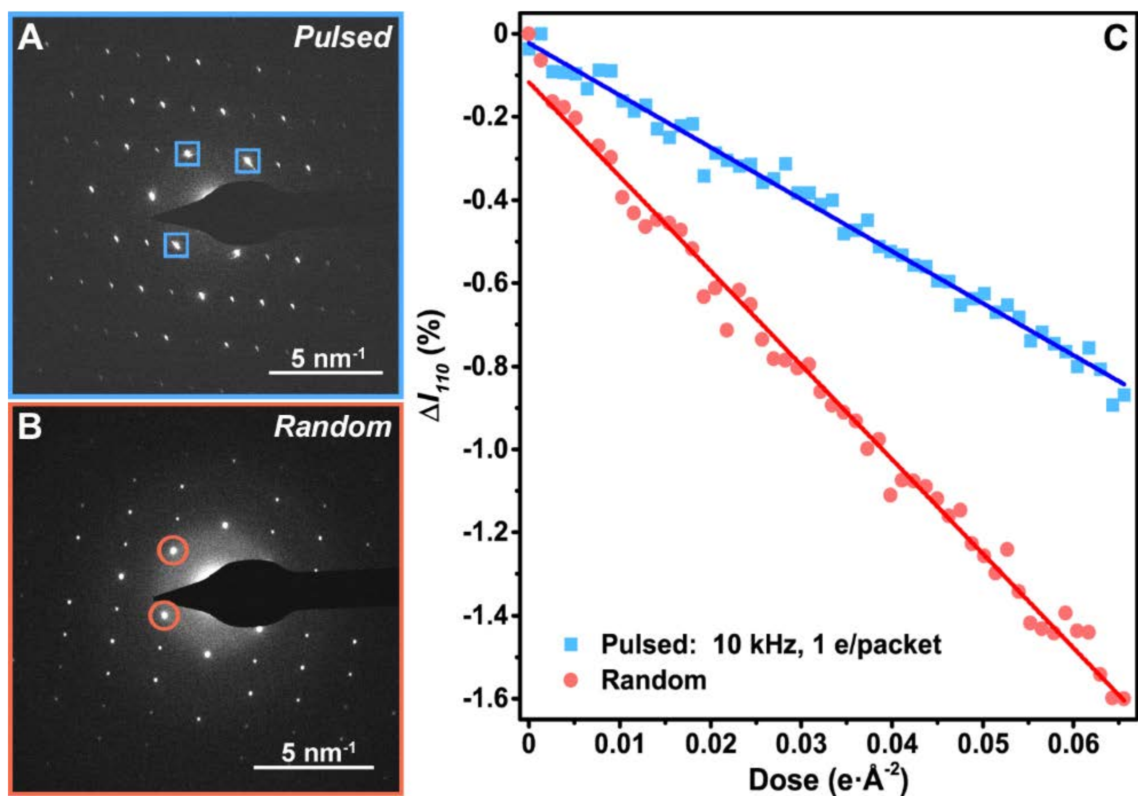

Figure 5.3 | Comparison of pulsed and random (thermionic) electron-beam damage for the same dose rate (7.8 x 10^{-7} e·$Å^{-2}$·s^{-1}). Representative (a) pulsed- and (b) random-beam diffraction patterns of a C36 microcrystal with the *110* Bragg spots used to generate the fading curves in panel (c) highlighted. (c) Fading curves and least-squares fits for the pulsed and random beams. The slope of the line fit to the random-beam data is steeper than that of the pulsed beam by a factor of 1.8. Pertinent specifications are as follows: Pulsed-beam current and illuminated area were 1.6 ± 0.24 fA and 132.4 μm^2, respectively (0.01 zeptoamps per nm^2). Random-beam current and illuminated area were 1.6 ± 0.22 fA and 131.5 μm^2, respectively. The pulsed beam was generated with a 300-fs FWHM pulsed laser operated at f = 10 kHz (f^{-1} = 100 μs). The laser pulse energy incident on the TEM

photocathode was set such that the number of electrons per packet was measured to be 1.03 ± 0.15.

Because the only difference between the two beam types was the temporal profile of electron arrivals (*i.e.*, electrons may arrive more closely together in time for conventional thermionic emission, whereas this is strictly controlled in the pulsed-beam case), the results shown in Figure 5.3 suggest that damage caused to the specimen is sensitive to shorter-than-average durations between electron arrivals. This then raises questions pertaining to the relationship between sequential electron arrival and damage accumulation in the specimen. That is, if two electrons arrive within a particular time interval and spatial proximity to one another, a description must be formed regarding what additional damage this would cause compared to the case in which the electrons arrive 100 μs apart, as well as what the relevant spatial radius and time scales are for additional damage to occur. To explore this, insight is drawn from the relevant physical damage mechanisms.

The primary damage mechanism – excitation and ejection of specimen electrons caused by collisions with incident electrons – occurs in femtoseconds and is essentially confined to a single molecule.[248,443,444] This is because the inelastic scattering cross section of a high-energy electron makes it unlikely that more than one collision per incident electron occurs. Secondary electron damage caused by ejected and Auger electrons, which has been estimated to cause up to 80% of the damage to the specimen, also occurs very quickly, over tens of femtoseconds.[247] Because the energy deposited by incident electrons

(37 eV, on average, for paraffins) is much higher than the threshold for damage (4.8 eV), a single secondary electron can break multiple bonds and excite multiple additional electrons before its energy drops below the damage threshold.[247] This in essence constitutes a non-linear relationship between the number of damage events and the number of incident inelastic collisions. While the damage radius of an individual event for secondary electrons is spatially localized – on the order of ten unit cells – due to the relatively large scattering cross sections the non-trivial probability of multiple events occurring from one electron leads to an increased chance of multiple radicals and additional excited electrons being formed.[28,250,251] Therefore, the damage radius associated with secondary-electron excitation is significantly larger when relevant aspects of all associated excitations are accounted for. That is, the damage radius for all associated events arising from a single incident inelastic collision includes typical diffusion lengths, mean free paths, and lifetimes for the radicals generated, the products of the radical reactions, and the phonons excited during relaxation of each event.

Occurring on the order of nanoseconds after initial formation, free radicals react with the surrounding lattice or with small, diffusing molecules (*e.g.*, free H_2 and light hydrocarbons), though several factors dictate the precise reaction rate, including molecular identity, free-radical site reactivity and geometry, radical concentration, and local lattice energy.[248] Degradation of unstable species follows the initial reactions, subsequently causing structural deterioration manifest as loss of crystallinity and Bragg-spot intensity fading.[248,249] This process continues for hundreds of nanoseconds to microseconds, though again the precise duration is dependent upon free-radical concentration and on local

energy.[248,445] Because the manner in which this process proceeds is dependent upon local energy, radical concentration, and diffusion rates, the thermal energy available significantly influences the damage sustained. For example, a temperature increase of 1 K produces an additional 3% damage, while an increase of 9 K produces an additional 28%.[252,253] This is noteworthy because while the global increase in equilibrium temperature is negligible at low beam currents, the energy released locally during excited electron relaxation is not, as evidenced by the processes described above.[253,254,441,446] Illustratively, excited phonons vibrating in the 5 to 15 THz range have 3 to 10 meV of energy, which corresponds to local temperature increase of 30 to 110 K.[447,448] (Note that while it may not be technically correct to use temperature as a descriptor of thermal energy at these length scales, it is nonetheless instructive to consider the kT energies involved.) This energy will be distributed over tens to hundreds of nanometers, per the damage radius discussion above, and will persist for hundreds of nanoseconds to microseconds.[26,116]

From this discussion, it is therefore reasonable to assume that local phonon excitation, while not sufficient to significantly raise the global thermalized lattice temperature, can cause appreciable increases in energy locally at the excitation site, thereby causing a non-linear increase in the damage caused by free radicals and higher diffusion rates. The combination of dominant damage mechanisms, and the associated compounding synergistic effects (*e.g.*, Arrhenius-type increases in reaction and diffusion rates with local energy), suggests that incident electrons impinging upon the specimen within hundreds of nanoseconds to microseconds and tens to hundreds of nanometers of one another could produce a degree of irreversible damage that would not occur if reactive species, phonons,

and secondary electrons were allowed significantly more relaxation time between electron arrival. Following these arguments, one would then expect events of electrons arriving with shorter-than-average durations between them to result in more extensive irreversible structural damage from otherwise reversible processes owing to increased accumulation of local lattice energy and a higher spatiotemporal number density (*i.e.*, species per volume per time) of reactive species during moments of greater instantaneous dose in the random beam. See the Supporting Information for details of the measures taken to account and control for sources of both random and systematic error.

5.2.2 Effect of Shortening Time Between Pulses

To test the hypotheses stated in Section 3.2.1, a set of pulsed-beam experiments were conducted, wherein both the time between electrons (f^{-1}) and the number of electrons in each packet were systematically varied and compared to the random thermionic-beam method and to one another. Figure 5.4 shows the result of reducing f^{-1} to 5 μs (f = 200 kHz) for 1.04 ± 0.11 electrons per packet, again compared to the random-beam approach administered at the same dose rate (in this case, 9 x 10^{-6} e·Å^{-2}·s^{-1} owing to a higher f). A statistically-significant reduction in damage at a given accumulated dose (here, up to 0.077 e·Å^{-2}) is again observed for the pulsed beam. Interestingly, damage for the pulsed-beam approach is again reduced by nearly a factor of two relative to the conventional low-dose method. This reduction in damage recurred nearly identically in a repetition of the experiment (see Table 5.1), demonstrating the repeatability of the result. The damage at a common accumulated dose (*e.g.*, 0.066 e·Å^{-2}), however, is higher by approximately 15%

for both the pulsed and the random beams when compared to that sustained with the lower dose rate shown in Figure 5.3. This supports the hypothesis that contributions by irreversible aspects of otherwise reversible mechanisms to the accumulated damage sensitively depend upon the time between arrival of each individual electron at the specimen.

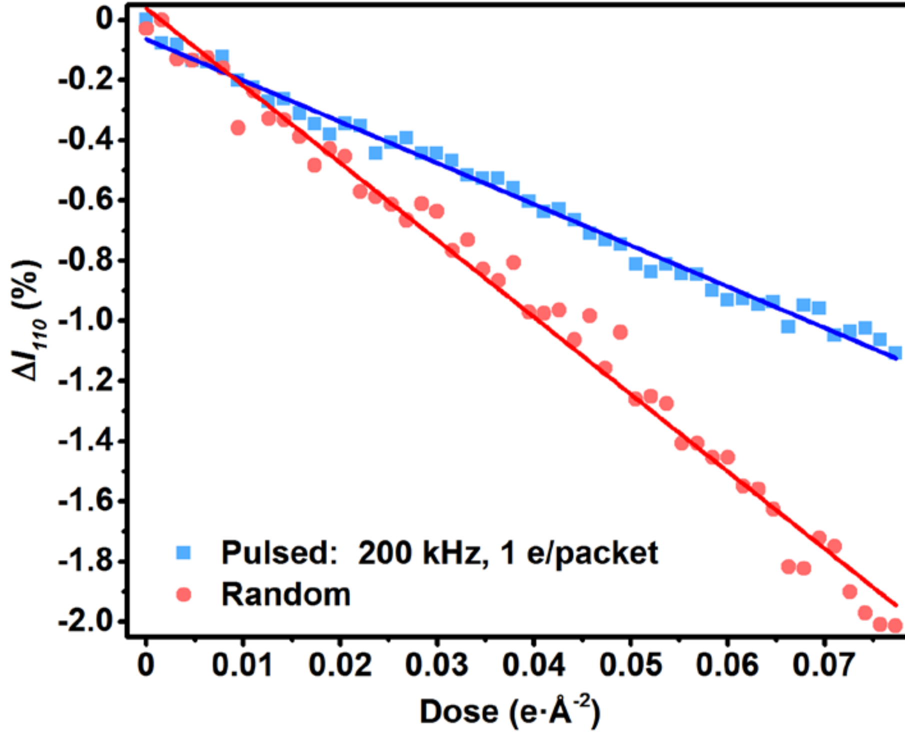

Figure 5.4 | Comparison of damage induced by pulsed and random (thermionic) electron-beam irradiation for the same dose rate (9 x 10^{-6} e·$Å^{-2}$·s^{-1}). Fading curves and least-squares fits for the pulsed and random beams are shown. The slope of the line fit to the random-beam data is steeper than that of the pulsed beam by a factor of 1.9. Pertinent specifications are as follows: Pulsed-beam current and illuminated area were 31.7 ± 3.54 fA and 219.4 μm^2, respectively. Random-beam current and illuminated area were 32.0 ± 3.45 fA and 220.7 μm^2, respectively. The pulsed beam was generated with a 300-fs FWHM pulsed laser operated at f = 200 kHz (f^{-1} = 5 μs). The laser pulse energy was set such that the number of electrons per packet was measured to be 1.04 ± 0.11.

5.2.3 Increasing the Number of Electrons Per Packet

The effect of the number of electrons in each packet on damage was also studied, the results of which are summarized in Figure 5.5. Because two factors were tested (f^{-1} and the number of electrons per packet), a two-level factorial approach was taken in order to avoid conflation. It was observed that the degree of damage sustained at a given accumulated dose is significantly higher when the number of electrons per packet is increased (here, from one to five; Figure 5.5a). Reducing f^{-1} for the 5-electron packets from 100 μs to 5 μs produced a further increase in damage, potentially to a larger degree than for the 1-electron packets. An analysis of variance shows that both factors are statistically-significant predictors of damage (to 95% confidence), but no super-additive effect was apparent at this confidence level. That is, the results do not indicate that varying both factors produces any additional effect beyond the additive ones observed. This said, an unexplored region of the very-large parameter space may indeed exist where super-additive effects do occur. Interestingly, the deleterious effects caused by increasing the number of electrons per packet are substantially more significant than those caused by decreasing f^{-1}; the five-fold increase in electrons per packet produces a greater increase in damage than a five-fold decrease in f^{-1}.

The dramatic increase in damage caused by a modest increase in the number of electrons per packet suggests that, for a given f^{-1}, a point should be reached where all benefits provided by pulsing the source compared to the conventional low-dose approach are lost. Figure 5.5b shows a comparison of pulsed- and random-beam irradiation, where the number of electrons per packet for the pulsed beam was increased to 20 (f^{-1} = 5 μs;

same dose rate = 1.8×10^{-4} $e\cdot Å^{-2}\cdot s^{-1}$). As can be seen, no statistical difference (to 95% confidence) at a given dose (here, 0.063 $e\cdot Å^{-2}$) is present, indicating that the amount of damage caused by the arrival of 20 electrons at the specimen over an estimated 2-ps time period [increased from 300 fs due to Coulomb repulsion] is comparable to that occurring during the conventional low-dose approach.[161] It is reasonable to speculate that the quantitative behaviors observed here are material dependent, but more work is needed. Taken together, these results support the hypothesis that, despite being administered at the same dose rate, the statistical generation of multiple electrons over a shorter-than-average period of time during conventional emission processes is the source of the observed increased damage compared to the precision pulsed-source approach.

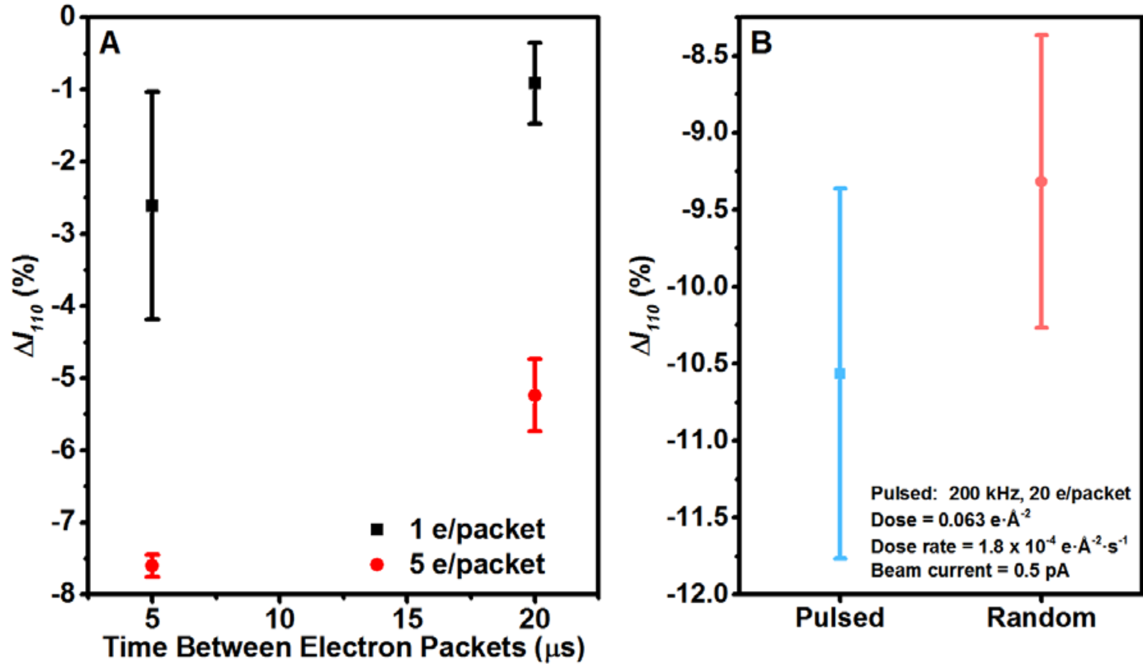

Figure 5.5 | Effect of the number of electrons per packet and the duration between each packet on damage. (a) Change in I_{110} after a total accumulated dose of 0.063 e·Å^{-2}. Error bars represent the standard error over four separate experiments. All data points were generated using a pulsed beam, and the same size specimen area was irradiated for each (within 0.5%). (b) Change in I_{110} after a total accumulated dose of 0.063 e·Å^{-2} for a pulsed beam with 20 electrons per packet and f^{-1} = 5 μs (f = 200 kHz) compared to a random (thermionic) beam of the same current (0.5 pA) and for the same size irradiated specimen area (within 1%; same dose rate = 1.8 x 10^{-4} e·Å^{-2}·s^{-1}). Error bars represent the standard error over five separate experiments.

5.3 | Summary and Conclusion

Via systematic studies and direct, statistical comparisons to conventional methods, we have conclusively shown that delivering dose using a precise, highly-controlled pulsed-

beam approach in a TEM can reduce the damage sustained by beam-sensitive materials. We accomplish this by using the highly regular and stable emission from a fs pulsed laser to strictly control critical aspects of electron emission from the source. We find that the degree of damage is sensitive to both the duration between arrival of each electron at the specimen and to the number of electrons per packet. Increased damage with increased electrons per packet, as well as the observation of a loss of advantageous effects, suggests the temporally random emission occurring during conventional low-dose methods is a significant contributor to beam-induced damage and that the pulsed-beam approach in essence mitigates the cumulative effects of sequential inelastic events occurring within a damage-mechanism-specific spatiotemporal window. The results of this work open an entirely new avenue of research into fundamental studies of radiation-damage mechanisms and into mitigation of the associated deleterious effects. Myriad future studies are envisioned, including quantifiably testing the effects on spatial resolution and extension of the approach to probing biological structures, biomaterials, biological macromolecules, radiation-sensitive organic and inorganic materials (*e.g.*, organic semiconductors, hybrid perovskites, and zeolites), liquid environments, and cryo-EM.

Chapter 6 | Pulsed Beam Damage Mitigation & Elucidation in Metal Halide Perovskites

As discussed in Section 1.4, electron beam damage to perovskite specimens during TEM experiments limits the efficacy of TEM and related techniques to provide insight into specimen structures and morphology. In addition, MHPs are a particularly useful test case for using pulsed beams as a kinetic tool as their stability upon exposure to stimuli such as light, strong bias, and heat has been outpaced by efficiency improvements.[277,278] Thus, structural understanding of various degraded phases of MHPs is valuable and the many tools associated with TEM, such as EBIC, STEM, and EDX, have a high potential to aid in this effort. Additionally, parallels have been drawn between degradation via electron beam and similar pathways followed upon exposure to light and heat.[273,276,309] This work uses the prototypical MHP $MAPbI_3$ as a test material. Electron beam degradation in $MAPbI_3$ is thought to be initiated by iodide migration, as evidenced by careful high-resolution TEM analysis as well as theoretical calculations highlighting the low activation energies of iodide vacancies and interstitials compared to other point defects.[272,274,276,325,449] Observed self-healing processes in MHPs suggest that a temporal component to the damage mechanism, even a certain reversibility, is possible and may be exploited through temporal manipulation of the material.[333,334,355,450–452] Therefore, the work discussed in this chapter is two-fold.

First, we explore fs laser-driven pulsed TEM for mitigating damage in MHPs, specifically methylammonium lead iodide ($CH_3NH_3PbI_3$ or $MAPbI_3$). Our main goal was to determine – all else being equal – if a pulsed beam leads to a reduction in $MAPbI_3$

damage compared to a conventional beam. Accordingly, we focused on quantitatively comparing damage caused by pulsed beams to that of conventional thermionic beams at the same dose rates and the same total doses. We also studied the effects of the number of electrons per pulse (E/P) and the duration between pulse arrival at the specimen (f^{-1}, where f is the laser repetition rate). We find a clear reduction in damage for pulsed beams compared to random (thermionic) beams, as well as an apparent exacerbation of damage with increasing instantaneous dose (*i.e.*, with more electrons per pulse) even with longer time elapsed between the arrival of each. We also observe a crossover effect, where pulsed beams become more detrimental than random beams. Interestingly, the degree to which damage is reduced in $MAPbI_3$ is lower than that for $C_{36}H_{74}$, supporting the hypothesis that the pulsed-beam effect is material and mechanism dependent.

Then, we explore differences in degradation behavior of MAPbI3 according to the temporal profile of the electron beam used. The fine control exhibited over the temporal profile of the pulsed beam may allow for new information in kinetic processes due to the triggering of different components of the energy landscape upon successive electron arrival, although effects like texturing may also have some effect. We use pulsed electron beams to exhibit a potential second kinetic step in the degradation of MHPs. This technique was used to manipulate two time constants independently, opening the door to further kinetic experiments using pulsed electron beams.

6.1 Experimental Methods

6.1.1 Data Collection & Experimental Parameters

Overall, the data collection for these experiments was very similar to that described in Chapter 5. Specifically, a polycrystalline specimen of $MAPbI_3$ was irradiated with the electron beam at a given dose rate. Specifics for the experimental apparatus are given in Section 2.2, and the procedure for measuring dose rate is given in Section 2.2.3. The fading of the diffraction pattern was used as a proxy for damage. Beam currents were significantly higher in these experiments than those shown in Chapter 5, as MHPs are more resistant to radiation damage than organic paraffin crystals. In this case, they ranged between 4 and 900 pA. Details of each experimental run used in this chapter are shown in Table 6.1.

Exp.	Beam Type	TBP (us)	E/P	E/P Error	Beam Current (pA)	Beam Current Error (pA)	Beam Area (um^2)	Dose Rate (e·Å^{-2}·s^{-1})	Acq. Time (s)	Total Time (min)	Final ΔI (%)
P11	Pulsed	2	50.42	0.99	4.03	0.08	245.1	0.001	30.0	162.01	19.37
P8	Pulsed	2	50.44	1.84	4.04	0.15	245.1	0.001	30.0	161.93	19.37
P3	Pulsed	4	99.63	1.65	3.99	0.07	246.0	0.001	20.0	164.59	21.14
P6	Pulsed	4	100.41	1.36	4.02	0.05	244.1	0.001	10.0	162.09	20.81
P9	Pulsed	4	100.19	1.85	4.01	0.07	245.1	0.001	30.0	163.05	20.91
P10	Pulsed	4	100.31	1.99	4.01	0.08	245.1	0.001	30.0	162.86	21.07
T8	Therm	N/A	N/A	N/A	4.03	0.07	245.1	0.001	5.0	162.34	23.24
T11	Therm	N/A	N/A	N/A	4.08	0.08	245.1	0.001	30.0	160.19	23.31
P7	Pulsed	2	199.63	1.64	15.97	0.13	99.2	0.010	20.0	16.56	27.92
P5	Pulsed	2	199.04	2.10	15.92	0.17	99.9	0.010	5.0	16.73	28.15
P4	Pulsed	4	396.34	3.67	15.85	0.15	99.9	0.010	1.0	16.81	34.47
P2	Pulsed	4	398.51	2.10	15.94	0.08	99.9	0.010	20.0	16.71	34.67
T10	Therm	N/A	N/A	N/A	15.91	0.14	99.9	0.010	1.0	16.74	31.27
T1	Therm	N/A	N/A	N/A	16.02	0.16	99.5	0.010	0.5	16.56	30.99
T5	Therm	N/A	N/A	N/A	16.23	0.17	99.5	0.010	1.0	16.35	30.83
T4	Therm	N/A	N/A	N/A	881.90	0.15	366.7	0.150	1.0	1.11	44.85
T6	Therm	N/A	N/A	N/A	882.18	0.16	369.4	0.149	1.0	1.12	44.88
T7	Therm	N/A	N/A	N/A	895.75	0.17	369.4	0.152	1.0	1.10	44.72
T9	Therm	N/A	N/A	N/A	878.86	0.13	368.0	0.149	1.0	1.12	44.88

Table 6.1 | Experimental parameters and associated errors for all experiments presented in Chapter 6. Exp. = Experiment number, where the letter identifies whether the experiment was pulsed (P) or thermionic (T) and the number identifies the order in which the experiments were conducted. Beam Type = pulsed beam (Pulsed) or random thermionic beam (Therm). TBP = time between electron-packet arrival at the specimen. E/P = electrons per packet. Beam Area = size of the electron beam. Acq. Time = camera exposure used to acquire each diffraction pattern. Total Time = the total time required to conduct the fading-curve experiment up to a predetermined total dose. Final ΔI_{110} = the

final average intensity value of the *110* Bragg spots up to the total accumulated dose specific to the experiment.

6.1.2 Diffraction Pattern Analysis

Due to the polycrystalline nature of these specimens, DPs were azimuthally averaged to enable tracking of peak intensity. A circular Hough transform was not possible due to the low number of crystallites included in each DP and therefore the incompleteness of the polycrystalline DP circles (Figure 6.1a inset). Instead, Fiji and Digital Micrograph were used to measure at least ten opposing peaks (corresponding to various planes) and the center point was calculated as an average of the center points for each measurement. As many of these experiments did not include a beam block due to their low beam currents, visual confirmation with the *[000]* peak was used to ensure the result seemed reasonable.

Upon azimuthally averaging, peaks were fit to Gaussian functions to confirm their centers corresponded with the expected locations for the I4/mcm space group (another check on the center-finding method) and the peak intensity was calculated using integration (Figure 6.1b). Only peaks corresponding to expected I4/mcm $MAPbI_3$ planes were included, in order to avoid noise from the appearance of other phases or species during the damage process. As in Chapter 5, damage was therefore quantified using a fading-curve method, where a reduction in Bragg-beam intensities (ΔI; indicative of destruction of $MAPbI_3$ crystalline order) was tracked as a function of accumulated dose (Figure 6.1c).[253] Peaks arising from planes with $d < 6.3$ Å were used to monitor damage effects for both beam types (*i.e.*, pulsed and conventional). Note that $\Delta I = (I - I_o)/I_o$, which is the

normalized change in intensity relative to that at nominally zero dose (I_o). This is especially important in this work because of the low number of crystals within the selected area aperture, leading to a polycrystalline diffraction pattern that does not manifest as smooth rings and in which certain phases are likely to be over- or underrepresented. A total accumulated dose of 10 $e \cdot Å^{-2}$ was used as the reference point throughout.

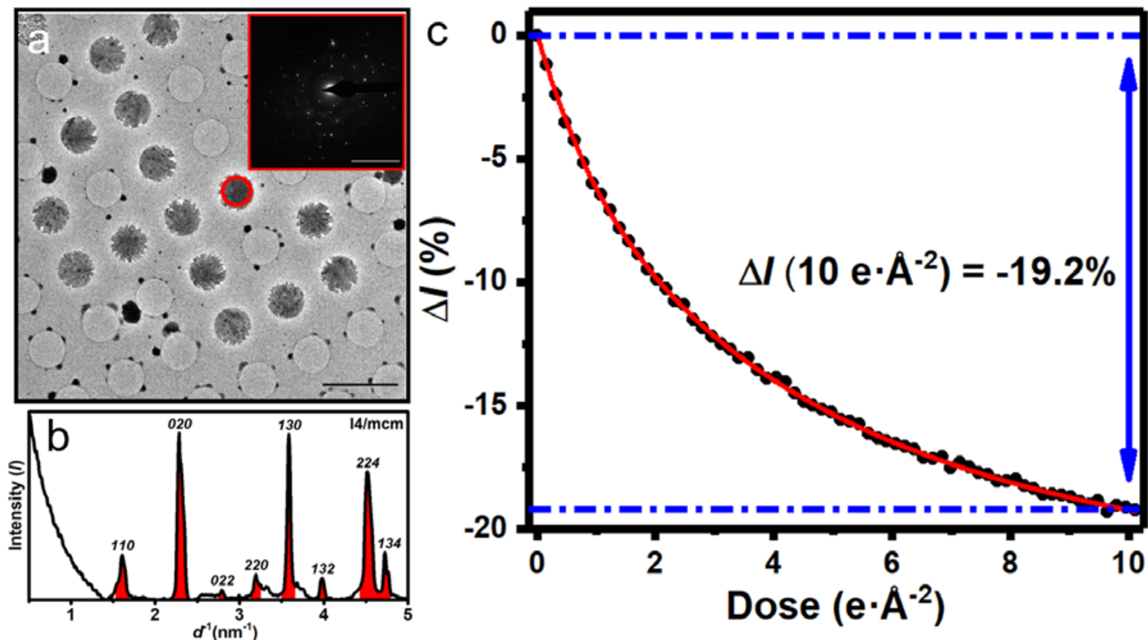

Figure 6.1 | Quantification of damage to $MAPbI_3$. (a) Low-magnification bright-field image of the TEM specimens (scale bar = 5 μm). The diffraction pattern (inset; scale bar = 5 nm^{-1}) was obtained from the red-circled region. (b) Intensity plot from azimuthally averaging the pattern in (a). Red peaks are those used for monitoring beam-induced intensity changes. The space group used for indexing was *I4*/*mcm*, though the structure is not yet universally agreed upon.[1,2,277] (c) Bragg-intensity fading curve for a pulsed electron beam (dose rate = 0.001 $e \cdot Å^{-2} \cdot s^{-1}$; beam size = 245 ± 3 $μm^2$; 50.4 ± 1.0 E/P; f^{-1} = 2 μs). Red curve is to determine ΔI at 10 $e \cdot Å^{-2}$, which here is -19.2%.

6.1.3 Bragg Peak Analysis

To determine the existence of disparate damage effects on certain crystallographic planes, Bragg peaks were also analyzed separately, rather than being summed as shown above. Due to the disparate prevalence of certain orientations in each specimen, only four

planes were tracked as these corresponded to the Bragg peaks that appeared most consistently with sufficient SNR in the DPs. These peaks, the 022, 110, 020, and 220, were integrated and fitted with Gaussians similarly to the procedure described in Section 6.1.2 and tracked individually.

After the peak intensities were calculated for each frame of each experiment, these were plotted vs dose, similarly to what is shown in Figure 6.5. Each plot was fitted with a double exponential, corresponding to the Equation 6.1.

$$I = I_{final} + A_1 * \exp\left(-\frac{D}{t_1}\right) + A_2 * \exp\left(-\frac{D}{t_2}\right) \qquad (6.1)$$

In Equation 6.1, I corresponds to the intensity, A_1 and A_2 are fitting constants, D corresponds to the accumulated total dose, and $t1$ and $t2$ are time constants for the two exponentials. This equation was chosen because it fits much better than a single exponential (average R^2 coefficient of 0.99 rather than ~0.9) for the process which experienced a fast initial decay (*e.g.*, the 200 E/P *020* plane shown in blue in Figure 6.5b). Of course, a triple exponential produces an even higher R^2 coefficient, but in accordance with practices to avoid overfitting, the simplest possible function that provides a satisfactory fit (satisfactory being subjective but in this case meaning an R^2 coefficient of over 0.97) was chosen to represent the data. Complicating matters is the fact that the peaks which did not experience a comparatively fast initial decay (*e.g.*, the thermionic *020* plane shown in red in Figure 6.5b) also fit quite well to a single exponential (average R^2 coefficient of 0.98). Equation 6.1 was still used for these plots in order to facilitate comparison, operating under the assumption that the damage mechanism is the same in both cases and that the relative kinetic rates of the various steps are the main differentiator

(more details on this in Section 6.2.4). However, it is possible that the two damage profiles are in fact indicative of two entirely different damage mechanisms. Future work will be needed to further elucidate this.

After fitting, the ΔI for each peak in each experiment was determined, in the identical manner to the determination of the overall ΔI shown in Figure 6.1c. In order to compare the effect of disparate damage to certain peaks without conflation with the overall damage caused to the specimen, the peak intensities were not only normalized to the original intensity but also compared (via subtraction) to the total ΔI. For example, if the overall specimen experienced a 30% loss in intensity over the course of 10 A delivered dose, but the 022 peak experienced a 33% loss in intensity, the disparate damage to the 022 peak was reported as 3%. If the 110 peak experienced a 27% loss in intensity, the disparate damage to the 110 peak was reported as -3%. This value is intended for ease of comparison and does not necessarily correspond to a phenomenological value (*i.e.*, actual damage to the 022 plane is not necessarily 6% higher than actual damage to the 110 plane if measured by atomic displacement or some other physical metric, in the example given above).

6.1.4 Planar Density of Iodide

Planar densities of iodide were calculated in order to determine correlation between planar iodide content and disparate damage to a specific plane. First, CrystalMaker was used to slice a model of the unit cell to eliminate ions that do not intersect the plane.[453] The I4/mcm space group was used as it is the most commonly measured space group at room temperature, although some disagreement on the crystal symmetry for $MAPbI_3$ does

exist.[1,2] The resulting planes are shown in Figure 6.5a-c. In the images, carbon, nitrogen, and hydrogen were not shown for the sake of simplicity and because they contribute minorly to the percent iodide result. They were, however, included in the calculation itself to maximize accuracy. The number of ions of each species centered on the plane were determined using the CrystalMaker model. Then, the total area on the plane taken by each ion was calculated using ionic radii.[453] To account for ions that were not entirely contained within the unit cell, ions on the corner of the plane were counted as ¼ of their total area, and ions on the edge of the plane were counted as ½ their total area.[454]

The percent iodide reported below is defined as the percentage of the area taken up by iodide ions centered on the plane, divided by the total area taken up by ions centered on the plane. This denominator is not intended to be indicative of the total area of the plane, as there are nearby ions which are not centered on the plane but for which a portion of the electron cloud takes up space on the plane. Of course, some of these ions are iodide as well. Accordingly, there is an alternative method to calculate percent iodide in which the portions of the electron cloud which overlap with the plane in question are also counted in the calculation. This method was not used as it is not the crystallographic standard, but there could be an argument made for it as the electron cloud does interact with the incoming electrons as well.[28,88] As the use of this latter method of calculation changes the percent iodide values significantly, it will be relevant to consider the method of calculation carefully in work building from these results. This is especially true if the future work seeks to confirm iodide migration as the source of one of the time constants, testing the hypotheses laid out in Section 6.2.3.

6.2 Results and Discussion

6.2.1 Direct Comparison: Pulsed vs. Thermionic Electron Beam

Comparison of damage caused to $MAPbI_3$ by a pulsed beam to that of a conventional thermionic beam is shown in Figure 6.2. For a common dose rate (0.001 $e \cdot Å^{-2} \cdot s^{-1}$ for an illuminated area of 245 ± 3 μm^2), there is a clear reduction in the extent to which the intensities fade for the pulsed beam under the conditions used for this experiment (50.4 ± 1.0 E/P and f^{-1} = 2 μs). At a total accumulated dose of 10 $e \cdot Å^{-2}$, the intensity change for the pulsed beam is -19.2%, while that of the thermionic beam is -23.2%. The experiments shown correspond to P11 and T8 in Table 6.1. Experiments P8 and T11 repeat the result.

This shows that providing temporally-regular pauses in electron-beam irradiation, and thus providing regular periods of specimen relaxation and a reduction in exacerbating effects (*e.g.*, multi-electron impact within a specific damage radius), leads to enhanced preservation of $MAPbI_3$ structural order compared to conventional random-beam low-dose methods. Note that for pulsed-beam TEM experiments performed on $C_{36}H_{74}$ and bacteriorhodopsin, the extent to which damage was reduced was greater than seen here, though evidence indicates the degree of reduction also depends on f^{-1}.[353,354] This suggests the extent to which damage is reduced is material and mechanism dependent (perhaps strongly so) and that the overall effect of pulsed beams with respect to damage reduction is a general one.

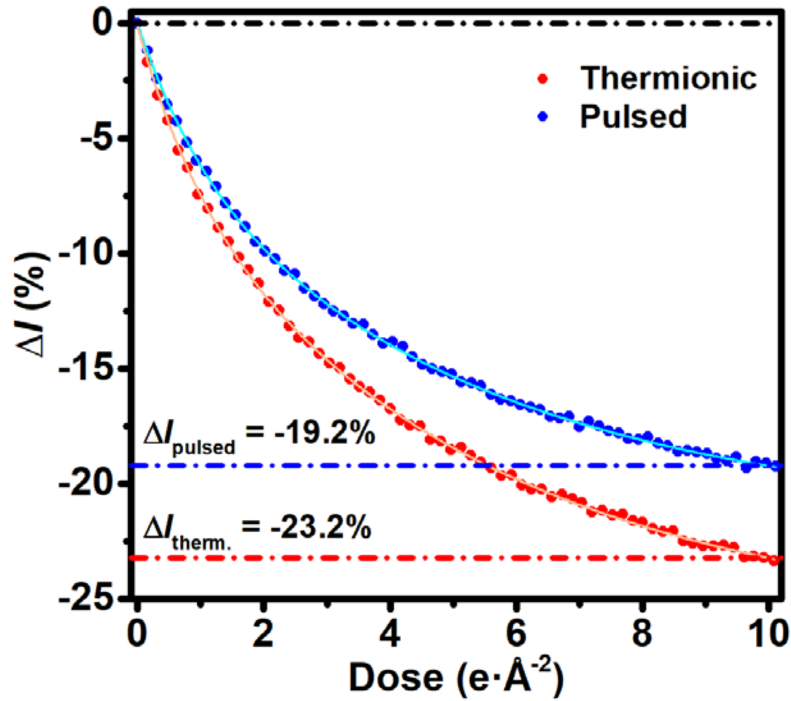

Figure 6.2 | Comparison of pulsed and thermionic beam. Shown are Bragg-peak intensity fading curves for $MAPbI_3$ for pulsed (blue) and thermionic (red) beams delivered at the same dose rate (0.001 $e\cdot Å^{-2}\cdot s^{-1}$). Fits to the data are for determining ΔI at 10 $e\cdot Å^{-2}$, which here is -19.2% for the pulsed beam and -23.2% for the conventional thermionic beam (as indicated by the blue and red horizontal dot-dashed lines, respectively). The beam was spread over an area of 245 ± 3 μm^2 for both types. The pulsed beam consisted of 50.4 ± 1.0 E/P and f^{-1} = 2 μs (*i.e.*, a 500-kHz repetition rate).

6.2.2 Effect of Varying Time Between Pulses and Electrons per Packet

A number of effects and conditions – in addition to beam-induced damage to crystalline order – can produce an apparent dose-dependent drop in Bragg-beam intensities. Thus, drawing conclusions from direct comparisons made across multiple measurements

and specimens requires control of myriad variables that might influence, interfere with, and overwhelm the intrinsic beam-damage behavior (*e.g.*, specimen thickness and lateral dimensions, specimen bending under the beam, lab and instrument temperature stability, specimen and beam drift, *etc.*). Accordingly, sources of error and artifacts were identified and accounted for *via* control experiments and monitoring of experimental conditions. Detailed descriptions of the measures taken here are reported elsewhere.[353] As an example of the requirements needing to be met for data to be accepted, experiments were rejected and repeated when the beam current, as well as the beam size, differed by more than 1% before and after acquisition of a data series. Experiments were conducted after observable directional specimen drift ceased. Further, experiments were rejected if the specimen was found to have directionally drifted more than 1% of the substrate hole diameter (*i.e.*, 25 nm) between the start and the finish of data acquisition. Pre-irradiation was eliminated by navigating specimen movement systematically and ensuring no two experiments were conducted within two beam diameters of one another. Data presented here consists of multiple experimental trials conducted over several days.

To better understand the origins of damage reduction when using a pulsed beam, effects of varying E/P and f^{1} were systematically explored (Figure 6.3). Depending upon the mechanisms at work, one might intuitively expect an increase in damage with increased E/P, due to more inelastic electron/specimen collisions occurring within a given pulse, and also with decreased f^{1}, due to there being less time between electron arrival at the specimen (thus reducing relaxation and recovery time and increasing the probability of simultaneous or near-simultaneous impact within a particular damage radius).[351,353,354] However,

regimes do exist wherein the benefits gained by increasing f^{-1} are lost when simultaneously increasing E/P, as observed for $C_{36}H_{74}$.[353] This is indeed the case for $MAPbI_3$. For dose rates of 0.001 e·Å^{-2}·s^{-1} and 0.01 e·Å^{-2}·s^{-1} (Figure 6.3a and 6.3b, respectively), damage increases with increased E/P despite an accompanying modest increase in f^{-1} from 2 μs to 4 μs for the larger electron pulses. Such an effect was also observed in single crystals of $C_{36}H_{74}$, where going from 1 E/P to 5 E/P had a substantially larger effect on damage than did decreasing f^{-1} from 20 μs to 5 μs.[353] Taken altogether, these results suggest that specimen relaxation and recovery processes that are at work during the few microseconds between pulses can be overwhelmed by exacerbating effects of multi-electron impact within a given damage radius. That is, additional energy deposited into the already-excited specimen region causes further structural damage that otherwise would have recovered – or would have been exponentially less significant (owing to exponential relationships for reaction kinetics, diffusion rates, and thermal energy) – during a single electron event isolated in space and time.

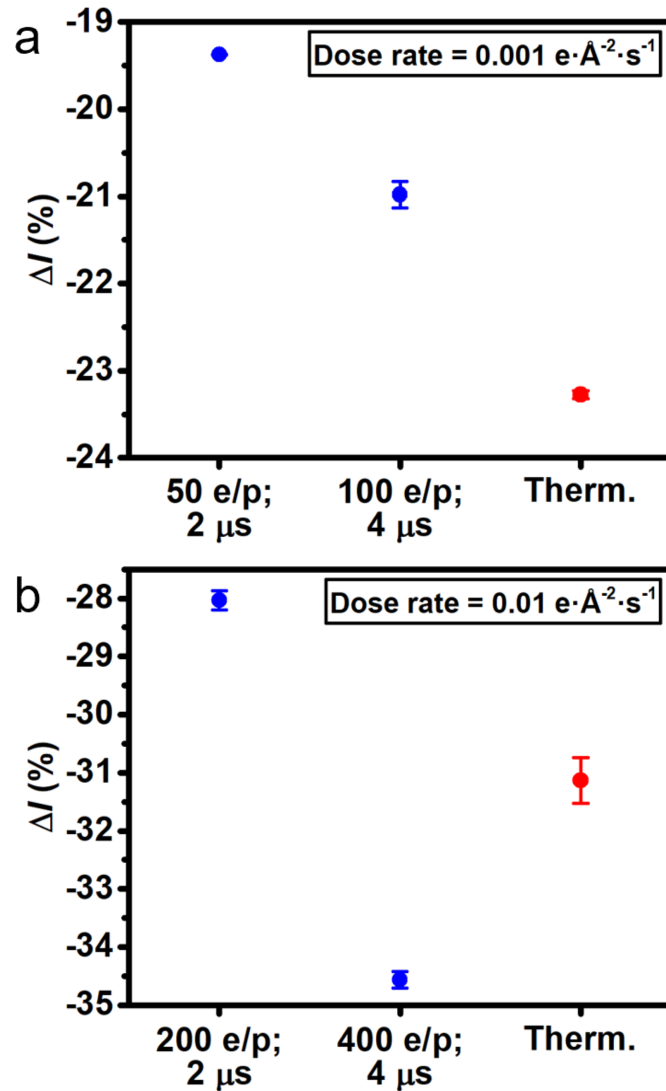

Figure 6.3 | Effect of E/P and f^{-1} on damage to $MAPbI_3$ for a total dose of 10 e·Å^{-2}. (a) Bragg-intensity reduction (ΔI) for pulsed (blue) and thermionic (therm., red) beams administered at a dose rate of 0.001 e·Å^{-2}·s^{-1}. The time between electron pulses in microseconds (f^{-1}) is noted below the number of electrons per pulse (E/P). Error bars for 50 E/P, 100 E/P, and thermionic are one standard deviation over 2, 4, and 2 separate experiments, respectively. (b) Bragg-intensity reduction (ΔI) for pulsed (blue) and

thermionic (therm., red) beams administered at a dose rate of 0.01 $e \cdot Å^{-2} \cdot s^{-1}$. Error bars for 200 E/P, 400 E/P, and thermionic are one standard deviation over 2, 2, and 3 separate experiments, respectively.

In addition to the overall trends shown in Figure 6.3, a type of crossover or threshold region exists, where more – rather than less – damage is caused by the pulsed beam as compared to a conventional beam delivered at the same dose rate (Figure 6.3b). Here, such a crossover is seen when increasing from 200 E/P separated by 2 μs to 400 E/P separated by 4 μs. This behavior lends support to the hypothesis that it is multi-electron impact leading to compounding effects that is driving the dramatic increase in damage with increasing E/P.[353] In essence, this is due to additional energy being deposited into already-excited specimen regions prior to full relaxation back to ground-state conditions. Interestingly, the instantaneous dose rate for a single pulse of 400 electrons confined to a 300-fs window (more likely a few picoseconds due to Coulombic expansion) is 5×10^4 $e \cdot Å^{-2} \cdot s^{-1}$, assuming uniform illumination across the 245-μm^2 beam area.[161] It is therefore perhaps surprising that such a beam does not produce substantially more damage than observed, though the number of electrons per $Å^2$ per pulse is only 2×10^{-8}. Though the time-averaged reduction in damage for pulsed beams is clear, pulse-to-pulse behaviors and the resulting specimen effects are largely unknown and require additional investigation.

Damage reduction (and increase at the crossover) to $MAPbI_3$ when using pulsed-beam TEM is likely driven by temporal processes that are active on the pulse-to-pulse timescales.[349–351,353,354] Such processes include thermal effects which, while not yet well

understood for electron-beam excitation and damage in $MAPbI_3$, are important in similar low-thermal-conductivity materials.[246,253,263] The effect of thermal processes in damage reduction can be appreciated by noting timescales of thermal diffusion and relaxation in $MAPbI_3$ relative to f^{-1}. Using known constants, it is estimated that thermal energy deposited into a 2.5-μm diameter $MAPbI_3$ crystal would largely dissipate into the carbon substrate within several microseconds.[455–458] Note, however, that temperature from the perspective of the entire specimen is likely too coarse a view when considering pulsed-beam damage mechanisms and temporal aspects of molecular-scale excitations. Nevertheless, this estimate indicates thermal-dissipation times are comparable to f^{-1}, suggesting complete relaxation of increased vibrational energies prior to a subsequent inelastic collision is a plausible source of reduced damage when electron delivery to the specimen is strictly temporally controlled.

Timescales of electron-phonon coupling and lattice thermalization are also worth noting. Electron-phonon coupling in $MAPbI_3$ films occurs on the order of hundreds of femtoseconds, while lattice thermalization takes a few picoseconds.[459] Owing to the electron-pulse duration, most or all will arrive within this time frame. Further, increasing E/P generally causes an increase in pulse duration, thus creating an environment where the likelihood of exacerbating effects contributing to damage is increased.[161] Systematic pulse duration experiments may shed light on such effects. Indeed, similar arguments can be made regarding specimen charging, charge dissipation, and electron-pulse durations and timing.

6.2.3 Preferential Damage of Iodide-Containing Planes

While the results in Section 6.2.1 and 6.2.2 are based on the sum of all Bragg peaks within 5 nm^{-1} of the DP center, analyzing some of these peaks separately provides additional insight. Specifically, it shows how specific planes are damaged differently from one another, and this can be related to the qualities of the electron beam in each experiment. An example of how manipulation of the beam temporal profile affects the damage sustained by $MAPbI_3$ crystals is shown in Figure 6.4. This figure compares damage sustained by planes with varying planar densities of iodide during illumination by a conventional beam (red, red triangles), a pulsed beam with 200 E/P (blue dashed line, blue hollow squares) and a pulsed beam with 400 E/P (blue dotted line, blue solid circles). All beam profiles have the same illuminated area (100 μm^2) and dose rate (0.01 $e\cdot Å^{-2}\cdot s^{-1}$). For all beam profiles, planes with higher densities of iodide sustained greater damage, which is expected based on previous work on damage mechanisms. However, the degree of difference, that is the degree to which planes with more iodide are damaged more than those with less iodide, is greatest for the 400 E/P pulsed profile, and least for the thermionic profile. This can be seen most easily by comparing the slopes in Figure 6.4d.

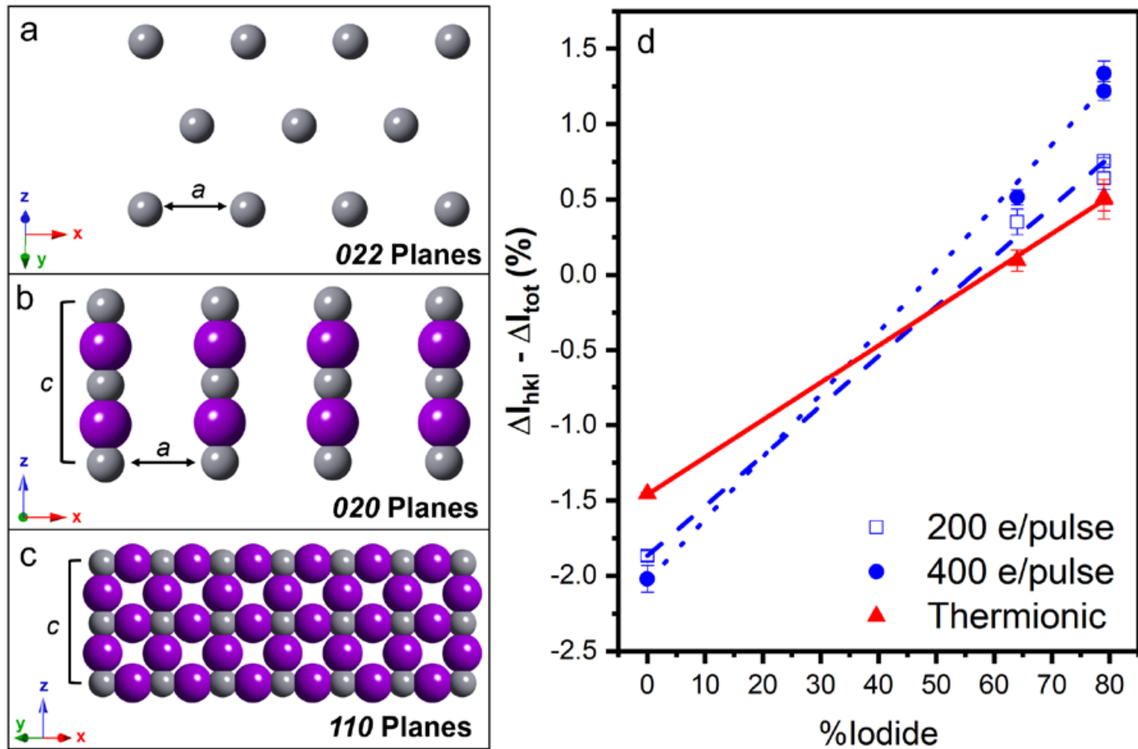

Figure 6.4 | Correlating iodide planar density with damage and beam profile. (a) 0% iodine peak is the 022 family of planes. Iodine is shown in purple and lead in grey. (b) 66% iodine peak is the 020 family of planes. Iodine is shown in purple and lead in grey. (c) 79% iodine peak is the 110 family of planes. Iodine is shown in purple and lead in grey. In (a)-(c), nitrogen, carbon, and hydrogen are not shown in the figure. They are included in the calculation but affect the % iodine value by 2% or less. (d) Comparison of damage caused to planes corresponding to different amounts of iodide by beams with different temporal profiles. Damage is shown in terms of intensity loss compared with the overall specimen; see Section 6.1.3 for more details. Linear fits are added for illustrative purposes, to make slope differences obvious, and are not necessarily phenomenologically correlated to any physical process. Damage caused by thermionic beam shown in red, with a solid line and solid red triangles. Damage caused by 200 E/P pulsed beam shown in blue, with

a dashed line and hollow blue squares. Damage caused by 400 E/P pulsed beam shown in blue, with a dotted line and solid blue circles. Error bars are standard deviation over 2, 2, and 3 independent experiments (for pulsed 200, pulsed 400, and thermionic, respectively).

There are several possible reasons that the iodide-containing planes sustain more damage. One is a general orientational dependence to the damage. As stated above, the perovskite specimens are polycrystalline but consist of large crystallites relative to the size of the overall specimen, meaning that only a small number of crystallites (on the order of tens) are selected in each selected area aperture and therefore represented in each DP. Because of this, a certain orientation in each specimen receiving greater irradiation than any other cannot be ruled out. It has been shown that electron beam damage can have an orientational dependence. In fact, the damage mechanism may even be entirely different depending on the zone axis orientation during irradiation.[460] Therefore, a texturing-like phenomenon, in which certain zone axes are overrepresented in the DPs, is possible and could lead to disparate results for certain planes and certain temporal beam profiles. Further work using specimens with consistent zone axis orientations (either truly random polycrystalline specimens or single-crystalline specimens with a known and constant zone axis) would need to be completed to elucidate the role of orientation.

However, while texturing cannot be ruled out, it is important to note that the results shown in Figure 6.4d represent the average of two to three experiments per data point, in which each experiment was completed on a new polycrystalline $MAPbI_3$ specimen. As can be seen from the error bars, the variation within repetition of experiments is low.

Therefore, it is possible to reason that while the effect of crystallite orientation cannot be detangled from other effects, that the chances each experiment happened to be completed using a specimen that happened to show the same orientational dependence as those used during repetitions, but different from those used during experiments with other temporal profiles, seems unlikely. Therefore, the consistency of the trend and low variability between experimental repetitions leads one to believe there may be some other processes contributing to the trends shown in Figure 6.4d.

In order to hypothesize a source for this other process, we note that the primary difference between the three beam profiles is the instantaneous dose rate at various points in time. In the thermionic case, the instantaneous dose rate is likely to be near the average dose rate, although certainly varying in time due to the stochastic nature of thermionic emission. In the case of the pulsed beam, the instantaneous dose rate during the arrival of the electron pulses is high, offset by a long period (long in comparison with the length of the pulse) in which the instantaneous dose rate is zero. Importantly, the instantaneous dose rate is related to the amount of energy that is deposited within a certain period of time, meaning that assuming the same number of damage-inducing collisions in each case, in the pulsed beam case, many of these collisions are happening within close temporal proximity. This translates to a high amount of energy deposited in the specimen during each pulse in the case of the pulsed beam, to a degree that is not statistically likely in the thermionic case.

Fast deposition of energy into the specimen can be a trigger for ion migration, as has been shown through thermal studies. As stated in Section 5.2, because the deposition of energy is localized near the collision with the incoming electron, thermal energy in this

area can be much higher than a specimen temperature would indicate as phonon populations build up.[237,238,429,434–436] This excess energy can serve to overcome activation barriers for defect formation at a higher rate, as well as allowing for faster diffusion of vacancies and interstitials.[326] Iodide has been shown to be the main diffusing defect, as they have a low formation energy and a low diffusion barrier.[276,321,323] Therefore, it is possible that the high instantaneous dose rate caused by pulsing the beam could accelerate the degradation of iodide-containing planes as vacancies and interstitials form and migrate.

6.2.4 Relationship Between Fading Curve and Beam Temporal Profile

Interestingly, when the results in Figure 6.4 are compared with the total damage sustained to the crystal, it is clear that the beam profiles that cause the most damage are not necessarily those that cause the most disproportionate damage to the iodide-containing planes (Figure 6.5a). That is, there is no strong correlation between preferential destruction of iodide-containing planes and total damage to the crystal. Specifically, the 200 E/P pulsed beam causes less damage to the overall crystal than thermionic beam, but is more disproportionately destructive to iodide-containing planes than the thermionic beam.

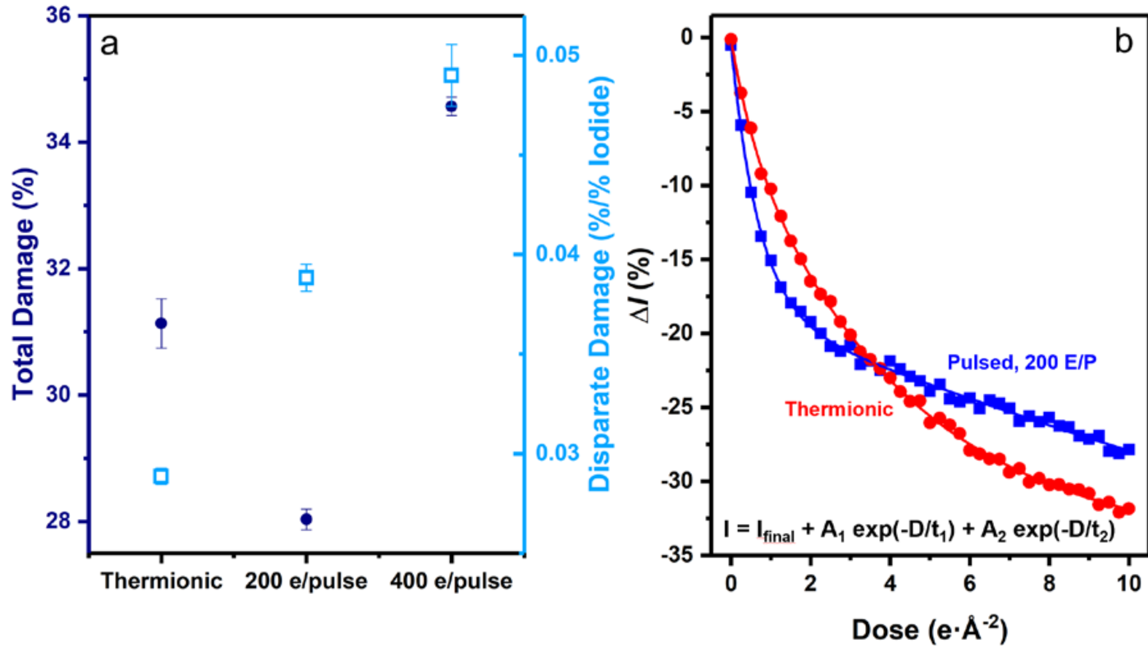

Figure 6.5 | Demonstration of the two-step mechanism in perovskite damage processes. (a) Total damage (dark blue, filled circles) is plotted on the same graph as degree of disparate damage to iodide containing planes (light blue, hollow squares). Note that in this plot, in both cases, the highest degree of damage is at the top of the plot, which is reversed from earlier plots in this chapter. Error bars for total damage are standard deviations over 3, 2, and 2 experiments, respectively. Error bars for disparate damage are standard errors of the linear fit. (b) Fading curve for the *020* plane, damaged using a pulsed 200 E/P beam (blue squares) and a thermionic beam (red circles) both at a dose rate of 0.01 $e \cdot Å^{-2} \cdot s^{-1}$. These plots correspond to experiment numbers T10 and P5. Fits are plotted alongside the data; equation 6.1 was used as the equation of best fit in both cases.

In order to understand this phenomenon, it is instructive to compare the fading curve shapes created by different beam profiles (Figure 6.5b). It is immediately visible

that while the initial damage occurs more quickly in the case of the pulsed beam, the process eventually slows and is overtaken by thermionic fading curve, in which the damage occurs more slowly but results in a greater total degree of damage. In both cases, a double-exponential fit (Equation 6.1) is used to describe the fading curve. See discussion in Section 6.1.3 for more information about the choice of fit equation. In the context of kinetics, a double exponential curve for a reactant typically corresponds with a two-step mechanism in which the first step is reversible. Note that this definition of reversibility is quite different from that used to determine whether a given event can be studied using UEM, discussed in Chapter 1. In this case, it refers to a step in which the forward and reverse reaction are taking place simultaneously, usually at different rates, which typically corresponds with a two-step mechanism. Drawing the analogy to the current system may be instructive. One could treat the initial structure as the reactant which is degrading over time, via two reaction steps which depend on one another, corresponding to two different time constants.

The two time constants vary with respect to one another, depending on beam profile. In the example given in Figure 6.5b, the pulsed beam has a faster initial step and then a slower second step, compared with the thermionic beam. It is necessary, however, to take a more holistic look at the interplay of the two time constants given varying beam conditions. In Figure 6.6, we plot the ratio of the two time constants (t_1/t_2) for each beam temporal profile within the 0.01 $e \cdot Å^{-2} \cdot s^{-1}$ dose rate. This ratio is related to the shape of the curve; when t_1/t_2 is higher, the fading curve looks more like a single exponential and damage increases more gradually (similarly to the red square data in Figure 6.5b), and

when t_1/t_2 is lower, the fading curve falls off more quickly before leveling off (similarly to the blue circle data in Figure 6.5b). In the case of the thermionic beam profile, all four measured sets of Bragg reflections experience similar shapes, and are all more gradual. In both pulsed beam cases, however, there is a significant difference between the damage profiles of the Bragg reflections that represent planes containing iodide and those that represent planes not containing iodide. Again, there is a correlation in the shape of the curve depending on the makeup of the Bragg plane.

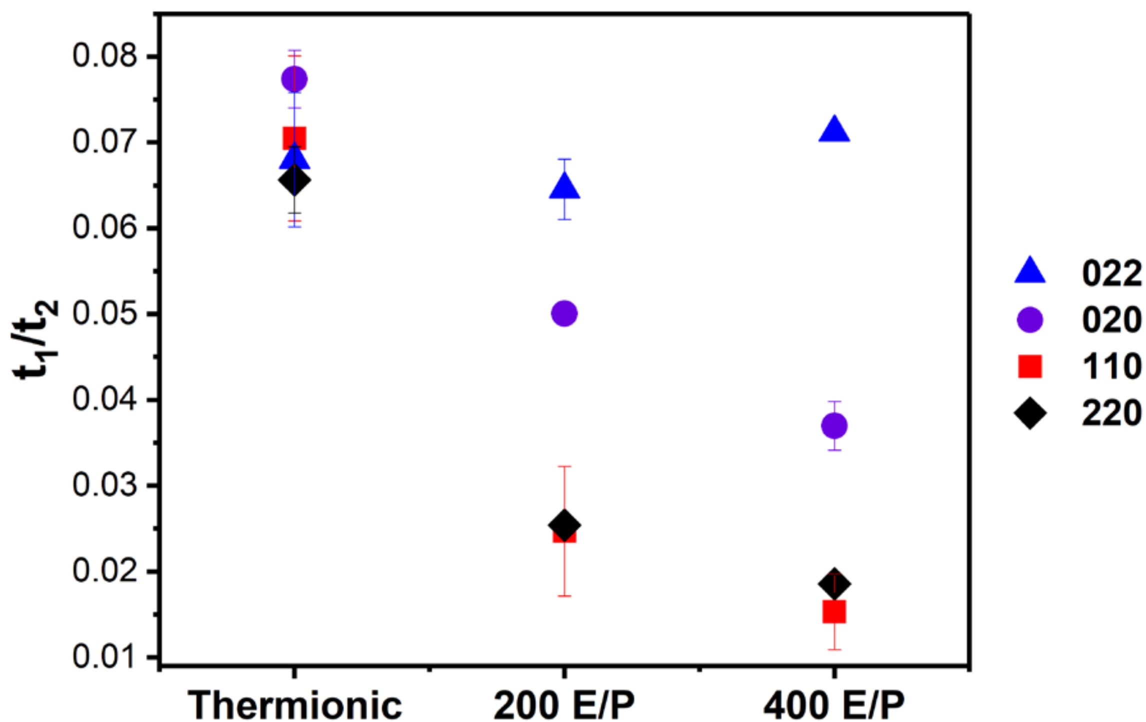

Figure 6.6 | Effect of beam temporal profile on damage time constants. Plotted is the ratio between the first and second time constants (variables described further in Section 6.1.3) for each electron beam temporal profile. Each plane from Figure 6.4 is plotted separately. Error bars are standard deviations over 3, 2, and 2 experiments respectively.

Again, the difference between the effect observed in the thermionic case and the pulsed beam cases is likely to be due to their main difference, the periodic variation in the instantaneous dose rate. However, a thorough explanation of this phenomenon will not be offered here as further experiments are needed. The role of orientational dependence must be elucidated, and a model of the kinetics will be necessary to fully understand the role of each species or step in the damage mechanism. One interesting direction in which to begin is the intertwined role of organic cation migration and iodide migration. There is some

debate in the literature over the respective roles of these two ions in the damage process, and both are likely to be occurring simultaneously.[274,276,277,323,449,461–465] Theoretical calculations suggest methylammonium (MA) fragmentation may produce byproducts which react with iodide ions and facilitate the migration of anions and lead.[277,466–469] If this is indeed the process occurring, there are many potential kinetic pathways and intermediates, making it difficult to identify which species or reaction may be affecting the damage rate profile. The role of hydrogen is also currently unsettled, and the reaction of hydrogen and iodide has been suggested as a pathway for damage as well, in concert with the MA fragmentation described above.[277,470,471] Further experiments, likely combined with theoretical calculations, will be necessary to determine the role of these various processes and the rate-profile-determining steps in the kinetic process of beam damage. Such experiments could include more thoroughly exploring the parameter space of the beam temporal profile, altering the specimen lattice constants to change defect diffusion barriers (e.g., alloying cations or halides or applying strain), or changing the electronic environment and diffusion rates through application of an electric field.[323]

6.3 Summary and Conclusions

In conclusion, for common total doses and dose rates, we have discovered a regime where using a pulsed-beam TEM leads to reduced damage to $MAPbI_3$. The degree of reduction is enhanced by using pulses with fewer electrons, while the duration between pulses appears to have a smaller but still non-trivial effect. We also discover a crossover effect, in which pulsed beams cause more damage than an otherwise identical conventional

beam. This constitutes the first example of these effects for direct-comparison experiments at dose rates commonly used in low-dose TEM. The findings also support the hypothesis that the behavior is material and mechanism dependent owing to differences when compared to other materials systems. In addition, this work shows that certain crystallographic planes are preferentially damaged in the TEM, and that degree of disparate damage is correlated to the temporal profile of the beam and the time frame in which energy is deposited. While this result is not yet conclusive and more experiments are necessary to determine whether this correlation is actually causation, it is the first step towards using pulsed TEM beams for radiation damage kinetic studies. These results have fundamental and practical implications, in that fs-laser-driven pulsed TEM offers a combination of stability and tunability that affords studying specific damage mechanisms and durability of $MAPbI_3$, as well as providing structural, chemical, electronic, and dynamic information from less-damaged specimens.

Chapter 7 | Conclusion & Outlook

To summarize, this thesis presents work on how pulsed electron beams can be used to elucidate materials properties and behavior in three new ways. One of those ways is through ultrafast experiments, where mapping thermal energy and tracking CAP behavior can be used in both directions – to understand how these phenomena interact with known heterogeneities in the specimen, and to learn more about the heterogeneities through their interaction with well-understood transient structural motion. The second way is by reducing the total damage caused to the material, allowing more robust and complete electron microscopy experiments on radiation-sensitive specimens. Pulsing the beam can allow for a lower total damage for a given dose, due to the reversible and nonlinear nature of certain damage mechanisms such as charging and heating. The third way is through the use of a pulsed beam to deliver precise doses of electrons at prescribed times which can elucidate damage mechanisms in new ways.

Each of these projects have interesting and useful outlooks going forward. Since the work shown in Chapter 3, fellow Flannigan group member Ryan Gnabasik has done impressive work on other ways to access specimen temperature at specific locations.(cite thesis) Several group members also continue to work on using UEM and the structural motions observed therein to better understand how specimen morphology, such as interfaces and step edges, affects phonon propagation, even taking it so far as to quantify the energy and resulting strain of these transient waves. This work will undoubtedly extend the usefulness of techniques such as the CAP spectroscopy explored in Chapter 4. The use of pulsed beams to reduce damage, as discussed in Chapter 5, has spurred significant

interest and continued study. Work is under way to incorporate pulsed beams into conventional TEMs specifically for damage reduction, and several funded projects are now exploring the implications of pulsed beams for radiation-sensitive specimens. I look forward to seeing where this interest leads, as there are many open questions left by this preliminary work. Finally, the use of pulsed beams in TEM to explore and better understand damage mechanisms is also relatively new, and continued work by future Flannigan group members as well as others who are working on this could uncover many interesting results.

I am very grateful to have had the chance to work on several relatively disparate projects, as they provided substantial intellectual stimulation and allowed me to connect ideas between subfields in a way I couldn't have done if I was focused entirely on one project. I look forward to seeing where this work, and the UEM/pulsed TEM field in general, goes over the next years and decades, as the potential is enormous and largely unexplored due to its novelty. I feel honored to have had access to such a unique research area and to have contributed to the accumulation of knowledge in the basic energy sciences.

Bibliography

(1) Stoumpos, C. C.; Malliakas, C. D.; Kanatzidis, M. G. Semiconducting Tin and Lead Iodide Perovskites with Organic Cations: Phase Transitions, High Mobilities, and Near-Infrared Photoluminescent Properties. *Inorg. Chem.* **2013**, *52* (15), 9019–9038.

(2) Yamada, Y.; Yamada, T.; Phuong, L. Q.; Maruyama, N.; Nishimura, H.; Wakamiya, A.; Murata, Y.; Kanemitsu, Y. Dynamic Optical Properties of $CH_3NH_3PbI_3$ Single Crystals As Revealed by One- and Two-Photon Excited Photoluminescence Measurements. *J. Am. Chem. Soc.* **2015**, *137* (33), 10456–10459.

(3) Knoll, M.; Ruska, E. Beitrag zur geometrischen Elektronenoptik. I. *Ann. Phys.* **1932**, *404* (5), 607–640.

(4) Haguenau, F.; Hawkes, P. W.; Hutchison, J. L.; Satiat–Jeunemaître, B.; Simon, G. T.; Williams, D. B. Key Events in the History of Electron Microscopy. *Microsc. Microanal.* **2003**, *9* (2), 96–138.

(5) Heidenreich, R. D. Electron Microscope and Diffraction Study of Metal Crystal Textures by Means of Thin Sections. *J. Appl. Phys.* **1949**, *20* (10), 993–1010.

(6) van Landuyt, J.; Gevers, R.; Amelinckx, S. On the Determination of the Nature of Stacking Faults in F.C.C. Metals from the Bright Field Image. *Phys. Status Solidi B* **1966**, *18* (1), 167–172.

(7) Gevers, R.; van Landuyt, J.; Amelinckx, S. The Fine Structure of Spots in Electron Diffraction Resulting from the Presence of Planar Interfaces and Dislocations. *Phys. Status Solidi B* **1966**, *18* (1), 343–361.

(8) Hirsch, P. B.; Howie, A.; Whelan, M. J. A Kinematical Theory of Diffraction Contrast of Electron Transmission Microscope Images of Dislocations and Other Defects. *Philos. Trans. R. Soc. Math. Phys. Eng. Sci.* **1960**, *252* (1017), 499–529.

(9) Geil, P. H. Nylon Single Crystals. *J. Polym. Sci.* **1960**, *44* (144), 449–458.

(10) Petermann, J.; Gleiter, H. Direct Observation of Amorphous and Crystalline Regions in Polymers by Defocus Imaging. *Philos. Mag. J. Theor. Exp. Appl. Phys.* **1975**, *31* (4), 929–934.

(11) Greis, O.; Xu, Y.; Asano, T.; Petermann, J. Morphology and Structure of Syndiotactic Polystyrene. *Polymer* **1989**, *30* (4), 590–594.

(12) Geiss, R. H.; Street, G. B.; Volksen, W.; Economy, J. Polymer Structure Determination Using Electron Diffraction Techniques. *IBM J. Res. Dev.* **1983**, *27* (4), 321–329.

(13) Bernhard, W.; Haguenau, F.; Oberling, Ch. L'ultra-Structure du Nucléole de Quelques Cellules Animales, Révélée par le Microscope Electronique. *Experientia* **1952**, *8* (2), 58–59.

(14) Dalton, A. J. Observations of the Golgi Substance with the Electron Microscope. *Nature* **1951**, *168* (4267), 244–245.

(15) Monneron, A.; Bernhard, W. Fine Structural Organization of the Interphase Nucleus in Some Mammalian Cells. *J. Ultrastruct. Res.* **1969**, *27* (3–4), 266–288.

(16) Palade, G. E. The Fine Structure of Mitochondria. *Anat. Rec.* **1952**, *114* (3), 427–451.

(17) Porter, K. R.; Claude, A.; Fullam, E. F. A Study of Tissue Culture Cells by Electron Microscopy. *J. Exp. Med.* **1945**, *81* (3), 233–246.

(18) Ruthemann, G. Diskrete Energieverluste mittelschneller Elektronen beim Durchgang durch dünne Folien. *Ann. Phys.* **1948**, *437* (3–4), 113–134.

(19) Hillier, J.; Baker, R. F. Microanalysis by Means of Electrons. *J. Appl. Phys.* **1944**, *15* (9), 663–675.

(20) Egerton, R. F.; Whelan, M. J. The Electron Energy Loss Spectrum and Band Structure of Diamond. *Philos. Mag. J. Theor. Exp. Appl. Phys.* **1974**, *30* (4), 739–749.

(21) Porter, D. A.; Edington, J. W.; Raynor, G. V. Microanalysis and Cell Boundary Velocity Measurements for the Cellular Reaction in a Mg-9% Al Alloy. *Proc. R. Soc. Lond. Math. Phys. Sci.* **1978**, *358* (1694), 335–350.

(22) Li, C.; Song, D.; Li, M.; Tang, C.; Xue, D.; Wan, D.; Pennycook, S. J. Atomic Scale Characterization of Point and Extended Defects in Niobate Thin Films. *Ultramicroscopy* **2019**, *203*, 82–87.

(23) Zuo, J.-M.; Shao, Y.-T. Scanning Convergent Beam Electron Diffraction (CBED), the Essential Questions of Why, What and How? *Microsc. Microanal.* **2018**, *24* (S1), 172–173.

(24) Krivanek, O. L.; Dellby, N.; Hachtel, J. A.; Idrobo, J.-C.; Hotz, M. T.; Plotkin-Swing, B.; Bacon, N. J.; Bleloch, A. L.; Corbin, G. J.; Hoffman, M. V.; Meyer, C. E.; Lovejoy, T. C. Progress in Ultrahigh Energy Resolution EELS. *Ultramicroscopy* **2019**, *203*, 60–67.

(25) Yang, J.; Zeng, Z.; Kang, J.; Betzler, S.; Czarnik, C.; Zhang, X.; Ophus, C.; Yu, C.; Bustillo, K.; Pan, M.; Qiu, J.; Wang, L.-W.; Zheng, H. Formation of Two-Dimensional Transition Metal Oxide Nanosheets with Nanoparticles as Intermediates. *Nat. Mater.* **2019**, *18* (9), 970–976.

(26) Cremons, D. R.; Du, D. X.; Flannigan, D. J. Picosecond Phase-Velocity Dispersion of Hypersonic Phonons Imaged with Ultrafast Electron Microscopy. *Phys. Rev. Mater.* **2017**, *1* (7), 073801.

(27) Urban, K. W. The New Paradigm of Transmission Electron Microscopy. *MRS Bull.* **2007**, *32* (11), 946–952.

(28) Williams, D. B.; Carter, C. B. *Transmission Electron Microscopy: A Textbook for Materials Science*, 2nd ed.; Springer: Boston MA, 2009.

(29) Scherzer, O. Über Einige Fehler von Elektronenlinsen. *Z. Für Phys.* **1936**, *101* (9–10), 593–603.

(30) Batson, P. E.; Dellby, N.; Krivanek, O. L. Sub-Ångstrom Resolution Using Aberration Corrected Electron Optics. *Nature* **2002**, *418* (6898), 617–620.

(31) Hetherington, C. Aberration Correction for TEM. *Mater. Today* **2004**, *7* (12), 50–55.

(32) Scherzer, O. Spharische Und Chromatische Korrektur von Elektronen-Linsen. *Optik* **1947**, *2*, 114–132.

(33) Scherzer, O. The Theoretical Resolution Limit of the Electron Microscope. *J. Appl. Phys.* **1949**, *20* (1), 20–29.

(34) Koops, H.; Kuck, G.; Scherzer, O. Test of an Electron-Optical Achromator. *Optik* **1977**, *48* (2), 225–236.

(35) Hely, H. Messungen an Einem Verbesserten Korrigierten Elektronenmikroskop. **1982**.

(36) Rose, H. Aplanatic Electron-Lenses. *Optik* **1971**, *34* (3), 285-.

(37) Haider, M.; Rose, H.; Uhlemann, S.; Schwan, E.; Kabius, B.; Urban, K. A Spherical-Aberration-Corrected 200kV Transmission Electron Microscope. *Ultramicroscopy* **1998**, *75* (1), 53–60.

(38) Bleloch, A.; Lupini, A. Imaging at the Picoscale. *Mater. Today* **2004**, *7* (12), 42–48.

(39) Lentzen, M. Progress in Aberration-Corrected High-Resolution Transmission Electron Microscopy Using Hardware Aberration Correction. *Microsc. Microanal.* **2006**, *12* (03), 191–205.

(40) Smith, D. J. Development of Aberration-Corrected Electron Microscopy. *Microsc. Microanal.* **2008**, *14* (1), 2–15.

(41) Rose, H. Prospects for Aberration-Free Electron Microscopy. *Ultramicroscopy* **2005**, *103* (1), 1–6.

(42) Ercius, P.; Boese, M.; Duden, T.; Dahmen, U. Operation of TEAM I in a User Environment at NCEM. *Microsc. Microanal.* **2012**, *18* (4), 676–683.

(43) Kisielowski, C.; Freitag, B.; Bischoff, M.; van Lin, H.; Lazar, S.; Knippels, G.; Tiemeijer, P.; van der Stam, M.; von Harrach, S.; Stekelenburg, M.; Haider, M.; Uhlemann, S.; Müller, H.; Hartel, P.; Kabius, B.; Miller, D.; Petrov, I.; Olson, E. A.; Donchev, T.; Kenik, E. A.; Lupini, A. R.; Bentley, J.; Pennycook, S. J.; Anderson, I. M.; Minor, A. M.; Schmid, A. K.; Duden, T.; Radmilovic, V.; Ramasse, Q. M.; Watanabe, M.; Erni, R.; Stach, E. A.; Denes, P.; Dahmen, U. Detection of Single Atoms and Buried Defects in Three Dimensions by Aberration-Corrected Electron Microscope with 0.5-Å Information Limit. *Microsc. Microanal.* **2008**, *14* (5), 469–477.

(44) Lentzen, M.; Jahnen, B.; Jia, C. L.; Thust, A.; Tillmann, K.; Urban, K. High-Resolution Imaging with an Aberration-Corrected Transmission Electron Microscope. *Ultramicroscopy* **2002**, *92* (3–4), 233–242.

(45) Hutchison, J. L.; Titchmarsh, J. M.; Cockayne, D. J. H.; Doole, R. C.; Hetherington, C. J. D.; Kirkland, A. I.; Sawada, H. A Versatile Double Aberration-Corrected, Energy Filtered HREM/STEM for Materials Science. *Ultramicroscopy* **2005**, *103* (1), 7–15.

(46) Suri, P. K.; Yan, J.; Mandrus, D. G.; Flannigan, D. J. Dynamical Scattering and Electron Channeling in Orthorhombic and Tetragonal LaFeAsO. *J. Phys. Chem. C* **2016**, *120* (33), 18931–18938.

(47) Gage, T. E.; Dulal, P.; Solheid, P. A.; Flannigan, D. J.; Stadler, B. J. H. Si-Integrated Ultrathin Films of Phase-Pure $Y_3Fe_5O_{12}$ (YIG) via Novel Two-Step Rapid Thermal Anneal. *Mater. Res. Lett.* **2017**, *5* (6), 379–385.

(48) Krivanek, O. L.; Dellby, N.; Lupini, A. R. Towards Sub-Å Electron Beams. *Ultramicroscopy* **1999**, *78*, 1–11.

(49) Rose, H. H. Future Trends in Aberration-Corrected Electron Microscopy. *Philos. Trans. R. Soc. Math. Phys. Eng. Sci.* **2009**, *367* (1903), 3809–3823.

(50) Jia, C.-L.; Lentzen, M.; Urban, K. High-Resolution Transmission Electron Microscopy Using Negative Spherical Aberration. *Microsc. Microanal.* **2004**, *10* (02), 174–184.

(51) Jiang, Y.; Chen, Z.; Han, Y.; Deb, P.; Gao, H.; Xie, S.; Purohit, P.; Tate, M. W.; Park, J.; Gruner, S. M.; Elser, V.; Muller, D. A. Electron Ptychography of 2D Materials to Deep Sub-Ångström Resolution. *Nature* **2018**, *559* (7714), 343–349.

(52) Ricolleau, C.; Nelayah, J.; Oikawa, T.; Kohno, Y.; Braidy, N.; Wang, G.; Hue, F.; Florea, L.; Pierron Bohnes, V.; Alloyeau, D. Performances of an 80–200kV Microscope Employing a Cold-FEG and an Aberration-Corrected Objective Lens. *Microscopy* **2013**, *62* (2), 283–293.

(53) Benner, G.; Matijevic, M.; Orchowski, A.; Schindler, B.; Haider, M.; Hartel, P. State of the First Aberration-Corrected, Monochromized 200kV FEG-TEM. *Microsc. Microanal.* **2003**, *9* (S03), 38–39.

(54) Thrauchi, M.; Kuzuo, R.; Satoh, F.; Thnaka, M.; Tsuno, K.; Ohyama, J. Performance of a New High-Resolution Electron Energy-Loss Spectroscopy Microscope. *Microsc. Microanal. Microstruct.* **1991**, *2* (2–3), 351–358.

(55) Tsuno, K. Monochromators in Electron Microscopy. *Nucl. Instrum. Methods Phys. Res. Sect. Accel. Spectrometers Detect. Assoc. Equip.* **2011**, *645* (1), 12–19.

(56) Mook, H. W.; Kruit, P. Construction and Characterization of the Fringe Field Monochromator for a Field Emission Gun. *Ultramicroscopy* **2000**, *81* (3), 129–139.

(57) Krivanek, O. L.; Lovejoy, T. C.; Dellby, N.; Aoki, T.; Carpenter, R. W.; Rez, P.; Soignard, E.; Zhu, J.; Batson, P. E.; Lagos, M. J.; Egerton, R. F.; Crozier, P. A. Vibrational Spectroscopy in the Electron Microscope. *Nature* **2014**, *514* (7521), 209–212.

(58) Kimoto, K. Practical Aspects of Monochromators Developed for Transmission Electron Microscopy. *Microscopy* **2014**, *63* (5), 337–344.

(59) Tiemeijer, P. C.; Bischoff, M.; Freitag, B.; Kisielowski, C. Using a Monochromator to Improve the Resolution in TEM to below 0.5Å. Part I: Creating Highly Coherent Monochromated Illumination. *Ultramicroscopy* **2012**, *114*, 72–81.

(60) Tiemeijer, P. C. Section 5: Analytical Electron Microscopy-Operation Modes of a TEM Monochromator. In *Institute of Physics Conference Series*; Adam Hilger, Ltd.: Bristol, England, 1999; Vol. 161, pp 191–194.

(61) Mukai, M.; Kim, J. S.; Omoto, K.; Sawada, H.; Kimura, A.; Ikeda, A.; Zhou, J.; Kaneyama, T.; Young, N. P.; Warner, J. H.; Nellist, P. D.; Kirkland, A. I. The

Development of a 200kV Monochromated Field Emission Electron Source. *Ultramicroscopy* **2014**, *140*, 37–43.

(62) Rose, H. Prospects for Realizing a Sub-Å Sub-EV Resolution EFTEM. *Ultramicroscopy* **1999**, *78* (1), 13–25.

(63) Essers, E.; Benner, G.; Mandler, T.; Meyer, S.; Mittmann, D.; Schnell, M.; Höschen, R. Energy Resolution of an Omega-Type Monochromator and Imaging Properties of the MANDOLINE Filter. *Ultramicroscopy* **2010**, *110* (8), 971–980.

(64) Krivanek, O. L.; Lovejoy, T. C.; Dellby, N.; Carpenter, R. W. Monochromated STEM with a 30 MeV-Wide, Atom-Sized Electron Probe. *Microscopy* **2013**, *62* (1), 3–21.

(65) Krivanek, O. L.; Ursin, J. P.; Bacon, N. J.; Corbin, G. J.; Dellby, N.; Hrncirik, P.; Murfitt, M. F.; Own, C. S.; Szilagyi, Z. S. High-Energy-Resolution Monochromator for Aberration-Corrected Scanning Transmission Electron Microscopy/Electron Energy-Loss Spectroscopy. *Philos. Trans. R. Soc. Math. Phys. Eng. Sci.* **2009**, *367* (1903), 3683–3697.

(66) Nellist, P. D. Direct Sub-Angstrom Imaging of a Crystal Lattice. *Science* **2004**, *305* (5691), 1741.

(67) Krivanek, O. L.; Bleloch, A. L.; Dellby, N.; Lovejoy, T. C.; Shi, C.; Zhou, W. Improving the STEM Spatial Resolution Limit. *Microsc. Microanal.* **2018**, *24* (S1), 18–19.

(68) Egerton, R. F. *Electron Energy-Loss Spectroscopy in the Electron Microscope*; Springer Science & Business Media, 2011.

(69) Egerton, R. F. Electron Energy-Loss Spectroscopy in the TEM. *Rep. Prog. Phys.* **2009**, *72* (1), 016502.

(70) Kimoto, K.; Kothleitner, G.; Grogger, W.; Matsui, Y.; Hofer, F. Advantages of a Monochromator for Bandgap Measurements Using Electron Energy-Loss Spectroscopy. *Micron* **2005**, *36* (2), 185–189.

(71) Chen, S.-Y.; Gloter, A.; Zobelli, A.; Wang, L.; Chen, C.-H.; Colliex, C. Electron Energy Loss Spectroscopy and Ab Initio Investigation of Iron Oxide Nanomaterials Grown by a Hydrothermal Process. *Phys. Rev. B* **2009**, *79* (10), 104103.

(72) Hirsch, P. B. Direct Observations of Dislocations by Transmission Electron Microscopy: Recollections of the Period 1946-56. *Proc. R. Soc. Lond. Math. Phys. Sci.* **1980**, *371* (1744), 160–164.

(73) Hirsch, P. B.; Horne, R. W.; Whelan, M. J. Direct Observations of the Arrangement and Motion of Dislocations in Aluminium. *Philos. Mag.* **1956**, *1* (7), 677–684.

(74) Sinclair, R. Studies of Material Reactions by *In Situ* High-Resolution Electron Microscopy. *MRS Bull.* **1994**, *19* (6), 26–31.

(75) Marks, L. D.; Warren, O. L.; Minor, A. M.; Merkle, A. P. Tribology in Full View. *MRS Bull.* **2008**, *33* (12), 1168–1173.

(76) Minor, A. M.; Lilleodden, E. T.; Stach, E. A.; Morris, J. W. Direct Observations of Incipient Plasticity during Nanoindentation of Al. *J. Mater. Res.* **2004**, *19* (1), 176–182.

(77) Oh, S. H.; Legros, M.; Kiener, D.; Dehm, G. *In Situ* Observation of Dislocation Nucleation and Escape in a Submicrometre Aluminium Single Crystal. *Nat. Mater.* **2009**, *8* (2), 95–100.

(78) Wall, M. A.; Dahmen, U. An *In Situ* Nanoindentation Specimen Holder for a High Voltage Transmission Electron Microscope. *Microsc. Res. Tech.* **1998**, *42* (4), 248–254.

(79) Shan, Z. W.; Mishra, R. K.; Syed Asif, S. A.; Warren, O. L.; Minor, A. M. Mechanical Annealing and Source-Limited Deformation in Submicrometre-Diameter Ni Crystals. *Nat. Mater.* **2008**, *7* (2), 115–119.

(80) Demczyk, B. G.; Wang, Y. M.; Cumings, J.; Hetman, M.; Han, W.; Zettl, A.; Ritchie, R. O. Direct Mechanical Measurement of the Tensile Strength and Elastic Modulus of Multiwalled Carbon Nanotubes. *Mater. Sci. Eng. A* **2002**, 6.

(81) Legros, M.; Gianola, D. S.; Hemker, K. J. *In Situ* TEM Observations of Fast Grain-Boundary Motion in Stressed Nanocrystalline Aluminum Films. *Acta Mater.* **2008**, *56* (14), 3380–3393.

(82) Tanase, M.; Petford-Long, A. K. *In Situ* TEM Observation of Magnetic Materials. *Microsc. Res. Tech.* **2009**, *72* (3), 187–196.

(83) Tan, X.; Xu, Z.; Shang, J. K. *In Situ* Transmission Electron Microscopy Observations of Electric-Field-Induced Domain Switching and Microcracking in Ferroelectric Ceramics. *Mater. Sci. Eng. A* **2001**, *314* (1–2), 157–161.

(84) Allard, L. F.; Overbury, S. H.; Bigelow, W. C.; Katz, M. B.; Nackashi, D. P.; Damiano, J. Novel MEMS-Based Gas-Cell/Heating Specimen Holder Provides Advanced Imaging Capabilities for *In Situ* Reaction Studies. *Microsc. Microanal.* **2012**, *18* (4), 656–666.

(85) Zink, N.; Therese, H. A.; Pansiot, J.; Yella, A.; Banhart, F.; Tremel, W. *In Situ* Heating TEM Study of Onion-like WS_2 and MoS_2 Nanostructures Obtained via MOCVD. *Chem. Mater.* **2008**, *20* (1), 65–71.

(86) Rankin, J.; Sheldon, B. W. *In Situ* TEM Sintering of Nano-Sized ZrO_2 Particles. *Mater. Sci. Eng. A* **1995**, *204* (1–2), 48–53.

(87) Kröger, A.; Dziaszyk, S.; Frenzel, J.; Somsen, Ch.; Dlouhy, A.; Eggeler, G. Direct Transmission Electron Microscopy Observations of Martensitic Transformations in Ni-Rich NiTi Single Crystals during in Situ Cooling and Straining. *Mater. Sci. Eng. A* **2008**, *481–482*, 452–456.

(88) De Graef, M. *Introduction to Conventional Transmission Electron Microscopy*; Cambridge University Press, 2003.

(89) Zhang, Z.; Su, D. Behaviour of TEM Metal Grids during In-Situ Heating Experiments. *Ultramicroscopy* **2009**, *109* (6), 766–774.

(90) Miller, B. K.; Crozier, P. A. System for *In Situ* UV-Visible Illumination of Environmental Transmission Electron Microscopy Samples. *Microsc. Microanal.* **2013**, *19* (2), 461–469.

(91) Cavalca, F.; Laursen, A. B.; Kardynal, B. E.; Dunin-Borkowski, R. E.; Dahl, S.; Wagner, J. B.; Hansen, T. W. *In Situ* Transmission Electron Microscopy of Light-Induced Photocatalytic Reactions. *Nanotechnology* **2012**, *23* (7), 075705.

(92) Hauwiller, M. R.; Ondry, J. C.; Chan, C. M.; Khandekar, P.; Yu, J.; Alivisatos, A. P. Gold Nanocrystal Etching as a Means of Probing the Dynamic Chemical Environment in Graphene Liquid Cell Electron Microscopy. *J. Am. Chem. Soc.* **2019**, *141* (10), 4428–4437.

(93) Crozier, P. A.; Wang, R.; Sharma, R. *In Situ* Environmental TEM Studies of Dynamic Changes in Cerium-Based Oxides Nanoparticles during Redox Processes. *Ultramicroscopy* **2008**, *108* (11), 1432–1440.

(94) Creemer, J. F.; Helveg, S.; Hoveling, G. H.; Ullmann, S.; Molenbroek, A. M.; Sarro, P. M.; Zandbergen, H. W. Atomic-Scale Electron Microscopy at Ambient Pressure. *Ultramicroscopy* **2008**, *108* (9), 993–998.

(95) Kraus, T.; de Jonge, N. Dendritic Gold Nanowire Growth Observed in Liquid with Transmission Electron Microscopy. *Langmuir* **2013**, *29* (26), 8427–8432.

(96) Wang, M.; Dissanayake, T. U.; Park, C.; Woehl, T. J. Spatially Mapping Heterogeneous Nucleation Kinetics of Silver Nanocrystals with Liquid Cell Scanning Transmission Electron Microscopy. *Microsc. Microanal.* **2019**, *25* (S2), 1422–1423.

(97) Shimada, Y.; Yoshida, K.; Inoue, K.; Shiraishi, T.; Kiguchi, T.; Nagai, Y.; Konno, T. J. Evaluation of Spatial and Temporal Resolution on in Situ Annealing Aberration-Corrected Transmission Electron Microscopy with Proportional–Integral–Differential Controller. *Microscopy* **2019**, *68* (3), 271–278.

(98) Battaglia, M.; Contarato, D.; Denes, P.; Doering, D.; Duden, T.; Krieger, B.; Giubilato, P.; Gnani, D.; Radmilovic, V. Characterisation of a CMOS Active Pixel Sensor for Use in the TEAM Microscope. *Nucl. Instrum. Methods Phys. Res. Sect. Accel. Spectrometers Detect. Assoc. Equip.* **2010**, *622* (3), 669–677.

(99) Periwal, P.; Thomsen, J. D.; Reuter, M. C.; Zakharov, D.; Gignac, L.; Booth, T. J.; Hofmann, S.; Ross, F. M. *In Situ* TEM Approaches to Controlling the Growth of Semiconductors on 2D Materials. *Microsc. Microanal.* **2019**, *25* (S2), 1424–1425.

(100) He, K.; Zhang, S.; Li, J.; Yu, X.; Meng, Q.; Zhu, Y.; Hu, E.; Sun, K.; Yun, H.; Yang, X.-Q.; Zhu, Y.; Gan, H.; Mo, Y.; Stach, E. A.; Murray, C. B.; Su, D. Visualizing Non-Equilibrium Lithiation of Spinel Oxide via *In Situ* Transmission Electron Microscopy. *Nat. Commun.* **2016**, *7* (1), 11441.

(101) Zhang, P.; Borgnia, M. J.; Mooney, P.; Shi, D.; Pan, M.; O'Herron, P.; Mao, A.; Brogan, D.; Milne, J. L.; Subramaniam, S. Automated Image Acquisition and Processing Using a New Generation of 4K× 4K CCD Cameras for Cryo Electron Microscopic Studies of Macromolecular Assemblies. *J. Struct. Biol.* **2003**, *143* (2), 135–144.

(102) Faruqi, A. R.; Subramaniam, S. CCD Detectors in High-Resolution Biological Electron Microscopy. *Q. Rev. Biophys.* **2000**, *33* (1), 1–27.

(103) Taheri, M. L.; Stach, E. A.; Arslan, I.; Crozier, P. A.; Kabius, B. C.; LaGrange, T.; Minor, A. M.; Takeda, S.; Tanase, M.; Wagner, J. B.; Sharma, R. Current Status and Future Directions for in Situ Transmission Electron Microscopy. *Ultramicroscopy* **2016**, *170*, 86–95.

(104) Ruskin, R. S.; Yu, Z.; Grigorieff, N. Quantitative Characterization of Electron Detectors for Transmission Electron Microscopy. *J. Struct. Biol.* **2013**, *184* (3), 385–393.

(105) Faruqi, A. R.; Henderson, R. Electronic Detectors for Electron Microscopy. *Curr. Opin. Struct. Biol.* **2007**, *17* (5), 549–555.

(106) McMullan, G.; Faruqi, A. R.; Henderson, R. Direct Electron Detectors. *Methods Enzymol.* **2016**, *579*, 1–17.

(107) Tate, M. W.; Purohit, P.; Chamberlain, D.; Nguyen, K. X.; Hovden, R.; Chang, C. S.; Deb, P.; Turgut, E.; Heron, J. T.; Schlom, D. G.; Ralph, D. C.; Fuchs, G. D.;

Shanks, K. S.; Philipp, H. T.; Muller, D. A.; Gruner, S. M. High Dynamic Range Pixel Array Detector for Scanning Transmission Electron Microscopy. *Microsc. Microanal.* **2016**, *22* (1), 237–249.

(108) Browning, N. D.; Campbell, G. H.; Evans, J. E.; LaGrange, T. B.; Reed, B. W. Electron Microscopy and Spectroscopy on the Ultrafast Timescale. *ChemPhysChem* **2010**, *11* (4), 781–782.

(109) LaGrange, T.; Campbell, G. H.; Reed, B. W.; Taheri, M.; Pesavento, J. B.; Kim, J. S.; Browning, N. D. Nanosecond Time-Resolved Investigations Using the *In Situ* of Dynamic Transmission Electron Microscope (DTEM). *Ultramicroscopy* **2008**, *108* (11), 1441–1449.

(110) King, W. E.; Campbell, G. H.; Frank, A.; Reed, B.; Schmerge, J. F.; Siwick, B. J.; Stuart, B. C.; Weber, P. M. Ultrafast Electron Microscopy in Materials Science, Biology, and Chemistry. *J Appl Phys* **2005**, *97*, 111101.

(111) LaGrange, T.; Campbell, G. H.; Colvin, J. D.; Reed, B.; King, W. E. Nanosecond Time Resolved Electron Diffraction Studies of the A→β in Pure Ti Thin Films Using the Dynamic Transmission Electron Microscope (DTEM). *J. Mater. Sci.* **2006**, *41* (14), 4440–4444.

(112) Lagrange, T.; Campbell, G.; Turchi, P.; King, W. Rapid Phase Transformation Kinetics on a Nanoscale: Studies of the A→β Transformation in Pure, Nanocrystalline Ti Using the Nanosecond Dynamic Transmission Electron Microscope. *Acta Mater.* **2007**, *55* (15), 5211–5224.

(113) Bostanjoglo, O.; Rosin, T. Ultrasonically Induced Magnetic Reversals Observed by Stroboscopic Electron Microscopy. *Opt. Acta Int. J. Opt.* **1977**, *24* (6), 657–664.

(114) Bostanjoglo, O.; Rosin, Th. Resonance Oscillations of Magnetic Domain Walls and Bloch Lines Observed by Stroboscopic Electron Microscopy. *Phys. Status Solidi A* **1980**, *57* (2), 561–568.

(115) Spivak, G. V.; Pavlyuchenko, O. P.; Petrov, V. I. Electron Microscopic Observation of Alterations of the Domain Structure of Magnetic Films. *Bull. Acad. Sci. USSR Phys. Ser.* **1966**, *30*, 822–826.

(116) McKenna, A. J.; Eliason, J. K.; Flannigan, D. J. Spatiotemporal Evolution of Coherent Elastic Strain Waves in a Single MoS_2 Flake. *Nano Lett.* **2017**, *17* (6), 3952–3958.

(117) Kim, J. S.; LaGrange, T.; Reed, B. W.; Taheri, M. L.; Armstrong, M. R.; King, W. E.; Browning, N. D.; Campbell, G. H. Imaging of Transient Structures Using Nanosecond *In Situ* TEM. *Science* **2008**, *321* (5895), 1472–1475.

(118) Tao, Z.; Han, T.-R. T.; Ruan, C.-Y. Anisotropic Electron-Phonon Coupling Investigated by Ultrafast Electron Crystallography: Three-Temperature Model. *Phys. Rev. B* **2013**, *87* (23), 235124.

(119) Mannebach, E. M.; Li, R.; Duerloo, K.-A.; Nyby, C.; Zalden, P.; Vecchione, T.; Ernst, F.; Reid, A. H.; Chase, T.; Shen, X.; Weathersby, S.; Hast, C.; Hettel, R.; Coffee, R.; Hartmann, N.; Fry, A. R.; Yu, Y.; Cao, L.; Heinz, T. F.; Reed, E. J.; Dürr, H. A.; Wang, X.; Lindenberg, A. M. Dynamic Structural Response and Deformations of Monolayer MoS_2 Visualized by Femtosecond Electron Diffraction. *Nano Lett.* **2015**, *15* (10), 6889–6895.

(120) Kwon, O.-H.; Barwick, B.; Park, H. S.; Baskin, J. S.; Zewail, A. H. Nanoscale Mechanical Drumming Visualized by 4D Electron Microscopy. *Nano Lett.* **2008**, *8* (11), 3557–3562.

(121) Valley, D. T.; Ferry, V. E.; Flannigan, D. J. Imaging Intra- and Interparticle Acousto-Plasmonic Vibrational Dynamics with Ultrafast Electron Microscopy. *Nano Lett.* **2016**, *16* (11), 7302–7308.

(122) Minor, A. M.; Syed Asif, S. A.; Shan, Z.; Stach, E. A.; Cyrankowski, E.; Wyrobek, T. J.; Warren, O. L. A New View of the Onset of Plasticity during the Nanoindentation of Aluminium. *Nat. Mater.* **2006**, *5* (9), 697–702.

(123) Edgerton, H. E. Edgerton Digital Collections Project https://mitmuseum.mit.edu/collection/edgerton-digital-collections-project-website (accessed 2021 -06 -28).

(124) Edgerton, H. E. Shock Wave Photography of Large Subjects in Daylight. *Rev. Sci. Instrum.* **1958**, *29* (2), 171–172.

(125) Edgerton, H. E. Silhouette Photography of Small Active Subjects. *J. Microsc.* **1977**, *110* (1), 79–81.

(126) Edgerton, H. E. Double-Flash Microsecond Silhouette Photography. *Rev. Sci. Instrum.* **1952**, *23* (10), 532–533.

(127) Edgerton, H. E.; Germeshausen, J. K.; Grier, H. E. High Speed Photographic Methods of Measurement. *J. Appl. Phys.* **1937**, *8* (1), 2–9.

(128) Petrov, V. I.; Spivak, G. V. On a Stroboscopic Lorentz Microscopy. *Z. Angew. Phys.* **1969**, *27* (3), 188–190.

(129) Bostanjoglo, O.; Kornitzky, J.; Tornow, R. P. Nanosecond Double-Frame Electron Microscopy of Fast Phase Transitions. *J. Phys. [E]* **1989**, *22* (12), 1008–1011.

(130) Bostanjoglo, O.; Niedrig, R.; Wedel, B. Ablation of Metal Films by Picosecond Laser Pulses Imaged with High-speed Electron Microscopy. *J. Appl. Phys.* **1994**, *76* (5), 3045–3048.

(131) Bostanjoglo, O.; Nink, T. Hydrodynamic Instabilities in Laser Pulse-produced Melts of Metal Films. *J. Appl. Phys.* **1996**, *79* (11), 8725–8729.

(132) Bostanjoglo, O.; Nink, T. Liquid Motion in Laser Pulsed Al, Co and Au Films. *Appl. Surf. Sci.* **1997**, *109–110*, 101–105.

(133) Nink, T.; Mao, Z. L.; Bostanjoglo, O. Melt Instability and Crystallization in Thin Amorphous Ni–P Films. *Appl. Surf. Sci.* **2000**, *154–155*, 140–145.

(134) Balandin, V. Yu.; Otte, D.; Bostanjoglo, O. Thermocapillary Flow Excited by Focused Nanosecond Laser Pulses in Contaminated Thin Liquid Iron Films. *J. Appl. Phys.* **1995**, *78* (3), 2037–2044.

(135) Balandin, V. Yu.; Gernert, U.; Nink, T.; Bostanjoglo, O. Segregation and Surface Transport of Impurities: New Mechanisms Affecting the Surface Morphology of Laser Treated Metals. *J. Appl. Phys.* **1997**, *81* (6), 2835–2838.

(136) Balandin, V. Yu.; Nink, T.; Bostanjoglo, O. Pulsation of a Liquid Excited by a Fast-Moving Crystallization Front with Segregation of Surface Active Impurities. *J. Appl. Phys.* **1998**, *84* (11), 6355–6358.

(137) Dömer, H.; Bostanjoglo, O. High-Speed Transmission Electron Microscope. *Rev. Sci. Instrum.* **2003**, *74* (10), 4369–4372.

(138) Dömer, H.; Bostanjoglo, O. Laser Ablation of Thin Films with Very High Induced Stresses. *J. Appl. Phys.* **2002**, *91* (8), 5462–5467.

(139) Bostanjoglo, O.; Elschner, R.; Mao, Z.; Nink, T.; Weingärtner, M. Nanosecond Electron Microscopes. *Ultramicroscopy* **2000**, *81* (3–4), 141–147.

(140) Bostanjoglo, O.; Tornow, R. P.; Tornow, W. Nanosecond Transmission Electron Microscopy and Diffraction. *J. Phys. [E]* **1987**, *20* (5), 556–557.

(141) Bostanjoglo, O.; Endruschat, E. Time-Resolved TEM of Laser-Annealing. *Phys. Status Solidi A* **1984**, *82* (1), K1–K3.

(142) Bostanjoglo, O. High-Speed Electron Microscopy. *Adv. Imaging Electron Phys.* **2002**, *121*, 1–51.

(143) Oldfield, L. C. A Rotationally Symmetric Electron Beam Chopper for Picosecond Pulses. *J. Phys. [E]* **1976**, *9* (6), 455–463.

(144) Fehr, J.; Reiners, W.; Balk, L. J.; Kubalek, E.; Köther, D.; Wolff, I. A 100-Femtosecond Electron Beam Blanking System. *Microelectron. Eng.* **1990**, *12* (1–4), 221–226.

(145) Brunner, M.; Winkler, D.; Schmitt, R.; Lischke, B. Electron-Beam Test System for High-Speed Devices. *Scanning* **1987**, *9* (5), 201–204.

(146) May, P.; Halbout, J. -M.; Chiu, G. Picosecond Photoelectron Scanning Electron Microscope for Noncontact Testing of Integrated Circuits. *Appl. Phys. Lett.* **1987**, *51* (2), 145–147.

(147) May, P. G.; Halbout, J.-M.; Chiu, G. L.-T. Noncontact High-Speed Waveform Measurements with the Picosecond Photoelectron Scanning Electron Microscope. *IEEE J. Quantum Electron.* **1988**, *24* (2), 234–239.

(148) Ura, K.; Fujioka, H.; Hosokawa, T. Picosecond Pulse Stroboscopic Scanning Electron Microscope. *J. Electron Microsc. (Tokyo)* **1978**, *27* (4), 247–252.

(149) King, W. E.; Armstrong, M.; Malka, V.; Reed, B. W.; Rousse, A. Ultrafast Imaging of Materials: Exploring the Gap of Space and Time. *MRS Bull.* **2006**, *31* (8), 614–619.

(150) Armstrong, M. R.; Boyden, K.; Browning, N. D.; Campbell, G. H.; Colvin, J. D.; DeHope, W. J.; Frank, A. M.; Gibson, D. J.; Hartemann, F.; Kim, J. S.; King, W. E.; LaGrange, T. B.; Pyke, B. J.; Reed, B. W.; Shuttlesworth, R. M.; Stuart, B. C.; Torralva, B. R. Practical Considerations for High Spatial and Temporal Resolution Dynamic Transmission Electron Microscopy. *Ultramicroscopy* **2007**, *107* (4–5), 356–367.

(151) LaGrange, T.; Armstrong, M. R.; Boyden, K.; Brown, C. G.; Campbell, G. H.; Colvin, J. D.; DeHope, W. J.; Frank, A. M.; Gibson, D. J.; Hartemann, F. V.; Kim, J. S.; King, W. E.; Pyke, B. J.; Reed, B. W.; Shirk, M. D.; Shuttlesworth, R. M.; Stuart, B. C.; Torralva, B. R.; Browning, N. D. Single-Shot Dynamic Transmission Electron Microscopy. *Appl. Phys. Lett.* **2006**, *89* (4), 044105.

(152) LaGrange, T.; Reed, B. W.; Masiel, D. J. Movie-Mode Dynamic Electron Microscopy. *MRS Bull.* **2015**, *40* (1), 22–28.

(153) Zewail, A. H. 4D Ultrafast Electron Diffraction, Crystallography, and Microscopy. *Annu. Rev. Phys. Chem.* **2006**, *57* (1), 65–103.

(154) Lobastov, V. A.; Srinivasan, R.; Zewail, A. H. Four-Dimensional Ultrafast Electron Microscopy. *Proc. Natl. Acad. Sci.* **2005**, *102* (20), 7069–7073.

(155) Flannigan, D. J.; Zewail, A. H. 4D Electron Microscopy: Principles and Applications. *Acc. Chem. Res.* **2012**, *45* (10), 1828–1839.

(156) Barwick, B.; Zewail, A. H. Photonics and Plasmonics in 4D Ultrafast Electron Microscopy. *ACS Photonics* **2015**, *2* (10), 1391–1402.

(157) Flannigan, D. J. Spreadsheet-Based Program for Simulating Atomic Emission Spectra. *J. Chem. Educ.* **2014**, *91* (10), 1736–1738.

(158) Flannigan, D. J.; Cremons, D. R.; Du, D. X.; McKenna, A. J.; Plemmons, D. A. Imaging Coherent Structural Dynamics with Ultrafast Electron Microscopy. *Microsc. Microanal.* **2018**, *24* (S1), 1838–1839.

(159) Schäfer, S.; Liang, W.; Zewail, A. H. Primary Structural Dynamics in Graphite. *New J. Phys.* **2011**, *13* (6), 063030.

(160) Barwick, B.; Park, H. S.; Kwon, O.-H.; Baskin, J. S.; Zewail, A. H. 4D Imaging of Transient Structures and Morphologies in Ultrafast Electron Microscopy. *Science* **2008**, *322* (5905), 1227–1231.

(161) Plemmons, D. A.; Flannigan, D. J. Ultrafast Electron Microscopy: Instrument Response from the Single-Electron to High Bunch-Charge Regimes. *Chem. Phys. Lett.* **2017**, *683*, 186–192.

(162) Weathersby, S. P.; Brown, G.; Centurion, M.; Chase, T. F.; Coffee, R.; Corbett, J.; Eichner, J. P.; Frisch, J. C.; Fry, A. R.; Gühr, M.; Hartmann, N.; Hast, C.; Hettel, R.; Jobe, R. K.; Jongewaard, E. N.; Lewandowski, J. R.; Li, R. K.; Lindenberg, A. M.; Makasyuk, I.; May, J. E.; McCormick, D.; Nguyen, M. N.; Reid, A. H.; Shen, X.; Sokolowski-Tinten, K.; Vecchione, T.; Vetter, S. L.; Wu, J.; Yang, J.; Dürr, H. A.; Wang, X. J. Mega-Electron-Volt Ultrafast Electron Diffraction at SLAC National Accelerator Laboratory. *Rev. Sci. Instrum.* **2015**, *86* (7), 073702.

(163) Feist, A.; Bach, N.; Rubiano da Silva, N.; Danz, T.; Möller, M.; Priebe, K. E.; Domröse, T.; Gatzmann, J. G.; Rost, S.; Schauss, J.; Strauch, S.; Bormann, R.; Sivis, M.; Schäfer, S.; Ropers, C. Ultrafast Transmission Electron Microscopy Using a Laser-Driven Field Emitter: Femtosecond Resolution with a High Coherence Electron Beam. *Ultramicroscopy* **2017**, *176*, 63–73.

(164) Chergui, M.; Zewail, A. H. Electron and X-Ray Methods of Ultrafast Structural Dynamics: Advances and Applications. *ChemPhysChem* **2009**, *10* (1), 28–43.

(165) Piazza, L.; Masiel, D. J.; LaGrange, T.; Reed, B. W.; Barwick, B.; Carbone, F. Design and Implementation of a Fs-Resolved Transmission Electron Microscope Based on Thermionic Gun Technology. *Chem. Phys.* **2013**, *423*, 79–84.

(166) Miller, R. J. D. Femtosecond Crystallography with Ultrabright Electrons and X-Rays: Capturing Chemistry in Action. *Science* **2014**, *343* (6175), 1108–1116.

(167) Plemmons, D. A.; Suri, P. K.; Flannigan, D. J. Probing Structural and Electronic Dynamics with Ultrafast Electron Microscopy. *Chem. Mater.* **2015**, *27* (9), 3178–3192.

(168) Bücker, K.; Picher, M.; Crégut, O.; LaGrange, T.; Reed, B. W.; Park, S. T.; Masiel, D. J.; Banhart, F. Electron Beam Dynamics in an Ultrafast Transmission Electron Microscope with Wehnelt Electrode. *Ultramicroscopy* **2016**, *171*, 8–18.

(169) Lindenberg, A. M.; Johnson, S. L.; Reis, D. A. Visualization of Atomic-Scale Motions in Materials via Femtosecond X-Ray Scattering Techniques. *Annu. Rev. Mater. Res.* **2017**, *47* (1), 425–449.

(170) Gardner, D. F.; Tanksalvala, M.; Shanblatt, E. R.; Zhang, X.; Galloway, B. R.; Porter, C. L.; Karl Jr, R.; Bevis, C.; Adams, D. E.; Kapteyn, H. C.; Murnane, M. M.; Mancini, G. F. Subwavelength Coherent Imaging of Periodic Samples Using a 13.5 Nm Tabletop High-Harmonic Light Source. *Nat. Photonics* **2017**, *11* (4), 259–263.

(171) Adhikari, A.; Eliason, J. K.; Sun, J.; Bose, R.; Flannigan, D. J.; Mohammed, O. F. Four-Dimensional Ultrafast Electron Microscopy: Insights into an Emerging Technique. *ACS Appl. Mater. Interfaces* **2017**, *9* (1), 3–16.

(172) Flannigan, D. J.; Lindenberg, A. M. Atomic-Scale Imaging of Ultrafast Materials Dynamics. *MRS Bull.* **2018**, *43* (7), 485–490.

(173) Yang, D.-S.; Liao, B.; Mohammed, O. F. Scanning Ultrafast Electron Microscopy: Four-Dimensional Imaging of Materials Dynamics in Space and Time. *MRS Bull.* **2018**, *43* (7), 491–496.

(174) Niekiel, F.; Kraschewski, S. M.; Müller, J.; Butz, B.; Spiecker, E. Local Temperature Measurement in TEM by Parallel Beam Electron Diffraction. *Ultramicroscopy* **2017**, *176*, 161–169.

(175) Bonneaux, J.; Guymont, M. Study of the Order–Disorder Transition Series in AuCu by *In Situ* Temperature Electron Microscopy. *Intermetallics* **1999**, *7* (7), 797–805.

(176) Gao, Y.; Bando, Y.; Liu, Z.; Golberg, D.; Nakanishi, H. Temperature Measurement Using a Gallium-Filled Carbon Nanotube Nanothermometer. *Appl. Phys. Lett.* **2003**, *83* (14), 2913–2915.

(177) Gong, N. W.; Lu, M. Y.; Wang, C. Y.; Chen, Y.; Chen, L. J. Au(Si)-Filled β-Ga_2O_3 Nanotubes as Wide Range High Temperature Nanothermometers. *Appl. Phys. Lett.* **2008**, *92* (7), 073101.

(178) Begtrup, G. E.; Ray, K. G.; Kessler, B. M.; Yuzvinsky, T. D.; Garcia, H.; Zettl, A. Probing Nanoscale Solids at Thermal Extremes. *Phys. Rev. Lett.* **2007**, *99* (15), 155901.

(179) Watanabe, M.; Someya, T.; Nagahama, Y. Temperature Rise of Specimen Due to Electron Irradiation. *J. Phys. Appl. Phys.* **1970**, *3* (10), 1461.

(180) Thornburg, D. D.; Wayman, C. M. Specimen Temperature Increases during Transmission Electron Microscopy. *Phys. Status Solidi A* **1973**, *15* (2), 449–453.

(181) Brintlinger, T.; Qi, Y.; Baloch, K. H.; Goldhaber-Gordon, D.; Cumings, J. Electron Thermal Microscopy. *Nano Lett.* **2008**, *8* (2), 582–585.

(182) Ligges, M.; Rajkovic, I.; Zhou, P.; Posth, O.; Hassel, C.; Dumpich, G.; von der Linde, D. Observation of Ultrafast Lattice Heating Using Time Resolved Electron Diffraction. *Appl. Phys. Lett.* **2009**, *94* (10), 101910.

(183) Schäfer, S.; Liang, W.; Zewail, A. H. Structural Dynamics of Nanoscale Gold by Ultrafast Electron Crystallography. *Chem. Phys. Lett.* **2011**, *515* (4–6), 278–282.

(184) Frigge, T.; Hafke, B.; Tinnemann, V.; Krenzer, B.; Horn-von Hoegen, M. Nanoscale Heat Transport from Ge Hut, Dome, and Relaxed Clusters on Si(001) Measured by Ultrafast Electron Diffraction. *Appl. Phys. Lett.* **2015**, *106* (5), 053108.

(185) Yurtsever, A.; Zewail, A. H. 4D Nanoscale Diffraction Observed by Convergent-Beam Ultrafast Electron Microscopy. *Science* **2009**, *326* (5953), 708–712.

(186) Yurtsever, A.; Zewail, A. H. Kikuchi Ultrafast Nanodiffraction in Four-Dimensional Electron Microscopy. *Proc. Natl. Acad. Sci.* **2011**, *108* (8), 3152–3156.

(187) Yurtsever, A.; Schaefer, S.; Zewail, A. H. Ultrafast Kikuchi Diffraction: Nanoscale Stress–Strain Dynamics of Wave-Guiding Structures. *Nano Lett.* **2012**, *12* (7), 3772–3777.

(188) Feist, A.; Rubiano da Silva, N.; Liang, W.; Ropers, C.; Schäfer, S. Nanoscale Diffractive Probing of Strain Dynamics in Ultrafast Transmission Electron Microscopy. *Struct. Dyn.* **2018**, *5* (1), 014302.

(189) Takaoka, A.; Ura, K. Temperature Measurement on Micro-Area of Specimen in TEM by Using Thermal Diffuse Scattering Effect. *J. Electron Microsc. (Tokyo)* **1990**, *39* (1), 69–70.

(190) Wehmeyer, G.; Bustillo, K. C.; Minor, A. M.; Dames, C. Measuring Temperature-Dependent Thermal Diffuse Scattering Using Scanning Transmission Electron Microscopy. *Appl. Phys. Lett.* **2018**, *113* (25), 253101.

(191) Eggeman, A. S.; Illig, S.; Troisi, A.; Sirringhaus, H.; Midgley, P. A. Measurement of Molecular Motion in Organic Semiconductors by Thermal Diffuse Electron Scattering. *Nat. Mater.* **2013**, *12* (11), 1045–1049.

(192) de Cotret, L. P. R.; Pöhls, J.-H.; Stern, M. J.; Otto, M. R.; Sutton, M.; Siwick, B. J. Time- and Momentum-Resolved Phonon Population Dynamics with Ultrafast Electron Diffuse Scattering. *Phys. Rev. B* **2019**, *100* (21), 214115.

(193) Gnabasik, R. Real-Space Imaging of Picosecond Structural Dynamics in Metals with Ultrafast Transmission Electron Microscopy, University of Minnesota, Minneapolis, 2021.

(194) Kutty, A. P. G.; Vaidya, S. N. Mean-Square Atomic Displacements in f.c.c. Crystals. *J. Phys. Chem. Solids* **1980**, *41* (11), 1163–1170.

(195) Sciaini, G.; Harb, M.; Kruglik, S. G.; Payer, T.; Hebeisen, C. T.; Heringdorf, F.-J. M. zu; Yamaguchi, M.; Hoegen, M. H.; Ernstorfer, R.; Miller, R. J. D. Electronic Acceleration of Atomic Motions and Disordering in Bismuth. *Nature* **2009**, *458* (7234), 56–59.

(196) Waldecker, L.; Bertoni, R.; Hübener, H.; Brumme, T.; Vasileiadis, T.; Zahn, D.; Rubio, A.; Ernstorfer, R. Momentum-Resolved View of Electron-Phonon Coupling in Multilayer WSe_2. *Phys. Rev. Lett.* **2017**, *119* (3), 036803.

(197) Waldecker, L.; Bertoni, R.; Vorberger, J.; Ernstorfer, R. Electron-Phonon Coupling and Energy Flow in a Simple Metal beyond the Two-Temperature Approximation. *Phys. Rev. X* **2016**, *6* (2), 021003.

(198) Harb, M.; Ernstorfer, R.; Dartigalongue, T.; Hebeisen, C. T.; Jordan, R. E.; Miller, R. J. D. Carrier Relaxation and Lattice Heating Dynamics in Silicon Revealed by Femtosecond Electron Diffraction. *J. Phys. Chem. B* **2006**, *110* (50), 25308–25313.

(199) Zheng, Q.; Shen, X.; Sokolowski-Tinten, K.; Li, R. K.; Chen, Z.; Mo, M. Z.; Wang, Z. L.; Weathersby, S. P.; Yang, J.; Chen, M. W.; Wang, X. J. Dynamics of Electron–Phonon Coupling in Bicontinuous Nanoporous Gold. *J. Phys. Chem. C* **2018**, *122* (28), 16368–16373.

(200) Park, H.; Wang, X.; Nie, S.; Clinite, R.; Cao, J. Direct and Real-Time Probing of Both Coherent and Thermal Lattice Motions. *Solid State Commun.* **2005**, *136* (9–10), 559–563.

(201) Lee, Y. M.; Kim, Y. J.; Kim, Y.-J.; Kwon, O.-H. Ultrafast Electron Microscopy Integrated with a Direct Electron Detection Camera. *Struct. Dyn.* **2017**, *4* (4), 044023.

(202) Oguz Er, A.; Chen, J.; Tang, J.; Rentzepis, P. M. Coherent Acoustic Wave Oscillations and Melting on Ag(111) Surface by Time Resolved x-Ray Diffraction. *Appl. Phys. Lett.* **2012**, *100* (15), 151910.

(203) Zhu, P.; Chen, J.; Li, R.; Chen, L.; Cao, J.; Sheng, Z.; Zhang, J. Laser-Induced Short-Range Disorder in Aluminum Revealed by Ultrafast Electron Diffuse Scattering. *Appl. Phys. Lett.* **2013**, *103* (23), 231914.

(204) Flannigan, D. J.; Zewail, A. H. Optomechanical and Crystallization Phenomena Visualized with 4D Electron Microscopy: Interfacial Carbon Nanotubes on Silicon Nitride. *Nano Lett.* **2010**, *10* (5), 1892–1899.

(205) Cremons, D. R.; Flannigan, D. J. Direct in Situ Thermometry: Variations in Reciprocal-Lattice Vectors and Challenges with the Debye–Waller Effect. *Ultramicroscopy* **2016**, *161*, 10–16.

(206) Allen, C. S.; Liberti, E.; Kim, J. S.; Xu, Q.; Fan, Y.; He, K.; Robertson, A. W.; Zandbergen, H. W.; Warner, J. H.; Kirkland, A. I. Temperature Dependence of Atomic Vibrations in Mono-Layer Graphene. *J. Appl. Phys.* **2015**, *118* (7), 074302.

(207) Li, R.; Zhu, P.; Chen, J.; Cao, J.; Rentzepis, P. M.; Zhang, J. Direct Observation of Ultrafast Thermal and Non-Thermal Lattice Deformation of Polycrystalline Aluminum Film. *Appl. Phys. Lett.* **2017**, *111* (4), 041105.

(208) Tam, A. C. Applications of Photoacoustic Sensing Techniques. *Rev. Mod. Phys.* **1986**, *58* (2), 381–431.

(209) Ruello, P.; Gusev, V. E. Physical Mechanisms of Coherent Acoustic Phonons Generation by Ultrafast Laser Action. *Ultrasonics* **2015**, *56*, 21–35.

(210) Li, R.; Ashour, O. A.; Chen, J.; Elsayed-Ali, H. E.; Rentzepis, P. M. Femtosecond Laser Induced Structural Dynamics and Melting of Cu (111) Single Crystal. An Ultrafast Time-Resolved x-Ray Diffraction Study. *J. Appl. Phys.* **2017**, *121* (5), 055102.

(211) Cremons, D. R.; Plemmons, D. A.; Flannigan, D. J. Femtosecond Electron Imaging of Defect-Modulated Phonon Dynamics. *Nat. Commun.* **2016**, *7* (1), 11230.

(212) Cremons, D. R.; Plemmons, D. A.; Flannigan, D. J. Defect-Mediated Phonon Dynamics in TaS_2 and WSe_2. *Struct. Dyn.* **2017**, *4* (4), 044019.

(213) Winterstein, J. P.; Lin, P. A.; Sharma, R. Temperature Calibration for *In Situ* Environmental Transmission Electron Microscopy Experiments. *Microsc. Microanal.* **2015**, *21* (6), 1622–1628.

(214) Davidovikj, D.; Slim, J. J.; Cartamil-Bueno, S. J.; van der Zant, H. S. J.; Steeneken, P. G.; Venstra, W. J. Visualizing the Motion of Graphene Nanodrums. *Nano Lett.* **2016**, *16* (4), 2768–2773.

(215) Cremons, D. R.; Schliep, K. B.; Flannigan, D. J. Diffraction Contrast as a Sensitive Indicator of Femtosecond Sub-Nanoscale Motion in Ultrafast Transmission Electron Microscopy; Liu, Z., Ed.; San Diego, California, United States, 2013; p 884507.

(216) Nie, S.; Wang, X.; Park, H.; Clinite, R.; Cao, J. Measurement of the Electronic Grüneisen Constant Using Femtosecond Electron Diffraction. *Phys. Rev. Lett.* **2006**, *96* (2), 025901.

(217) Tang, J. Coherent Phonon Excitation and Linear Thermal Expansion in Structural Dynamics and Ultrafast Electron Diffraction of Laser-Heated Metals. *J. Chem. Phys.* **2008**, *128* (16), 164702.

(218) Hostetler, J. L.; Smith, A. N.; Czajkowsky, D. M.; Norris, P. M. Measurement of the Electron-Phonon Coupling Factor Dependence on Film Thickness and Grain Size in Au, Cr, and Al. *Appl. Opt.* **1999**, *38* (16), 3614.

(219) Ashcroft, N. W.; Mermin, N. D. *Solid State Physics*; Holt, Rinehart and Winston, 1976.

(220) Kittel, C. *Introduction to Solid State Physics*; John Wiley & Sons, 1962.

(221) Othonos, A. Probing Ultrafast Carrier and Phonon Dynamics in Semiconductors. *J. Appl. Phys.* **1998**, *83* (4), 1789–1830.

(222) Axt, V. M.; Kuhn, T. Femtosecond Spectroscopy in Semiconductors: A Key to Coherences, Correlations and Quantum Kinetics. *Rep. Prog. Phys.* **2004**, *67* (4), 433–512.

(223) Mueller, B. Y.; Rethfeld, B. Relaxation Dynamics in Laser-Excited Metals under Nonequilibrium Conditions. *Phys. Rev. B* **2013**, *87* (3), 035139.

(224) Chen, J. K.; Beraun, J. E.; Tham, C. L. Investigation of Thermal Response Caused by Pulse Laser Heating. *Numer. Heat Transf. Part Appl.* **2003**, *44* (7), 705–722.

(225) van Driel, H. M. Influence of Hot Phonons on Energy Relaxation of High-Density Carriers in Germanium. *Phys. Rev. B* **1979**, *19* (11), 5928–5932.

(226) Stern, E. A.; Brewe, D. Delay of Laser Excited Electron/Hole Interaction with Germanium Lattice. *J. Phys. Conf. Ser.* **2009**, *190*, 012053.

(227) Yu, P.; Cardona, M. *Fundamentals of Semiconductors: Physics and Materials Properties*; Springer Science & Business Media, 2010.

(228) Akhmanov, S. A.; Gusev, V. É. Laser Excitation of Ultrashort Acoustic Pulses: New Possibilities in Solid-State Spectroscopy, Diagnostics of Fast Processes, and Nonlinear Acoustics. *Sov. Phys. Uspekhi* **1992**, *35* (3), 153–191.

(229) Zhang, Y.; Flannigan, D. J. Observation of Anisotropic Strain-Wave Dynamics and Few-Layer Dephasing in MoS_2 with Ultrafast Electron Microscopy. *Nano Lett.* **2019**, *19* (11), 8216–8224.

(230) Reisbick, S. A.; Zhang, Y.; Flannigan, D. J. Influence of Discrete Defects on Observed Acoustic–Phonon Dynamics in Layered Materials Probed with Ultrafast Electron Microscopy. *J. Phys. Chem. A* **2020**, *124* (9), 1877–1884.

(231) Rogers, J. A.; Maznev, A. A.; Banet, M. J.; Nelson, K. A. Optical Generation and Characterization of Acoustic Waves in Thin Films: Fundamentals and Applications. *Annu. Rev. Mater. Sci.* **2000**, *30* (1), 117–157.

(232) Gusev, V. E.; Ruello, P. Advances in Applications of Time-Domain Brillouin Scattering for Nanoscale Imaging. *Appl. Phys. Rev.* **2018**, *5* (3), 031101.

(233) Steigerwald, A.; Xu, Y.; Qi, J.; Gregory, J.; Liu, X.; Furdyna, J. K.; Varga, K.; Hmelo, A. B.; Lüpke, G.; Feldman, L. C.; Tolk, N. Semiconductor Point Defect Concentration Profiles Measured Using Coherent Acoustic Phonon Waves. *Appl. Phys. Lett.* **2009**, *94* (11), 111910.

(234) Mechri, C.; Ruello, P.; Breteau, J. M.; Baklanov, M. R.; Verdonck, P.; Gusev, V. Depth-Profiling of Elastic Inhomogeneities in Transparent Nanoporous Low-k Materials by Picosecond Ultrasonic Interferometry. *Appl. Phys. Lett.* **2009**, *95* (9), 091907.

(235) Steigerwald, A.; Hmelo, A. B.; Varga, K.; Feldman, L. C.; Tolk, N. Determination of Optical Damage Cross-Sections and Volumes Surrounding Ion Bombardment Tracks in GaAs Using Coherent Acoustic Phonon Spectroscopy. *J. Appl. Phys.* **2012**, *112* (1), 013514.

(236) Gregory, J.; Steigerwald, A.; Takahashi, H.; Hmelo, A.; Tolk, N. Ion Implantation Induced Modification of Optical Properties in Single-Crystal Diamond Studied by Coherent Acoustic Phonon Spectroscopy. *Appl. Phys. Lett.* **2012**, *101* (18), 181904.

(237) Yarotski, D.; Fu, E.; Yan, L.; Jia, Q.; Wang, Y.; Taylor, A. J.; Uberuaga, B. P. Characterization of Irradiation Damage Distribution near TiO_2/$SrTiO_3$ Interfaces Using Coherent Acoustic Phonon Interferometry. *Appl. Phys. Lett.* **2012**, *100* (25), 251603.

(238) Nikitin, S. M.; Chigarev, N.; Tournat, V.; Bulou, A.; Gasteau, D.; Castagnede, B.; Zerr, A.; Gusev, V. E. Revealing Sub-Mm and Mm-Scale Textures in H_2O Ice at Megabar Pressures by Time-Domain Brillouin Scattering. *Sci. Rep.* **2015**, *5* (1), 1–11.

(239) Kuriakose, M.; Raetz, S.; Chigarev, N.; Nikitin, S. M.; Bulou, A.; Gasteau, D.; Tournat, V.; Castagnede, B.; Zerr, A.; Gusev, V. E. Picosecond Laser Ultrasonics for Imaging of Transparent Polycrystalline Materials Compressed to Megabar Pressures. *Ultrasonics* **2016**, *69*, 259–267.

(240) Danworaphong, S.; Tomoda, M.; Matsumoto, Y.; Matsuda, O.; Ohashi, T.; Watanabe, H.; Nagayama, M.; Gohara, K.; Otsuka, P. H.; Wright, O. B. Three-Dimensional Imaging of Biological Cells with Picosecond Ultrasonics. *Appl. Phys. Lett.* **2015**, *106* (16), 163701.

(241) Pérez-Cota, F.; Smith, R. J.; Moradi, E.; Marques, L.; Webb, K. F.; Clark, M. High Resolution 3D Imaging of Living Cells with Sub-Optical Wavelength Phonons. *Sci. Rep.* **2016**, *6* (1), 39326.

(242) Pérez-Cota, F.; Smith, R. J.; Moradi, E.; Marques, L.; Webb, K. F.; Clark, M. Thin-Film Optoacoustic Transducers for Subcellular Brillouin Oscillation Imaging of Individual Biological Cells. *Appl. Opt.* **2015**, *54* (28), 8388–8398.

(243) Ramanathan, S.; Cahill, D. G. High-Resolution Picosecond Acoustic Microscopy for Non-Invasive Characterization of Buried Interfaces. *J. Mater. Res.* **2006**, *21* (5), 1204–1208.

(244) Lomonosov, A. M.; Ayouch, A.; Ruello, P.; Vaudel, G.; Baklanov, M. R.; Verdonck, P.; Zhao, L.; Gusev, V. E. Nanoscale Noncontact Subsurface Investigations of Mechanical and Optical Properties of Nanoporous Low- *k* Material Thin Film. *ACS Nano* **2012**, *6* (2), 1410–1415.

(245) Zewail, A. H. Four-Dimensional Electron Microscopy. *Science* **2010**, *328* (5975), 187–193.

(246) Egerton, R. F. Radiation Damage to Organic and Inorganic Specimens in the TEM. *Micron* **2019**, *119*, 72–87.

(247) Egerton, R. F. Mechanisms of Radiation Damage in Beam-Sensitive Specimens, for TEM Accelerating Voltages between 10 and 300kV. *Microsc. Res. Tech.* **2012**, *75* (11), 1550–1556.

(248) Fryer, J. R. The Effect of Dose Rate on Imaging Aromatic Organic Crystals. *Ultramicroscopy* **1987**, *23* (3–4), 321–327.

(249) Henderson, R.; Glaeser, R. M. Quantitative Analysis of Image Contrast in Electron Micrographs of Beam-Sensitive Crystals. *Ultramicroscopy* **1985**, *16* (2), 139–150.

(250) Ashley, J. C.; Williams, M. W. Electron Mean Free Paths in Solid Organic Insulators. *Radiat. Res.* **1980**, *81* (3), 364–373.

(251) Gauduel, Y. A.; Fritzler, S.; Hallou, A.; Glinec, Y.; Malka, V. Femtosecond Relativistic Electron Beam Triggered Early Bioradical Events; Avrillier, S., Tualle, J.-M., Eds.; Strasbourg, France, 2004; p 86.

(252) Orth, V. H.; Fischer, E. W. Änderungen der Gitterstruktur hochpolymerer Einkristalle durch Bestrahlung im Elektronenmikroskop. *Makromol. Chem.* **1965**, *88* (1), 188–214.

(253) Grubb, D. T. Radiation Damage and Electron Microscopy of Organic Polymers. *J. Mater. Sci.* **1974**, *9* (10), 1715–1736.

(254) Egerton, R. F. Control of Radiation Damage in the TEM. *Ultramicroscopy* **2013**, *127*, 100–108.

(255) Dubochet, J. On the Development of Electron Cryo-Microscopy (Nobel Lecture). *Angew. Chem. Int. Ed.* **2018**, *57* (34), 10842–10846.

(256) Glaeser, R. M.; Taylor, K. A. Radiation Damage Relative to Transmission Electron Microscopy of Biological Specimens at Low Temperature: A Review. *J. Microsc.* **1978**, *112* (1), 127–138.

(257) Frank, J. Single-Particle Reconstruction of Biological Molecules-Story in a Sample (Nobel Lecture). *Angew. Chem. Int. Ed.* **2018**, *57* (34), 10826–10841.

(258) Kourkoutis, L. F.; Plitzko, J. M.; Baumeister, W. Electron Microscopy of Biological Materials at the Nanometer Scale. *Annu. Rev. Mater. Res.* **2012**, *42* (1), 33–58.

(259) Cheng, Y. Single-Particle Cryo-EM—How Did It Get Here and Where Will It Go. *Science* **2018**, *361* (6405), 876–880.

(260) Henderson, R. From Electron Crystallography to Single Particle CryoEM (Nobel Lecture). *Angew. Chem. Int. Ed.* **2018**, *57* (34), 10804–10825.

(261) Salih, S. M.; Cosslett, V. E. Reduction in Electron Irradiation Damage to Organic Compounds by Conducting Coatings. *Philos. Mag.* **1974**, *30* (1), 225–228.

(262) Unwin, P. N. T.; Henderson, R. Molecular Structure Determination by Electron Microscopy of Unstained Crystalline Specimens. *J. Mol. Biol.* **1975**, *94* (3), 425–440.

(263) Fryer, J. R. Radiation Damage in Organic Crystalline Films. *Ultramicroscopy* **1984**, *14* (3), 227–236.

(264) Evans, J. E.; Hetherington, C.; Kirkland, A.; Chang, L.-Y.; Stahlberg, H.; Browning, N. Low-Dose Aberration Corrected Cryo-Electron Microscopy of Organic Specimens. *Ultramicroscopy* **2008**, *108* (12), 1636–1644.

(265) Keskin, S.; de Jonge, N. Reduced Radiation Damage in Transmission Electron Microscopy of Proteins in Graphene Liquid Cells. *Nano Lett.* **2018**, *18* (12), 7435–7440.

(266) Glaeser, R. M.; McMullan, G.; Faruqi, A. R.; Henderson, R. Images of Paraffin Monolayer Crystals with Perfect Contrast: Minimization of Beam-Induced Specimen Motion. *Ultramicroscopy* **2011**, *111* (2), 90–100.

(267) Li, X.; Mooney, P.; Zheng, S.; Booth, C. R.; Braunfeld, M. B.; Gubbens, S.; Agard, D. A.; Cheng, Y. Electron Counting and Beam-Induced Motion Correction Enable near-Atomic-Resolution Single-Particle Cryo-EM. *Nat. Methods* **2013**, *10* (6), 584–590.

(268) Zhang, D.; Zhu, Y.; Liu, L.; Ying, X.; Hsiung, C.-E.; Sougrat, R.; Li, K.; Han, Y. Atomic-Resolution Transmission Electron Microscopy of Electron Beam–Sensitive Crystalline Materials. *Science* **2018**, *359* (6376), 675–679.

(269) Egger, D. A.; Bera, A.; Cahen, D.; Hodes, G.; Kirchartz, T.; Kronik, L.; Lovrincic, R.; Rappe, A. M.; Reichman, D. R.; Yaffe, O. What Remains Unexplained about the Properties of Halide Perovskites? *Adv. Mater.* **2018**, *30* (20), 1800691.

(270) Doherty, T. A. S.; Winchester, A. J.; Macpherson, S.; Johnstone, D. N.; Pareek, V.; Tennyson, E. M.; Kosar, S.; Kosasih, F. U.; Anaya, M.; Abdi-Jalebi, M.; Andaji-Garmaroudi, Z.; Wong, E. L.; Madéo, J.; Chiang, Y.-H.; Park, J.-S.; Jung, Y.-K.; Petoukhoff, C. E.; Divitini, G.; Man, M. K. L.; Ducati, C.; Walsh, A.; Midgley, P. A.; Dani, K. M.; Stranks, S. D. Performance-Limiting Nanoscale Trap Clusters at Grain Junctions in Halide Perovskites. *Nature* **2020**, *580* (7803), 360–366.

(271) Divitini, G.; Cacovich, S.; Matteocci, F.; Cinà, L.; Di Carlo, A.; Ducati, C. *In Situ* Observation of Heat-Induced Degradation of Perovskite Solar Cells. *Nat. Energy* **2016**, *1* (2), 15012.

(272) Rothmann, M. U.; Li, W.; Zhu, Y.; Liu, A.; Ku, Z.; Bach, U.; Etheridge, J.; Cheng, Y. Structural and Chemical Changes to $CH_3NH_3PbI_3$ Induced by Electron and Gallium Ion Beams. *Adv. Mater.* **2018**, *30* (25), 1800629.

(273) Ran, J.; Dyck, O. O.; Wang, X.; Yang, B.; Geohegan, D. B.; Xiao, K. Electron-Beam-Related Studies of Halide Perovskites: Challenges and Opportunities. *Adv. Energy Mater.* **2020**, *n/a* (n/a), 1903191.

(274) Ball, J. M.; Petrozza, A. Defects in Perovskite-Halides and Their Effects in Solar Cells. *Nat. Energy* **2016**, *1* (11), 16149.

(275) Rothmann, M. U.; Li, W.; Zhu, Y.; Bach, U.; Spiccia, L.; Etheridge, J.; Cheng, Y.-B. Direct Observation of Intrinsic Twin Domains in Tetragonal $CH_3NH_3PbI_3$. *Nat. Commun.* **2017**, *8* (1), 14547.

(276) Chen, S.; Zhang, X.; Zhao, J.; Zhang, Y.; Kong, G.; Li, Q.; Li, N.; Yu, Y.; Xu, N.; Zhang, J.; Liu, K.; Zhao, Q.; Cao, J.; Feng, J.; Li, X.; Qi, J.; Yu, D.; Li, J.; Gao, P. Atomic Scale Insights into Structure Instability and Decomposition Pathway of Methylammonium Lead Iodide Perovskite. *Nat. Commun.* **2018**, *9* (1), 1–8.

(277) Park, B.; Seok, S. I. Intrinsic Instability of Inorganic–Organic Hybrid Halide Perovskite Materials. *Adv. Mater.* **2019**, *31* (20), 1805337.

(278) Correa-Baena, J.-P.; Saliba, M.; Buonassisi, T.; Grätzel, M.; Abate, A.; Tress, W.; Hagfeldt, A. Promises and Challenges of Perovskite Solar Cells. *Science* **2017**, *358* (6364), 739–744.

(279) Aristidou, N.; Sanchez-Molina, I.; Chotchuangchutchaval, T.; Brown, M.; Martinez, L.; Rath, T.; Haque, S. A. The Role of Oxygen in the Degradation of Methylammonium Lead Trihalide Perovskite Photoactive Layers. *Angew. Chem.* **2015**, *127* (28), 8326–8330.

(280) Niu, G.; Guo, X.; Wang, L. Review of Recent Progress in Chemical Stability of Perovskite Solar Cells. *J. Mater. Chem. A* **2015**, *3* (17), 8970–8980.

(281) Boyd, C. C.; Cheacharoen, R.; Leijtens, T.; McGehee, M. D. Understanding Degradation Mechanisms and Improving Stability of Perovskite Photovoltaics. *Chem. Rev.* **2018**, *119* (5), 3418–3451.

(282) Zhou, Y.; Zhao, Y. Chemical Stability and Instability of Inorganic Halide Perovskites. *Energy Environ. Sci.* **2019**, *12* (5), 1495–1511.

(283) Bodnarchuk, M. I.; Boehme, S. C.; Ten Brinck, S.; Bernasconi, C.; Shynkarenko, Y.; Krieg, F.; Widmer, R.; Aeschlimann, B.; Günther, D.; Kovalenko, M. V. Rationalizing and Controlling the Surface Structure and Electronic Passivation of Cesium Lead Halide Nanocrystals. *ACS Energy Lett.* **2018**, *4* (1), 63–74.

(284) Khan, J.; Zhang, X.; Yuan, J.; Wang, Y.; Shi, G.; Patterson, R.; Shi, J.; Ling, X.; Hu, L.; Wu, T. Tuning the Surface-Passivating Ligand Anchoring Position Enables Phase Robustness in $CsPbI_3$ Perovskite Quantum Dot Solar Cells. *ACS Energy Lett.* **2020**, *5* (10), 3322–3329.

(285) Chen, S.; Zhang, Y.; Zhang, X.; Zhao, J.; Zhao, Z.; Su, X.; Hua, Z.; Zhang, J.; Cao, J.; Feng, J. General Decomposition Pathway of Organic–Inorganic Hybrid Perovskites through an Intermediate Superstructure and Its Suppression Mechanism. *Adv. Mater.* **2020**, *32* (29), 2001107.

(286) Schulz, P.; Cahen, D.; Kahn, A. Halide Perovskites: Is It All about the Interfaces? *Chem. Rev.* **2019**, *119* (5), 3349–3417.

(287) Ito, S.; Tanaka, S.; Manabe, K.; Nishino, H. Effects of Surface Blocking Layer of Sb_2S_3 on Nanocrystalline TiO_2 for $CH_3NH_3PbI_3$ Perovskite Solar Cells. *J. Phys. Chem. C* **2014**, *118* (30), 16995–17000.

(288) O'Mahony, F. T.; Lee, Y. H.; Jellett, C.; Dmitrov, S.; Bryant, D. T.; Durrant, J. R.; O'Regan, B. C.; Graetzel, M.; Nazeeruddin, M. K.; Haque, S. A. Improved Environmental Stability of Organic Lead Trihalide Perovskite-Based Photoactive-Layers in the Presence of Mesoporous TiO 2. *J. Mater. Chem. A* **2015**, *3* (14), 7219–7223.

(289) Bryant, D.; Aristidou, N.; Pont, S.; Sanchez-Molina, I.; Chotchunangatchaval, T.; Wheeler, S.; Durrant, J. R.; Haque, S. A. Light and Oxygen Induced Degradation Limits the Operational Stability of Methylammonium Lead Triiodide Perovskite Solar Cells. *Energy Environ. Sci.* **2016**, *9* (5), 1655–1660.

(290) Abdelmageed, G.; Jewell, L.; Hellier, K.; Seymour, L.; Luo, B.; Bridges, F.; Zhang, J. Z.; Carter, S. Mechanisms for Light Induced Degradation in $MAPbI_3$ Perovskite Thin Films and Solar Cells. *Appl. Phys. Lett.* **2016**, *109* (23), 233905.

(291) deQuilettes, D. W.; Zhang, W.; Burlakov, V. M.; Graham, D. J.; Leijtens, T.; Osherov, A.; Bulović, V.; Snaith, H. J.; Ginger, D. S.; Stranks, S. D. Photo-Induced Halide Redistribution in Organic–Inorganic Perovskite Films. *Nat. Commun.* **2016**, *7* (1), 11683.

(292) Joshi, P. H.; Zhang, L.; Hossain, I. M.; Abbas, H. A.; Kottokkaran, R.; Nehra, S. P.; Dhaka, M.; Noack, M.; Dalal, V. L. The Physics of Photon Induced Degradation of Perovskite Solar Cells. *AIP Adv.* **2016**, *6* (11), 115114.

(293) Huang, S.; Li, Z.; Wang, B.; Zhu, N.; Zhang, C.; Kong, L.; Zhang, Q.; Shan, A.; Li, L. Morphology Evolution and Degradation of $CsPbBr_3$ Nanocrystals under Blue Light-Emitting Diode Illumination. *ACS Appl. Mater. Interfaces* **2017**, *9* (8), 7249–7258.

(294) Zu, F.-S.; Amsalem, P.; Salzmann, I.; Wang, R.-B.; Ralaiarisoa, M.; Kowarik, S.; Duhm, S.; Koch, N. Impact of White Light Illumination on the Electronic and Chemical Structures of Mixed Halide and Single Crystal Perovskites. *Adv. Opt. Mater.* **2017**, *5* (9), 1700139.

(295) Xu, R.-P.; Li, Y.-Q.; Jin, T.-Y.; Liu, Y.-Q.; Bao, Q.-Y.; O'Carroll, C.; Tang, J.-X. *In Situ* Observation of Light Illumination-Induced Degradation in Organometal Mixed-Halide Perovskite Films. *ACS Appl. Mater. Interfaces* **2018**, *10* (7), 6737–6746.

(296) Ding, Y.; Shen, Y.; Peng, C.; Huang, M.; Hu, P. Unraveling the Photogenerated Electron Localization on the Defect-Free $CH_3NH_3PbI_3$ (001) Surfaces: Understanding and Implications from a First-Principles Study. *J. Phys. Chem. Lett.* **2020**, *11* (19), 8041–8047.

(297) Cho, J.; Kamat, P. V. How Chloride Suppresses Photoinduced Phase Segregation in Mixed Halide Perovskites. *Chem. Mater.* **2020**, *32* (14), 6206–6212.

(298) Lim, S.; Kim, J.; Park, J. Y.; Min, J.; Yun, S.; Park, T.; Kim, Y.; Choi, J. Suppressed Degradation and Enhanced Performance of $CsPbI_3$ Perovskite Quantum Dot Solar Cells via Engineering of Electron Transport Layers. *ACS Appl. Mater. Interfaces* **2021**, *13* (5), 6119–6129.

(299) Szymonski, M.; Droba, A.; Goryl, M.; Kolodziej, J. J.; Krok, F. Alkali Halide Decomposition and Desorption by Photons—the Role of Excited Point Defects and Surface Topographies. *J. Phys. Condens. Matter* **2006**, *18* (30), S1547.

(300) Shamsi, J.; Rastogi, P.; Caligiuri, V.; Abdelhady, A. L.; Spirito, D.; Manna, L.; Krahne, R. Bright-Emitting Perovskite Films by Large-Scale Synthesis and Photoinduced Solid-State Transformation of $CsPbBr_3$ Nanoplatelets. *ACS Nano* **2017**, *11* (10), 10206–10213.

(301) Yuan, Y.; Wang, Q.; Shao, Y.; Lu, H.; Li, T.; Gruverman, A.; Huang, J. Electric-field-driven Reversible Conversion between Methylammonium Lead Triiodide Perovskites and Lead Iodide at Elevated Temperatures. *Adv. Energy Mater.* **2016**, *6* (2), 1501803.

(302) Birkhold, S. T.; Precht, J. T.; Liu, H.; Giridharagopal, R.; Eperon, G. E.; Schmidt-Mende, L.; Li, X.; Ginger, D. S. Interplay of Mobile Ions and Injected Carriers Creates Recombination Centers in Metal Halide Perovskites under Bias. *ACS Energy Lett.* **2018**, *3* (6), 1279–1286.

(303) Xu, B.; Wang, W.; Zhang, X.; Liu, H.; Zhang, Y.; Mei, G.; Chen, S.; Wang, K.; Wang, L.; Sun, X. W. Electric Bias Induced Degradation in Organic-Inorganic Hybrid Perovskite Light-Emitting Diodes. *Sci. Rep.* **2018**, *8* (1), 1–7.

(304) Cho, H.; Kim, Y.-H.; Wolf, C.; Lee, H.-D.; Lee, T.-W. Improving the Stability of Metal Halide Perovskite Materials and Light-emitting Diodes. *Adv. Mater.* **2018**, *30* (42), 1704587.

(305) Lee, H.; Ko, D.; Lee, C. Direct Evidence of Ion-Migration-Induced Degradation of Ultrabright Perovskite Light-Emitting Diodes. *ACS Appl. Mater. Interfaces* **2019**, *11* (12), 11667–11673.

(306) Dong, Q.; Lei, L.; Mendes, J.; So, F. Operational Stability of Perovskite Light Emitting Diodes. *J. Phys. Mater.* **2020**, *3* (1), 012002.

(307) Ye, Q.-Q.; Li, M.; Shi, X.-B.; Zhuo, M.-P.; Wang, K.-L.; Igbari, F.; Wang, Z.-K.; Liao, L.-S. UV-Stable and Highly Efficient Perovskite Solar Cells by Employing Wide Band Gap $NaTaO_3$ as an Electron-Transporting Layer. *ACS Appl. Mater. Interfaces* **2020**, *12* (19), 21772–21778.

(308) Dang, Z.; Luo, Y.; Xu, Y.; gao, P.; Wang, X.-S. Transformation and Degradation of Metal Halide Perovskites Induced by Energetic Electrons and Their Practical Implications. *Nano Futur.* **2021**.

(309) Dang, Z.; Luo, Y.; Wang, X.-S.; Imran, M.; Gao, P. Electron-Beam-Induced Degradation of Halide-Perovskite-Related Semiconductor Nanomaterials. *Chin. Opt. Lett.* **2021**, *19* (3), 030002.

(310) Rothmann, M. U.; Li, W.; Etheridge, J.; Cheng, Y.-B. Microstructural Characterisations of Perovskite Solar Cells - From Grains to Interfaces: Techniques, Features, and Challenges. *Adv. Energy Mater.* **2017**, *7* (23), 1700912.

(311) Jariwala, S.; Sun, H.; Adhyaksa, G. W. P.; Lof, A.; Muscarella, L. A.; Ehrler, B.; Garnett, E. C.; Ginger, D. S. Local Crystal Misorientation Influences Non-Radiative Recombination in Halide Perovskites. *Joule* **2019**, *3* (12), 3048–3060.

(312) Tennyson, E. M.; Doherty, T. A.; Stranks, S. D. Heterogeneity at Multiple Length Scales in Halide Perovskite Semiconductors. *Nat. Rev. Mater.* **2019**, *4* (9), 573–587.

(313) Marronnier, A.; Roma, G.; Boyer-Richard, S.; Pedesseau, L.; Jancu, J.-M.; Bonnassieux, Y.; Katan, C.; Stoumpos, C. C.; Kanatzidis, M. G.; Even, J. Anharmonicity and Disorder in the Black Phases of Cesium Lead Iodide Used for Stable Inorganic Perovskite Solar Cells. *ACS Nano* **2018**, *12* (4), 3477–3486.

(314) Lee, J.-W.; Bae, S.-H.; De Marco, N.; Hsieh, Y.-T.; Dai, Z.; Yang, Y. The Role of Grain Boundaries in Perovskite Solar Cells. *Mater. Today Energy* **2018**, *7*, 149–160.

(315) Yang, B.; Ming, W.; Du, M.-H.; Keum, J. K.; Puretzky, A. A.; Rouleau, C. M.; Huang, J.; Geohegan, D. B.; Wang, X.; Xiao, K. Real-Time Observation of Order-Disorder Transformation of Organic Cations Induced Phase Transition and Anomalous Photoluminescence in Hybrid Perovskites. *Adv. Mater.* **2018**, *30* (22), 1705801.

(316) Adhyaksa, G. W. P.; Brittman, S.; Āboliņš, H.; Lof, A.; Li, X.; Keelor, J. D.; Luo, Y.; Duevski, T.; Heeren, R. M. A.; Ellis, S. R.; Fenning, D. P.; Garnett, E. C. Understanding Detrimental and Beneficial Grain Boundary Effects in Halide Perovskites. *Adv. Mater.* **2018**, *30* (52), 1804792.

(317) Chu, Z.; Yang, M.; Schulz, P.; Wu, D.; Ma, X.; Seifert, E.; Sun, L.; Li, X.; Zhu, K.; Lai, K. Impact of Grain Boundaries on Efficiency and Stability of Organic-Inorganic Trihalide Perovskites. *Nat. Commun.* **2017**, *8* (1), 2230.

(318) Jin, B.; Zhao, D.; Liang, F.; Liu, L.; Liu, D.; Wang, P.; Qiu, M. Electron-Beam Irradiation Induced Regulation of Surface Defects in Lead Halide Perovskite Thin Films. *Research* **2021**, *2021*.

(319) Alberti, A.; Bongiorno, C.; Smecca, E.; Deretzis, I.; La Magna, A.; Spinella, C. Pb Clustering and PbI_2 Nanofragmentation during Methylammonium Lead Iodide Perovskite Degradation. *Nat. Commun.* **2019**, *10* (1), 2196.

(320) Minns, J. L.; Zajdel, P.; Chernyshov, D.; Van Beek, W.; Green, M. A. Structure and Interstitial Iodide Migration in Hybrid Perovskite Methylammonium Lead Iodide. *Nat. Commun.* **2017**, *8* (1), 1–5.

(321) Azpiroz, J. M.; Mosconi, E.; Bisquert, J.; De Angelis, F. Defect Migration in Methylammonium Lead Iodide and Its Role in Perovskite Solar Cell Operation. *Energy Environ. Sci.* **2015**, *8* (7), 2118–2127.

(322) Haruyama, J.; Sodeyama, K.; Han, L.; Tateyama, Y. First-Principles Study of Ion Diffusion in Perovskite Solar Cell Sensitizers. *J. Am. Chem. Soc.* **2015**, *137* (32), 10048–10051.

(323) Yang, D.; Ming, W.; Shi, H.; Zhang, L.; Du, M.-H. Fast Diffusion of Native Defects and Impurities in Perovskite Solar Cell Material $CH_3NH_3PbI_3$. *Chem. Mater.* **2016**, *28* (12), 4349–4357.

(324) Li, C.; Tscheuschner, S.; Paulus, F.; Hopkinson, P. E.; Kießling, J.; Köhler, A.; Vaynzof, Y.; Huettner, S. Iodine Migration and Its Effect on Hysteresis in Perovskite Solar Cells. *Adv. Mater.* **2016**, *28* (12), 2446–2454.

(325) Eames, C.; Frost, J. M.; Barnes, P. R. F.; O'Regan, B. C.; Walsh, A.; Islam, M. S. Ionic Transport in Hybrid Lead Iodide Perovskite Solar Cells. *Nat. Commun.* **2015**, *6* (1), 7497.

(326) Xiao, C.; Li, Z.; Guthrey, H.; Moseley, J.; Yang, Y.; Wozny, S.; Moutinho, H.; To, B.; Berry, J. J.; Gorman, B.; Yan, Y.; Zhu, K.; Al-Jassim, M. Mechanisms of Electron-Beam-Induced Damage in Perovskite Thin Films Revealed by Cathodoluminescence Spectroscopy. *J. Phys. Chem. C* **2015**, *119* (48), 26904–26911.

(327) Yu, Y.; Zhang, D.; Kisielowski, C.; Dou, L.; Kornienko, N.; Bekenstein, Y.; Wong, A. B.; Alivisatos, A. P.; Yang, P. Atomic Resolution Imaging of Halide Perovskites. *Nano Lett.* **2016**, *16* (12), 7530–7535.

(328) Li, Y.; Zhou, W.; Li, Y.; Huang, W.; Zhang, Z.; Chen, G.; Wang, H.; Wu, G.-H.; Rolston, N.; Vila, R.; Chiu, W.; Cui, Y. Unravelling Degradation Mechanisms and Atomic Structure of Organic-Inorganic Halide Perovskites by Cryo-EM. *Joule* **2019**, *3* (11), 2854–2866.

(329) Jiang, N.; Spence, J. C. H. On the Dose-Rate Threshold of Beam Damage in TEM. *Ultramicroscopy* **2012**, *113*, 77–82.

(330) Favaudon, V.; Caplier, L.; Monceau, V.; Pouzoulet, F.; Sayarath, M.; Fouillade, C.; Poupon, M.-F.; Brito, I.; Hupé, P.; Bourhis, J.; Hall, J.; Fontaine, J.-J.; Vozenin, M.-C. Ultrahigh Dose-Rate FLASH Irradiation Increases the Differential Response between Normal and Tumor Tissue in Mice. *Sci. Transl. Med.* **2014**, *6* (245), 245ra93-245ra93.

(331) Johnston-Peck, A. C.; DuChene, J. S.; Roberts, A. D.; Wei, W. D.; Herzing, A. A. Dose-Rate-Dependent Damage of Cerium Dioxide in the Scanning Transmission Electron Microscope. *Ultramicroscopy* **2016**, *170*, 1–9.

(332) Babayan, N.; Hovhannisyan, G.; Grigoryan, B.; Grigoryan, R.; Sarkisyan, N.; Tsakanova, G.; Haroutiunian, S.; Aroutiounian, R. Dose-Rate Effect of Ultrashort Electron Beam Radiation on DNA Damage and Repair in Vitro. *J. Radiat. Res. (Tokyo)* **2017**, *58* (6), 894–897.

(333) Lang, F.; Nickel, N. H.; Bundesmann, J.; Seidel, S.; Denker, A.; Albrecht, S.; Brus, V. V.; Rappich, J.; Rech, B.; Landi, G.; Neitzert, H. C. Radiation Hardness and Self-Healing of Perovskite Solar Cells. *Adv. Mater.* **2016**, *28* (39), 8726–8731.

(334) Nie, W.; Blancon, J.-C.; Neukirch, A. J.; Appavoo, K.; Tsai, H.; Chhowalla, M.; Alam, M. A.; Sfeir, M. Y.; Katan, C.; Even, J.; Tretiak, S.; Crochet, J. J.; Gupta, G.; Mohite, A. D. Light-Activated Photocurrent Degradation and Self-Healing in Perovskite Solar Cells. *Nat. Commun.* **2016**, *7* (1), 11574.

(335) Laschinsky, L.; Baumann, M.; Beyreuther, E.; Enghardt, W.; Kaluza, M.; Karsch, L.; Lessmann, E.; Naumburger, D.; Nicolai, M.; Richter, C.; Sauerbrey, R.; Schlenvoigt, H.-P.; Pawelke, J. Radiobiological Effectiveness of Laser Accelerated Electrons in Comparison to Electron Beams from a Conventional Linear Accelerator. *J. Radiat. Res. (Tokyo)* **2012**, *53* (3), 395–403.

(336) Bonham, R. A.; Kennerly, R. E. Pulsed Electron Beams to Reduce Radiation Damage? *Ann. N. Y. Acad. Sci.* **1978**, *306* (1 Short Wavelen), 85–94.

(337) Chapman, H. N.; Caleman, C.; Timneanu, N. Diffraction before Destruction. *Philos. Trans. R. Soc. B Biol. Sci.* **2014**, *369* (1647), 20130313.

(338) Egerton, R. F. Outrun Radiation Damage with Electrons? *Adv. Struct. Chem. Imaging* **2015**, *1* (1), 5.

(339) Spence, J. C. H.; Subramanian, G.; Musumeci, P. Hollow Cone Illumination for Fast TEM, and Outrunning Damage with Electrons. *J. Phys. B At. Mol. Opt. Phys.* **2015**, *48* (21), 214003.

(340) Spence, J. C. H. Outrunning Damage: Electrons vs X-Rays—Timescales and Mechanisms. *Struct. Dyn.* **2017**, *4* (4), 044027.

(341) Gahlmann, A.; Tae Park, S.; Zewail, A. H. Ultrashort Electron Pulses for Diffraction, Crystallography and Microscopy: Theoretical and Experimental Resolutions. *Phys. Chem. Chem. Phys.* **2008**, *10* (20), 2894.

(342) Li, R. K.; Musumeci, P. Single-Shot MeV Transmission Electron Microscopy with Picosecond Temporal Resolution. *Phys. Rev. Appl.* **2014**, *2* (2), 024003.

(343) Kealhofer, C.; Schneider, W.; Ehberger, D.; Ryabov, A.; Krausz, F.; Baum, P. All-Optical Control and Metrology of Electron Pulses. *Science* **2016**, *352* (6284), 429–433.

(344) Mankos, M.; Shadman, K.; Siwick, B. J. A Novel Electron Mirror Pulse Compressor. *Ultramicroscopy* **2017**, *183*, 77–83.

(345) Qiu, J.; Ha, G.; Jing, C.; Baryshev, S. V.; Reed, B. W.; Lau, J. W.; Zhu, Y. GHz Laser-Free Time-Resolved Transmission Electron Microscopy: A Stroboscopic High-Duty-Cycle Method. *Ultramicroscopy* **2016**, *161*, 130–136.

(346) Verhoeven, W.; van Rens, J. F. M.; Kieft, E. R.; Mutsaers, P. H. A.; Luiten, O. J. High Quality Ultrafast Transmission Electron Microscopy Using Resonant Microwave Cavities. *Ultramicroscopy* **2018**, *188*, 85–89.

(347) Bormann, R.; Strauch, S.; Schäfer, S.; Ropers, C. An Ultrafast Electron Microscope Gun Driven by Two-Photon Photoemission from a Nanotip Cathode. *J. Appl. Phys.* **2015**, *118* (17), 173105.

(348) Houdellier, F.; Caruso, G. M.; Weber, S.; Kociak, M.; Arbouet, A. Development of a High Brightness Ultrafast Transmission Electron Microscope Based on a Laser-Driven Cold Field Emission Source. *Ultramicroscopy* **2018**, *186*, 128–138.

(349) Flannigan, D. J.; Lobastov, V. A.; Zewail, A. H. Controlled Nanoscale Mechanical Phenomena Discovered with Ultrafast Electron Microscopy. *Angew. Chem. Int. Ed.* **2007**, *46* (48), 9206–9210.

(350) Kwon, O.-H.; Ortalan, V.; Zewail, A. H. Macromolecular Structural Dynamics Visualized by Pulsed Dose Control in 4D Electron Microscopy. *Proc. Natl. Acad. Sci.* **2011**, *108* (15), 6026–6031.

(351) Kisielowski, C.; Specht, P.; Freitag, B.; Kieft, E. R.; Verhoeven, W.; van Rens, J. F. M.; Mutsaers, P.; Luiten, J.; Rozeveld, S.; Kang, J.; McKenna, A. J.; Nickias, P.; Yancey, D. F. Discovering Hidden Material Properties of $MgCl_2$ at Atomic Resolution with Structured Temporal Electron Illumination of Picosecond Time Resolution. *Adv. Funct. Mater.* **2019**, *29* (11), 1807818.

(352) Laschinsky, L.; Karsch, L.; Leßmann, E.; Oppelt, M.; Pawelke, J.; Richter, C.; Schürer, M.; Beyreuther, E. Radiobiological Influence of Megavoltage Electron Pulses of Ultra-High Pulse Dose Rate on Normal Tissue Cells. *Radiat. Environ. Biophys.* **2016**, *55* (3), 381–391.

(353) VandenBussche, E. J.; Flannigan, D. J. Reducing Radiation Damage in Soft Matter with Femtosecond-Timed Single-Electron Packets. *Nano Lett.* **2019**, *19* (9), 6687–6694.

(354) Choe, H.; Ponomarev, I.; Montgomery, E.; Lau, J. W.; Zhu, Y.; Zhao, Y.; Liu, A.; Kanareykin, A.; Jing, C. Mitigation of Radiation Damage in Macromolecules via Tunable Ultrafast Stroboscopic TEM. *bioRxiv* **2020**, 2020.05.15.099036.

(355) Ceratti, D. R.; Rakita, Y.; Cremonesi, L.; Tenne, R.; Kalchenko, V.; Elbaum, M.; Oron, D.; Potenza, M. A. C.; Hodes, G.; Cahen, D. Self-Healing Inside $APbBr_3$ Halide Perovskite Crystals. *Adv. Mater.* **2018**, *30* (10), 1706273.

(356) Aduev, B. P.; Belokurov, G. M.; Grechin, S. S.; Tupitsin, E. V. Peculiarities of the Kinetics of Explosive Decomposition of Silver Azide Initiated by a Pulsed Electron Beam. *Tech. Phys. Lett.* **2004**, *30* (9), 774–775.

(357) Botman, J. I. M.; Derksen, A. T. A. M.; van Herk, A. M.; Jung, M.; Kuchta, F.-D.; Manders, L. G.; Timmermans, C. J.; de Voigt, M. J. A. A Linear Accelerator as a Tool for Investigations into Free Radical Polymerization Kinetics and Mechanisms by Means of Pulsed Electron Beam Polymerization. *Nucl. Instrum. Methods Phys. Res. Sect. B Beam Interact. Mater. At.* **1998**, *139* (1), 490–494.

(358) Bretagne, J.; Godart, J.; Puech, V. Kinetic Study of Electron Beam Excited Argon. *Beitr. Aus Plasmaphys.* **1983**, *23* (3), 295–312.

(359) Fricke, H.; Thomas, J. K. Pulsed Electron Beam Kinetics. *Radiat. Res. Suppl.* **1964**, *4*, 35–53.

(360) Lorents, D. C. The Physics of Electron Beam Excited Rare Gases at High Densities. *Phys. BC* **1976**, *82* (1), 19–26.

(361) Lysenko, E. N.; Vlasov, V. A.; Surzhikov, A. P. Investigation of Kinetics of Lithium Ferrite Formation under Electron Beam Treatment. *Nucl. Instrum. Methods Phys. Res. Sect. B Beam Interact. Mater. At.* **2020**, *466*, 31–36.

(362) Morozov, A.; Krücken, R.; Wieser, J.; Ulrich, A. Gas Kinetic Studies Using a Table-Top Set-up with Electron Beam Excitation: Quenching of Molecular Nitrogen Emission by Water Vapour. *Eur. Phys. J. - At. Mol. Opt. Plasma Phys.* **2005**, *33* (2), 207–211.

(363) Penetrante, B. M. Simultaneous Removal of NO_x and SO_2 from Combustion Flue Gas by Pulsed Electron Beams. *Combust. Sci. Technol.* **1998**, *133* (1–3), 135–150.

(364) Yakovlev, S.; Libera, M. Dose-Limited Spectroscopic Imaging of Soft Materials by Low-Loss EELS in the Scanning Transmission Electron Microscope. *Micron* **2008**, *39* (6), 734–740.

(365) Pushkarev, A. I.; Remnev, G. E. Vibrational Character of the Hydrogen-Oxidation Process Initiated by a Pulsed Electron Beam. *Combust. Explos. Shock Waves* **2005**, *41* (4), 375–378.

(366) Onda, K.; Kasuga, Y.; Kato, K.; Fujiwara, M.; Tanimoto, M. Electric Discharge Removal of SO_2 and NO_x from Combustion Flue Gas by Pulsed Corona Discharge. *Energy Convers. Manag.* **1997**, *38* (10), 1377–1387.

(367) Tandon, J. L.; Golecki, I.; Nicolet, M.; Sadana, D. K.; Washburn, J. Pulsed Electron Beam Induced Recrystallization and Damage in GaAs. *Appl. Phys. Lett.* **1979**, *35* (11), 867–869.

(368) Greenwald, A. C.; Kirkpatrick, A. R.; Little, R. G.; Minnucci, J. A. Pulsed-electron-beam Annealing of Ion-implantation Damage. *J. Appl. Phys.* **1979**, *50* (2), 783–787.

(369) Kennedy, E. F.; Lau, S. S.; Golecki, I.; Mayer, J. W.; Tseng, W.; Minnucci, J. A.; Kirkpatrick, A. R. Pulsed Electron Beam Annealing of Ion Implanted Si Layers. *AIP Conf. Proc.* **1979**, *50* (1), 470–474.

(370) Remnev, G. E.; Pushkarev, A. I. Research of Chain Plasmochemical Synthesis of Superdispersed Silicon Dioxide by Pulsed Electron Beam. *IEEJ Trans. Fundam. Mater.* **2004**, *124* (6), 483–486.

(371) Schindelin, J.; Arganda-Carreras, I.; Frise, E.; Kaynig, V.; Longair, M.; Pietzsch, T.; Preibisch, S.; Rueden, C.; Saalfeld, S.; Schmid, B.; Tinevez, J.-Y.; White, D. J.; Hartenstein, V.; Eliceiri, K.; Tomancak, P.; Cardona, A. Fiji: An Open-Source Platform for Biological-Image Analysis. *Nat. Methods* **2012**, *9* (7), 676–682.

(372) Egerton, R. F.; Li, P.; Malac, M. Radiation Damage in the TEM and SEM. *Micron* **2004**, *35* (6), 399–409.

(373) Antipenko, A. P.; Bochek, G. L.; Blazhevich, S. V.; Kulibaba, V. I.; Maslov, N. I.; Truten', V. I.; Shramenko, B. I.; Shul'Ga, N. F. The Influence of Crystal Thickness on Scattering and Radiation of High-Energy Electrons in Oriented Crystals. *Nucl. Instrum. Methods Phys. Res. Sect. B Beam Interact. Mater. At.* **1990**, *48* (1), 291–295.

(374) Teare, P. W. The Crystal Structure of Orthorhombic Hexatriacontane, $C_{36}H_{74}$. *Acta Crystallogr.* **1959**, *12* (4), 294–300.

(375) Nyburg, S. C.; Potworowski, J. A. Prediction of Unit Cells and Atomic Coordinates for the *n* -Alkanes. *Acta Crystallogr. B* **1973**, *29* (2), 347–352.

(376) Dorset, D. L. The Interpretation of Quasi-Kinematical Single-Crystal Electron Diffraction Intensity Data from Paraffins. *Acta Crystallogr.* **1976**, *32* (2), 207–215.

(377) Dorset, D. L. Electron Diffraction Intensities from Bent Molecular Organic Crystals. *Acta Crystallogr. A* **1980**, *36* (4), 592–600.

(378) Momma, K.; Izumi, F. VESTA 3 for Three-Dimensional Visualization of Crystal, Volumetric and Morphology Data. *J. Appl. Crystallogr.* **2011**, *44* (6), 1272–1276.

(379) Du, D. X.; Reisbick, S. A.; Flannigan, D. J. UEMtomaton: A Source-Available Platform to Aid in Start-up of Ultrafast Electron Microscopy Labs. *Ultramicroscopy* **2021**, *223*, 113235.

(380) Bullough, P.; Henderson, R. Use of Spot-Scan Procedure for Recording Low-Dose Micrographs of Beam-Sensitive Specimens. *Ultramicroscopy* **1987**, *21* (3), 223–230.

(381) Downing, K. H. Observations of Restricted Beam-Induced Specimen Motion with Small-Spot Illumination. *Ultramicroscopy* **1988**, *24* (4), 387–397.

(382) Varlot, K.; Martin, J. M.; Quet, C.; Kihn, Y. Towards Sub-Nanometer Scale EELS Analysis of Polymers in the TEM. *Ultramicroscopy* **1997**, *68* (2), 123–133.

(383) Reisbick, S. A. Defect-Mediated Structural Dynamics in 1T-TaS_2 Using Ultrafast Electron Microscopy, University of Minnesota, Minneapolis, 2020.

(384) Han, T.-R. T.; Zhou, F.; Malliakas, C. D.; Duxbury, P. M.; Mahanti, S. D.; Kanatzidis, M. G.; Ruan, C.-Y. Exploration of Metastability and Hidden Phases in Correlated Electron Crystals Visualized by Femtosecond Optical Doping and Electron Crystallography. *Sci. Adv.* **2015**, *1* (5), e1400173.

(385) Vanacore, G. M.; van der Veen, R. M.; Zewail, A. H. Origin of Axial and Radial Expansions in Carbon Nanotubes Revealed by Ultrafast Diffraction and Spectroscopy. *ACS Nano* **2015**, *9* (2), 1721–1729.

(386) Haupt, K.; Eichberger, M.; Erasmus, N.; Rohwer, A.; Demsar, J.; Rossnagel, K.; Schwoerer, H. Ultrafast Metamorphosis of a Complex Charge-Density Wave. *Phys. Rev. Lett.* **2016**, *116* (1), 016402.

(387) Yang, D.-S.; Baum, P.; Zewail, A. H. Ultrafast Electron Crystallography of the Cooperative Reaction Path in Vanadium Dioxide. *Struct. Dyn.* **2016**, *3* (3), 034304.

(388) Yang, J.; Guehr, M.; Shen, X.; Li, R.; Vecchione, T.; Coffee, R.; Corbett, J.; Fry, A.; Hartmann, N.; Hast, C.; Hegazy, K.; Jobe, K.; Makasyuk, I.; Robinson, J.; Robinson, M. S.; Vetter, S.; Weathersby, S.; Yoneda, C.; Wang, X.; Centurion, M. Diffractive Imaging of Coherent Nuclear Motion in Isolated Molecules. *Phys. Rev. Lett.* **2016**, *117* (15), 153002.

(389) Cesar, D.; Maxson, J.; Musumeci, P.; Sun, Y.; Harrison, J.; Frigola, P.; O'Shea, F. H.; To, H.; Alesini, D.; Li, R. K. Demonstration of Single-Shot Picosecond Time-Resolved MeV Electron Imaging Using a Compact Permanent Magnet Quadrupole Based Lens. *Phys. Rev. Lett.* **2016**, *117* (2), 024801.

(390) Mancini, G. F.; Latychevskaia, T.; Pennacchio, F.; Reguera, J.; Stellacci, F.; Carbone, F. Order/Disorder Dynamics in a Dodecanethiol-Capped Gold Nanoparticles Supracrystal by Small-Angle Ultrafast Electron Diffraction. *Nano Lett.* **2016**, *16* (4), 2705–2713.

(391) Frigge, T.; Hafke, B.; Witte, T.; Krenzer, B.; Streubühr, C.; Samad Syed, A.; Mikšić Trontl, V.; Avigo, I.; Zhou, P.; Ligges, M.; von der Linde, D.; Bovensiepen, U.; Horn-von Hoegen, M.; Wippermann, S.; Lücke, A.; Sanna, S.; Gerstmann, U.; Schmidt, W. G. Optically Excited Structural Transition in Atomic Wires on Surfaces at the Quantum Limit. *Nature* **2017**, *544* (7649), 207–211.

(392) Hada, M.; Saito, S.; Tanaka, S.; Sato, R.; Yoshimura, M.; Mouri, K.; Matsuo, K.; Yamaguchi, S.; Hara, M.; Hayashi, Y.; Röhricht, F.; Herges, R.; Shigeta, Y.; Onda, K.; Miller, R. J. D. Structural Monitoring of the Onset of Excited-State Aromaticity in a Liquid Crystal Phase. *J. Am. Chem. Soc.* **2017**, *139* (44), 15792–15800.

(393) Konstantinova, T.; Rameau, J. D.; Reid, A. H.; Abdurazakov, O.; Wu, L.; Li, R.; Shen, X.; Gu, G.; Huang, Y.; Rettig, L.; Avigo, I.; Ligges, M.; Freericks, J. K.; Kemper, A. F.; Dürr, H. A.; Bovensiepen, U.; Johnson, P. D.; Wang, X.; Zhu, Y. Nonequilibrium Electron and Lattice Dynamics of Strongly Correlated $Bi_2Sr_2CaCu_2O_{8+d}$ Single Crystals. *Sci. Adv.* **2018**, *4* (4), 7427.

(394) Stern, M. J.; René de Cotret, L. P.; Otto, M. R.; Chatelain, R. P.; Boisvert, J.-P.; Sutton, M.; Siwick, B. J. Mapping Momentum-Dependent Electron-Phonon Coupling and Nonequilibrium Phonon Dynamics with Ultrafast Electron Diffuse Scattering. *Phys. Rev. B* **2018**, *97* (16), 165416.

(395) Najafi, E.; Liao, B.; Scarborough, T.; Zewail, A. Imaging Surface Acoustic Wave Dynamics in Semiconducting Polymers by Scanning Ultrafast Electron Microscopy. *Ultramicroscopy* **2018**, *184*, 46–50.

(396) Schliep, K. B.; Quarterman, P.; Wang, J.-P.; Flannigan, D. J. Picosecond Fresnel Transmission Electron Microscopy. *Appl. Phys. Lett.* **2017**, *110* (22), 222404.

(397) Takaoka, A.; Ura, K. Accuracy of Temperature Measurement in Micro-Areas of Polycrystalline Film with Transmission Electron Microscope. *Meas. Sci. Technol.* **1994**, *5* (2), 105–109.

(398) Killean, R. C. G. An Investigation of the Debye-Waller Factor and Debye Temperature of Aluminium Using Nearest Neighbour Central Force Pair Interactions. *J. Phys. F Met. Phys.* **1974**, *4* (11), 1908–1915.

(399) Shukla, R. C.; Hübschle, H. Atomic Mean-Square Displacement of a Solid: A Green's-Function Approach. *Phys. Rev. B* **1989**, *40* (3), 1555–1559.

(400) Nix, F. C.; MacNair, D. The Thermal Expansion of Pure Metals: Copper, Gold, Aluminum, Nickel, and Iron. *Phys. Rev.* **1941**, *60* (8), 597–605.

(401) McDonald, D. L. Neutron Diffraction Study of the Debye–Waller Factor for Aluminum. *Acta Crystallogr.* **1967**, *23* (2), 185–191.

(402) Brown, L.; Hovden, R.; Huang, P.; Wojcik, M.; Muller, D. A.; Park, J. Twinning and Twisting of Tri- and Bilayer Graphene. *Nano Lett.* **2012**, *12* (3), 1609–1615.

(403) Shevitski, B.; Mecklenburg, M.; Hubbard, W. A.; White, E. R.; Dawson, B.; Lodge, M. S.; Ishigami, M.; Regan, B. C. Dark-Field Transmission Electron Microscopy and the Debye-Waller Factor of Graphene. *Phys. Rev. B* **2013**, *87* (4), 045417.

(404) Meyer, J. C.; Geim, A. K.; Katsnelson, M. I.; Novoselov, K. S.; Obergfell, D.; Roth, S.; Girit, C.; Zettl, A. On the Roughness of Single- and Bi-Layer Graphene Membranes. *Solid State Commun.* **2007**, *143* (1), 101–109.

(405) Mitchell, D. R. G. Circular Hough Transform Diffraction Analysis: A Software Tool for Automated Measurement of Selected Area Electron Diffraction Patterns within Digital Micrograph^{TM}. *Ultramicroscopy* **2008**, *108* (4), 367–374.

(406) Meyer, J. C.; Geim, A. K.; Katsnelson, M. I.; Novoselov, K. S.; Booth, T. J.; Roth, S. The Structure of Suspended Graphene Sheets. *Nature* **2007**, *446* (7131), 60–63.

(407) Krämer; Mayer. Using the Hough Transform for HOLZ Line Identification in Convergent Beam Electron Diffraction: Hough Transform for HOLZ Line Identification. *J. Microsc.* **1999**, *194* (1), 2–11.

(408) Mecklenburg, M.; Hubbard, W. A.; White, E. R.; Dhall, R.; Cronin, S. B.; Aloni, S.; Regan, B. C. Nanoscale Temperature Mapping in Operating Microelectronic Devices. *Science* **2015**, *347* (6222), 629–632.

(409) Tracy, D. P.; Knorr, D. B. Texture and Microstructure of Thin Copper Films. *J. Electron. Mater.* **1993**, *22* (6), 611–616.

(410) Koch, R. The Intrinsic Stress of Polycrystalline and Epitaxial Thin Metal Films. *J. Phys. Condens. Matter* **1994**, *6* (45), 9519–9550.

(411) Thompson, C. V. Structure Evolution During Processing of Polycrystalline Films. *Annu. Rev. Mater. Sci.* **2000**, *30* (1), 159–190.

(412) Thompson, C. V.; Carel, R. Stress and Grain Growth in Thin Films. *J. Mech. Phys. Solids* **1996**, *44* (5), 657–673.

(413) Gianola, D. S.; Van Petegem, S.; Legros, M.; Brandstetter, S.; Van Swygenhoven, H.; Hemker, K. J. Stress-Assisted Discontinuous Grain Growth and Its Effect on the Deformation Behavior of Nanocrystalline Aluminum Thin Films. *Acta Mater.* **2006**, *54* (8), 2253–2263.

(414) Niekiel, F.; Kraschewski, S. M.; Schweizer, P.; Butz, B.; Spiecker, E. Texture Evolution and Microstructural Changes during Solid-State Dewetting: A Correlative Study by Complementary *In Situ* TEM Techniques. *Acta Mater.* **2016**, *115*, 230–241.

(415) Hu, J.; Vanacore, G. M.; Cepellotti, A.; Marzari, N.; Zewail, A. H. Rippling Ultrafast Dynamics of Suspended 2D Monolayers, Graphene. *Proc. Natl. Acad. Sci.* **2016**, *113* (43), E6555–E6561.

(416) Falkovsky, L. A.; Mishchenko, E. G. Electron-Lattice Kinetics of Metals Heated by Ultrashort Laser Pulses. *J. Exp. Theor. Phys.* **1999**, *88* (1), 84–88.

(417) Chen, J. K.; Beraun, J. E.; Grimes, L. E.; Tzou, D. Y. Modeling of Femtosecond Laser-Induced Non-Equilibrium Deformation in Metal Films. *Int. J. Solids Struct.* **2002**, *39* (12), 3199–3216.

(418) van Omme, J. T.; Zakhozheva, M.; Spruit, R. G.; Sholkina, M.; Pérez Garza, H. H. Advanced Microheater for in Situ Transmission Electron Microscopy; Enabling Unexplored Analytical Studies and Extreme Spatial Stability. *Ultramicroscopy* **2018**, *192*, 14–20.

(419) Hu, B. Y.-K.; Stanton, C. J.; Wilkins, J. W. Acoustic Mode with Time-Dependent Phase Velocity in Photoexcited Semiconductors. *Phys. Rev. B* **1991**, *44* (20), 11067–11071.

(420) Kutt, W. A.; Albrecht, W.; Kurz, H. Generation of Coherent Phonons in Condensed Media. *IEEE J. Quantum Electron.* **1992**, *28* (10), 2434–2444.

(421) Mutti, P.; Sklar, Z.; Briggs, G. A. D.; Jeynes, C. Elastic Properties of GaAs during Amorphization by Ion Implantation. *J. Appl. Phys.* **1995**, *77* (6), 2388–2392.

(422) Rubanov, S.; Munroe, P. R. Invesitagation of the Structure of Damage Layers in TEM Samples Prepared Using a FIB. *J. Mater. Sci. Lett.* **2001**, *20* (13), 1181–1183.

(423) Kato, N. I. Reducing Focused Ion Beam Damage to Transmission Electron Microscopy Samples. *J. Electron Microsc. (Tokyo)* **2004**, *53* (5), 451–458.

(424) An, B.-S.; Kwon, Y.; Cha, H.-W.; Kang, M.-C.; Oh, J.-S.; Yang, C.-W. Quantification of Crystallinity Using Zero-Loss Filtered Electron Diffraction. *Microsc. Res. Tech.* **2019**, *82* (1), 39–46.

(425) VandenBussche, E. J.; Flannigan, D. J. Sources of Error in Debye–Waller-Effect Measurements Relevant to Studies of Photoinduced Structural Dynamics. *Ultramicroscopy* **2019**, *196*, 111–120.

(426) Cottam, R. I.; Saunders, G. A. The Elastic Constants of GaAs from 2 K to 320 K. *J. Phys. C Solid State Phys.* **1973**, *6* (13), 2105–2118.

(427) Schall, J. D.; Gao, G.; Harrison, J. A. Elastic Constants of Silicon Materials Calculated as a Function of Temperature Using a Parametrization of the Second-Generation Reactive Empirical Bond-Order Potential. *Phys. Rev. B* **2008**, *77* (11), 115209.

(428) De Sandre, G.; Colombo, L.; Bottani, C. Calculation of Elastic Constants in Defected and Amorphous Silicon by Quantum Simulations. *Phys. Rev. B* **1996**, *54* (17), 11857–11860.

(429) Ridgway, M. C.; Glover, C. J.; Foran, G. J.; Yu, K. M. Characterization of the Local Structure of Amorphous GaAs Produced by Ion Implantation. *J. Appl. Phys.* **1998**, *83* (9), 4610–4614.

(430) Duggal, A. R.; Rogers, J. A.; Nelson, K. A. Real-time Optical Characterization of Surface Acoustic Modes of Polyimide Thin-film Coatings. *J. Appl. Phys.* **1992**, *72* (7), 2823–2839.

(431) Liu, R.; Sanders, G. D.; Stanton, C. J.; Kim, C. S.; Yahng, J. S.; Jho, Y. D.; Yee, K. J.; Oh, E.; Kim, D. S. Femtosecond Pump-Probe Spectroscopy of Propagating Coherent Acoustic Phonons in $In_xGa_{1-x}N/GaN$ Heterostructures. *Phys. Rev. B* **2005**, *72* (19), 195335.

(432) Ogi, H.; Fujii, M.; Nakamura, N.; Shagawa, T.; Hirao, M. Resonance Acoustic-Phonon Spectroscopy for Studying Elasticity of Ultrathin Films. *Appl. Phys. Lett.* **2007**, *90* (19), 191906.

(433) Hettich, M.; Jacob, K.; Ristow, O.; He, C.; Mayer, J.; Schubert, M.; Gusev, V.; Bruchhausen, A.; Dekorsy, T. Imaging of a Patterned and Buried Molecular Layer by Coherent Acoustic Phonon Spectroscopy. *Appl. Phys. Lett.* **2012**, *101* (19), 191606.

(434) Mante, P.-A.; Stoumpos, C. C.; Kanatzidis, M. G.; Yartsev, A. Electron–Acoustic Phonon Coupling in Single Crystal $CH_3NH_3PbI_3$ Perovskites Revealed by Coherent Acoustic Phonons. *Nat. Commun.* **2017**, *8* (1), 14398.

(435) Dorset, D. L.; Holland, F. M.; Fryer, J. R. The “Quasi-Thermal” Mechanism for Electron Beam Damage of n-Paraffins. *Ultramicroscopy* **1984**, *13* (3), 305–310.

(436) Grubb, D. T.; Groves, G. W. Rate of Damage of Polymer Crystals in the Electron Microscope: Dependence on Temperature and Beam Voltage. *Philos. Mag.* **1971**, *24* (190), 815–828.

(437) Salih, S. M.; Cosslett, V. E. Radiation Damage in Electron Microscopy of Organic Materials: Effect of Low Temperatures. *J. Microsc.* **1975**, *105* (3), 269–276.

(438) Dorset, D. L. Electron Crystal Structure Analysis of Small Organic Molecules. *J. Electron Microsc. Tech.* **1985**, *2* (2), 89–128.

(439) Dorset, D. L. Structural Changes in Electron-Irradiated Paraffin Crystals at <15 K and Their Relevance to Lattice Imaging Experiments. *J. Electron Microsc. Tech.* **1985**, *17* (3), 229–235.

(440) Ohno, T. Intensity Changes Induced by Beam Damage in Electron Diffraction from Behenic Acid Multiple Monolayers. *Ultramicroscopy* **1993**, *48* (3), 359–363.

(441) Egerton, R. F.; Rauf, I. Dose-Rate Dependence of Electron-Induced Mass Loss from Organic Specimens. *Ultramicroscopy* **1999**, *80* (4), 247–254.

(442) Glaeser, R. M. Specimen Behavior in the Electron Beam. In *Methods in Enzymology*; Elsevier, 2016; Vol. 579, pp 19–50.

(443) Dewhurst, H. A.; Samuel, A. H.; Magee, J. L. A Theoretical Survey of the Radiation Chemistry of Water and Aqueous Solutions. *Radiat. Res.* **1954**, *1* (1), 62–84.

(444) Fryer, J. R.; Holland, F. High Resolution Electron Microscopy of Molecular Crystals III. Radiation Processes at Room Temperature. *Proc. R. Soc. Lond. Math. Phys. Sci.* **1984**, *393* (1805), 353–369.

(445) Ungar, G.; Grubb, D. T.; Keller, A. Spatial Nonuniformity of Cross-Linking in Crystalline Alkanes of Different Chain Length. *Radiat. Phys. Chem. 1977* **1983**, *22* (3), 849–860.

(446) Dorset, D. L.; Turner, J. N. Thermal Effects in Electron-Beam Damage of Organic Crystals. *Naturwissenschaften* **1976**, *63* (3), 145–146.

(447) Henry, A.; Chen, G.; Plimpton, S. J.; Thompson, A. 1D-to-3D Transition of Phonon Heat Conduction in Polyethylene Using Molecular Dynamics Simulations. *Phys. Rev. B* **2010**, *82* (14), 144308.

(448) Wang, X.; Kaviany, M.; Huang, B. Phonon Coupling and Transport in Individual Polyethylene Chains: A Comparison Study with the Bulk Crystal. *Nanoscale* **2017**, *9* (45), 18022–18031.

(449) Kosasih, F. U.; Cacovich, S.; Divitini, G.; Ducati, C. Nanometric Chemical Analysis of Beam-Sensitive Materials: A Case Study of STEM-EDX on Perovskite Solar Cells. *Small Methods* **2020**, *5* (2), 2000835.

(450) Nan, G.; Zhang, X.; Lu, G. Self-Healing of Photocurrent Degradation in Perovskite Solar Cells: The Role of Defect-Trapped Excitons. *J. Phys. Chem. Lett.* **2019**, *10* (24), 7774–7780.

(451) Yu, Y.; Zhang, F.; Yu, H. Self-Healing Perovskite Solar Cells. *Sol. Energy* **2020**, *209*, 408–414.

(452) Zhao, Y.; Wei, J.; Li, H.; Yan, Y.; Zhou, W.; Yu, D.; Zhao, Q. A Polymer Scaffold for Self-Healing Perovskite Solar Cells. *Nat. Commun.* **2016**, *7* (1), 1–9.

(453) Frohna, K.; Deshpande, T.; Harter, J.; Peng, W.; Barker, B. A.; Neaton, J. B.; Louie, S. G.; Bakr, O. M.; Hsieh, D.; Bernardi, M. Inversion Symmetry and Bulk Rashba Effect in Methylammonium Lead Iodide Perovskite Single Crystals. *Nat. Commun.* **2018**, *9*, 1829.

(454) De Graef, M.; McHenry, M. E. *Structure of Materials: An Introduction to Crystallography, Diffraction and Symmetry*; Cambridge University Press, 2012.

(455) Pisoni, A.; Jaćimović, J.; Barišić, O. S.; Spina, M.; Gaál, R.; Forró, L.; Horváth, E. Ultra-Low Thermal Conductivity in Organic–Inorganic Hybrid Perovskite $CH_3NH_3PbI_3$. *J. Phys. Chem. Lett.* **2014**, *5* (14), 2488–2492.

(456) Qian, X.; Gu, X.; Yang, R. Lattice Thermal Conductivity of Organic-Inorganic Hybrid Perovskite $CH_3NH_3PbI_3$. *Appl. Phys. Lett.* **2016**, *108* (6), 063902.

(457) Onoda-Yamamuro, N.; Matsuo, T.; Suga, H. Calorimetric and IR Spectroscopic Studies of Phase Transitions in Methylammonium Trihalogenoplumbates. *J. Phys. Chem. Solids* **1990**, *51* (12), 1383–1395.

(458) Baikie, T.; Barrow, N. S.; Fang, Y.; Keenan, P. J.; Slater, P. R.; Piltz, R. O.; Gutmann, M.; Mhaisalkar, S. G.; White, T. J. A Combined Single Crystal Neutron/X-Ray Diffraction and Solid-State Nuclear Magnetic Resonance Study of the Hybrid Perovskites $CH_3NH_3PbX_3$ (X = I, Br and Cl). *J. Mater. Chem. A* **2015**, *3* (17), 9298–9307.

(459) Ghosh, T.; Aharon, S.; Etgar, L.; Ruhman, S. Free Carrier Emergence and Onset of Electron–Phonon Coupling in Methylammonium Lead Halide Perovskite Films. *J. Am. Chem. Soc.* **2017**, *139* (50), 18262–18270.

(460) Zhang, X.; Zhang, B.-B.; Ma, X.; Fu, M.; Zha, G.; Jie, W. Orientational Dependence of Electron Beam Irradiation Damage in Lead-Free Halide Double Perovskite $Cs_2AgBiBr_6$. *J. Phys. Chem. C* **2021**, *125* (23), 13033–13040.

(461) Yin, W.-J.; Shi, T.; Yan, Y. Unique Properties of Halide Perovskites as Possible Origins of the Superior Solar Cell Performance. *Adv. Mater.* **2014**, *26* (27), 4653–4658.

(462) Yan, Y.; Yin, W.-J.; Shi, T.; Meng, W.; Feng, C. Defect Physics of $CH_3NH_3PbX_3$ (X= I, Br, Cl) Perovskites. In *Organic-Inorganic Halide Perovskite Photovoltaics*; Springer, 2016; pp 79–105.

(463) Buin, A.; Comin, R.; Xu, J.; Ip, A. H.; Sargent, E. H. Halide-Dependent Electronic Structure of Organolead Perovskite Materials. *Chem. Mater.* **2015**, *27* (12), 4405–4412.

(464) Buin, A.; Pietsch, P.; Xu, J.; Voznyy, O.; Ip, A. H.; Comin, R.; Sargent, E. H. Materials Processing Routes to Trap-Free Halide Perovskites. *Nano Lett.* **2014**, *14* (11), 6281–6286.

(465) Yang, W. S.; Park, B.-W.; Jung, E. H.; Jeon, N. J.; Kim, Y. C.; Lee, D. U.; Shin, S. S.; Seo, J.; Kim, E. K.; Noh, J. H.; Seok, S. I. Iodide Management in Formamidinium-Lead-Halide–Based Perovskite Layers for Efficient Solar Cells. *Science* **2017**, *356* (6345), 1376–1379.

(466) Erk, B.; Boll, R.; Trippel, S.; Anielski, D.; Foucar, L.; Rudek, B.; Epp, S. W.; Coffee, R.; Carron, S.; Schorb, S. Imaging Charge Transfer in Iodomethane upon X-Ray Photoabsorption. *Science* **2014**, *345* (6194), 288–291.

(467) Southwick, P. L.; Christman, D. R. Reactions of Iodine—Amine Complexes with Unsaturated Compounds. II. An Investigation of the Scope of the Reaction with the Iodine—Morpholine Complex. *J. Am. Chem. Soc.* **1953**, *75* (3), 629–632.

(468) Brunetti, B.; Cavallo, C.; Ciccioli, A.; Gigli, G.; Latini, A. On the Thermal and Thermodynamic (In)Stability of Methylammonium Lead Halide Perovskites. *Sci. Rep.* **2016**, *6* (1), 31896.

(469) Delugas, P.; Filippetti, A.; Mattoni, A. Methylammonium Fragmentation in Amines as Source of Localized Trap Levels and the Healing Role of Cl in Hybrid Lead-Iodide Perovskites. *Phys. Rev. B* **2015**, *92* (4), 045301.

(470) Egger, D. A.; Kronik, L.; Rappe, A. M. Theory of Hydrogen Migration in Organic–Inorganic Halide Perovskites. *Angew. Chem. Int. Ed.* **2015**, *54* (42), 12437–12441.

(471) Marom, R.; Levi, C.; Weiss, T.; Rosenwaks, S.; Zeiri, Y.; Kosloff, R.; Bar, I. Quantum Tunneling of Hydrogen Atom in Dissociation of Photoexcited Methylamine. *J. Phys. Chem. A* **2010**, *114* (36), 9623–9627.

Appendix A | List of Common Abbreviations & Acronyms

Å	Angstrom
BBO	Beta barium borate
C36	Hexatriacontane ($C_{36}H_{74}$)
CAP	Coherent acoustic phonon
CCD	Charge coupled device
CMOS	Complementary metal-oxide-semiconductor
DP	Diffraction pattern
DTEM	Dynamic transmission electron microscopy/microscope
DW	Debye-Waller
e	Electron
E/P	Electrons per packet
eV	Electron volt
f	Repetition rate
f^{-1}	Time between electron pulses

fA	Femtoamp
FEG	Field emission gun
FIB	Focused ion beam
fps	Frames per second
fwhm	Full-width half max
keV	Kilo-electron volt
kHz	Kilohertz
MA	Methylammonium (CH_3NH_3)
$MAPbI_3$	Methylammonium lead iodide ($CH_3NH_3PbI_3$)
MEMS	Microelectromechanical systems
meV	Milli-electron volt
MHP	Metal-halide perovskite
nA	Nanoamp
nm	Nanometer
ns	Nanosecond
pA	Picoamp
pm	Picometer
SEM	Scanning electron microscopy/microscope
SHG-FROG	Second harmonic generation frequency resolved optical grating
SNR	Signal-to-noise ratio
TEM	Transmission electron microscopy/microscope
UED	Ultrafast electron diffraction
UEM	Ultrafast electron microscopy/microscope
V1	Pre-annealed experiment in Chapter 4
V2	Post-annealed experiment in Chapter 4
W	Watts
Yb:KGW	Ytterbium doped Potassium-Gadolinium Tungstate [Yb: $KGd(WO_4)_2$]
μJ	Microjoules
μm	Micrometer

μs	Microsecond

Appendix B | List of Publications, Presentations, and Posters

B.1 | Publications

Flannigan, D. J.; Chen, J.; Curtis, W.; Du, D.; Engen, P.; VandenBussche, E. J.; Zhang, Y. Time-resolved TEM Beyond Fast Detectors. *Acta Cryst. A* **2021**, (*accepted*).

VandenBussche, E. J. The Need for Sustainable Apparel. *Humphrey Policy Annual Review Blog* **2020**.

VandenBussche, E. J.; Clark, C. P.; Holmes, R. J.; Flannigan, D. J. Mitigating Damage to Hybrid Perovskites Using Pulsed-Beam TEM. *ACS Omega* **2020**, *5* (49), 31867–31871.

VandenBussche, E. J.; Flannigan, D. J. High-Resolution Analogue of Time-Domain Phonon Spectroscopy in the Transmission Electron Microscope. *Philos. Trans. R. Soc. A* **2020**, *378* (2186), 20190598.

VandenBussche, E. J.; Clark, C. P.; Holmes, R. J.; Flannigan, D. J. Pulsed Electron Beams for Mitigating Damage in Next-Generation Electronic Materials. *Microsc. Microanal.* **2020**, *26* (Suppl. 2), 2866-2868.

VandenBussche, E. J.; Flannigan, D. J. Using UEM to Probe Buried Structures in Real Space: An Analog to Phonon Spectroscopy. *Microsc. Microanal*. **2020**, *26* (Suppl. 2), 216-217.

VandenBussche, E. J.; Flannigan, D. J. Reducing Radiation Damage in Soft Matter with Femtosecond-Timed Single-Electron Packets. *Nano Lett*. **2019**, *19* (9), 6687-6694.

VandenBussche, E. J.; Flannigan, D. J. Reducing Radiation Damage Using Pulsed Electron Beams in the TEM. *Microsc. Microanal*. **2019**, *25* (Suppl. 2), 1646-1647.

VandenBussche, E. J.; Flannigan, D. J. Sources of Error in Debye-Waller-Effect Measurements Relevant to Studies of Photoinduced Structural Dynamics. *Ultramicroscopy* **2019**, 196, 111-120.

VandenBussche, E. J.; Flannigan, D. J. The Effect of a Pulsed Electron Beam on Damage Threshold. *Microsc. Microanal*. **2018**, *24* (Suppl. 1), 2002-2003.

VandenBussche, E. J.; Flannigan, D. J. Effects of Photoinduced Elastic Responses on Debye-Waller Temperature Measurements. *Microsc. Microanal.* **2018**, *24* (Suppl. 1), 1896-1897.

B.2 | Oral Presentations

Presenter name is underlined.

VandenBussche, E. J.; Clark, C. P.; Holmes, R. J.; Flannigan, D. J. "Understanding and Mitigating Damage in Hybrid Organic-Inorganic Perovskites Using Pulsed Electron Beams" MRS Virtual Meeting, Nov 29- Dec 4, 2020.

VandenBussche, E. J.; Clark, C. P.; Holmes, R. J.; Flannigan, D. J. "Elucidation and Mitigation of Radiation Damage in Hybrid Organic-Inorganic Perovskites Using Pulsed Electron Beams" AIChE Virtual Meeting, Nov 16-20, 2020.

VandenBussche, E. J.; Zhang, Y.; Reisbick, S. A.; Flannigan, D. J. "Nonequilibrium Light-Matter Interactions Investigated with Ultrafast Electron Microscopy" AIChE Virtual Meeting, Nov 16-20, 2020.

VandenBussche, E. J.; Clark, C. P.; Holmes, R. J.; Flannigan, D. J. "Pulsed electron beams in TEM for understanding and mitigating damage in hybrid organic-inorganic perovskites" ACS Virtual Meeting, Aug 17-20, 2020.

VandenBussche, E. J.; Clark, C. P.; Holmes, R. J.; Flannigan, D. J. "Pulsed Electron Beams for Mitigating Damage in Next-Generation Electronic Materials" Microscopy and Microanalysis Virtual Meeting, Aug 4-7, 2020.

VandenBussche, E. J.; Flannigan, D. J. "Using UEM to Probe Buried Structures in Real Space: An Analog to Phonon Spectroscopy" Microscopy and Microanalysis Virtual Meeting, Aug 4-7, 2020.

VandenBussche, E. J.; Flannigan, D. J. "Reducing Radiation Damage Using Pulsed Electron Beams in the TEM" Microscopy and Microanalysis Meeting, Portland, OR, Aug. 4-8, 2019.

Flannigan, D. J., VandenBussche, E. J., Du, D. X., Zhang, Y. "Imaging Ultrafast Coherent Phenomena and Mitigating Radiation Damage with Ultrafast Electron Microscopy" FEMMS 2019, Asheville, NC, Sept. 1-6, 2019.

VandenBussche, E. J.; Flannigan, D. J. "Effects of Pulsed Electron-Beam Characteristics on Radiation Sensitive Materials for Energy Applications" MRS Spring Meeting, Phoenix, AZ, April 22-26, 2019.

B.3 | Poster Presentations

Presenter name is underlined.

VandenBussche, E. J.; Flannigan, D. J. "Strongly Structure-Directed Phonon Dynamics in GaAs Observed by Ultrafast Electron Microscopy" MRS Virtual Meeting, Nov 29- Dec 4, 2020.

VandenBussche, E. J.; Flannigan, D. J. "Effects of Ultrafast Structural Dynamics on the Accuracy of Transient Debye-Waller Temperature Measurements" MRS Spring Meeting, Phoenix, AZ, April 22-26, 2019.

VandenBussche, E. J.; Flannigan, D. J. "Ultrafast Nanoscale Heat Transport in Semiconductors" Joint Undertaking for an African Materials Institute, Kampala, Uganda, December 10, 2018.

VandenBussche, E. J.; Flannigan, D. J. "The Effect of a Pulsed Electron Beam on Damage Threshold" Microscopy and Microanalysis Meeting, Baltimore, MD, Aug. 5-9, 2018.

VandenBussche, E. J.; Flannigan, D. J. "Effects of Photoinduced Elastic Responses on Debye-Waller Temperature Measurements" Microscopy and Microanalysis Meeting, Baltimore, MD, Aug. 5-9, 2018.

Appendix C | Derivation of Equation 3.3

The following is a derivation of Equation 3.3 from Equation 3.2 in the main text.

$$s_{\mathbf{g}} = \frac{-\mathbf{g} \cdot (2\mathbf{k} + \mathbf{g})}{2|\mathbf{k} + \mathbf{g}|\cos\beta} \quad (3.2)$$

Using the distributive property and the definition of a dot product,

$$s_{\mathbf{g}} = \frac{-2(\mathbf{g} \cdot \mathbf{k}) - (\mathbf{g} \cdot \mathbf{g})}{2|\mathbf{k} + \mathbf{g}|\cos\beta} \qquad \text{(C1)}$$

$$s_{\mathbf{g}} = \frac{-2|\mathbf{g}||\mathbf{k}|\cos\varphi - |\mathbf{g}|^2}{2|\mathbf{k} + \mathbf{g}|\cos\beta} \qquad \text{(C2)}$$

where φ is defined as the angle between the vectors **g** and **k**.

$$s_{\mathbf{g}} = \frac{-2|\mathbf{g}||\mathbf{k}|\cos\varphi - |\mathbf{g}|^2}{2|\mathbf{k} + \mathbf{g}|\cos\beta} \qquad \text{(C3)}$$

Also, by definition,

$$|\mathbf{k} + \mathbf{g}| = \sqrt{(\mathbf{k} + \mathbf{g}) \cdot (\mathbf{k} + \mathbf{g})} \qquad \text{(C4)}$$

$$= \sqrt{(\mathbf{k} \cdot \mathbf{k}) + (\mathbf{k} \cdot \mathbf{g}) + (\mathbf{g} \cdot \mathbf{k}) + (\mathbf{g} \cdot \mathbf{g})} \qquad \text{(C5)}$$

$$= \sqrt{|\mathbf{k}|^2 + 2|\mathbf{k}||\mathbf{g}|\cos\varphi + |\mathbf{g}|^2} \qquad \text{(C6)}$$

Therefore,

$$s_{\mathbf{g}} = \frac{-2(\mathbf{g} \cdot \mathbf{k}) - (\mathbf{g} \cdot \mathbf{g})}{2|\mathbf{k} + \mathbf{g}|\cos\beta} = \frac{-2|\mathbf{g}||\mathbf{k}|\cos\varphi - |\mathbf{g}|^2}{2\cos\beta\sqrt{|\mathbf{k}|^2 + 2|\mathbf{k}||\mathbf{g}|\cos\varphi + |\mathbf{g}|^2}} \qquad \text{(3.3)}$$